The
University
Of
Sheffield.

DEPARTMENT OF MECHANICAL ENGINEERING
THESIS SUBMITTED FOR THE DEGREE OF DOCTOR OF PHILOSOPHY

ADDITIVE MANUFACTURING FOR RAILWAY TRACK COMPONENT LIFE EXTENSION WITH PREMIUM LASER CLAD COATING

KATHERINE TOMLINSON

10th December 2021

Abstract

The lifespan of conventional grades of rail steel is limited by wear and rolling contact fatigue and can be costly to repair or replace. Additive manufacturing of premium rail materials with higher yield points which are more resistant to plastic damage could potentially increase the life of rails across the network. Laser cladding offers a feasible method of in-situ application on targeted areas which are more susceptible to damage. This study assesses laser clad low carbon Martensitic Stainless Steel (MSS) alloy with 14.64% chromium as a material for repair of railway track components considering the effect of the substrate rail.

The laser clad coatings resistance to strain presents challenges in characterisation, a novel method was developed to extract the Shear Yield Stress – Plastic Shear Strain (SYS-PSS) relationship from minimal twin-disc tests. A further set of low cycle twin-disc tests were conducted to determine the rate of strain accumulation within the materials. These experiments provided the data required to quantify plasticity using an empirical ratcheting model, a development to the modelling technique was made with the incorporation of a surface roughness model to generate the contact pressures which cause the plastic deformation in the top few microns of the laser clad coated rails. Hertzian contact pressures were assumed due to the low levels of plasticity within the novel rail materials. It was found that due to the higher yield stress of the new and novel rail materials that smooth Hertzian contact pressures were not sufficient to predict the depth and magnitude of ratcheting in the laser clad coating and substrate rail. A study into the surface topography and its effect of subsurface shear stress was conducted. The asperity peak wavelength and asperity tip radius were calculated from these measurements and further used in numerical simulations to calculate the asperity contact half width and asperity maximum Hertzian contact pressure, which was shown to be up to six times higher than the smooth contact.

In conclusion laser clad coating is considered to be a viable enhancement process for railway track component life extension using Martensitic Stainless Steel (MSS) alloy with 14.64% chromium. The laser process parameters and the depth of laser clad coating must be carefully controlled to achieve the desired quality, if the coating is too thin and the peak contact stress occurs below it, plastic shear strain accumulates within the substrate. The low levels of plastic shear strain observed in this work indicates that the wear and RCF performance would be improved compared to conventional rail steels. There is potential to reduce rail replacement frequency if applied to areas in track prone to damage. It is shown in the repair tests that this can cause the coating to become elongated and creep along the surface.There is further potential to utilise the laser clad coating method for in-situ repairs. A series of twin-disc tests were designed to test the integrity, wear and RCF of laser clad repairs using three candidate materials. A repair with a homogeneous material to the parent rail provided the most effective repair as the comparable ratcheting rate prevented material flow of the parent rail over the repair site, reducing crack initiation points. The geometry of the repair must be carefully controlled to avoid a thin coating at the surface interface as it is shown in the repair tests that this can cause the coating to become elongated and creep along the surface.

Acknowledgements

Declaration

I, Katherine Tomlinson, confirm that the Thesis is my own work. I am aware of the University's guidance on the use of unfair means (www.sheffield.ac.uk/ssid/unfair-means). This work has not been previously been presented for an award at this, or any other, university.

Publications arising from this thesis

Peer reviewed journal publications

1. Tomlinson, K., Fletcher, D.I., Lewis, R., "Measuring material plastic response to cyclic loading in modern rail steels from a minimal number of twin-disc tests" Proceedings of the Institution of Mechanical Engineers, Part F: Journal of Rail and Rapid Transit, First published 8th February 2021, DOI 10.1177/0954409721993615

Contents

Acronyms

BEM	Boundary Element Modelling
CoT	Coefficient of Traction
CWR	Continuous Welded Rail
EBSD	Electron Back Scatter Diffraction
EDM	Electro-Discharge Machining
ESDU	Engineering Science Data Unit
FEM	Finite Element Modelling
HAZ	Heat Affected Zone
HCF	High Cycle Fatigue
HP	High Performance
HWR	Head Wash Repair
IBJ	Insulated Block Joint
LIBS	Laser-induced Breakdown Spectroscopy
LCF	Low Cycle Fatigue
MSS	Martensitic Stainless Steel
PSS	Plastic Shear Strain
RCF	Rolling Contact Fatigue
RPM	Revolutions per Minute
SAW	Submerged Arc Welding
SEM	Scanning Electron Microscope
SIF	Stress Intensity Factor
SUROS	Sheffield University ROlling Sliding Twin-Disc Machine
SUROS 2	Sheffield University ROlling Sliding 2: TE 72 Roller Machine
SYS	Shear Yield Stress
WEL	White Etching Layer

Nomenclature

a_n	Asperity Contact Half Width	mm
b	Contact Half Width	mm
E	Elastic Modulus	Pa
E^*	Reduced Elastic Modulus	Pa
H	Hardness	MPa
γ_c	Critical Shear Strain (Limit of Ductility)	
γ_p	Plastic Shear Strain	
L	Length	mm
λ	Roughness Wavelength	μm
μ	Coefficient of Traction	
μ_{eff}	Effective Coefficient of Traction	
ν	Poisson's ratio	
τ_{zx}	Shear Stress	Pa
k_0	Initial Shear Yield Stress	Pa
k_{eff}	Effective Shear Yield Stress	Pa
N	Number of Asperities	
N_{eff}	Number of Effective Cycles	
p_0	Maximum Hertzian Contact Pressure	Pa
p_x	Pressure Distribution	Pa
P	Load	N
P_{eff}	Effective Ratcheting Load	N
P_r	Net Ratcheting Load	N
P_s	Plastic Shakedown Limit	Pa
R	Radius	mm
Ra	Average Roughness Profile	μm
ρ	Asperity Tip Radius	μm
σ_y	Tensile Yield Stress	Pa
$V(x)$	Vertical Displacement	μm

Chapter 1

Introduction

1.1 Background

This thesis explores the feasibility of in-situ bulk scale additive manufacture with a laser clad coating to extend the life of railway track components. The deposition of a composite material with benefits such as wear and rolling contact fatigue resistance, higher yield strength and less susceptibility to plastic deformation is a desirable method to increase the durability of rail whilst retaining the cost and strength advantages of bulk rail steels. Rail in service is subject to high compressive and shear loading on relatively small contact areas (around 1 cm^2) in a combination of rolling and sliding where it is contact with a wheel. Typically, such loading results in stresses exceeding the rail material's yield point and repeated cyclic loading in this manner can result in accumulated plastic shear strain in a process referred to as ratcheting, leading to large scale plastic deformation within the rail, which, if left untreated, can lead to wear and crack initiation reducing the lifespan of the rail.

A low carbon grade of Martensitic Stainless Steel (MSS) alloy with 14.64% chromium, the chemical composition of which is shown in Table 1.1, is selected as the laser clad coating material for researching in this project due to the strong bond at the interface and the increased wear and Rolling Contact Fatigue (RCF) resistance properties it provides [1, 2]. The MSS coating is formulated as a powder mix and applied with a one-step laser cladding process in which the powder is fed into a focused laser beam and scanned across the surface of the substrate material leaving a layer of the coating behind. The substrate material selected for the focus of the thesis is R260 grade rail steel, which is a 0.62% carbon steel alloy, due to its prominence across the UK network and the resulting harder clad coating compared with R200 grade rail steel seen in previous trials [2].

Across the network different grades of rail steel are in place, which vary in hardness and can be installed to best suit the type of loads they are likely to experience depending on the type of component and their position in track. Common pearlitic rail steel grades, widely reported in literature internationally are R200 and R260 with Brinell Hardness (HB) 200 HB and 260 HB respectively, these are often found in tangent track [3], the main difference between the alloys is the carbon content. High-performance rail HP335 has been developed to reduce wear and RCF with additional alloys and a higher percentage of carbon to improve the basic pearlitic structure and increase the hardness to 335 HB without the need for heat treatment, this is often installed in curved track or highly trafficked areas [4]. Crossing components are regularly made from Hadfield steel (cast manganese) which has 13.12% manganese and 1.21% carbon which provides its capability to work harden under impact loading when it may achieve a yield stress of up to 1,000 MPa [5]. A requirement of rail being installed on the network is that it is maintainable with

the ability to be repaired. Chemical compositions of the rail steels discussed here are shown in Table 1.1.

Element (wt %)	MSS	Stellite 6	R260	R200	HP335	Hadfield
Carbon (C)	0.06	1.2	0.62/0.80	0.40/0.60	0.87/0.97	1.21
Silicon (Si)	0.46	min	0.15/0.58	0.15/0.58	0.75/1.00	0.52
Manganese (Mn)	1.22	min	0.70/1.20	0.70/1.20	0.75/1.00	13.12
Phosphorus (P)	0.009	-	$\leqslant 0.025$	$\leqslant 0.035$	$\leqslant 0.020$	0.033
Sulfur (S)	0.005	-	0.008/0.025	0.008/0.025	0.008/0.025	0.035
Chromium (Cr)	14.64	28.0	$\leqslant 0.15$	$\leqslant 0.15$	$\leqslant 0.10$	-
Aluminium (Al)	0.01	-	$\leqslant 0.004$	$\leqslant 0.004$	$\leqslant 0.004$	-
Vanadium (V)	0.51	-	$\leqslant 0.03$	$\leqslant 0.03$	0.09/0.13	-
Hydrogen (H2(ppm))	-	-	$\leqslant 2.5$	$\leqslant 3.0$	$\leqslant 2.5$	-
Nickel (Ni)	3.31	min	-	-	-	-
Molybdenum (Mo)	0.42	min	-	-	-	-
Cobalt (Co)	2.01	Bal	-	-	-	-
Tungsten (W)	0.62	4.5	-	-	-	-
Nitrogen (N)	0.04	-	-	-	-	-
Iron (Fe)	Bal	min	Bal	Bal	Bal	Bal

Table 1.1: Chemical composition (% by mass) of MSS laser clad coating [2], Stellite 6 laser clad coating [6] and rail steel grades R260 [3], R200 [3], HP335 [4] and Hadfield [5].

Research in small scale additive manufacturing with laser clad coatings has previously shown promising results in laboratory tests for reducing wear in rail, as highlighted in the literature review of laser clad coatings in Chapter 2. Figure 1.1 shows an example of a full size rail clad trial with a MSS coating successfully applied to a section of R260 grade rail steel.
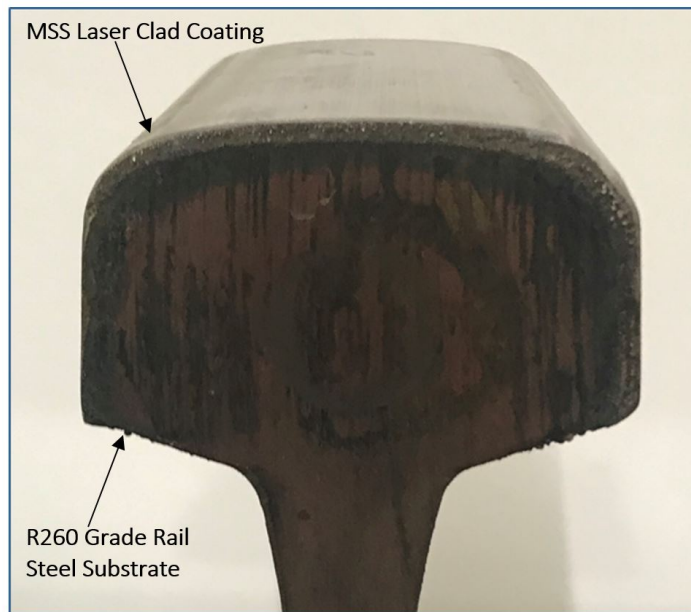
Figure 1.1: Section of standard grade rail steel with a demonstration of MSS laser clad coating applied to the surface manufactured for Lewis et al. [7].

The advancement of this laser clad coating application in this thesis includes developing methods to test the material properties of laser clad coatings, quantifying plasticity at the surface of laser clad coated rails and experimentally testing the wear and RCF performance of laser clad repairs.

The motivation for the thesis comes from Network Rail's expressed interest in applying a laser clad coating in-situ as a repair or enhancement technique as it is a promising method of extending the life of railway track components either through repair or enhancement, particularly benefiting relatively small, high value components such as switches and crossings (the moveable sections of track which allow trains to cross paths). Maintenance of rails must be planned carefully to minimise disruption to the network as engineering work requires a railway track to be closed. Typical maintenance of the rails includes a scheduled profile grinding program and regular monitoring using specialised equipment to identify flaws which require the rail to be repaired or replaced. New methods to extend the lifespan of railway track components to reduce the frequency of replacement would limit disruption to passengers. A successful in-situ repair method would also extend the lifespan of railway track components resulting in fewer line closures for additional maintenance, increased capacity and reduced maintenance costs, having a positive impact on the rail network in the UK.

Economic context

The rail network in the UK is ordinarily extremely busy as it is shared by freight and passenger trains. Freight on the rails (quantified as billion net tonne kilometre) had a decline around 2015 as coal-based energy was phased out. The proportion of freight moved by rail within the UK has however increased with around 9% of all freight being transported by rail in 2017. In 2018/19 rail freight had increased to 17.4 billion net tonne kilometres [8], but then dropped slightly to

16.6 billion net tonne kilometres in 2018/19 [9]. The 2020/21 pandemic caused a decrease in freight transported on the rail but not to the same extent that passenger usage was affected. Both quarter 1 and quarter 2 2020/21 saw the lowest quarterly freight transported since records began in 1998/99, although a recovery in quarter 2 can be seen with a 23.1% increase on quarter 1. Plans to increase capacity on the network with investment in infrastructure projects such as HS2 should see more space for freight on the existing network with the aim of reducing carbon emissions and congestion on the roads [10], this could lead to heavier loads on the existing rails.

At the initiation of this project passenger demand was continually increasing, as it had since rail privatisation in the mid 1990s, with a record 1.8 billion journeys taken in the year 2018/19 [8]. The Covid-19 pandemic of 2020/21, however, halted this trend as the initial national lockdown caused a rapid decline in passenger journeys predominately seen in Quarter 1 (April - June) 2020/21 where only 35 million journeys were made compared with 439 million journeys in the same period the previous year, Figure 1.2 [11, 12]. As lock-downs were lifted and reintroduced the level of passenger journeys fluctuated, returning to 182 million journeys in the first quarter of 2021/22 but this is still much lower than passenger usage prior to the pandemic.
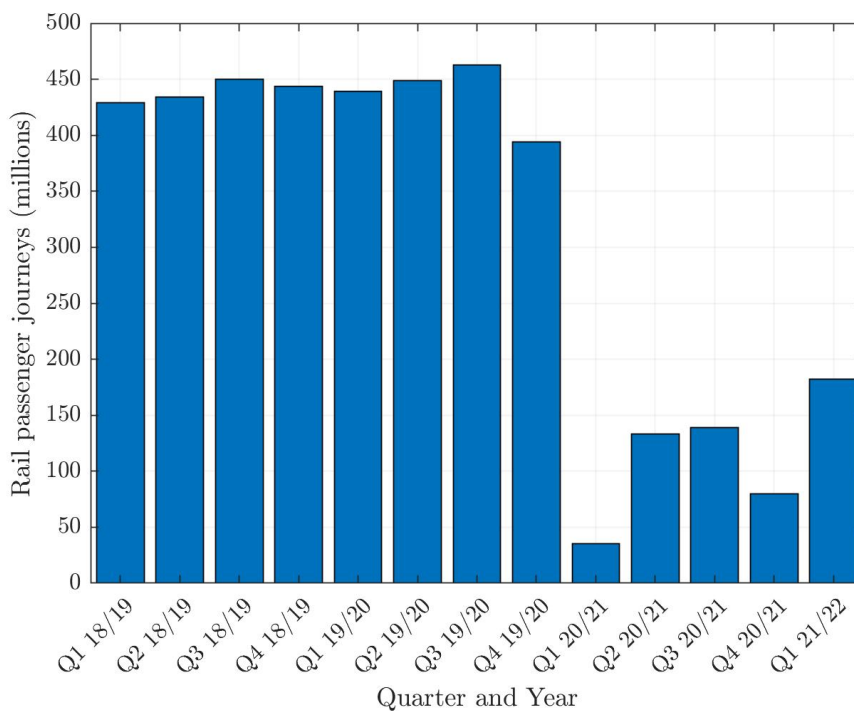
Figure 1.2: Rail passenger journeys UK showing the income from rail passenger journeys from 2018 to the sudden decrease in 2020/21 due to the Covid-19 pandemic [11, 12]

The rail industry incurs high costs in operating and maintaining infrastructure. The annual expenditure of Network Rail in the year 2019-20 was £8.4 bn [13], of which 20% (£1.7 bn) was spent on the maintenance of the 20,000 miles of track in England, Scotland and Wales which they are responsible for, Figure 1.3.
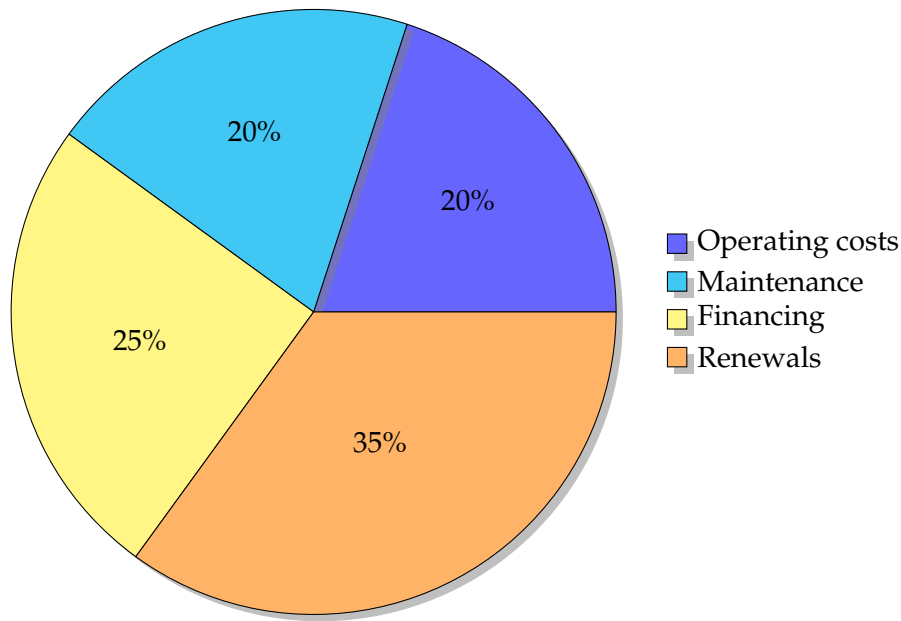
Figure 1.3: Network Rail Expenditure 2019/20 showing that maintenance and renewals account for 55% of the total expenditure.

1.2 Novelty

Laser clad coatings were shown to have the potential to enhance and extend the lifespan of rail within the literature review. It was hypothesised that laser clad coatings could be utilised as an in-situ method to repair damaged rails. New data was collected to assess wear and RCF of laser clad surfaces, with a particular focus on application of the technique as a repair method. Observations of the repair integrity were made and potential crack initiation points were identified as laser clad repairs were tested under typical cyclic rail-wheel loading for the first time.

A novel method to extract material properties of laser clad coatings from minimal twin disc tests has been developed. This was necessary as quantifying physical properties of such materials with yield points much higher than conventional rail steel is challenging as less strain is accumulated and the laser clad coating depths are often too thin for traditional tensile testing. The method developed provides a cost and time effective way to obtain the data required to characterise the Shear Yield Stress-Plastic Shear Strain (SYS-PSS) material response to load. Laser clad coatings, despite being highly resistant to plasticity, still experience some at depths comparable to asperity stress fields. Plastic ratcheting was quantified in laser clad coatings for the first time with a model developed using the effect of surface roughness. These methods can be applied to other new rail materials which have either limited test samples or are more resistant to strain.

Despite the improvements to wear and RCF resistance seen previously with the application of a laser clad coating, plasticity is still seen within the shallow depths below the rail-wheel contact and testing shows that it is still the main mechanism responsible for initiation of damage. Standard modelling with a smooth Hertzian contact does not predict the ratcheting observed in the laser clad coatings due to the high yield stress of the material. To explain this the surface rough-

ness was assumed to create a series of individual asperity Hertzian contacts since the plasticity was low. These individual contacts were then superpositioned across the full contact area. To allow accurate modelling surface topography was measured using an Alicona PortableRL Infinite Focus microscope. This is the first time that the surface topography of laser clad coatings has been studied in this way with the calculation of asperity peak wavelength and asperity tip radius. This was further incorporated into modelling plastic ratcheting in the laser clad coated rail.

1.3   Aims and objectives

The aim was to quantify plastic damage and identify its causes and consequences in novel rail materials. The methods developed should be generalisable to a wide range of materials but the focus of this study is a novel rail system consisting of low carbon Martensitic Stainless Steel (MSS) alloy with 14.64% chromium applied through laser cladding to 0.62% carbon steel alloy substrates. Considering cases where the alloy is loaded by contact pressures in the order of 800 to 1500 MPa simulating plain line rail components. The motivation for this study was assessing these materials for application in repair of railway track components.

The aim was achieved by:

- Producing a method to enable the characterisation of laser clad coating material properties including the extraction of the SYS-PSS relationship.

- Testing the integrity, wear and Rolling Contact Fatigue (RCF) of twin disc samples repaired with inserts of laser clad coatings.

- Developing a surface roughness contact model to allow computation of the shear stresses experienced in the shallow depths of the laser clad coating.

- Quantifying plasticity in laser clad coated rail steels incorporating the surface roughness model to explain the resultant shallow depths of plastic deformation observed in experiments.

1.4   Thesis structure

This preliminary chapter introduces the background to the project and clarifies the motivation behind it. The novelty and contribution of the project is identified and the aims and objectives have been set. The following chapters document the knowledge and understanding created in the following sequence.

Chapter 2

Chapter 2 is a literature review exploring the metallurgical properties and geometry of rail to understand the common defects arising from the complexities of rail-wheel contact which contributes to failure of conventional rail. The technical background presented in this chapter is followed by a literature review of previous research which has been conducted in fields relevant

to additive manufacturing with premium laser clad coating for the life extension of railway track components to identify gaps in knowledge.

Chapter 3

The material properties of low carbon MSS alloy with 14.64% chromium, applied to 0.62% carbon steel substrates and the impact of the thermal route taken during the production of additively manufactured components using these materials are determined in Chapter 3. Characterising the material response to load requires a novel method to be developed due to the small sample sizes and the high resistance to ratcheting. Through the work presented here a method is developed to quantify the material response to load and extract the SYS-PSS relationship of modern rail steels and laser clad coatings with the analysis of samples from twin-disc tests. The work in this chapter provides the material data to apply to modelling in Chapter 6 to enable the quantification of plastic ratcheting.

Chapter 4

Experimental results of twin disc tests using novel specimens manufactured from 0.62% carbon steel with six laser clad repair slots are presented in chapter 4. Two of the laser clad repair slots are filled with the low carbon MSS alloy with 14.64% chromium, two are filled with the same 0.62% carbon steel as the parent disc and the further two are filled with cobalt based Stellite alloy. This work is a first step to understanding how a laser clad repair will behave. It explores whether they survive under cyclic loading and what damage mechanisms exist at the clad to substrate interface. The material properties of the repairs and the surrounding substrate material are examined before and after wear and RCF tests, with observations of the repair site and heat affected zone integrity and a comparison to weld repair methods is made. The suitability of eddy current testing for identifying flaws within MSS is evaluated in this chapter to assess it as a non-destructive examination methods for laser clad repairs.

Chapter 5

Laser clad coatings can provide a wear and RCF resistant coating to extend the life of railway track components, however, plasticity is still observed within the top few microns of laser clad coatings and modern, harder rail materials with higher yield strengths than conventional rails. Standard modelling with a smooth Hertzian contact does not predict the depth or magnitude of plastic shear strain accumulation in the laser clad coating due to the high yield stress of the material. Chapter 5 presents the results of surface topography measurements of MSS laser clad coating and R260 grade rail steel. The asperity peak wavelength and asperity tip radius are then measured from this and used to calculate the maximum asperity Hertzian contact pressure, this method is considered to be applicable as the level of plasticity is low.

Chapter 6

Plastic shear strain can be an underlying cause of wear and rolling contact fatigue in conventional rail steels, it is quantified in laser clad coatings on rail steels in Chapter 6. Plasticity was modelled

using a layered representation of the MSS-R260 steel alloy system, building on literature documenting models of single material cases. Simulations are presented to demonstrate the depth and magnitude of plastic ratcheting in the laser clad coated railway track component, the results of which can be used to form specifications of laser clad coating depth to prevent ratcheting within the coating or substrate rail. This model is validated with the results of independent twin-disc testing.

Chapter 7

A high level discussion is presented in chapter 7, bringing together the individual discussions from each chapter. Linking these together allows an overview of the contribution this thesis has in terms of both scientific knowledge and industry application.

Chapter 8

Conclusions from the research presented in the thesis are presented in chapter 8. These conclusions are used as an initial point from which an understanding of the required tolerances, depth and morphology of in-situ application can begin to be developed for different grades of rail steel and different component types. Ideas are discussed on how to take the work further including how to get the laser process safely out of the lab and out on track to apply in-situ.

Chapter 2

Literature Review

2.1 Introduction

Prior to researching a method to extend the lifespan of railway track components it is imperative to consider the purpose of the rail, its metallurgical properties and geometry and to understand the common problems arising from rail-wheel contact which contributes to rail failure. This chapter will address the theory to provide context for the further sections, focusing on the mechanics and materials of the rail-wheel contact at which high train loads routinely take rail materials to extreme stress levels. The latter part of this chapter will explore the latest published research on how laser clad coatings have been developed with the intention of being applied to rail steels and determine opportunities to advance this area of research.

The UK rail network offers a safe and reliable method of transporting passengers and goods across the country daily, with vehicle and track working together in harmony. Railway vehicles, referred to as rolling stock, are designed to encase and protect their payload whilst providing a smooth journey from A to B. The railway track is designed to support and guide rolling stock on its journey, withstanding the high load and related forces whilst providing a safe environment for traction and braking forces.

The rail is the focus of this study, however, it is important to consider that the rail sits on top of a well-designed support foundation as illustrated in Figure 2.1. This configuration is often called ballasted track and each layer has its own role to play. Drainage is created in the sub-ballast as this is a permeable layer, taking water away from the surface and directing it into a channel or pipe. The layer of ballast and the ballast shoulder hold the sleepers in place, ensuring the correct distance, known as gauge, is maintained between rails and controls the stiffness of the track. The rails are then secured onto the sleepers with specially designed fixings which allow the control of the lateral position of the rail. The sleepers and fixings then distribute the high loads applied by rolling stock, from the rail into the ballast and substructure of the track [14].

The rail is designed as a smooth-running surface for rolling stock which guides wheels in a lateral direction. Rolling stock can accelerate and brake effectively due to adhesion with the rail. The rail takes the vertical loads and transverse forces from the wheel and distributes these to the sleepers and fixings. The rail must also be able to conduct electricity for signal currents and on electrified lines. The geometry and metallurgical properties are therefore crucial to meet the high demands placed upon the rail.
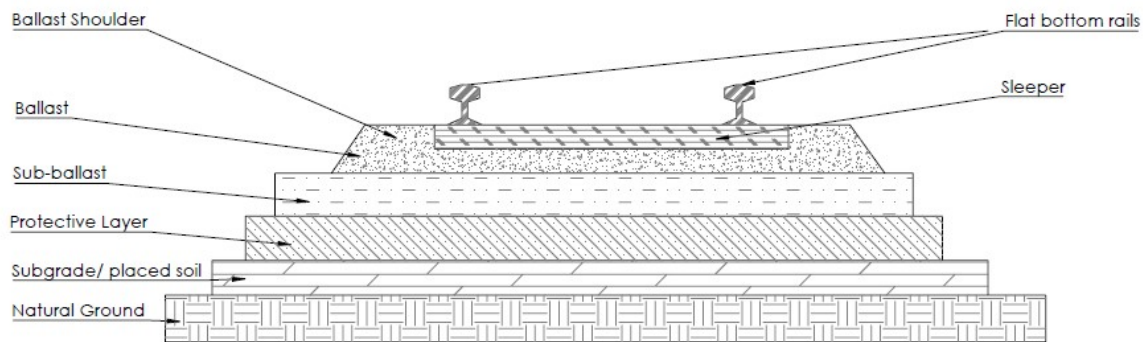
Figure 2.1: Schematic diagram of ballasted railway track structure illustrating the well-designed support foundation below the rail.

2.1.1 Rail geometry

There have been many designs of rail since they were first used in the sixteenth century, over time they have developed and today the most commonly used rail in straight track is the symmetrical flat-bottomed Vignole rail [15], the profile of which is shown in Figure 2.2.
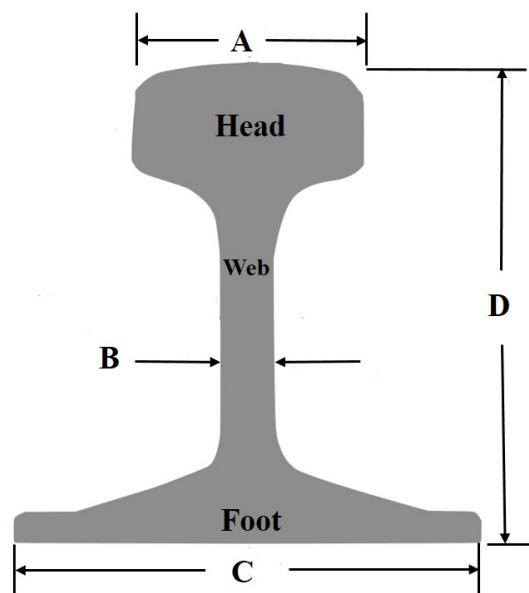
Figure 2.2: Section of symmetrical flat-bottomed Vignole rail with dimensions head width **A**, web thickness **B**, foot width **C** and rail height **D** which vary dependent on the profile.

The rail head is the part of the rail that the wheel is in contact with, it is designed and maintained to provide a good contact, the dimensions must be generous enough to provide a wear margin to provide an acceptable lifespan as the rail wears down over time. The rail web is designed to prevent buckling of the rail whilst supporting the head and it transfers the load through the rail. The rail foot provides stability and enables distribution of the load, the wide design of the foot in the Vignole rail enables a secure and stable fixing to the sleepers [14].

10

There are many different dimensions of Vignole rail in use across different parts of the network. One of the most common rail profiles in the UK and Europe is the 60 E1 (UIC 60), the dimensions of which are 172 mm from base of foot to top of head (D), the foot is 150 mm wide (C), the web has a thickness of 16.5 mm (B) and the head is 72 mm wide (A). It has a section weight of 60.21 kg per metre [16].

Some railway track components, such as those in switches and crossings, have a very different geometry as they are designed for different purposes. Switches and crossings allow a train to pass from one track to another to be able to change direction. These consist of high value components like crossing nose, switch blades, wing rails and check rails. These components experience different forces, like impact loading as the train passes over, and different problems to standard tangential rail due to their geometry and position. Of the 20,000 miles of track in the UK, less than 5% consists of switches and crossings. However, the limited lifespan of such components due to the high lateral forces experienced as trains move over them contributes to a significant proportion of the maintenance expenditure. The application of laser clad coatings to extend the lifespan of switch and crossing components could be beneficial. The focus of this thesis is the application of laser clad coatings to plain line components, however, in further work the methods developed here could be applied to switch and crossing components to further develop the technique.

2.1.2   Rail metallurgy

The rail metallurgy is critical in supporting rolling stock, it must be strong enough to endure both the high contact forces imposed on it and dynamic loads generated by irregularities of the rail or wheel [17]. Rails have been formed from steel since the late nineteenth century, the production of which has been developed and improved to meet the high demands of today. Rail steel, in general, has a higher percentage of carbon than construction steel. International standards specify the material properties which a rail in service must meet. Rail is categorised into different grades dependent on its chemical composition, this is to cater to the needs of different track conditions and types of component. Two common rail steel grades which meet the European standard EN 13674-1 are R200 and R260, the differences in chemical compositions is shown in Table 1.1.

Rail steel is manufactured using a heating and rolling process, the production process creates residual stresses within the rail which are controlled by balancing the tensile and compressive residual stresses to prevent crack growth. As the steel is heated and cooled it forms a layered microstructure consisting of ferrite (pure iron) and cementite (iron carbide), which is known as pearlite. Between the ferrite and cementite is interlamellar spacing, the size of which varies between different grades of rail steel, with finer spacing providing more resistance to wear. Figure 2.3 shows an SEM image of R260 grade rail steel using 3,000 x magnification, the dark area that can be seen is ferrite and the light areas are cementite.

Pearlitic steel is widely used for rail steel due to its ability to strain harden during the early cycles of load application providing wear resistant properties, it has a fairly low production cost due to the absence of alloying elements which is necessary due to the expanse required on the network [18]. Ferrite is ductile and soft (150 Hv), whereas cementite is brittle and hard (772 Hv), both have

different yield points. Plastic flow therefore occurs within the ferrite, reducing the interlamellar spacing, making the rail more wear resistant. The cementite, which is harder, and more wear resistant is in turn left with a higher proportion on the contact surface. The overall hardness of rail steel is between 220 and 400 Hv, dependent on the grade of rail steel, due to the metallurgical properties of pearlitic steel it can support the same loads and contact pressures as a 700 – 800 Hv rolling element bearing surface.

B23-NOP-0025   N   D5.0   x3.0k   30 µm

0 deg layer (shoulder region)
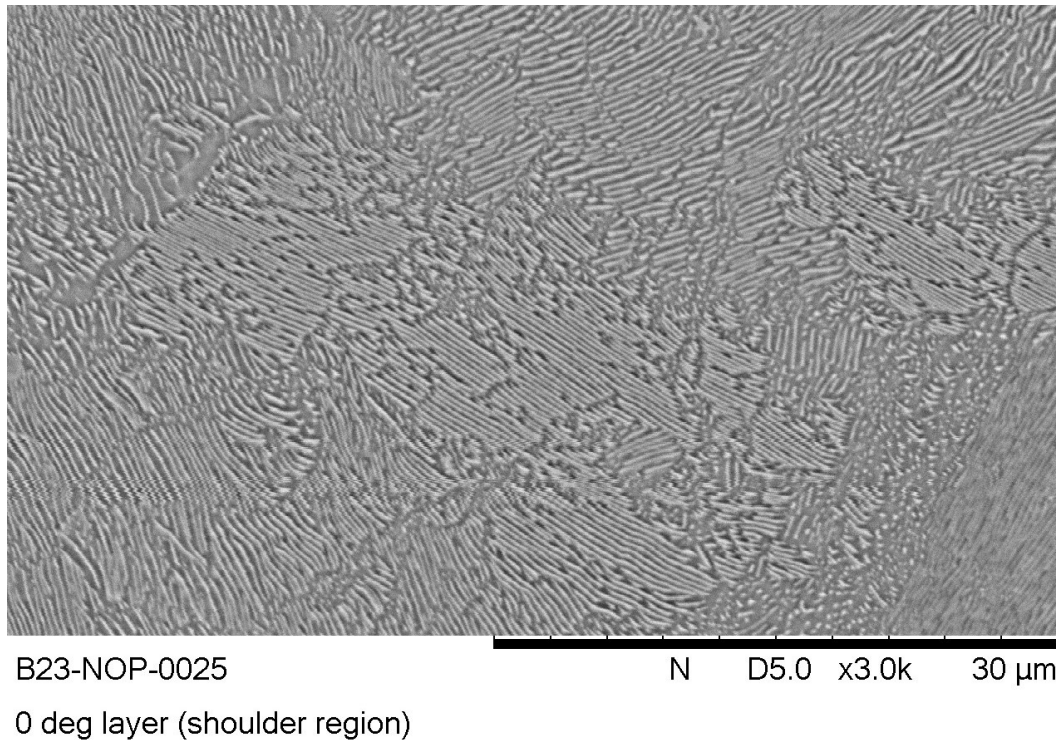
Figure 2.3: SEM image showing the two phased lamellar microstructure of pearlitic rail steel consisting of ferrite and cementite.

Perez-Unzueta et al. [19] tested pearlitic rail steel with a range of interlamellar spacings in pure sliding and rolling-sliding contact to simulate rail-wheel contact. They found that with plastic deformation the pearlite lamellae (in particular the cementite) become parallel to the wear surface. The cementite lamellae become thin and bent and form a network of flakes which increase the amount of harder cementite in the contact area, this provides pearlite with an advantage over martensite or bainitic rail which do not have such an adaptable microstructure. They also showed that a reduction in interlamellar spacing increases the hardness which in turn lowers the wear rate. The most wear resistant rails were said by Perez-Unzueta et al. to be those with fine interlamellar spacing and thin cementite lamellae.

Premium or heat treated rail steels are installed in some areas of track which experience heavy-haul and would otherwise require extra maintenance to keep them safe and compliant. British Steel introduced the high performance HP335 in 2012, it is a hypereutectoid steel with the carbon content increased to 0.87%. It has since been widely used by Network Rail across the UK mainline network and is reported to typically increase rail life by 66% [20]. Heat treated rails also known as head-hardened rails provide a more wear resistant rail by reducing the lamellar spacing in the

pearlite. The rail is heated and cooled in a controlled way to prevent unbalanced stresses, it is then often installed in curved or heavy haul tracks to prevent wear or fatigue in the rail foot [21].

2.2   Rail-wheel contact

Having considered the purpose, geometry and basic metallurgy of the rail the way in which rolling stock wheel comes into contact with the rail must be examined and the ways in which this complex contact can be modelled. Rail in service is subject to high compressive and shear loading on relatively small contact areas (around 1 cm^2) and a combination of rolling and sliding where it is in contact with a wheel. Typically, such loading results in stresses exceeding the yield point of the rail material and consequently in plastic strain occurring. The contact patch size and position vary with the geometry of each individual wheel and rail, the position and angle in the track and lateral shifts.

The contact of rail and wheel is complex and is dependent on many variables such as the wheel and rail profiles, the bogie design of the rolling stock, the curvature of the rail and environmental conditions. The rail-wheel contact varies in size and position as the train moves along the rail which in turn changes the contact stresses experienced in the rail. Considering a simplified cross section of the wheel and rail as shown in Figure 2.4, the contact area generally falls into one of three regions [22]. Contact in region A occurs when wheel tread meets rail head on a straight track, this type of contact is most common and produces the lowest contact and lateral forces. Contact in region B or C is much less likely to occur but experiences much higher stress and wear rates. Contact region B would occur when the wheel flange is in contact with the rail gauge corner. Region C is likely to occur on low rails or from incorrect steering as the field sides of the wheel and rail would be in contact.
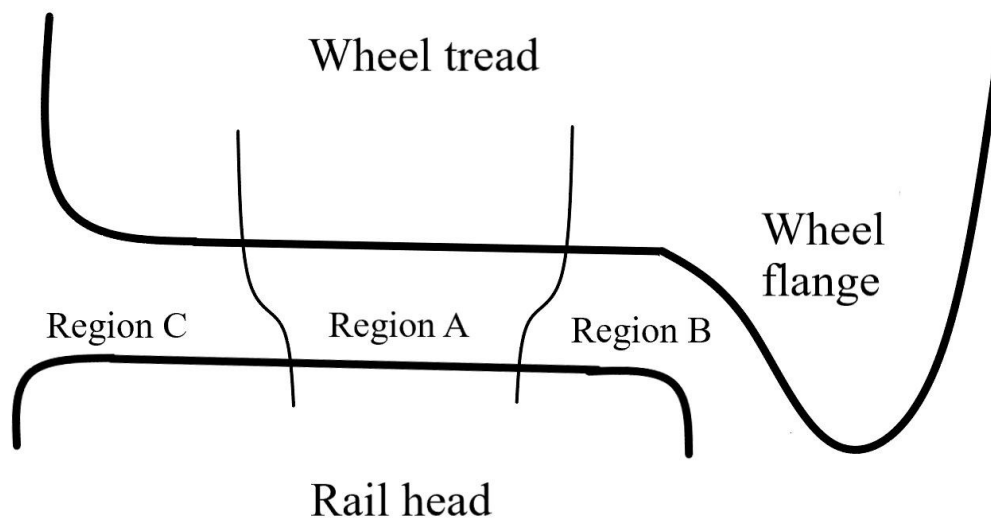
Figure 2.4: Simplified cross section of rail-wheel showing regions in which rail-wheel contact can occur.

In rail-wheel contact the term 'coefficient of traction' is used to describe the ratio of traction and

normal forces in contact. This is because the value varies over time which is thought to be due to the changes in the surface layer as deformation occurs, whereas Amonton's law of friction states that friction is a constant and only depends on the two materials in contact [23]. The coefficient of traction is more suitable as the ratio can be represented at any slip level, where as the coefficient of fraction is only defined at full slip. The level of traction in the contact and the Poisson's ratio of a material determine whether the peak in stress at the contact occurs at the surface or lower down in the material. For rail steel with Poisson's ratio $\nu = 0.3$ the maximum shear stress would be expected at the surface where the coefficient of traction is greater than 0.3, this is illustrated in Engineering Sciences Data Unit (ESDU) Contact Phenomena II [24].

When referring to wheel-rail contact adhesion levels describe the limiting friction from the tangential force between wheel and rail at the rail-wheel interface [25], indicating how much 'grip' is available between the wheel and rail. This adhesion created in the relatively small area of contact is required for both traction and braking. Traction requires an adhesion level of around 0.15 for a passenger train and up to 0.25 for freight, braking requires an adhesion level of around 0.1 to stop within the allowed maximum emergency stopping distance of 890 m, according to Railway Group Standard GMRT2045 section 2.3.2.6 [26].

Rail-wheel contact is tribologically an open-system which is exposed to external elements, meaning that within the contact dirt, leaves, debris or rain water, for example, could be present [17]. The level of adhesion is influenced by such environmental factors, clean rails whether wet or dry can produce an adhesion level of over 0.15, where rails with severe contamination such as leaves, or other pollution may have an adhesion level as low as 0.05 [14] which can increase braking distances and cause a dangerous situation. If the adhesion level is too high severe wear and deformation can occur or even derailment [27]. Creating an optimal level of adhesion or coefficient of traction as it also termed, is essential for rail safety and should be considered when designing and testing a surface coating to ensure safe traction and braking. Figure 2.5 demonstrates the direction of traction in the opposite way to the direction of rolling stock travel.
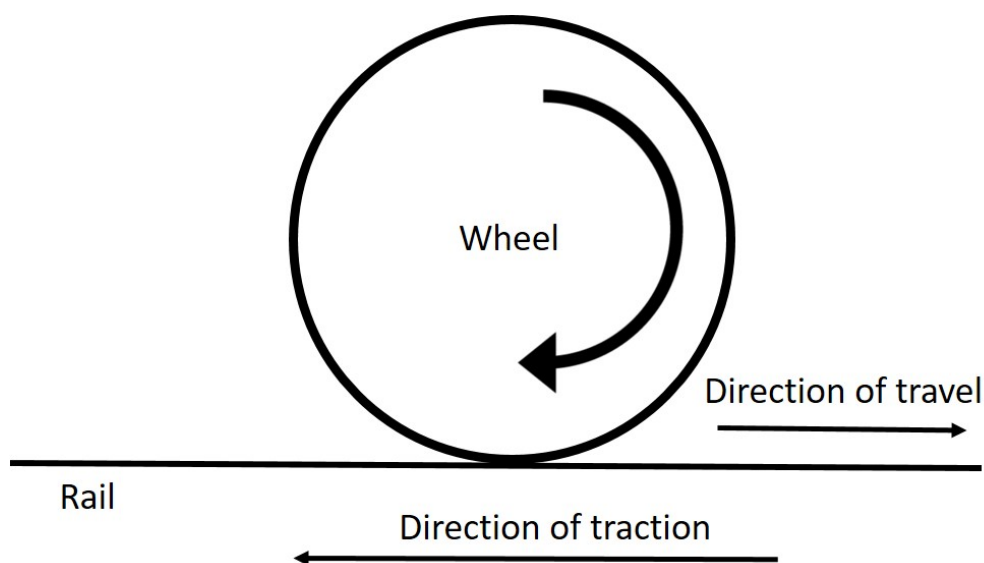
Figure 2.5: Direction of traction experienced by the rail opposed to the direction of travel of accelerating rolling stock.

The demands placed upon the rail are more extreme than most rolling contact situations as both accelerating and braking produce a combined rolling-sliding contact. When the train accelerates, the wheel turns marginally faster than pure rolling to generate a driving force. When the train brakes the wheel turns slightly slower than pure rolling to achieve a braking force. This rolling-sliding contact results in a non-uniform distribution of shear stress as the rail and wheel are put in tension and compression in different areas. The combined rolling-sliding contact causes traction, this along with the tangential forces generated as the train curves, is important as it leads to maximum stress at the surface which drives damage and causes the problems associated with maintenance or failure of the rail. Occasionally, where a wheel spin occurs or a wheel locks, the contact may change to pure sliding. The amount by which a wheel is turning faster or slower than pure rolling is known as slip or creep γ. This is quantified by a theoretical percentage for the overall contact, calculated by Equation 2.1.

$$\gamma = \frac{\omega_w R_2 - u_t}{u_t} \tag{2.1}$$

where ω_w represents the wheel angular velocity, R_2 is the wheel radius and u_t is the velocity of the train. In rail-wheel contact an element of slip is created at the trailing edge of the interface caused by the tractive force.

2.2.1 Modelling rail-wheel contact

Rail-wheel contact has commonly been modelled with the application of Hertz theory, developed by Heinrich Hertz in 1882 [28]. Assumptions are made that the contact area is small relative to the two bodies overall dimensions, the pressure profile is elliptical and the contact is smooth and frictionless when applying Hertz contact theory. Figure 2.6 shows a sketch of the elliptical area of contact, the forces and stresses in the contact.

The contact patch between wheel and rail is difficult to measure yet Hertz theory has been shown to be representative of the pressure distribution within the contact. This has been researched by comparing the results of Hertz theory with other methods such as finite element modelling [29] and ultrasound [30] and it is concluded within the literature that Hertz theory still provides a good estimate for a complex contact in cases where the level of plastic flow is relatively low.
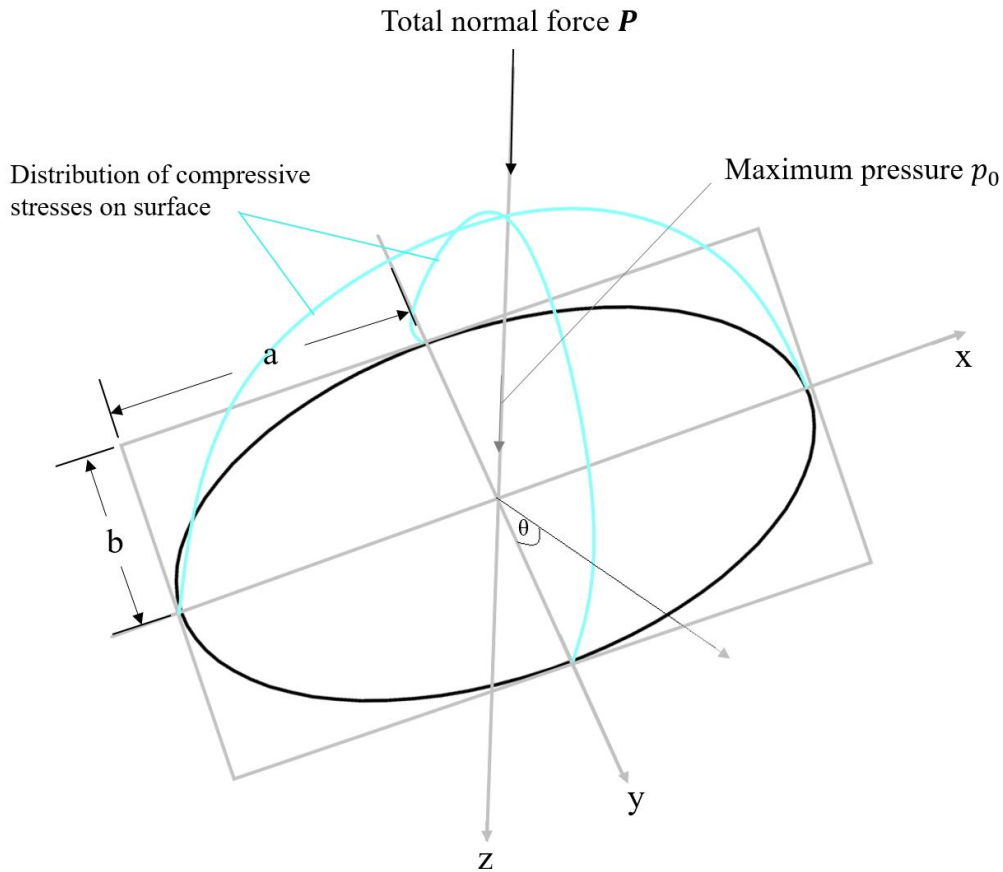
Figure 2.6: Sketch of elliptical contact area, forces and stresses in Hertzian contact.

This type of contact has a contact pressure which rises from zero to a peak pressure p_0 across a semi-ellipsoidal distribution. In three dimensional models the total load is related to the contact pressure with the integral in Equation 2.2 [31].

$$P = \int_0^a p(r)2\pi r dr = \frac{2}{3}p_0\pi a^2 \quad p(r) = p_0\{1 - \frac{r^2}{a^2}\}^{1/2} \tag{2.2}$$

where $r^2 = x^2 + y^2$. To calculate the maximum contact pressure p_0 the contact patch radius a must be calculated using Equation 2.3.

$$a = \left(\frac{3PR}{4E^*}\right)^{1/3} \tag{2.3}$$

In which the elastic properties of the rail and wheel must first be combined to find a reduced radius R, Equation 2.4.

$$\frac{1}{R} = \frac{1}{R_1} + \frac{1}{R_2} \tag{2.4}$$

And a reduced contact modulus E^*, Equation 2.5.

$$\frac{1}{E^*} = \frac{1 - \nu_1^2}{E_1} + \frac{1 - \nu_2^2}{E_2} \tag{2.5}$$

For laboratory simulations of rail-wheel contact twin-disc experiments are often used, in which two cylinders are loaded together in parallel. This can be represented by a simplified line contact as the ellipse becomes infinitely long [14]. This leads to simplified Hertzian equations in which the maximum contact pressure p_0 can be found using Equation 2.6.

$$p_0 = \frac{2P}{L\pi b} \tag{2.6}$$

The contact half-width b is given by Equation 2.7 with reduced radius R, Equation 2.4 and reduced modulus $E*$, Equation 2.5.

$$b = \sqrt{\frac{4PR}{L\pi E^*}} \tag{2.7}$$

The pressure distribution across the contact can further be calculated using Equation 2.8.

$$p_x = p_o(1 - (x/b)^2)^{1/2} \tag{2.8}$$

Experimental work has been carried out by Marshall et al. [30] to assess the real contact patch between rail and wheel using an ultrasonic reflection method. The shape of the contact is comparable to the elliptical contact which Hertzian contact modelling assumes. The work highlighted the difference in the pressure distribution at the contact depending on the state of the wheel and rail as they tested unused, sand damaged and worn rails, with the roughness of the surface affecting this.

The subsurface stress distribution generated from a Hertzian line contact is then dependent on the coefficient of traction μ in the contact. The equations for which are summarised in the ESDU International document [24] and further explained in Contact Mechanics by Johnson [31].

2.2.2 Contact of rough surfaces

Hertz is shown to provide a good estimate of the subsurface stresses in the contact, however it utilises the assumption that the surfaces in contact are smooth. In reality no surface is truly tribologically smooth, they consist of a series of asperities and when two surfaces are in contact with each other the actual contact would consist of a series of very small contact areas where the asperities meet. Johnson [31] states that surface irregularities have the potential to cause local plastic damage even when the bulk stress level remains elastic due to the intensification of the real contact pressure. This has the potential to locally affect the surface stresses as the contact pressure is proportional to the contact area. According to Saint-Venant's principle the interior stresses are expected to be greater directly below the individual contacts.

There has been a great deal of research in the contact of rough surfaces, but less relating this to surface roughness in rail wheel contact. Kapoor et al. [32] investigated surface roughness and the effect it has on plastic flow in rail-wheel contact. They considered the unexplained phenomena of the applied load not exceeding shakedown limits yet plastic flow occurring, constrained to the top few surface microns, they hypothesised that the cause may be that of asperity contact. Testing the effect of surface roughness in a series of twin-disc tests with rail discs turned or ground to different surface roughness finishes they found plastic deformation within the top 10 μm.

Kapoor et al [32] developed a modelling technique which calculated internal stresses and maximum contact pressures below the asperity contacts but did not extend the modelling to quantify the plasticity within the rail. They found the maximum contact pressures to be up to 8.84 times higher than that of the bulk contact. They stated that this would be high enough to make the contact fully plastic at those contact points and that with such high stresses the top 5 μm of the rail would be highly likely to experience plastic deformation despite the protective residual stresses in the material. For the modelling method they used they refer back to a similar numerical method by Nogi and Kato [33] which used a Conjugate Gradient Method to solve a set of linear equations and Fast Fourier Transform to evaluate subsurface stresses. They applied this method to a material with a hard surface layer which was comparable to the laser clad coatings, they found that the elastic limit is dependent on layer thickness and surface roughness.

The work by Nowell and Hills [34, 35] considered the effect of surface roughness when modelling the contact size in fretting. They considered the rough surface to be periodic but acknowledged the randomness of a real surface. They simplified the rough surface into asperities of constant height, regular wavelength λ and tip radius ρ as illustrated in Figure 2.7.
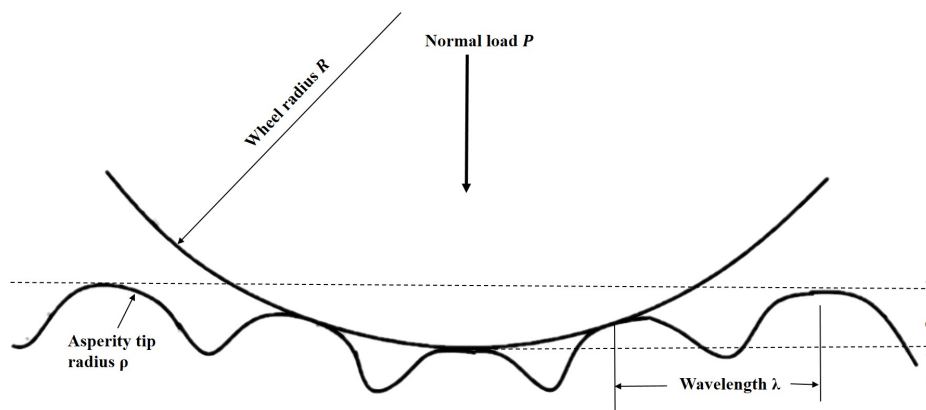
Figure 2.7: Rough surface contact with periodic asperities [34].

They conducted an experiment in which they tested opposing cylinders on a thick strap loaded with a typical Hertzian contact. They tested a ground surface with Ra=0.4 μm, asperity tip radius $\rho = 0.94$ mm and wavelength $\lambda = 0.15$ mm with cylinders of radius $R12$ to 150 mm, which meant that there was a small number of discrete contacts as illustrated in Figure 2.8.
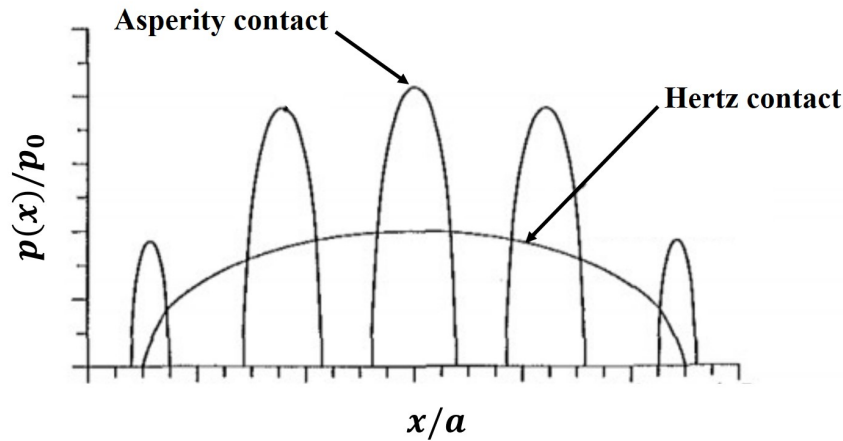
Figure 2.8: Typical contact pressure distribution of rough contact and smooth equivalent [34].

They found that when fewer asperities were in contact the subsurface stress was characterised entirely by the effect of the individual contacts. When the amount of contacts increased, by increasing the cylinder size, the subsurface stresses include a bulk contact in addition to the shallow stresses created by the individual contacts. This agrees with the work by Mihailidis et al. [36] in which they numerically model the difference in internal shear stress with varying roughness from Rq=0.014 μm to Rq=0.75 μm. They show that even where the roughness is low at Rq = 0.014 μm there is an effect on the internal stresses at a shallow surface depth.

Martini et al. [37] ran simulations of rough surface contacts in a simple model developed to analyse subsurface stresses in elastic-plastic rough components. They found that the smallest significant asperity was responsible for the location and magnitude of the maximum subsurface stress. There are many other approaches to modelling the contact of rough surfaces seen within the literature with varying methods and results. Many of the approaches begin with referring back to work on the contact of rough surfaces by Greenwood [38, 39] and the Greenwood-Williamson model from 1966 which was the first rough contact model. This model has the assumption that the rough surface has an array of asperities with spherical tips of a constant radius of curvature and the randomness of the height could be assigned to a probability distribution. Each asperity contact is then considered to be a Hertzian contact. The Greenwood-Williamson and Greenwood-Tripp methods are limited however as they only applies to elastic contacts.

In 1987 Chang et al. [40] developed a statistical method for elastic-plastic contacts through measuring the conservation of volume of the plastically deformed asperities. This method is identified by Jackson et al. [41] as having "flaws" after they apply their finite element method [42] and compare the results with other methods. The work further identifies the Greenwood-Williamson's method to be "limited" as statistical methods assume that the deformation is relatively small and only at the asperity tips. This paper is indicative of the complications involved in modelling rough surface contacts and that it is an ongoing area of research.

One of the issues with modelling rough surface contacts is the measurement of the surface itself. The early methods discussed within this section which use a statistical distribution are well-defined but are not strictly true to real surfaces. Methods of surface roughness are reliant on

roughness measurements which are dependent on resolution and scale of surface measurement instrumentation due to the fractal nature of a rough surface. The self similarity of the surface at different scales means that the method used will depend on the scale of observation. A fractal approach to modelling rough surfaces is demonstrated by Majumdar et al. [43], Gao and Bower [44] and Jourani [45]. All three fractal techniques use the Weierstrass-Mandelbrot function which is continuous but not differentiable and lends itself to the nature of fractal geometry and rough surfaces. Majumdar et al. [43] suggest that the different scales are proportional and that modelling at one scale would allow the prediction of another, ie. micro to macro scale.

Within the literature the many theories of rough surface contact are presented as models with very little emphasis or description on the actual measurement of the surface topography. The most descriptive paper is by Pogacnik and Kalin [46] which seeks to determine the load-carrying asperities. They describe using a stylus profiler to trace the surface and use this measurement to calculate the asperity tip height and radius and number of asperities across the surface. They investigate using a range of criteria to assess the asperity peaks and conclude that a 3-point method is the most reliable, in which an asperity is considered to be a peak where it is higher than the two closest points. They show that the number of asperities and the tip radius of the asperities both decrease as the surface roughness increases.

2.3 Rail defects and failures

2.3.1 Plastic ratcheting

The high compressive and shear loading on the relatively small contact area of wheel on rail (around 1 cm^2) along with a combination of rolling and sliding often results in stresses exceeding the rail material's yield point and consequently in plastic strain occurring. Repeated cyclic loading in this manner can result in incremental plastic shear strain accumulation in a process known as ratcheting, leading to large scale plastic deformation within conventional rail steels, which can lead to wear and crack initiation [47]. The properties of shakedown influence the design of railway tracks as well as bearings [32]. As rail steel is an elastic-plastic material the response to cyclic loading is dependent on the magnitude of the load. The stress-strain curves presented in Figure 2.9 demonstrate the four ways in which the rail material could behave [48, 49].

When the rail is subjected to light loads below the yield point, it behaves elastically, and no permanent change occurs in the material as the load moves away, this is perfectly elastic as illustrated by a) perfectly elastic. Once it reaches the elastic limit, the rail yields in some elements during the initial loading, however, because it strain hardens and has protective residual stresses, it enters elastic shakedown and has a perfectly elastic steady cyclic state as illustrated by b) elastic shakedown. Failure during these elastic cycles is rare and would only be likely to occur as high cycle fatigue (HCF), it would therefore be desirable to design the wheel-rail contact to operate below the elastic shakedown limit [22]. Loading beyond the elastic shakedown limit causes plastic deformation to occur. For loading up to the plastic shakedown limit the rail is in a steady state of an elastic-plastic loop, there is no permanent accumulation of plastic deformation, as illustrated by c) plastic shakedown. Once the plastic shakedown limit has been exceeded, with high loads, the

rail experiences permanent change and unidirectional plastic strain is accumulated in a process known as ratcheting as illustrated in d) ratcheting [47]. It is within large accumulated plastic shear strain that cracks appear [50]. The open cycle of plastic strain and resulting ratcheting shown in part d) Figure 2.9 [49] is demonstrated in the micrograph of R260 grade rail steel.
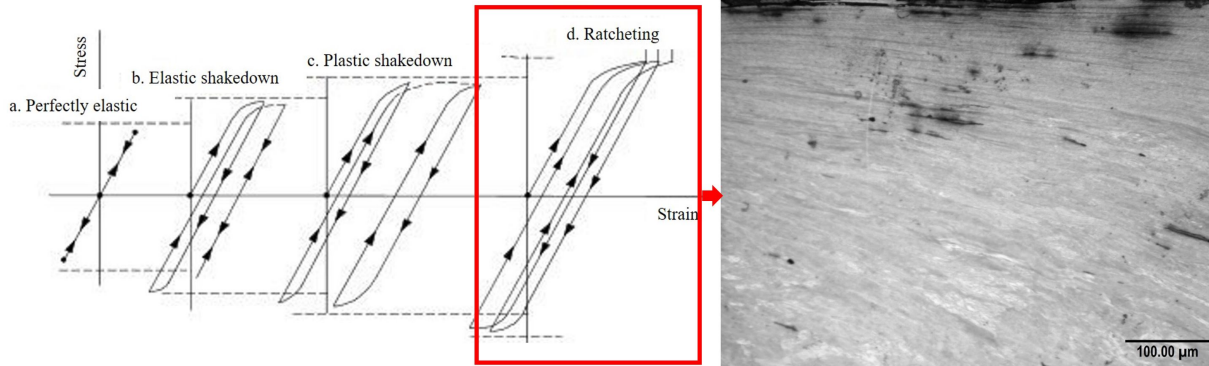
Figure 2.9: The four types of material response to cyclic loading [49] and typical resulting plastic deformation caused by ratcheting.

When the accumulated plastic shear strain exceeds a critical value failure will occur [51]. Ratcheting failure can occur in low cycle fatigue (LCF) when the materials ductility is exhausted due to extreme accumulation of plastic strain. Kapoor [50] investigated material failure by LCF using the Coffin-Manson relationship, Equation 2.9.

$$N_f = \left(\frac{2C}{\Delta \epsilon_f} \right)^{1/n} \tag{2.9}$$

where N_f is number of cycles to failure, C is the strain limit at failure, $\Delta \epsilon_f$ is alternating plastic strain and n is an exponent of approximately 0.5. Compared to material failure by ratcheting failure, Equation 2.10.

$$N_r = \frac{\epsilon_c}{\Delta \epsilon_r} \tag{2.10}$$

where N_r is number of cycles to ratcheting failure, ϵ_c is the critical strain limit at failure and $\Delta \epsilon_r$ is ratcheting strain. The two failure methods were considered to be independent and competitive, meaning that the material was deemed to fail by the method which occurred in the shortest number of cycles. It is mentioned that the damage from the two failure mechanisms may also be considered to be additive which would make the estimated component lifespan shorter than the chosen competitive theory, however, they conclude that the difference in lifespan is relatively small and the simplicity of competitive theory is more beneficial. The number of cycles to failure by ratcheting and low cycle fatigue increases with rolling-sliding contact under high hydrostatic pressures, such as typical rail-wheel contacts, due to strain hardening and strain to failure increases.

The accumulation of plastic shear strain can cause damage at just below the surface as voids or

microcrack initiation points. With repeated cyclic loading this accumulation of plastic shear strain can lead to the propagation of these microcracks into cracks large enough to produce a wear flake, which will delaminate from the surface, or rolling contact defect, such as a squat defect [52]. The ability to predict the level of plastic ratcheting within a rail is therefore crucial to maintain safety and prevent catastrophic failure. Different methods of modelling plastic deformation within the rail, found within the literature, are explored here.

Athukorala et al. [53] developed a modelling method to predict ratcheting in rail and they considered the effect of non-uniform hardness throughout the rail due to the effect of work hardening or heat treatment for example. They used finite element modelling and incorporated a combined kinematic and isotropic hardening model from Chaboche et al. [54]. They concluded that the depth of maximum plastic shear strain accumulation is not significantly affected by the change in hardness in the material. A similar approach to model ratcheting was taken by Zhu et al. [55] with a Abdel-Karim-Ohno hardening rule rather than the Chaboche method, which they stated to be beneficial as it required less material parameters.

Ratcheting behaviour of heavy haul premium rail has been studied in Australia. Pun et al. [56] developed a method using a non-Hertzian contact pressure found through finite element analysis and Carter's theory for tangential traction forces. The materials were found to accumulate plastic shear strain and surface cracks were initiated when the limit of ductility was reached. Further studies by Pun et al. [57] stated that the material response was dependent on the magnitude of both axial stress and shear stress.

Bower and Johnson [52, 58] developed non-linear kinematic hardening laws to predict the response of rail steel in rolling-sliding contact in the 1980s. They state that the combination of high normal and tangential loads in rail-wheel contact cause ratcheting to a depth of about 2 mm in rail which accumulates over thousands of cycles. This near surface deformation is said to be an underlying cause of sliding wear and RCF cracks. Hills et al. [59] also suggest that in rolling contact plastic flow would accelerate fatigue failure and that it would therefore be desirable to design components to operate below the shakedown limit to prevent plastic flow. Microcracks within the deformation are said to be the initiation points just below the surface which grow and join until longer cracks of around 10 - 20 μm are formed, which can then cause wear or may continue to propagate to a RCF defect.

Research in Sweden by Ekh et al. [60] analysed three methods for modelling plastic ratcheting in 2000. They conclude that the Armstrong-Frederick kinematic hardening law [61] combined with the isotropic hardening law is not sufficient to predict the rate or magnitude of plastic ratcheting. They also dismiss Bowers version of the kinematic hardening rule [52]. The kinematic hardening rule proposed by Jiang et al. [62] is shown to provide better results due to containing a larger number of material properties.

Johansson et al. [63] developed a multidisciplinary simulation method which involved simulating the wheel-rail dynamic loading, calculating the wheel-rail normal contact, the accumulated damage was then predicted and finally the rail profile was updated before the next iteration. Skrypnyk et al. [64] applied this to railway crossings in 2019, with the addition of a metamodel [65]

for wheel-rail normal contact which calculated a contact patch size and maximum contact pressure using Hertz theory rather than FE modelling. The computational time using this method remained high with 41,400 load cycles taking 20 hours for R350HT and 56 hours for Mn13. The method was then simplified further using an extrapolation technique after 2,760 load cycles in an attempt to reduce the computational time.

A numerical method for modelling plastic response to cyclic loading is introduced by Kapoor et al. [66] known now as the 'layer' model. The method was initially developed to explain delamination which Tyfour et al. [48] state as the mechanism responsible for material loss in pearlitic rail steel caused by unidirectional plastic strain accumulation. The rail material under load is divided into horizontal layers, these layers then fail by low cycle fatigue or ratcheting. This leads to delamination of the first layer, exposing the second layer and continues as the accumulated plastic shear strain of the surface layer reaches the level of critical strain the top layer delaminates, exposing the layer below. The strain cycle is dependent on the elastic plastic properties of the material, the friction coefficient and the applied load. This model was programmed to enable the incremental accumulation of strain of each layer to be recorded for each cycle. The thickness and hardness of the layers and the number of cycles to failure are related to the Archard wear coefficient. The model allows for changes to the wear rate due to strain hardening in the sub surface material.

The development of the layer model for the quantifying plastic shear strain within the rail is clearly explained by Kapoor et al. [67] with supporting experimental work. In the modelling the rail is divided into layers parallel to the surface. The model was run in Matlab with the output of a strain or hardness profile against depth in the rail for a required number of cycles. A flow chart describes how initial material properties and conditions are set, the Hertzian stress distribution is calculated before entering the iterative process where effective shear stress and accumulated plastic shear strain is calculated for each layer and each cycle. The layer model is shown to be a beneficial method for modelling plasticity as it is much faster than finite element methods, simulating tens of thousands of wheel passes in just a few minutes.

The model was developed using material properties for BS11 rail steel following on from work by Kapoor and Franklin [51] and Tyfour et al. [48]. The layer model is dependent on shear yield stress - plastic shear strain curves for the rail material which were found experimentally in twin-disc tests. Strain was measured as the angle of deformation within the sample 0.2 mm below the contact surface. The rate of strain accumulation used within the model was taken from the work by Tyfour et al. [48] where the relationship between shear strain and net ratcheting load and number of effective cycles was found experimentally.

Each layer of the model requires accurate material properties to be input, Kapoor et al. [67] conducted investigations into whether standard tensile testing in atmospheric pressure provided sufficient input data, or whether the data should be collected under realistic high hydrostatic pressure. They showed that results from the model using the tensile test input could predict trends in strain accumulation but not the rate of accumulation. They concluded that material data is more reliable when obtained under high hydrostatic pressure such as that generated by twin-disc

testing. Meyer et al. [68, 69, 70] studied the effect on plastic deformation in R260 grade rail steel on yield stress through a series of axial-torsion tests. They produced stress-strain curves for the deformed R260 in pure torsion and provide the yield points. This is indicative of the materials behaviour but is not realistic to rail-wheel contact loading which is under high hydrostatic loading.

The accumulation of plastic shear strain and its influence on wear and RCF is also modelled by Franklin et al. [71] with a method they call the 'brick' model. This is an extension of the layer model and divides the rail into bricks rather than layers, each with their own material properties and the ability for each to accumulate plastic strain independently. Each brick can lose integrity and fail, representing the microstructure of rail, they act independently from their neighbour and as such the brick model is neither FEM or BEM. As the bricks fail they are either lost from the surface as wear debris or represent crack initiation points. This method can therefore be used to model the interaction between wear and RCF. This method can further be found within the literature for modelling wear and crack initiation by Fletcher et al. [72] and Franklin et al. [73, 74] and for predicting the life of rails by Garnham et al. [75].

Wong et al. [76] and Dyson et al. [77] investigated the shakedown limits of surface engineered or coated materials. The surface is assumed to be harder than the base material and therefore have a higher yield stress k, the difference between the yield stress values of the two materials has an effect on the shakedown limit. The depth of coating in relation to the contact area also influences the shakedown limit, deeper coatings generally provide higher shakedown limits. When the coefficient of traction is over 0.3 the maximum shear stresses occur at the surface and a thin surface layer can still increase the shakedown limit.

2.3.2 Wear

Wear of rails refers to the loss of material from the surface due to the tribosystem created between rail and wheel and any contaminants between them. Rolling and sliding are both contributors to wear, the combination found in rail-wheel contact makes a system prone to wear. A common model to begin to describe the rate of wear is the Archard wear model [78]. This model states that wear V (mm^3) is directly proportional to the load P (N) and inversely proportional to the surface hardness H (Pa) of the rail [79], given by Equation 2.11, with dimensionless wear coefficient K and sliding distance d (m).

$$V = \frac{KPd}{H} \qquad (2.11)$$

It is assumed that in rail steel the local deformation of asperities is plastic and therefore the contact pressure is equal to the hardness H. To use this model accurately it must be known whether the wear for a material pair is mild or severe as each has a different wear coefficient K, most rail-wheel contact falls into the mild wear regime, rails falling into the severe regime will need frequent replacement.

An alternative method of quantifying wear seen within the literature [80, 81] is $T\gamma$. This is a

frictional work model in which T is the shear force in the contact patch and γ is the slip, it is representative of energy expended in the contact area. Wear rate is plotted against the normalised $T\gamma/A$, where A is the area, in Figure 2.10, taken from Lewis et al. [80] to demonstrate the wear regimes and generalised causes of wear within each regime.

There are different mechanisms of wear which affect the rail. On a microscopic scale the surface of rail and wheel are not smooth, they have asperities which come into contact with each other. Adhesive wear happens as the asperities of the wheel bond with those of the rail. This is a problem particularly common in wheel-rail interaction as they are both made from the same material. As the wheel then moves over the rail the asperities are broken and new ones are formed. As the asperities become loose they risk breaking off and becoming wear debris. Abrasive wear of the rail is also common, as material is lost due to a sharp asperity or a contaminant between the wheel and rail, 'scratching' or creating a groove in the surface of the rail.
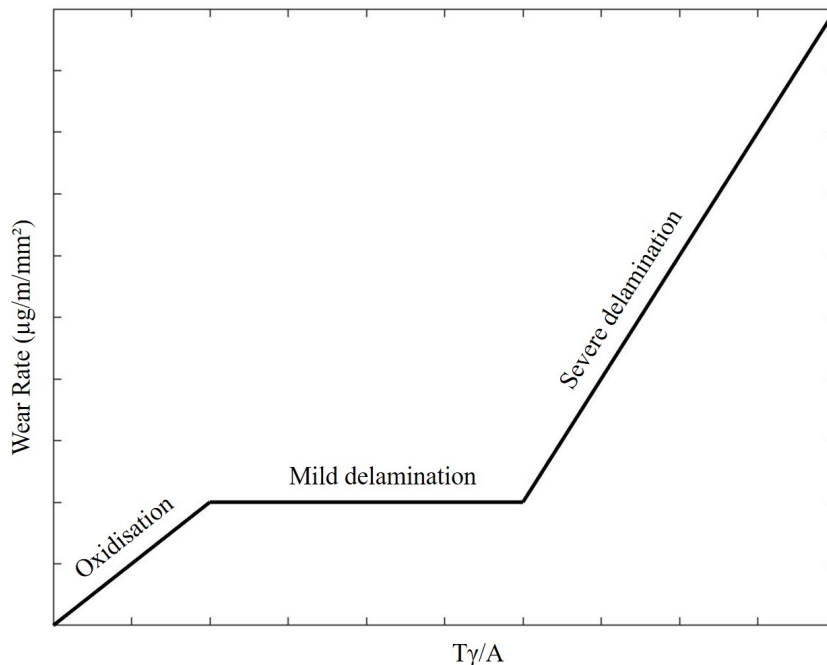
Figure 2.10: Schematic diagram of wear regimes and features.

Delamination is another wear mechanism which occurs within rails, as plastic shear strain accumulates with repeated rolling contact, thin layers are formed at the surface, loosen and become wear debris as first described by Suh et al. [82]. Wear can also occur through oxidation, due to the cycle of the protective oxide layer being destroyed by sliding contact and then reformed. Wear of rails is related to the microstructure of steel, with smaller interlamellar spacing S_t providing a more wear resistance rail, as described in section 2.1.2. This relationship of grain boundary strengthening can be described by combining the inverse proportionality of wear and hardness from Archard's wear model and a Hall-Petch type relationship, Equation 2.12.

$$V \propto \frac{Pd}{150 + \dfrac{2.15}{\sqrt{S_t}}} \tag{2.12}$$

2.3.3 Rolling Contact Fatigue

Rolling contact fatigue (RCF) is a potential mode of failure for rails, caused by the initiation and propagation of cracks over the duration of many load cycles. Garnham and Beynon [83] stated that rolling contact fatigue can cause cracks even in modern and head hardened rail steels. Both material properties and residual stress influence the rate at which RCF occurs [14]. In some cases the wear of the rail surface will act to remove the crack initiation sites and eliminates cracks before they can propagate or cause rail breaks. This isn't always the case and the presence of water or lubricant at the contact may propagate RCF cracks at an increased rate [84]. Rails must be closely monitored to spot the early signs of cracking. If small cracks are detected then grinding can be used to repair the rail, this not only removes the initiation of cracks but also re-profiles the rail to redistribute loads and reduce stresses. If cracks are too large the rail will need replacing, if cracks are not detected early enough or the growth rate is incorrectly predicted they present a potential failure as the rail could break causing a train derailment. Preventing and managing RCF is an essential consideration in creating a suitable laser clad coating.

The mode and rate in which a crack propagates is studied in fracture mechanics. There are three different modes of crack displacement, mode I is opening, mode II is sliding and mode III is tearing. In rail it is important to be able to predict how fast a crack will grow to prevent failure. Linear Elastic Fracture Mechanics (LEFM) is a method which represents fatigue and fracture mechanics assuming linear elastic material behaviour, one approach to predict crack growth is by crack tip stress analysis. The laser clad coatings are highly plastic resistant making this method relevant and the substrate rail enters a quasi elastic state due to shakedown. For a crack of length a, crack growth rate $\dfrac{da}{dN}$ can be related to stress intensity factor K with the Paris-Erdogan law [85]

$$\frac{da}{dN} = C\Delta K^m \tag{2.13}$$

where C and m are material dependent constants. The crack tip is described by a singularity point and as such the stress intensity factor K just ahead of the crack tip must be calculated to apply the Paris-Erdogan law. The stress intensity factor is specific to the mode of displacement.

Stress intensity factors for each mode are given by Equations 2.14-2.16 and the overall stress intensity factor for use within the Paris Erdogan law is given by Equation2.17. Where k and f_{ij} are proportionality constants dependent on mode and $K = k\sqrt{2\pi}$ [85].

$$\lim_{r \to 0} \sigma_{ij}^{(I)} = \frac{K_I}{\sqrt{2\pi r}} f_{ij}^{(I)}(\theta) \tag{2.14}$$

$$\lim_{r \to 0} \sigma_{ij}^{(II)} = \frac{K_{II}}{\sqrt{2\pi r}} f_{ij}^{(II)}(\theta) \tag{2.15}$$

26

$$\lim_{r \to 0} \sigma_{ij}^{(III)} = \frac{K_{III}}{\sqrt{2\pi r}} f_{ij}^{(III)}(\theta) \tag{2.16}$$

$$\sigma_{ij}^{(total)} = \sigma_{ij}^{(I)} + \sigma_{ij}^{(II)} + \sigma_{ij}^{(III)} \tag{2.17}$$

A common problem caused by RCF are 'squat' defects in which cracks grow at a shallow angle below the rail surface to between 25 and 50 mm. They can sometimes be identified by a small depression on the running surface of the rail. If not detected and repaired or replaced a fatigue failure will occur. 'Head checks' are another RCF defect, these effect the gauge corner and can be identified by cracks on the surface. This type of defect can cause parts of the gauge corner to break off reducing the contact area and in turn increasing the contact pressure.

Rolling contact fatigue in rails has been a keen topic of research for many years and there have been different ways suggested to analyse it. Mai et al. [86] use eXtended Finite Element Method (XFEM) to generate stress intensity factors (SIFs) and simulate crack growth under rail-wheel contact. They find that lower friction between the crack faces causes faster propagation indicating that lubrication accelerates the growth. Fletcher et al. [87, 88] use a three dimensional Boundary Element Method (BEM) and extend this to investigate the effect of contact temperature in the propagation of near surface cracks [89]. This work indicated that high temperatures between 500°C and 1,000°C at the contact contributes to crack growth.

A phenomena known as White Etching Layer (WEL) can exist on the rail surface where extreme plastic deformation is present as reported by Carroll and Beynon [90]. An area of WEL can be identified as a bright layer or area on the surface when sectioned and etched. They are said to be brittle areas with hardness around three times higher than the surrounding material by Vargolici et al. [91]. Although the area has higher hardness than the surrounding rail it is not comparable to a laser clad repair as it is created in an uncontrolled way allowing martensite to form making the WEL brittle. The study of WEL has drawn interest in the quest to understand RCF and squats. Carroll and Beynon [90] give detail of how WEL can be simulated in the lab through spot welding or gross sliding in twin-disc machine.

Cracks constrained within the WEL were observed and were also found at the interface of WEL and pearlitic rail structure by Clayton et al. [92]. Through a series of testing by Carroll and Beynon [90] it was seen that the spot welded WEL experienced cracks at the interface going into the pearlitic rail steel away from the WEL, this was due to plastic deformation and ductility exhaustion. Such cracks are said to pose a failure risk to the rail. Lian et al. [93] use a finite element model supported by microscopy on WEL in ex-service rail steel to predict the propagation of cracks around WEL. Mode II, shear mode was seen to be the dominant displacement within all modelled cracks. The two interfaces, the leading edge and trailing edge, were seen in micrograph observations to be the areas which were susceptible to crack propagation. On the leading edge the crack follows the direction of material flow, on the trailing edge growth is in one of two directions, following the interface boundary or crossing through the substrate rail and aligning with the direction of deformation. The research presented in this thesis shows that cracks do not propagate

in laser clad repairs and the controlled way in which the repair is applied prevents the formation of the martensite seen in WEL.

2.3.4   Inspection and Maintenance of rails in service

The prevention of defects plays a crucial role in the running of a safe railway, this is a complex task and involves methods of inspection and maintenance. Modelling techniques can be applied to predict fatigue life and the location of possible RCF, this can be used to aid the planning of maintenance. Pun et al. [94] use a Smith-Watson-Topper (SWT) method with finite element modelling to deduce a single parameter which can be used to evaluate stress state in the rail head for analysis. In support of modelling techniques inspection of rails is important to detect early stages of defects to allow corrective maintenance avoiding rail replacement where possible.

Non-destructive methods of inspection are employed including ultrasound, visual and eddy current techniques both manually and on inspection trains [95]. The results of inspection then help to determine maintenance planning. Detecting cracks is vitally important as if left they could lead to failure. Cracks can be hard to detect within the rail as most non-destructive testing techniques can only detect cracks over a certain size. Ultrasonic Testing Units (UTU) have been utilised in recent years. The early detection of cracks has significantly reduced the number of rail breaks per year, from 952 per year in 1998/99 to 95 in 2016/17 as reported by Network Rail [96]. The properties of new and novel rail materials must be known and should be maintainable by Network Rail techniques, i.e. not create false positive indication of a crack.

Wear and fatigue commonly occur in standard grade rail steels with the underlying cause being plastic shear strain accumulation through ratcheting. To maintain railway safety rails require regular maintenance such as surface grinding to remove this plastically damaged material that is otherwise susceptible to cracking. Rail grinding has been routinely used for a corrective and preventative maintenance method to remove surface damage on the rail and restore the original profile since the 1980's [97]. The grinding schedule may also be influenced by modelling rolling contact fatigue (RCF) as shown by Hyde and Fletcher [98] where the necessary depth and frequency of grinding can be defined. Magel et al. [99] also research the practice of rail grinding and look at models to improve the prediction of profile deterioration and fatigue. Although grinding helps to extend the life of rail it is not a technique that can be used indefinitely and the rail will still have to be replaced eventually.

An alternative method to reduce or alleviate deterioration of rail caused by repeated cyclic loading is that of additive manufacturing techniques where the damage is removed and the rail rebuilt with a new material. Different methods of additive manufacturing are available but the common theme is that they are all techniques involving the deposition of metal to a substrate rail. One available method is that of welding, techniques include electro gas arc welding, plasma arc welding and submerged arc welding. Head Wash Repair (HWR) method is also used by Network Rail under the Certificate of Acceptance [100] from 2013 which gives details of the types of defects which can be repaired in this way. It states that squat type defects and wheel-burns may be repaired in this way, with maximum allowable sizes and suitable locations for repairs given.

Weld repairs offer a method of extending the life of rails, however, the weld-repaired area is still susceptible to crack initiation. The initiation and growth of cracks in weld repairs was researched by Jun et al. [101, 102] and Lennart Josefson [103], they both found that residual stress influenced the rate of crack growth. They suggest that the possible causes of failure in weld-repaired rail could be from defects with the weld material like porosity in the weld, lamellar line cracks or a reduction in material hardness, or the changes in microstructure, chemical composition associated with the heat process. Other issues may occur from the thermal process involved in welding or improper pre-heating of the rail. Problems arising from this may include weld breaks, hot tears, porosity and the creation of a heat affected zone.

Submerged arc welding (SAW) is investigated as a rail repair method by Mortazavian et al. [104]. The advantage of SAW compared with other open methods of welding is that the welding wire and arc are entirely submerged in the flux stream which helps to prevent extreme heat radiation, provides a high deposition rate and creates a reliable weld. They conclude that the hardness of the SAW repair alone is lower than AREMA (American Railway Engineering and Maintenance-of-way Association) standards allow. To overcome this they introduce a post process water-quenching technique which raises the hardness to an acceptable level. The effect of the cooling rate on the microhardness following submerged arc welding is investigated by Kumar et al. [105] in which they conclude that the faster the cooling rate the lower the hardness.

Geometrically complex components such as switches and crossings require extra consideration when repairing. Xin et al. [106] consider repair welding and grinding for crossings as a cost saving method to replacement. Through experiment and modelling they find that if the original geometry is not correctly restored the location and magnitude of forces within the component are affected, however a benefit of spreading the impact forces over a larger area was observed. The importance of the quality of weld was highlighted with particular reference to the pre-heat and cooling rate to avoid the formation of martensite. One of the potential problems is that if the weld material does not match the surrounding rail material well, then it may have a different wear rate at the joint, resulting in a dip in the rail, causing higher impact loads as the train passes over [107].

2.4   Additive manufacturing with laser clad coatings

Laser cladding is a method of additive manufacturing used for enhancement or repair in many engineering scenarios such as aerospace [108] and in the oil and gas industry [109]. It is a method of surface engineering which has the capability of changing the properties of the surface of a component to give performance which cannot be achieved by the surface or bulk alone. In this section the literature review focuses on previous research which has been conducted in fields relevant to additive manufacturing with premium laser clad coating for the life extension of railway track components.

The laser cladding process is described in [110] by Lewis et al. as they explain the one-step laser cladding by powder injection used to create the samples for their experiment, the schematic of which can be seen in Figure 2.11. The cladding metal is created in an atomised form as a powder

which is fed into the laser beam with the use of an inert gas. The laser beam passes over the pre-heated substrate material in a single path at a high heat creating a thin melt pool, this happens simultaneously with the heating of the powder which fuses them together creating the clad layer on the substrate. This process is repeated in adjoining tracks, often referred to as beads within the literature, to cover the whole substrate as required, this creates a 'ploughed field appearance' which Lewis et al. [1] ground to a smooth surface finish. Clare et al. [111, 112] give detail of the laser cladding process parameters used in their experiments and discuss the importance of the parameters in creating a strong and crack free interface.

The laser cladding process heats the surface of the substrate material during the laser cladding process, fusing it with the powdered clad, creating a bonding zone. Niederhauser et al. [113] were concerned with ensuring that the interface between the clad layer and substrate material did not create a mode of failure as the bonding zone between the first layer of cladding and the substrate contains two different materials with different chemical compositions, as such, they suggest that the interface between subsequent layers of cladding would be stronger, as the clad mixes with clad of the same composition. This theory assumes that only a small percentage of the initial clad layer mixes with the substrate material and the composition at the top of the clad layer remains unmixed.
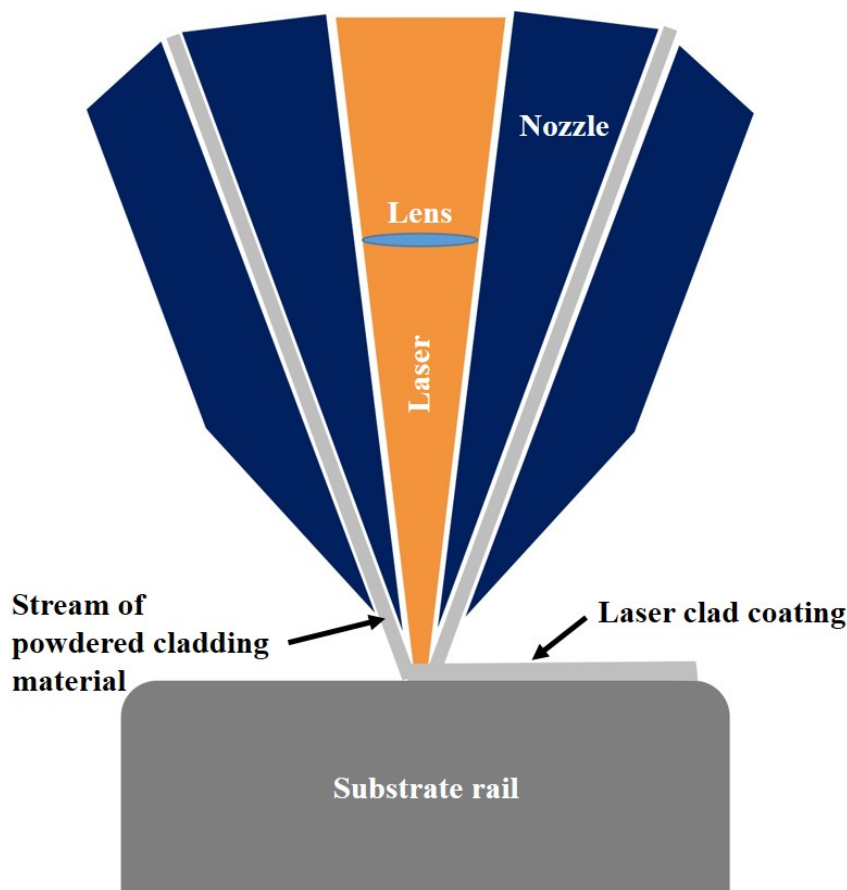
Figure 2.11: Schematic drawing of laser cladding process.

Over recent years there has been much interest and research into applying laser cladding to rails to extend their life by improving their wear and RCF resistance. Laser clad coatings offer a solu-

tion of depositing a harder rail material with superior wear and RCF resistance to railway track components which are more prone to damage, using the cheaper, standard substrate rail to provide the structure. Laser cladding was suggested by Hiensch et al. [49] in 2002 as a method to prevent RCF and reduce noise emissions in small radius curved rails as part of the European 5th Framework project INFRA-STAR project. Twin-disc tests under water lubricated conditions were conducted to test RCF properties of Durac 222 (370 Hv) and Durac 508 (410 Hv) laser clad coatings on UIC900A (270 Hv) substrate rail. No cracks were detected in the clad discs and a reduction in plastic deformation was observed with a depth of only 2 - 18 μm compared to 0.3 - 0.4 mm in unclad rail.

Hiensch et al. [114] presented the results of field tests once a section of laser clad rail has been in track for one year. The Durac laser clad coatings were installed in a tight radius curve section of track on the Paris Metro. Tests for squeal reduction were conducted and it was reported that the coatings did not work to reduce the noise. RCF tests were also conducted on the laser clad rail after 10 months and the DUROC 222 had no detectable cracks whereas the unclad reference rail had developed RCF. The Duroc 508, however, had developed cracks at the interface, for which the laser cladding process is reported not to have not been optimal.

Laser cladding was proposed as a possible method for extending the life of railway wheel surfaces by Niederhauser and Karlsson in 2004 [115] at Chalmers University of Technology, Sweden. This paper references a 1998 patent by Johan Lennart Olofsson [116] however there are no supporting research papers from this inventor at the time. The research conducted by Niederhauser et al. was inspired by the increased wear and fatigue experienced by wheels due to increased speeds and loads. They describe the method to apply a surface layer on the standard wheel substrate material as a cost and weight saving solution rather than using premium materials throughout the entire wheel.

Clare et al. [111] and [112] at the University of Nottingham conducted a study into extending the laser cladding process to railway track components rather than wheels as seen previously. Two research papers were published from this, the first from Clare et al. [111] in 2012, considers four different cladding materials and examines the hardness and microstructure of the clad, interface and substrate. The four clad materials tested were Nickel alloy, Stellite 6, Hadfield steel and maraging steel, which were all deposited onto standard R260 grade rail steel. All of which were shown to have higher levels of hardness compared with the substrate and showed potential to work in protecting the rail.

The research from Clare et al. [111] and [112] is concerned with maintaining work-hardening properties associated with rail track materials such as that found in pearlitic grades of steel which are widely used in rail. In 2013 the second paper from Clare et al. [112] show Stellite 6 as the most promising clad material from the previous research and carries out further testing to assess its suitability, they select this clad material as it is a cobalt based hard facing material, it has been shown to create a virtually crack and pore free deposit, it is wear resistant and has work-hardening abilities. Stellites have been successfully used for other purposes, such as structurally in extreme environments. Technical data fact sheet from Deloro Stellite states that "Stellite 6 cobalt base alloys

consist of complex carbides in an alloy matrix" which performs well under impact, is resistant to wear, erosion and corrosion, all of which are desirable for use on railway track components. This fact sheet contains all the technical data, such as hardness, density, melting range, elastic modulus, yield stress, ultimate tensile strength, thermal and electric conductivity, all of which may be used as comparison to lab test results found in this project.

Wang et al. [117, 118] conducted a series of experiments in which they applied cobalt based laser clad coatings to both the rail and the wheel in small scale laboratory tests. In the first set of tests they investigated the wear of the clad wheel/rail system in unlubricated testing. They reported that the wear was reduced by around 78.6% compared with a reference unclad wheel and rail. To support their work indicating excellent wear resistance they continued on to test for fatigue damage in the same cobalt based laser clad coating using oil lubricated small scale laboratory tests [118]. They found that with both wheel and rail clad that no surface cracks were detected. In all reported test specimens the Co-based alloy is well bonded with a uniform and compact microstructure.

A study was conducted by Lu et al. [2] on the contribution of the substrate rail material on the effectiveness of the laser clad coating . R200 and R260 grade rail steels (chemical compositions shown in Table 1.1) were chosen as the candidate substrate materials due to R200 often being found in track across Europe and R260 being the current UK standard rail material. The laser clad coating tested on the different substrates was 14.64% MSS deposited to a nominal thickness of 1.1 mm on twin discs. The paper reports that both substrate materials had a much lower wear rate than a reference R260 unclad sample, remaining below 5 μg tested to 30,000 cycles. Using the R260 grade rail steel as the substrate resulted in a harder clad than the R200, which in turns produces a higher shear yield strength, this could be beneficial to the wear and RCF performance of a clad rail.

Within the literature Mortazavian [104], whilst researching welding as a repair method for rail acknowledges that laser cladding is a favourable method for repair and enhancement of rail due to the wear and RCF resistant properties available with laser powder deposition. They highlight previous research that has investigated the material and mechanical properties of laser cladding applied to rail steels as an enhancement method. They state that although the potential to utilise the method for in-situ repairs is mentioned within the literature it has never investigated in published literature to date (2020). Mortazavian et al. do not take this further and instead investigate submerged arc welding as a repair method.

Hernandez et al. [119] consider the application of laser cladding to the heat affected zone of aluminothermic rail welds, which are prone to localised plastic deformation and dipping under wheel-rail contact conditions. A Fe-based alloy clad is chosen due to it being crack resistant during cooling, they state that the heating and cooling protocol development was a key aspect in a successful process due to the microstructure and hardness being defined by this which in turn is critical to the performance of the rail. A comprehensive study was presented in the research paper with thermal analysis, numerical simulations and full-scale experiments. They conclude that the parameters selected in this study increased the lifespan of laser clad railway track components by

up to 1400% compared with previous attempts tested in this study.

Fu et al. [120] select a Fe-based alloy laser clad coating with a Cr_7C_3 carbide to investigate the reduction in wear compared to unclad rail and wheel. They chose to clad both the wheel and rail discs in small scale rolling-sliding laboratory tests in the same way as Wang et al. [117, 118]. They report that the clad coating increases the hardness and wear resistance and that the wear particles are smaller than in unclad tests. A further significant development within this work is the addition of Lanthanum oxide (La_2O_3) to the Fe-based alloy powder through mechanical mixing prior to laser cladding, which is said to evenly adhere to the surface of Fe based alloy particles. This work is continued by Wang et al. [121] and the addition of La_2O_3 is seen to further increase the resistance of wear and RCF in Fe-based laser clad coatings. It is reported that the optimum amount of La_2O_3 is 1.2% and that it works in refining the laser cladding microstructure.

Lai et al. [122] present the results of an investigation, conducted in Australia, into the effect of the cladding direction and the heating and cooling process on the microstructure and mechanical properties of the rail. In this investigation a premium hypereutectoid rail steel is chosen as the substrate, as this is what is commonly used on heavy haul Australian railways, with a 410L grade stainless steel as the clad coating. They identify the influence of the cladding direction and pre/post heating treatments, and although the results of the investigation are specific to the rail grade and clad coating combinations tested, this is expected to be applicable to any laser clad rail.

The University of Sheffield have also carried out research, resulting in the publication of three research papers since 2015. The first of these, published in 2015 by Lewis et al. [110], considers four possible clad materials as surface treatments for railway track components and conducts wear and rolling contact fatigue tests on each using a twin-disc method. R260 rail grade was used as the case for comparison and the substrate, the materials tested were Hadfield, Stellite 6, Maraging and 316 Stainless Steel all of which were seen to be resistant to plastic deformation. The experiment was not thought to have run for long enough for all the coatings to work harden and as such, not all tests saw a reduction in wear rates relative to the base case. The paper describes the experiments and results in good detail and the Stellite 6 coating is indicated as being the most promising of the clad materials, with the least wear in both wet and dry tests.

A second paper from Lewis et al. published 2016 [1] sees a further six potential clad materials tested in the same way as before, using R260 rail grade as the substrate to better understand the wear performance. The clad materials chosen in this research paper are "A Multi-phase Manganese Steel Variant (MMV), Martensitic Stainless Steel (MSS), TWIP Steel, NiCrBSi, Stellite 12 and Stellite 6." It is described how the layers are 1 mm thick with either 1 or 2 layers applied in the samples. The width of the deposited track/bead of laser clad coating is 4 mm and as the twin-disc samples are 10 mm wide, several beads were applied to cover the entire surface.

2.4.1 Optimised Parameters

The cladding of rail sections for projects at the University of Sheffield has been conducted by Laser Cladding Technology (LCT) in Shireoaks through a joint project. To create a defect free

laser clad coating they developed optimised parameters for a deposition of Martensitic Stainless Steel on a 0.62% carbon rail steel alloy through initial trials to find the optimal combination of parameters such as laser power, rate of powder flow, layer depth and speed. LCT retain the optimal parameters as intellectual property. The Welding Institute (TWI) have conducted similar laser cladding of rail in a further project with the University of Sheffield in which they found that using a 2 kW CO_2 laser with their 'Trumpf DMD 505 laser deposition system' created a crack free deposition. No pre-heat was applied to the substrate rail and the final parameters are shown in Table 2.1.

Variable	Optimised parameter
Laser power	1340 kW
Head speed	600 mm/min
Powder flow	0.28 g/min
Nozzle gas	8 l/min
Carrier gas	3 l/min
Laser Spot size	2.1 mm
Layer height	0.35 mm
Track separation	1.3 mm

Table 2.1: Optimised parameters provided by TWI [123] for deposition of 14.64% chromium MSS on 0.62% carbon steel alloy

The EPSRC Alchemy project researched the influence the laser parameters have on the quality of clad coating produced. They found the correct parameters which produce a high quality, effective laser clad coating, however, if these parameters are incorrect, such as the laser power being insufficient, defects can occur, such as porosity. This is further demonstrated by Lewis et al. [1] when clad discs are sectioned and porosity is observed in some of the samples.

Further evidence of the importance of the laser clad coating process is found within the literature. The tempering procedure after the laser cladding process for the Duroc 508 installed in the Paris Metro [114] was reported to have not been optimal and cracks were observed at the interface of coating and substrate rail. It was also seen in the field tests which were conducted with Duroc laser clad coating on UIC900A substrate rail in Sweden in 2002 [49] that post clad grinding was important to prevent high peak pressures causing surface cracks. They also found that stop-start areas of cladding caused joins which were susceptible to crack initiation and therefore full lengths of rail were safer for laser cladding to avoid this.

Siddiqui et al. [124] conducted a review of laser cladding research for all applications, not restricted to rail, in which they also conclude that the process parameters such as the laser power, feed rate, clad angle and scan speed all affect the performance of the coating. They highlight one of the biggest challenges to be that of the skilled labour required in selecting and applying the optimum process parameters and the safety in doing so.

2.4.2 The effects of thermal processing

During the laser cladding process, the substrate material is usually pre-heated and then left to cool rapidly due to the large volume compared with the volume of the clad layer. This creates a change in microstructure of the substrate which is referred to as the HAZ. The effect of this zone is explored in some of the papers and despite the change in microstructure, there is no reported negative effect on the quality of the rail. Karlsson et al. [113] measured the hardness of the substrate, the macrohardness in the HAZ appeared "fairly constant and seems rather independent of the temperature history." It was observed that there were relatively few cracks present in the HAZ after testing indicating that this zone can also withstand high strain amplitudes.

An earlier paper by Niederhauser and Karlsson [115] tested residual stresses of laser clad steel in low cycle fatigue tests. They found that the process of laser cladding had high cooling rates in the clad layer, which they found created a very fine microstructure. It was also documented that residual stresses were present in the substrate, the reasons for which they state as the different thermal expansion coefficients in the clad and substrate, the different temperatures in the surface and substrate, and the linear expansion (of 1.5%) caused by the transformation from austenite to martensite. They found the clad had tensile residual stress, whilst the HAZ and substrate had compressive residual stress. Through the low cycle fatigue testing they discovered that residual stresses remain for small strain amplitudes but don't for high strain amplitudes.

Ringsberg et al. [125] conducted FEM analysis of laser clad rail and found that R260 grade rail clad with Co-Cr alloy coating caused a 'compressive residual hoop stress' due to the formation of martensite in the HAZ. They also found that the residual stress level in the rail after the laser cladding process influenced the risk of fatigue and acknowledged that there was the need for creating the correct design procedure. Clare et al. [112] also find that martensite is present in this region due to the rapid cooling.

Guo et al. [126] discuss how three regions are created when a Co-based alloy is laser clad to the substrate, these are the untreated substrate, the heat affected zone and the clad layer. Lai et al. [122] examined the microstructure of the HAZ and found that in the hypereutectoid rail grade the HAZ has four sub-regions, which they refer to as partially molten, coarse grained, fine grained and inter critical, all of which they state are influenced by their thermal history. Lewis et al. [110] describe how the HAZ is created as the substrate cools at a much faster rate than the clad layers due to the bulk volume of the substrate, with changes in the microstructure created which vary with material type and thermal expansion and contraction.

In many cases the substrate rail is pre heated during the laser cladding treatment, however, the laser clad coating is applied at a much higher temperature. The thin clad layer then has a greater difference in temperature than the bulk substrate rail to the ambient temperature. This is mentioned in the literature by Lewis et al. [110] who explain that residual stresses are formed through the differences in thermal expansions between the clad and substrate. Niederhauser et al. [115] conducted experiments in which they found that these stresses lead to an "asymmetry in the tensile and compressive peak stresses" and that the residual stress fields were unaffected during fatigue tests. Although the residual stress is mentioned in the literature the author has not

identified a model to represent how this would affect a laser clad rail in service.

FEM analysis in ABAQUS was conducted by Wu et al. [127] to model the distribution of residual stress throughout a Stellite coating and the carbon steel substrate it was applied to. The validation experiment for this model used a plasma transfer arc method of application rather than laser cladding, however, as the process is thermal it is comparable to laser cladding. The results of the paper show that the residual stress present in a coated steel is dependent on several factors, including the pre-heat temperature, the thickness of the base material, the thermal expansion coefficient and the heat transfer coefficient.

Narayanan et al. [128] also studied residual stresses in MSS laser clad coatings on R260 grade rail steel substrate. They considered that compressive residual stresses in the MSS laser clad coating are likely to have been created through the change in volume involved in the transformation into martensite. A method of non-destructive stress measurements were conducted using neutron diffraction which gave certainty from 0.4 mm below the surface. The stresses are compressive within the laser clad coating with the peak compressive stress being just above the interface. The stress returns to zero just below the interface and becomes slightly tensile in the substrate. This is similar to the results observed by Roy et al. [129], in which compressive residual stresses were measured in 410L low carbon content ferritic steel laser clad coating and tensile stresses in the head-hardened 0.93% carbon substrate rail with the transition occurring in the HAZ.

Hiensch et al. [49] found that the laser cladding process introduces compressive residual stresses in the DUROC 222 clad coating and tensile residual stresses in the substrate rail. They state three causes of this i) the different thermal expansion coefficients of the two materials, ii) the temperature gradient created by rapid solidification and iii) post manufacture grinding. A heat affected zone was created from this with a tempered martensitic or bainitic structure below the interface transforming into annealed pearlite and returning to pearlite further into the substrate rail. If the contact was within the shakedown limit then the compressive stresses would improve the safety margin, however above the shakedown limit the plastic flow accumulated in early cycles will make the response independent of the original stresses. Modelling of RCF in the laser clad rail was conducted by calculating wheel-rail contact loads, positions and sizes in GENSYS, a dynamic train-track interaction model, then applying these in finite element analysis to calculate rail stresses and shakedown of different coatings and traffic situations.

Lu et al. [2] show the HAZ and highlighted that the region has become austenitic during the laser cladding process and has then returned to a lamellar pearlitic structure resulting in coarser grain size due to high temperature experienced in this area. A method to control the pre-heat and post-heat of the laser cladding process is suggested by Meng et al. [130, 131] using a Laser Induction Hybrid Cladding (LIHC). The LIHC includes the laser cladding system with the addition of an induction heater and on-line temperature controlling device. The aim of the system is to avoid the transformation to martensite within the HAZ which can be pose a risk to rail safety due to its high hardness and low fracture toughness.

Roy et al. [132] address the problem of martensite formation in the clad coating and HAZ by trialling a method which involves a pre heat to 350°C, then a post heat to 350°C followed by a

controlled slow cooling which helps to stop the quenching phenomena. They find this is beneficial compared with pre heat alone. This research is further shown in Lai et al. [133] in which it is further shown that the microstructure of the HAZ is refined with subsequent layers of laser clad coating but the depth of the HAZ is not affected. Through the research conducted by Lai and Roy in Australia the optimum laser process parameters are finally determined in Lai et al. [133] as transverse speed 1000 mm/min and powder feed rate 3 RPM powder for 410L and transverse speed 1200 mm/min and powder feed rate 4 RPM powder for 420SS, Stellite 6 and Stellite 12.

2.4.3   Material properties, wear and RCF resistance of laser clad coatings

The material property requirements of the laser clad coating differ depending on the frequency and load of rail traffic in a specific country. The literature which is based on typical UK rail grade steels and loads is of most relevance to this project. Research on laser cladding for railway applications in the UK is first seen in 2004, since then there have been several research papers published showing promising results of railway track component life extension by this method. Franklin et al. [134] conducted twin disc experiments and metallurgical analysis of two unnamed coatings on R260 grade rail as part of an EU project, investigating the use of material coatings to reduce RCF and squeal noise. They conclude that the coatings bond well to the substrate rail and offer an improved resistance to RCF.

Whilst conducting a review of laser cladding Zhu et al. [135] also highlight that limited data is available on the mechanical properties of laser clad coatings or the resulting heat affected zones. The material properties of 410L grade stainless steel laser clad coating, the HAZ and substrate rail are evaluated through tensile tests by Roy et al. [136]. Due to the thin depth of laser clad coating a miniature tensile specimen had to be extracted from each layer using electro-discharge machining (EDM). The stress-strain curves from the monotonic tensile tests were then evaluated to extract the elastic modulus, yield strength, tensile strength and elongation. The pre and post process heating to 350°C followed by slow cooling used by Roy et al. [132] was seen to improve the tensile properties, in particular the elongation of the clad and HAZ resulting in a more ductile fracture behaviour. Further work by Lai et al [137] shows the ultimate shear strength and ultimate tensile stress of 410L are at least 80% higher than unclad rail.

Clare et al. [112] conducted further experiments to test Stellite 6 for hardness again, before a sliding test is conducted to assess wear, this test is achieved with a ball on disc tribometer which is not a realistic representation of wheel-rail contact as it does not simulate rolling, however, it provides a good test to further assess the work hardening ability by re-measuring the hardness after the test. The results of this paper "show that workhardenability of the cladding material is maintained with 30% increase in hardness." The hardness of the clad is recorded as 565 HB and the substrate as 310 HB.

Following the success of the small-scale testing, Lewis et al. [1] took the two most promising clad materials considering the wear rates and conducted full-scale experiments publishing their results in 2017 [7]. During this investigation MSS and Stellite 6 were clad onto full scale R260 grade rail

sections in a layer (1- 2 mm thick). These specimens were tested on a full-scale rail wheel test machine at The University of Sheffield, once again for wear, but also for plastic flow/lipping in an insulated block joint (IBJ) simulation. They were also tested in four-point bend fatigue. In the wear tests both clad materials saw a reduction in wear compared with the unclad R260, with the Stellite 6 having approximately 22% of the wear rate of the R260 and the MSS having approximately 11% of the wear rate of the R260. Both materials worked equally well in reducing plastic flow/lipping in the IBJ tests with the results showing that by cladding an IBJ it is able "to resist approximately 3 times the energy input into the contact as a standard unclad IBJ". The MSS performed better in the bend testing, however, this was thought to be due to inclusions in the Stellite 6 sample, indicating that the quality of the clad may be vital to the safety and performance of laser cladding of rails.

Lewis and Lewis produced an accompanying report [138] which contains further detail of the research project undertaken by The University of Sheffield to test a range of clad materials for wear, traction, surface roughness and fatigue. They conclude that Stellite 6 was the only clad material which outperformed the reference R260 rail grade sample under all tests. Results of tests using samples created with both one and two layers of cladding as seen in [7] are presented in more detail in this report, with the 2 layers Stellite 6 showing the lowest wear rates under both wet and dry conditions.

Of the clad materials tested the MSS, Stellite 6 and Stellite 12 produce lower wear rates in tests compared with the unclad samples and had no evidence of RCF crack initiation. The clad rail caused less wear to the wheel compared with unclad rail tests, this was also observed in results from Guo et al. [126]. Of these three materials Stellite 6 was described as "better than either the MSS or Stellite 12 having a virtually porosity free deposit and excellent fusion at the HAZ interface." This is important as any porosity has the potential to initiate cracks.

Christoforou et al. [81] include a laser clad coating in the benchmarking of wear mapping in premium rail materials. They conducted twin-disc tests to measure the wear of MSS laser clad coatings. They found the wear rate of the MSS to be significantly lower than any of the other tested materials at 1% slip. They also show that the wheel experiences less wear when run in contact with the MSS laser clad coatings compared with the other rail materials, which was also reported by Lewis et al. [139].

Lu et al. [2] present topography results of MSS clad coating on R260 after twin-disc testing (30,000 cycles) in comparison to an unclad R260 disc that has undergone the same test conditions. MSS on R260 had Ra = 0.6450 μm where as R260 unclad had Ra = 6.0614 μm shows much lower wear with clad coating and no wear flake formation. R260 has strain accumulation to point of ductility exhaustion. They further sectioned twin disc samples of MSS on both R200 and R260 and found deformation in the MSS at a shallow depth of 10 to 20 μm, observed visually using SEM. No cracks were found within this shallow depth of deformation and they conclude that the limit of ductility had not been reached during the ratcheting process.

Increased thickness of a coating is found to increase the wear and ratcheting resistance of a rail, with Ringsberg et al. [140] showing that the shakedown limit is higher the thicker the coat-

ing. They mention the feasibility of this in manufacturing not only down to cost, but also the limitations of process and application. Initial modelling of plasticity within laser clad coatings was conducted using the layer mode by Fletcher as part of the European Union's Horizon 2020 Shift2Rail/In2Track project [141]. Material properties for modern rail steels and laser clad coatings were not available and as such estimates were made by a scaled increase of the material response parameters found for BS11 rail by Kapoor et al. [67]. They found the depth of clad coating to be critical to increasing ratcheting resistance in the rail and to avoid peak stresses at the material interface. It is suggested that a 17 mm laser clad coating would be required on plain line to completely eradicate plastic damage.

2.5   Laser cladding for rail repairs

Seo et al. [142] conduct twin-disc tests with partial cladding specimens in which a section of rail material was removed from the rail disc and filled with a laser clad coating. They tested three candidate laser cladding materials, Stellite 21, Hastalloy C and Inconel 625. All of the partial cladding specimens experienced wear at the boundary with the substrate rail disc. The wear was proportional to the hardness of the repair material, with the hardest material Stellite 21 experiencing the most wear. Figures in the paper by show Seo et al. [142] show results with the heat affected zone visible and severe wear at the boundary with dense microstructure due to plastic deformation at the contact surface.

Nellian et al. [143] investigate laser clad coatings as a repair method for premium head hardened R350HT grade rail steel. The candidate laser clad coating material chosen is Stellite 6 which was applied to create a strong metallurgical bond at the interface without any porosity or voids present. The heat affected zone was seen to have a higher level of hardness than the clad coating or substrate rail due to the formation of martensite during the laser cladding process. Ball-on disc tribometer testing was used to assess wear of the coating rather than commonly used twin-disc testing. The wear volume reduced from 0.109 mm^2 for the unclad rail to 0.0587 mm^2 for the Stellite 6.

2.6   Identification of research gaps

The gaps identified in the literature are used to create the novelty in this thesis, as discussed in section 1.2. The material properties and response to cyclic loading are limited for laser clad coating materials. Within the literature the material properties are mostly found through tensile testing, which, although simple to conduct for standard rail materials is not representative of the compressive and shear stresses experienced in rail-wheel contact. Plasticity within laser clad coatings has not been quantified within the literature, most of the research measures only wear and rolling contact fatigue resistance of such coatings. The literature focused on full sections of laser clad coated rail with limited research or testing on laser clad coatings as a repair method.

Within this chapter a review of rail-wheel contact theory is presented highlighting the potential rail defects which can result from the high stresses generated by rail-wheel contact. Methods

to prevent defects through inspection and grinding are discussed along with current methods of weld repairs. The motivation to develop methods to repair and enhance rail to improve the longevity is ascertained. The existing research on laser cladding is then reviewed, similarities can be seen between weld repairs and laser clad coatings, however as the laser process is more localised it has the potential to reduce the risks associated with high heat input.

From the literature it is clear to see that laser clad coatings can be successfully applied to rails when the laser process parameters are optimised. The pre and post heating and cooling rate are shown to be critical in avoiding martensite within the clad coating and HAZ. The literature is predominately concerned with assessing the coating interface integrity, the wear and RCF performance. There are different clad coating materials tested within the existing research, all of which are shown to reduce wear and RCF compared with unclad rail. Most experiments test full sections of laser clad coated rails with limited tests conducted on repairs highlighting an opportunity to further develop this area of research.

Following the report by Lu et al. [2] R260 grade rail steel is chosen as the substrate rail material to further research in this project. The research by Lewis et al. [1, 7] recommends Martensitic Stainless Steel (MSS) and Stellite 6 as the best performing laser clad coating materials and as such are tested within this work. The work by Roy et al. [136] determines material properties of the laser clad coating using miniature tensile tests, indicating the difficulties in establishing properties due to the small dimensions of the coating. Kapoor et al. [67] find that material properties determined experimentally under high hydrostatic pressure are more reliable for rail materials. A gap is therefore established in developing a method to evaluate material properties of laser clad coatings.

Wear and RCF are shown in the literature to be reduced, but not eliminated, with plastic deformation reported in the top surface layers. The layer model by Kapoor et al. [67] shows potential for use with laser clad coatings as the material properties within each layer can be set accordingly to the coating, HAZ or substrate. With the plastic deformation seen in the surface depths of the laser clad coatings a comparison can be made with the subsurface stress fields generated by rough surface contacts as demonstrated by Mihailidis et al. [36]. This presents a further opportunity to investigate the surface roughness of laser clad coatings and the effect it has on plastic shear strain accumulation.

Following this review of literature, Chapter 3 describes the method developed to characterise the Shear Yield Stress - Plastic Shear Stress (SYS-PSS) relationship of the laser clad rail materials. Understanding the material response to load within these novel materials is a required predecessor to enable modelling of plastic damage within a laser clad rail steel alloy.

Chapter 3

Measuring material properties and plastic response to cyclic loading in laser clad coated rail steels

3.1 Introduction

Within the literature Kapoor et al. [67] highlight the importance of the Shear Yield Stress - Plastic Shear Strain (SYS-PSS) relationship of rail material, determined experimentally under high hydrostatic loading, for quantifying plasticity. The research described in this chapter quantifies plastic damage within the novel rail material consisting of laser clad low carbon Martensitic Stainless Steel (MSS) with 14.64% chromium applied to 0.62% carbon steel alloy, with the additional consideration of a Heat Affected Zone (HAZ) within the R260 substrate rail due to the laser cladding process as discussed in Chapter 2. The purpose of this chapter is to develop a method to characterise the SYS-PSS material response in these materials for the first time. This will support modelling of the behaviour of the clad layer under service loads and aid the quantification of the plastic damage within a laser clad rail steel alloy.

Quantifying the behaviour of these materials is challenging as the yield point is much higher than conventional rail steel resulting in less strain accumulation. Secondly, in common with other novel materials availability was limited for testing [144]. The shallow depth of the laser clad coating further makes testing by traditional methods difficult as demonstrated by Roy et al. [136] in the adaptation to miniature tensile tests. A successful method to characterise the SYS-PSS material response relationship of these materials using the lowest feasible number of twin-disc tests is presented in this chapter. The material properties, including hardness, modulus and micro-structure, of the MSS laser clad coating, R260 grade steel substrate and the HAZ are further assessed as part of this work. The material characteristics established in this chapter are all critical to the modelling of plasticity in the novel laser clad MSS-R260 rail alloy in Chapter 6.

Shear yield dependence on plastic strain for BS11 rail steel, which is a softer material than that typically used today, was quantified previously by Kapoor et al. [67] using data from a series of twin-disc tests conducted by Tyfour et al. [23]. The series of twin-disc test were conducted in a ratcheting investigation which used an increasing numbers of cycles. Following the ratcheting investigation tests the rail discs were sectioned and analysed to determine strain hardening and deformation at a depth of 200 μm below the surface, the material response curve was extracted from this. This method is suitable for materials with relatively low yield points which accumulate large shear strains and which have sufficient quantities available to perform multiple tests.

Kapoor et al. [67] tested whether the material stress-strain relationship could be taken from tensile testing results rather than twin-disc tests. They concluded that tensile tests gave unrealistic results and that the high hydrostatic pressure conditions of twin-disc testing were more representative of

rail-wheel contact as the material local to the contact is highly constrained by the surrounding rail material, which results in different material behaviour to that tested under atmospheric pressure conditions of monotonic tensile test conditions.

Measuring SYS-PSS under high hydrostatic loading requires adaptation for new materials which accumulate much lower plastic shear strain values and for novel materials of limited supply. Rolling-sliding twin-disc tests are chosen to generate ratcheting within the rail samples due to the high hydrostatic loading it provides. The method developed here takes multiple measurements from one sample at a range of depths below the contact surface, which crucially generates many more data points with fewer tests than required previously, hence reducing the time taken to characterise the material and reducing the cost and waste of samples. The material response to load is quantified through the SYS-PSS curves produced using this method providing a material characterisation to inform the suitability of MSS laser clad coating as a rail material for use in service by providing key parameters to model the plasticity resistance of laser clad coated rails in service.

3.2   Experimental and analysis methodology

The properties of the MSS laser clad coating, HAZ and R260 grade rail steel were observed prior to testing through a combination of optical microscopy, Electron Back Scatter Diffraction (EBSD), micro hardness measurements and nano-indentation to gain an insight into the MSS-R260 alloy. Samples of these materials were subjected to laboratory scale twin disc tests under high hydrostatic loading to generate plastic deformation comparable to that which may develop within rail steels in service. After testing, the materials were sectioned and analysed, measuring the hardness and the degree of plastic flow throughout the vertical longitudinal sub-surface plane. The twin-disc test plan is presented here, however, the design of the method means that the deformation history is unimportant providing tests have created an accumulation of plastic shear strain. The SYS-PSS relationship can be calculated from the moment in time that the analysis is conducted, providing a method which can be implemented in further work, for example in analysis of rail removed from service.

The material response to load was quantified within the following three rail materials to demonstrate the developed test method; (i) conventional R260 grade rail steel, (ii) novel laser clad coating rail material - MSS and (iii) the HAZ of the R260 grade rail substrate. R260 grade rail steel is known to experience ratcheting in service and was chosen for testing to show how the test method works when a large quantity of data can be easily generated. In contrast the MSS laser clad coating was selected as a novel material for which there was limited knowledge of its material properties. The HAZ of the R260 grade rail steel, created in the additive manufacturing process of the laser clad coating was treated as a separate material as it has properties distinct from the clad or substrate constituent materials.

3.2.1 Twin-disc experimental methodology (SUROS)

Twin-disc testing provides a contact replicating key features of the rail-wheel contact, with normal loading replicating the highly compressive stress environment characteristic of rail steel operation, and controlled slip replicating rolling/sliding contact. In combination these are characteristic conditions for generation of ratcheting, wear and rolling contact fatigue (RCF). Plastic shear strain was generated in samples of the three different rail materials using the Sheffield University ROlling Sliding (SUROS) twin-disc test machine [145] and is illustrated in the schematic Figure 3.1.
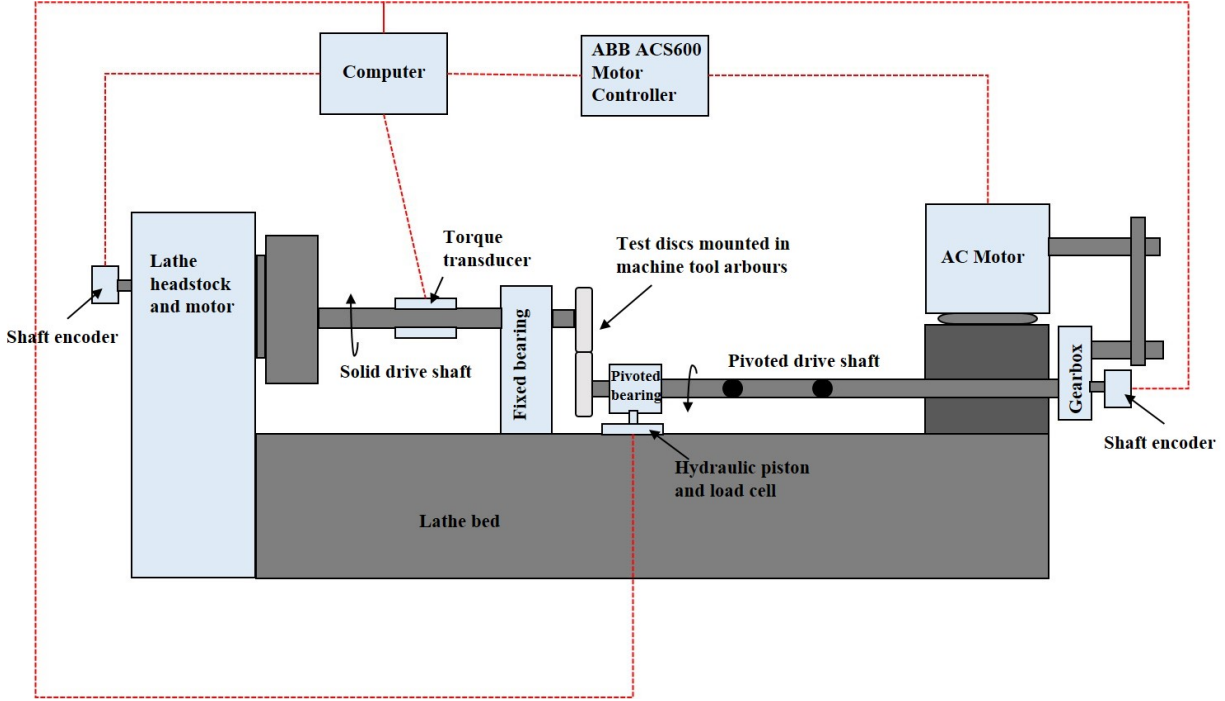
Figure 3.1: Schematic of Sheffield University ROlling Sliding (SUROS) twin disc test machine.

The SUROS machine requires the rail disc to be mounted as the upper disc which is driven by a modified Colchester Mascot lathe and is run at a speed of 400 RPM. The wheel disc is the lower specimen, controlled by the AC motor to counter-rotate, with the speed controlled by the connected computer. The required load is applied through the hydraulic piston and monitored with the load cell as the discs are bought into contact at the start of the test. Slip can be created between the discs as the closed loop of the AC motor, computer and shaft encoders ensure that as the rail disc remains at its constant speed the wheel disc will run at the required speed to generate the programmed slip level $S(\%)$, given by Equation 3.1.

$$S(\%) = \frac{200(R_r Vr - R_w V_w)}{R_r V_r + RwVw} \tag{3.1}$$

where R_r and R_w are the radii of the rail and wheel disc respectively (mm) and V_r and V_w are the number of revolutions of the rail and wheel discs respectively. The test variables of sample diameter and width, Young's modulus of the samples and the required maximum contact pressure and slip are set in the Labview programme on the attached computer. The coefficient of traction, de-

43

fined as the ratio of traction to normal load transmitted by the contact, can be calculated from the measurement of tractional torque between the discs monitored by the torque transducer.

Prior to the commencement of twin-disc testing the pair of rail and wheel discs were prepared by cleaning in an ultrasonic isopropanol bath for 2 minutes then the weight and diameter were measured and recorded. These measurements were repeated and recorded after testing. The pairs of sample discs were then mounted and secured in position as shown in Figure 3.1 with care being taken not to touch the disc which could cause contamination. Test length and parameters were chosen to ensure that a measurable level of strain would be present in the discs after testing. The maximum contact pressure was set at 1500 MPa in all of the tests, the rail disc was set at a speed of 400 RPM and the slip level was set at $-1\% \pm 0.01\%$ through variation of the wheel speed, including compensation for difference in disc diameter, this simulates a driving wheel. Each of the samples was run for 30,000 dry (unlubricated) cycles, enough to reach steady state, to generate an accumulation of plastic shear strain.
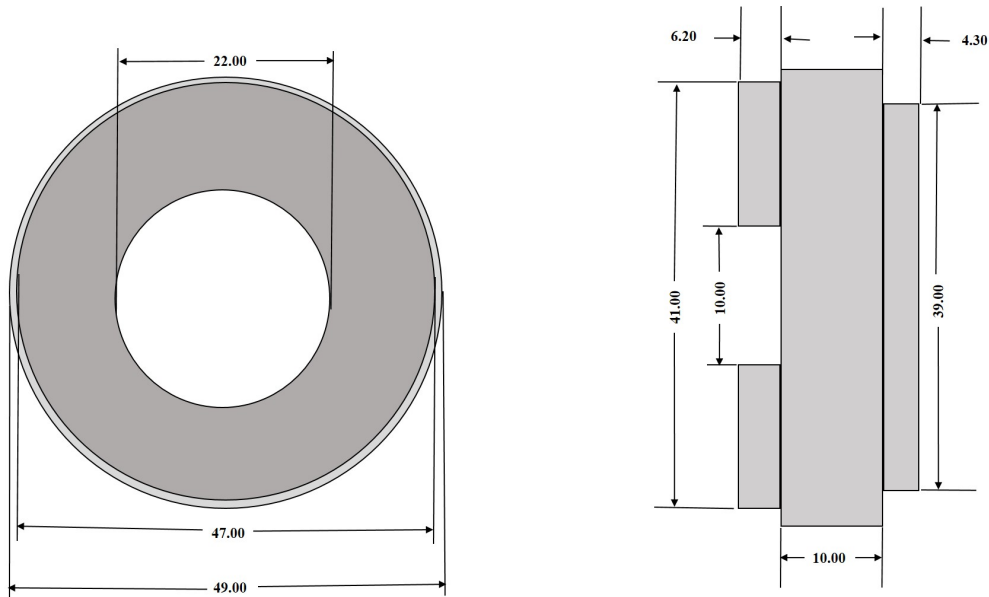
Figure 3.2: Standard dimensions of SUROS test disc specifications with the addition of a 1 mm laser clad coating.

The bulk of all the test discs were made from R260 grade rail steel, a cylinder of which is machined from a section of rail and then sectioned to create discs as shown in Figure 3.2, the unclad disc had a standard SUROS diameter of 47 mm. The laser clad discs were formed by machining the cylinder to 46 mm diameter and a one-step powder injection laser cladding system with optimised parameters, as described in Chapter 2 was used to deposit a 1 mm ± 0.1 MSS coating before the cylinder was then sectioned and machined into discs of 47 mm. The MSS laser clad coating is highly resistant to plasticity and trials with a 1 mm ± 0.1 coating showed little obvious plastic deformation in testing compared with unclad R260 tested under the same conditions as shown in Figure 3.3.
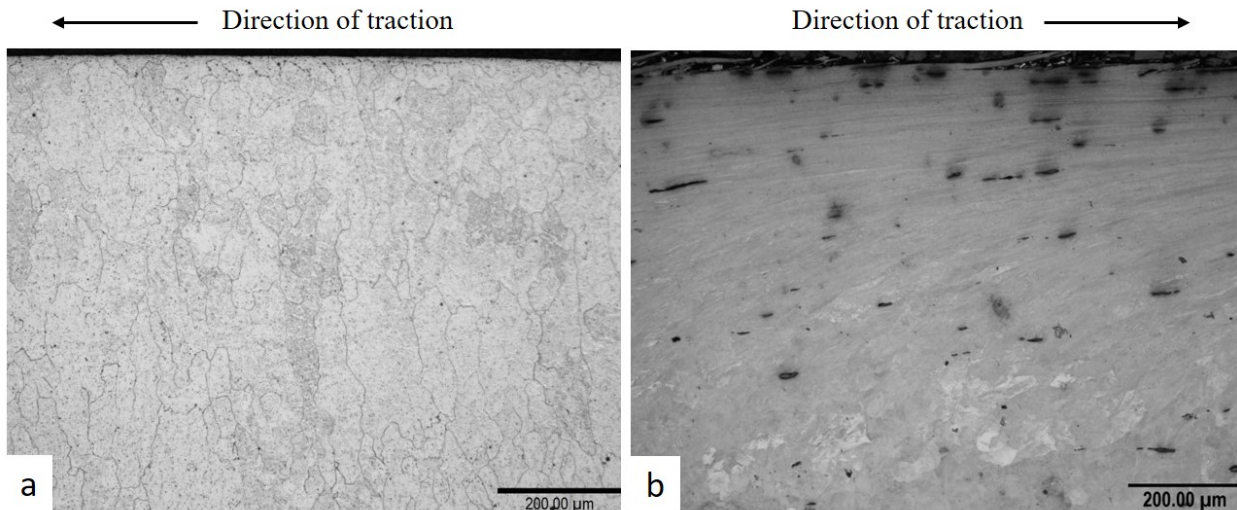
Figure 3.3: (a) MSS laser clad coating deposited to a 1 mm thickness on R260, showing a noticeably reduced level of plastic deformation compared with (b) unclad R260 following testing at 1500 MPa, -1% slip for 30,000 cycles.

The test plan is shown in Table 3.1 with the material investigated in each, the disc material and disc diameter.

Sample	Material investigated	Disc material	Disc diameter (mm)
Sample 1 (R252)	R260 substrate	R260	47.0
Sample 2 (CS43)	R260 HAZ	0.15 mm MSS Clad on R260	44.9
Sample 3 (CS44)	MSS	0.5 mm MSS Clad on R260	45.6
Sample 4 (R263)	R260 validation	R260	47.0

Table 3.1: Record of SUROS test samples, with the material of interest for each sample, the material composition of the disc and diameter of the disc.

Bespoke laser clad coated discs were manufactured for further investigation into the level of plasticity found within both the MSS and the HAZ post-testing, with varying coating thickness. Plastic deformation was only found in the shallow surface depths within all the MSS trials and it was decided that deformation measurements would be taken from rail discs which were created with a 0.5 mm ±0.1 thick MSS coating, resulting in an overall disc of 45.6 mm diameter. This thickness of coating ensured that the deformation was purely in the MSS and the HAZ remained unaffected.

A thin 0.15 mm ±0.05 coating, resulting in an overall disc diameter of 44.9 mm, was designed to allow the study of the HAZ. The change of diameter is taken into account in Equation 3.1 to ensure the tests are comparable. This is not representative of realistic end application thickness and was manufactured purely for the testing of the heat affected zone material. The contact stresses in this series of twin-disc testing was sufficient to drive a more extensive plastic flow into the substrate rail than when it was protected by a full clad layer. The wheel disc in each test was manufactured from a R8 wheel consisting of ER8 grade steel with $\leqslant$ 0.56 (% by mass) carbon content and 258-296

45

HB hardness [2]. Two vertical-longitudinal mid-track samples from each disc were extracted and analysed at multiple depths.

3.2.2 Shear yield stress-plastic shear strain analysis methodology

Following the twin-disc experiments the rail disc samples were sectioned to reveal the longitudinal sub-surface shear strain (with rolling direction x and depth z this is τ_{zx}) using standard metallographic techniques to achieve a $1\mu m$ diamond polish finish. DuraScan Micro Hardness laboratory tester was used to measure the Vickers hardness of the sub-surface material at a range of depths using a 0.2 kg load.

Etching was then required to reveal the microstructure of the materials prior to optical microscopy, the type of etchant and time required to reveal the structure was dependent on the material type. For the substrate R260 grade rail steel and the HAZ, the samples were submerged in 2% Nital (98% Industrial Methylated Spirit (IMS) mixed with 2% nitric acid) for approximately 45 seconds. The MSS laser clad coating is anti-corrosive and therefore required a harsher etchant solution and longer time. The etchant used was a mixture of 4.8% Nitric acid with the balance of equal volumes of Hydrochloric acid and water. The sample was submersed for around 5 minutes to reveal the microstructure of the MSS laser clad coating.

The plastic deformation was observed using an optical microscope with Buehler Omnimet 9.5 software used to measure the angle of plastic shear strain and the associated depth below the contact surface. Measuring the angle of deformation at a variety of depths which have different levels of plastic flow is where the method differs to previous techniques used by Tyfour et al. [48] in which the strain was only measured at a depth of $200\mu m$ below the contact surface following a series of tests of different durations to generate different extents of plastic flow.

Following measurement, the SYS-PSS relationship is then assembled from independent relationships established for shear yield stress variation with depth, and plastic shear strain variation with depth below the contact surface. This enables the generation of the full SYS-PSS curve from a single sample. The flow chart presented in Figure 3.4 shows the order in which the main analysis must be conducted in order to obtain the SYS-PSS curve for each material.
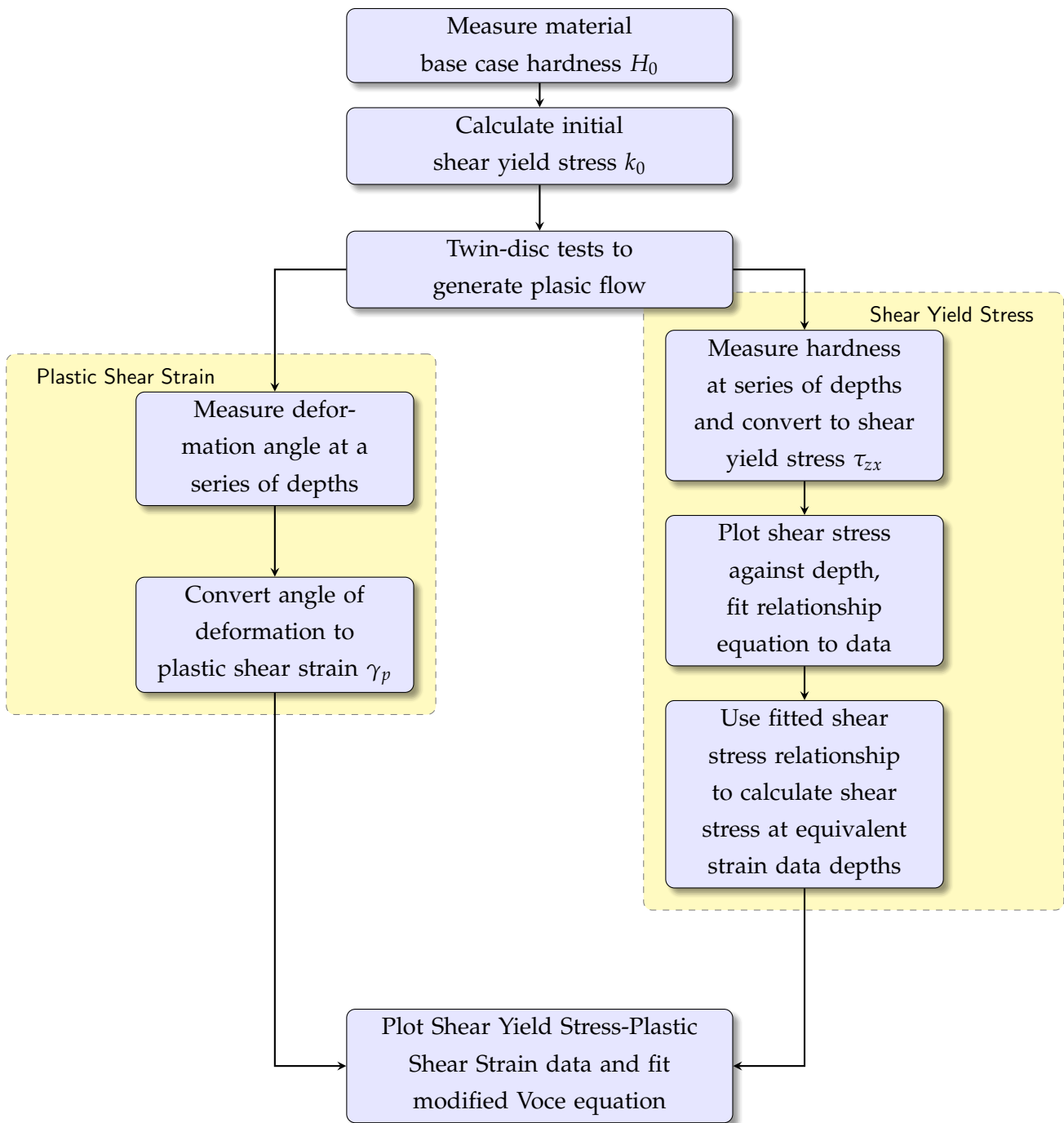
Figure 3.4: Analysis method for characterising Shear Yield Stress – Plastic Shear Strain relationship shown here in a flow chart. Illustrating the initial measurements required before twin-disc testing and the separate PSS and SYS analysis to be conducted before the final SYS-PSS curve is extracted.

3.3 Material properties prior to plastic damage

3.3.1 Microstructural observations

Prior to testing samples of the MSS-R260 alloy materials were sectioned and prepared for material property observations. Figure 3.5 shows the visual overview of the difference in microstructure in the different zones of a laser clad MSS-R260 alloy sample following etching in 2% Nital. The effect of the etchant is instantly visible, indicating the layers of MSS, HAZ and R260 substrate rail, which indicates that the three material zones could be analysed separately.

Figure 3.5: Polished (l) and etched (r) R260 grade SUROS with MSS laser clad coating samples

To further examine the difference in microstructure between zones images were taken with Scanning Electron Microscope (SEM) of the MSS-R260 alloy using a Hitachi TM3030 plus table top scanning electron microscope SEM. Figure 3.6 shows the the MSS laser clad coating, the coarse grain of the HAZ and substrate R260 grade steel.

Electron back scatter diffraction (EBSD) was carried out at the Sorby Centre at the University of Sheffield. Figure 3.7 shows the difference in micro-structure of the MSS laser clad coating and HAZ with the MSS grain structure significantly refined relative to the R260 grade (MSS grain dimensions approximately one tenth those of R260). The EBSD image showed the grains of grade R260 are much larger in the heat affected region just below the MSS layer than they are further from the surface. While this is a qualitative comparison it informs the interpretation of the response to load application quantified below through hardness and plastic shear strain measurements.
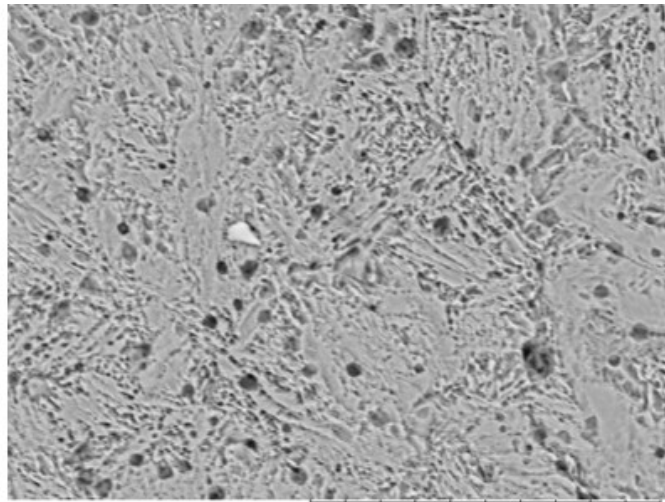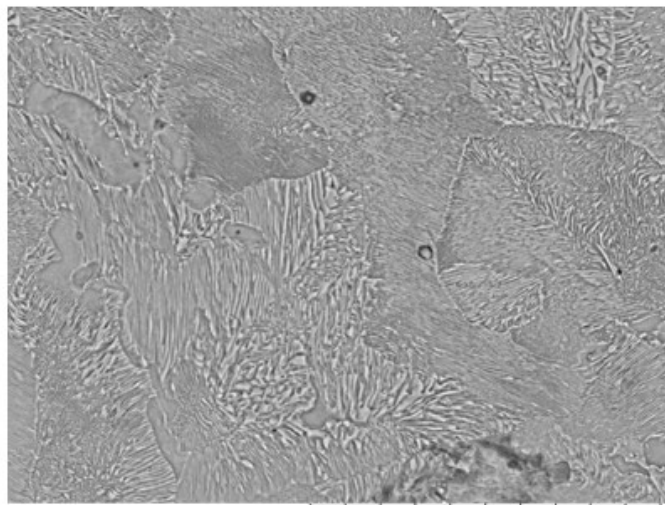
MSS Laser Clad Coating

R260 HAZ
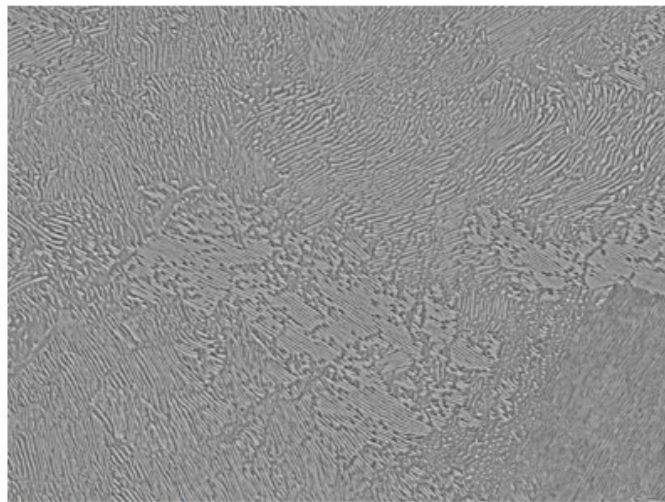
R260 Substrate

Figure 3.6: SEM material observation of MSS laser clad coating on substrate R260 grade rail steel. Showing the dense microstructure of the MSS laser clad coating, the reduced interlemellar spacing in the HAZ and the regular pearlite structure of the R260 grade rail steel.
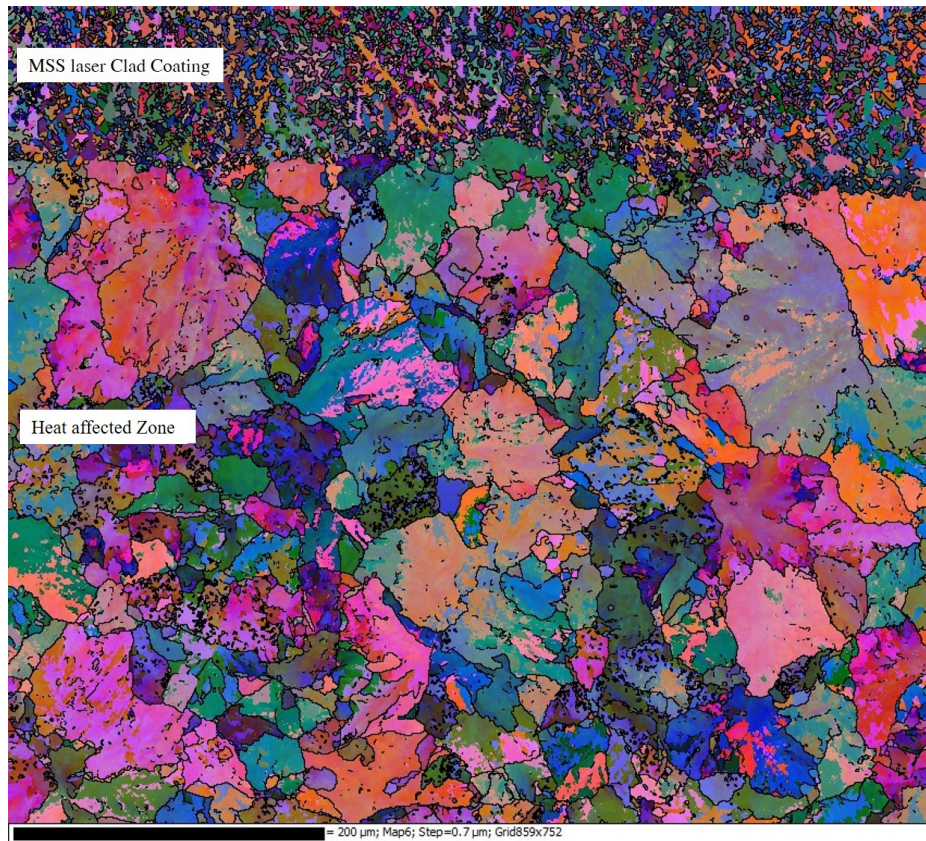
Figure 3.7: Electron Back Scatter Diffraction (EBSD) material observation of MSS laser clad coating on the Heat Affected Zone (HAZ) of the substrate R260 grade rail steel. Showing the comparison of grain structure in the MSS and R260 HAZ.

3.3.2 Hardness

Prior to rolling contact a DuraScan micro-hardness tester, with a 0.2 kg load was used to determine the hardness of MSS, HAZ and R260 grade rail steel using a twin disc sample manufactured with a 1 mm MSS laser clad coating. The Durascan micro-hardness tester can be used to measure the hardness of the rail sample using the Vickers method. This method uses a square based diamond pyramid indentation and calculates the standard Vickers pyramid number (V.P.N) as:

$$V.P.N = 1.854 \frac{P}{l^2} \tag{3.2}$$

where P is the applied load and l is the average length of the diagonal of the impression [146]. This method of hardness testing is quick and is used to obtain the initial microhardness. Results are shown in Figure 3.8, indicating that the hardness of the materials prior to testing differs, with the MSS laser clad coating being almost twice the hardness of R260 grade rail steel. The hardness in the HAZ is marginally higher than in the substrate. On the interface between the laser clad coating and the HAZ a small mechanical mix zone is present. This zone is less than 10 μm thick and therefore it is not possible to obtain the material response in this area, the data point at 487 $H_{v0.2}$ on the hardness map in Figure 3.8, however, is expected to be within the small mechanical mixed zone.
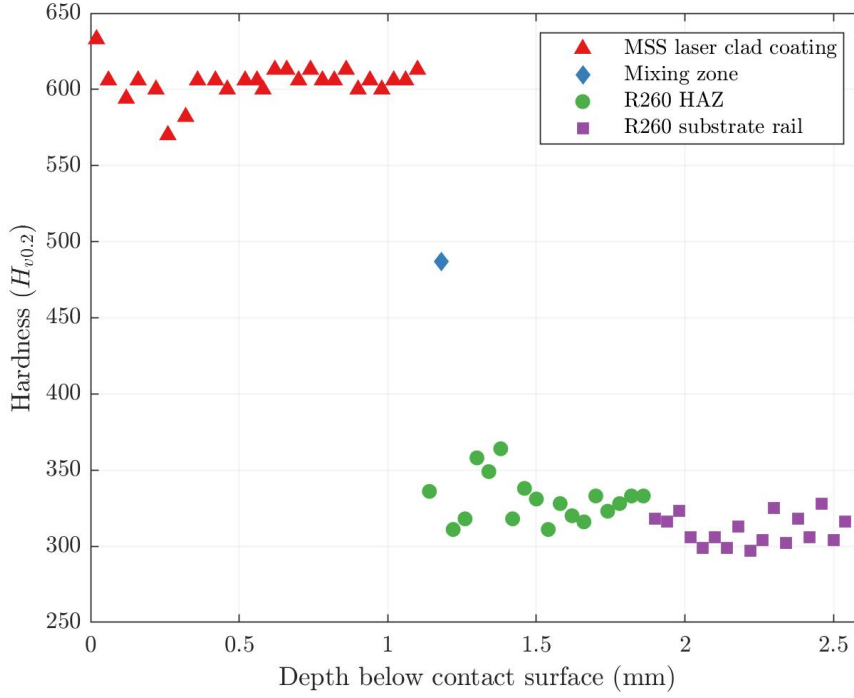
Figure 3.8: Vickers hardness $Hv_{0.2}$ through the vertical-longitudinal section of untested MSS laser clad coated R260 grade rail steel sample, showing the harder coating, the standard R260 substrate rail and the marginally hardened R260 Heat Affected Zone.

Micro indentation hardness results were used as a method to characterise the shear yield stress k of the materials. Hardness testing is useful as it applies a compressive stress environment similar to the rail operational conditions. The method of analysing shear yield stress through hardness measurements was also chosen due to requiring only small samples and being non-destructive other than the small hardness indents. Ashby et al. [147] shows that Vickers hardness H_v and yield strength σ_y have the relation shown in Equation 3.3:

$$H_v \approx \sigma_y/3 \tag{3.3}$$

The shear yield strength k, the point at which the materials begin to plastically deform is shown in Ashby et al. [148] to be Equation 3.4 using the Tresca yield criterion:

$$k_0 = \sigma_y/2 \tag{3.4}$$

The initial hardness measurements, H_{v0} were then used to calculate the initial shear yield strength, k_0, using Equation 3.5.

$$k_0 = \frac{3H_v}{2} \tag{3.5}$$

The average shear yield strength results of each material prior to rolling contact testing are presented in Table 3.2.

Zone	$(H_{v0.2})$	k_0 (MPa)
Substrate Rail Steel	302	454.1
Heat Affected Zone	339	508.5
Laser Clad Coating	606	906.0

Table 3.2: Average hardness and Tresca calculated Initial Shear Yield Stress of the three material zones R260 grade rail substrate, R260 HAZ and MSS laser clad coating.

3.3.3 Elastic Modulus

The laser clad coatings are formed by using a one-step powder injection method and the deposited material is usually of a depth of 0.5-2 mm [110] in a successful application. It would be unrepresentative of the laser clad coating to manufacture a solid tensile test specimen using this method nor would a specimen be able to be easily removed from the rail surface, hence another method to measure the elastic modulus of the novel rail materials. Nano-indentation testing was used to produce load-displacement plots from which the elastic modulus E for each material was calculated using the method described by Oliver and Pharr [149]. The reduced elastic modulus E_r, is found from the unloading curves and combines the modulus of both the indenter and the sample and can be calculated using the Oliver-Pharr method, Equation 3.6:

$$E_r = \frac{\sqrt{\pi}}{2\beta} \frac{S_u}{\sqrt{\sqrt{A(h_{cm})}}}$$ (3.6)

where β is a constant dependent on the shape of indenter, S_u is the initial slope of the unloading curve, $A(h_{cm})$ is the projected contact area at the maximum contact depth [149]. From the reduced modulus, the elastic modulus can be found when indenter elastic radius E_i, indenter Poisson's ratio ν_i and sample Poisson's ratio ν of the sample are known, Equation 3.7:

$$E = (1 - \nu^2)/[1/E_r - ((1 - \nu_i^2)/E_i)]$$ (3.7)

A series of nano-indentation tests were initially conducted on the laser clad MSS-R260 alloy samples using the Hysitron TI Premier [150]. Due to the large microstructural dimensions relative to the indenter the results from this were unreliable as individual indents may have, for example, fallen entirely in ferrite or cementite regions within the pearlite. This indicated that a more effective way to obtain informative results from nano-indentation of such a structured material was necessary and property mapping as shown in Figure 3.9, was conducted to generate a larger amount of data points across the material. It can further be seen from this that the MSS laser clad coating has a more consistent structure than the R260 grade rail steel.
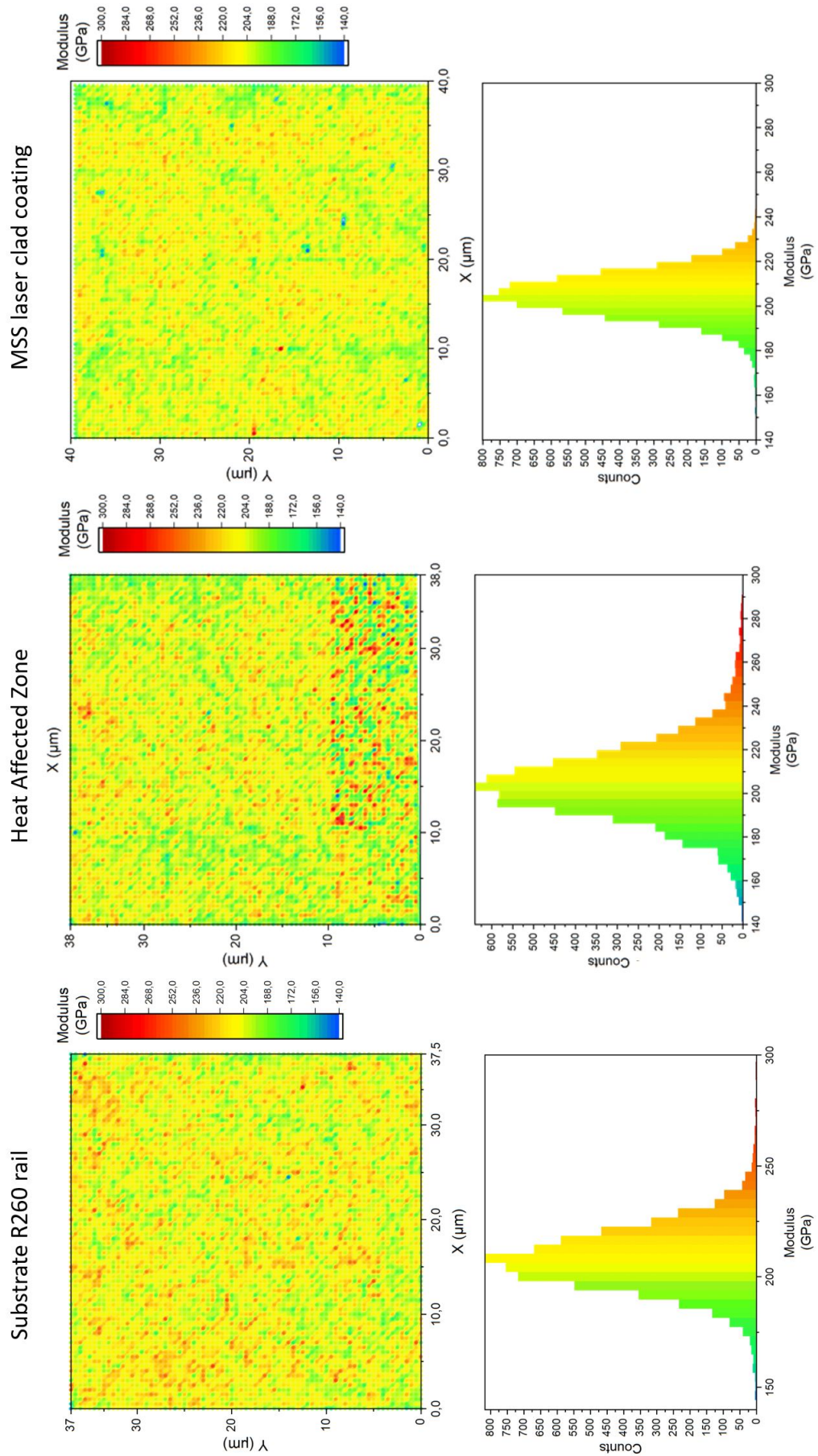
Figure 3.9: Nano-indentation mapping over $40\mu m^2$ area in R260 substrate rail, HAZ and MSS laser clad coating. Measuring the elastic modulus with 6400 indents, showing more variation across the microstructure of the pearlitic rail steel than the Martensitic Stainless Steel. [151]

The TI premier takes around 4 minutes to perform each individual indentation, therefore, the rest of the analysis was conducted with assistance of Bruker on the Hysitron TriboScanner which has the improved capability of conducting 2 indents per second. A map of 6400 indents was created over a $40\mu m^2$ area in the substrate R260 rail, HAZ and MSS laser clad coating. This method used a fast mapping technique with a diamond Berkovich probe calibrated on fused quartz. The plotted distribution of these data points is shown in Figure 3.10, together with the average and standard deviation of the elastic modulus for each material [151].
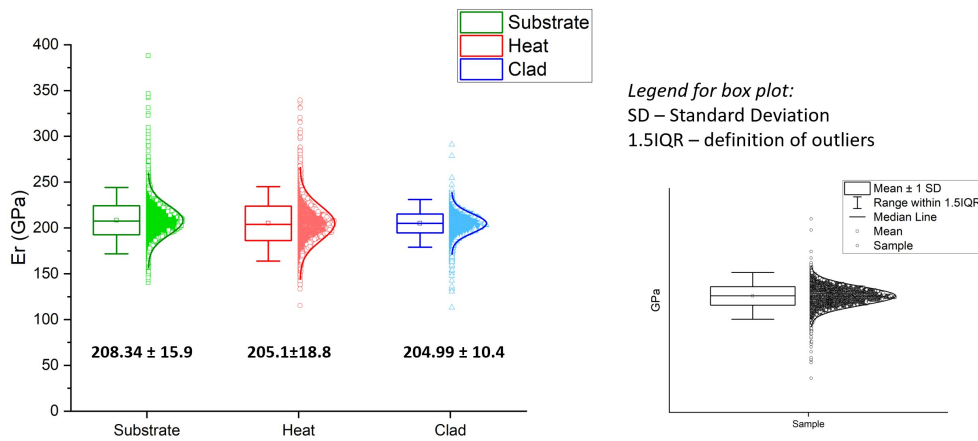
Figure 3.10: Box plot showing spread and standard deviation of Elastic modulus data results from the nano-indentation mapping [151].

3.4 Results

3.4.1 Coefficient of Traction in Testing

The tests on the three materials were each conducted in dry conditions with a maximum Hertzian contact pressure of 1500 MPa and a slip of -1% for 30,000 cycles. The coefficient of traction (CoT) was calculated from the measurement of tractional torque between the twin-discs in each test and the results are shown in Figure 3.11. It is defined as the ratio of traction to normal load transmitted by the contact. The level of CoT in twin-disc testing normally follows the same pattern as that shown in Figure 3.11, in which it reaches a peak and drops away, this may be explained by the evolution of the surface during testing. The peak CoT in the R260 test was 0.48, this measurement was used as an indicator that plastic damage would be expected within the disc, as ratcheting is recorded in tests conducted under the same dry conditions with a peak CoT of 0.44 by Tyfour et al. [23]. For the MSS clad surface, the peak CoT was marginally lower than for the R260 test, the 0.15 mm MSS laser clad coating had a peak CoT of 0.44 and the thinner 0.5 mm MSS laser clad coating produced a peak CoT of 0.43.
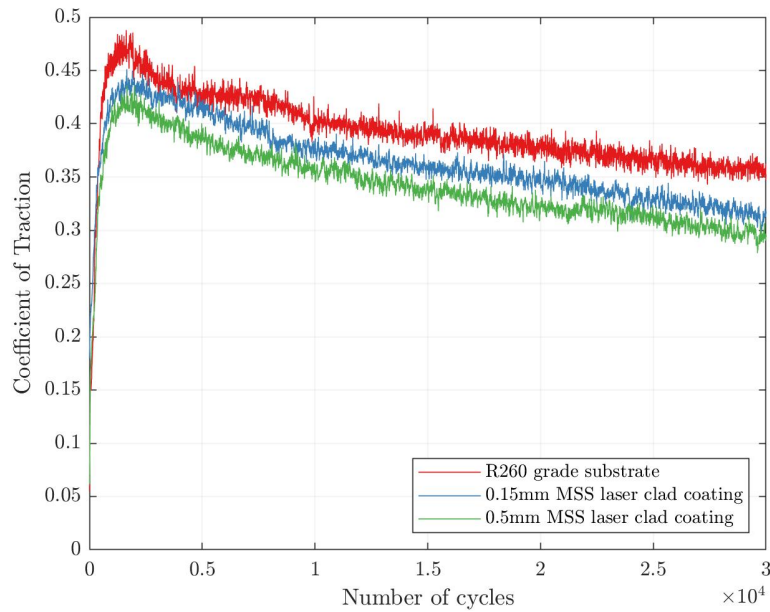
Figure 3.11: Twin-disc coefficient of traction (CoT) for R260, 0.5 mm and 0.15 mm MSS laser clad coatings when tested at 1500 MPa, -1% slip, 30,000 cycles. The peak CoT is 0.48 for R260, 0.44 for 0.15 mm MSS laser clad coating and 0.43 0.5 mm MSS laser clad coating.

3.4.2   Twin-disc results

After twin-disc testing of the three different material samples with the test conditions described in Section 3.2.1, vertical-longitudinal sections were extracted from the disc and prepared through standard metallographic techniques of mounting, grinding, polishing to 1 μm diamond finish and etching with 2% Nital to reveal the pearlitic microstrcture of the R260 steel alloy and the HAZ or etching with the 4.8% Nitric acid, equal parts Hydrochloric acid and water mixture as described in Section 3.2.2 to reveal the microstructure of the MSS laser clad coating.

The R260 steel alloy performed as expected with a large visible amount of plastic deformation down to around 450 μm below the contact surface. The wear rate of the tested rail disc was 9.67 μg/cycle and the wear rate of the wheel disc was 18.39 μg/cycle. The resultant deformation is shown through optical microscopy in Figure 3.12.

The 0.5 mm MSS laser clad coating, with its high resistance to ratcheting, again performed as expected. The substrate rail was completely protected and experienced no deformation below the coating. The MSS itself experienced very mild, shallow surface deformation to around 50 μm, as would be expected since R260 alone only experienced deformation to 450 μm. The resultant deformation is shown through optical microscopy in Figure 3.13. It is to be noted that the lines visible on the surface are grains in the microstructure enhanced by the etchant and are not cracks.

The wear rate of the tested rail disc was 3.92 μg/cycle and the wear rate of the wheel disc was 15.11 μg/cycle. The wheel disc experienced less wear when in contact with the harder MSS than when in contact with the R260, this follows previous research by Lewis et al. [1] in which wheel wear rate was seen to remain constant or reduce when in contact with laser clad rail discs, further research [139] has indicated that the wear rate of the wheel is dependent only on the material

properties of the wheel itself. The low wear rate of the laser clad coating reduces the amount of wear debris, less third body contact is likely to be a contributing factor of the reduction in wheel wear.

200.00 µm
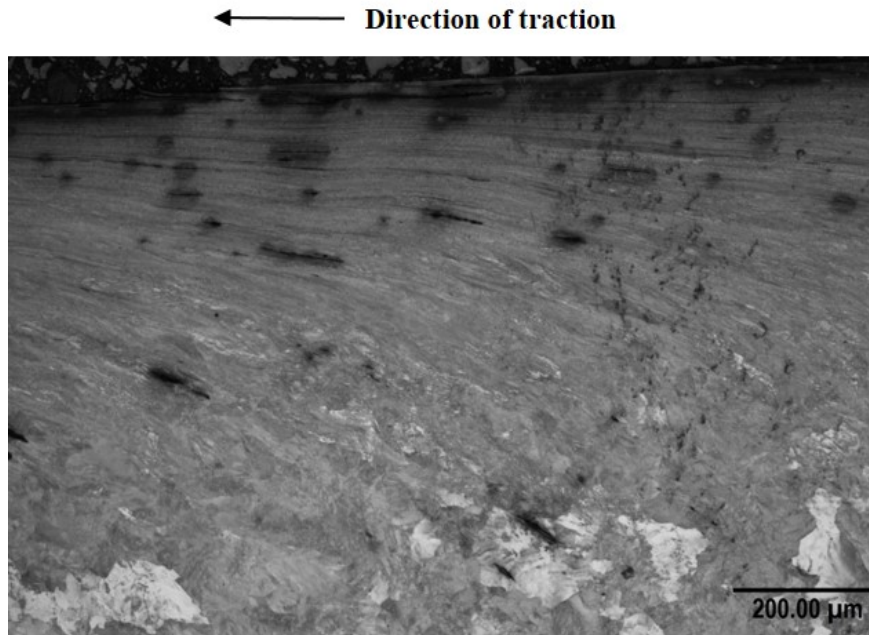
Figure 3.12: Sample 1: R260 steel alloy rail disc following testing at 1500 MPa, -1% slip for 30,000 cycles, with significant plastic deformation below the contact surface.

The 0.15 mm MSS laser clad coating experienced plastic deformation below the material interface within the HAZ, shown in Figure 3.14. Deformation was observed down to around 330 μm from the material interface, which considering the surface coating depth puts the deformation to a depth of 480 μm from the contact surface. This is slightly deeper than the deformation experienced in the unclad R260 rail steel and is reason to consider the properties of the heat affected zone independently. The wear rate of the tested rail disc was 7.41 μg/cycle and the wear rate of the wheel disc was 14.62 μg/cycle. As anticipated the depth of coating was not suitable for protecting the substrate rail from plastic flow or representative of the depth of coating which would be expected in service. This does, however, provide the deformation in the HAZ to measure and quantify the SYS-PSS which is the desired outcome of this test. A higher magnification of the thin laser clad coating above the HAZ is presented in Figure 3.15 with plastic deformation shown within the top 30 μm below the contact surface. It should be noted that the strong etchant has caused surface marks and that the lines do not represent cracks.

The Tyfour et al. [23] method of taking all strain measurements from 200 μm below the contact surface would have worked for the standard R260 grade of pearlitic rail steel, however, it can be seen that with the much shallower level of deformation within the MSS laser clad coating, it would not work and hence this new method is adopted, as described in Section 3.4.4.
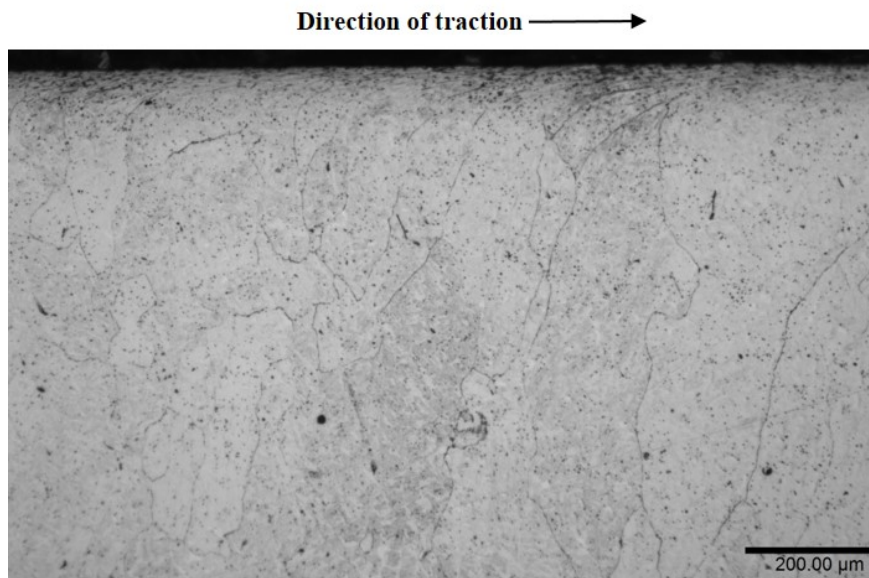
Figure 3.13: Sample 3: MSS laser clad coating following testing at 1500 MPa, -1% slip for 30,000 cycles, with minimal plastic deformation on the shallow surface only.
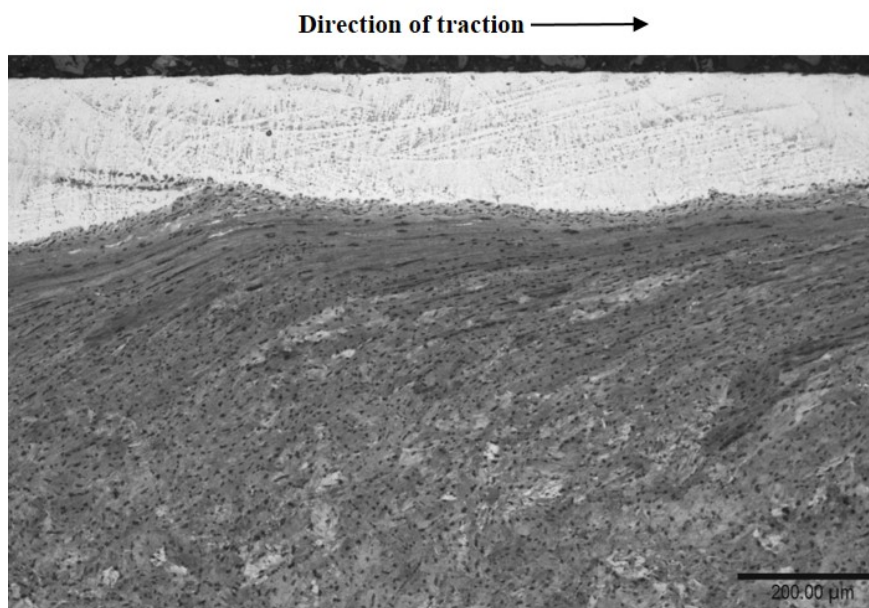
Figure 3.14: Sample 2: R260 HAZ below MSS laser clad coating following testing at 1500 MPa, -1% slip for 30,000 cycles, with plastic ratcheting below the interface of the laser clad coating in the Heat Affected Zone, where the depth of clad coating is unrealistic to what would be expected in service.
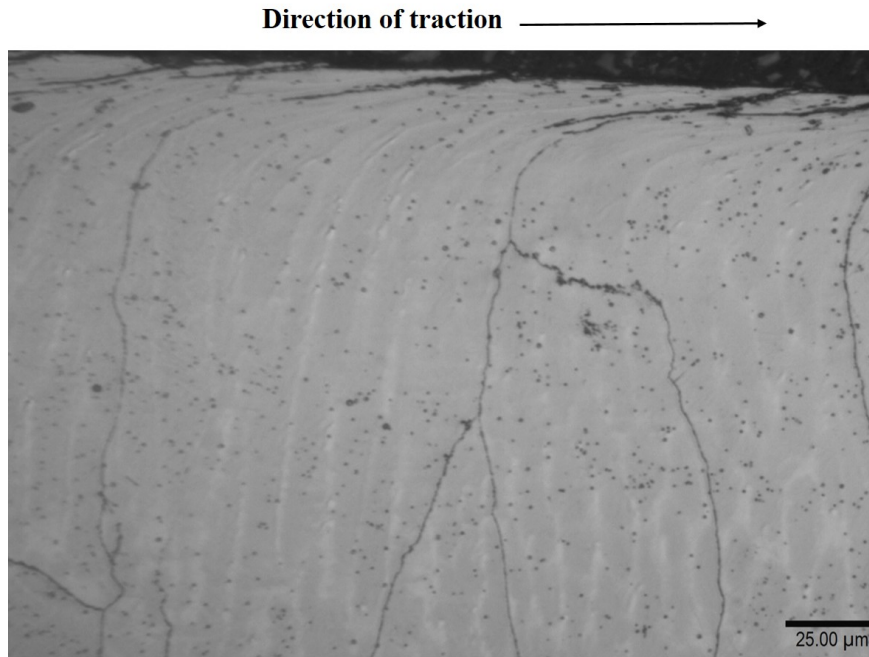
Figure 3.15: Sample 2: Thin 0.15 mm laser clad coating following testing at 1500 MPa, -1% slip for 30,000 cycles, with plastic ratcheting in the shallow surface depths.It should be noted that the strong etchant has caused surface marks and that the lines do not represent cracks.

3.4.3 Yield Stress variation with depth below the running surface

The hardness was measured using the DuraScan microhardness tester following the twin-disc testing for each of the material samples. Considering the data points closest to the surface, Figure 3.16 shows that the R260 grade rail steel hardened by up to 69%, this beneficial behaviour being one reason pearlitic steel is attractive for use in rail applications.
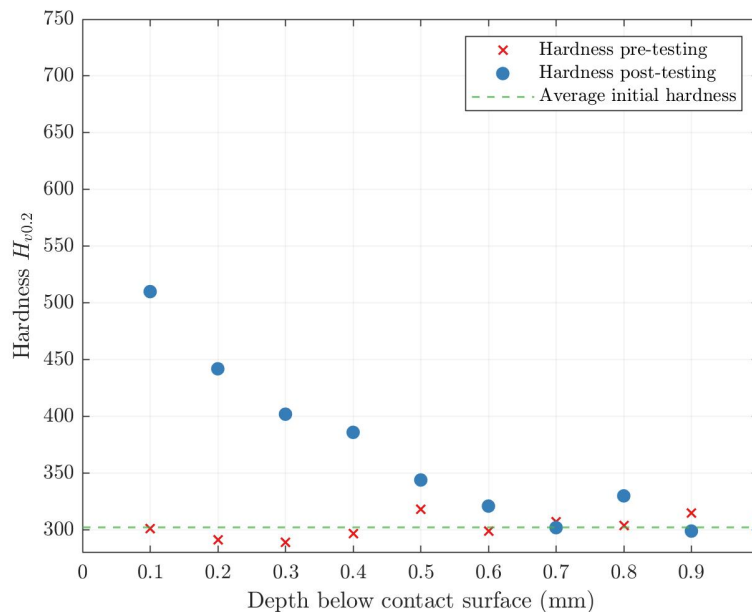
Figure 3.16: Sample 1: R260 grade rail steel. Increase in hardness after testing at 1500 MPa, -1% slip and 30,000 cycles compared with material hardness pre-testing.

Figure 3.17 shows hardening in the HAZ below the 0.15 mm laser clad coating, at the same test conditions. The hardness increased up to to 33% at the interface which is less than the unclad R260 grade rail HAZ specimen being protected by the MSS laser clad coating.

The MSS laser clad coating itself, tested in sample 3 was found to have increased in hardness by only 13% as shown in Figure 3.18. The shallow nature of the plastic flow meant that fewer data points could be collected in this case.
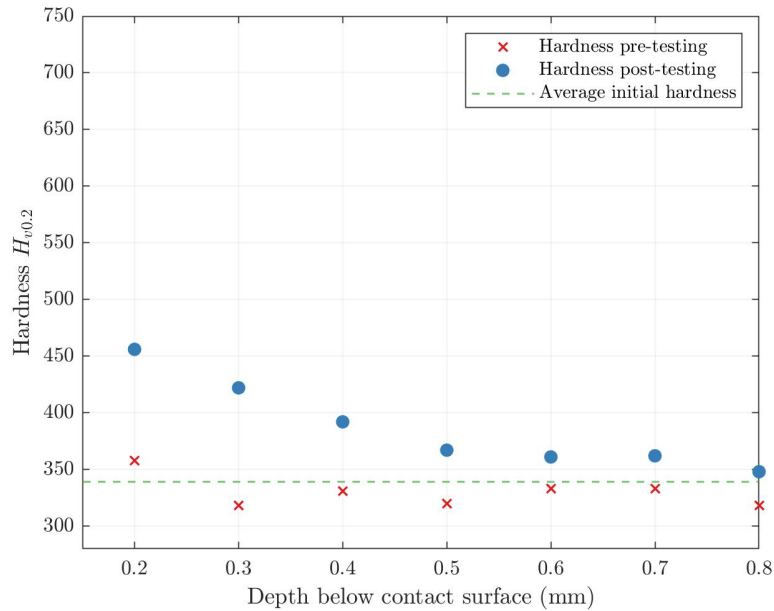
Figure 3.17: Sample 2: R260 HAZ. Slight increase in hardness after testing at 1500 MPa, -1% slip and 30,000 cycles compared with material hardness pre-testing.
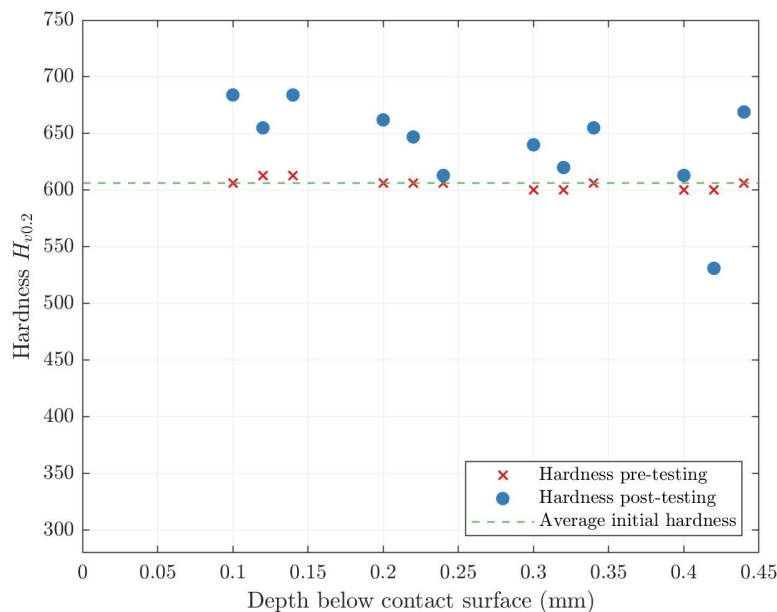
Figure 3.18: Sample 3: MSS laser clad coating. Minor increase in hardness after testing at 1500 MPa, -1% slip and 30,000 cycles compared with material hardness pre-testing.

Using the initial hardness results from the untested samples together with the post-test hardness measurements, the effective shear yield stress k_{eff} was calculated for a range of depths x below the contact surface using Equation 3.8:

$$k_{eff} = k_0 \frac{Hv_{eff}}{Hv_0} \tag{3.8}$$

The hardness measurements for the R260 grade rail steel after testing at 1500 MPa, -1%, 30,000 cycles are shown in Table 3.3 with the respective effective shear yield stress which is calculated using Equation 3.8 and the average hardness and initial shear yield stress given in Table 3.2. The relationship between depth and shear yield stress is then found from the relationship between the depth and shear yield stress data, shown in Figure 3.19.

Depth (mm)	0.1	0.2	0.3	0.4	0.5	0.6	0.7	0.8	0.9	1.0
Hv	510	442	402	386	344	321	302	330	299	300
k_{eff} (MPa)	767	665	604	580	517	483	454	496	450	451

Table 3.3: Sample 1: R260 depth below contact surface (mm), hardness pre-testing, hardness post-testing and effective Shear Yield Stress

The hardness measurements and corresponding effective shear yield stress values for the HAZ are shown in Table 3.4. The relationship between depth and shear yield stress is once again found from the line of best fit to the depth and shear yield stress data, shown in Figure 3.20.

Depth (mm)	0.2	0.3	0.4	0.5	0.6	0.7	0.8
Hv	456	422	392	367	361	362	348
k_{eff} (MPa)	684	633	588	551	542	543	522

Table 3.4: Sample 2: HAZ depth below contact surface (mm), hardness pre-testing, hardness post-testing and effective Shear Yield Stress

The depth of the MSS laser clad coating limited the number of hardness measurements which could be taken, to overcome this staggered rows of hardness measurements were recorded to expand the amount of data available. The hardness measurements and corresponding effective shear yield stress values for the MSS are shown in Table 3.5

Depth (mm)	0.10	0.12	0.14	0.20	0.22	0.24	0.30	0.32	0.34	0.40
Hv	684	655	684	662	647	613	640	620	655	613
k_{eff} (MPa)	1023	979	1023	990	967	916	957	927	979	916

Table 3.5: Sample 3: MSS depth below contact surface (mm), hardness pre-testing, hardness post-testing and effective Shear Yield Stress
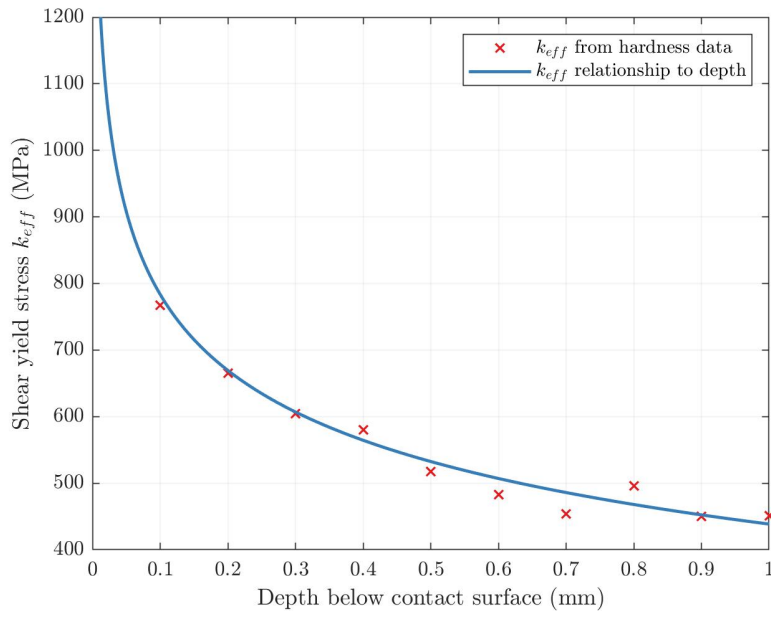
Figure 3.19: Sample 1: R260 line of best fit showing the Shear Yield Stress relationship with depth
x, $\qquad k_{eff} = 1068x^{-0.1216} - 629.4$
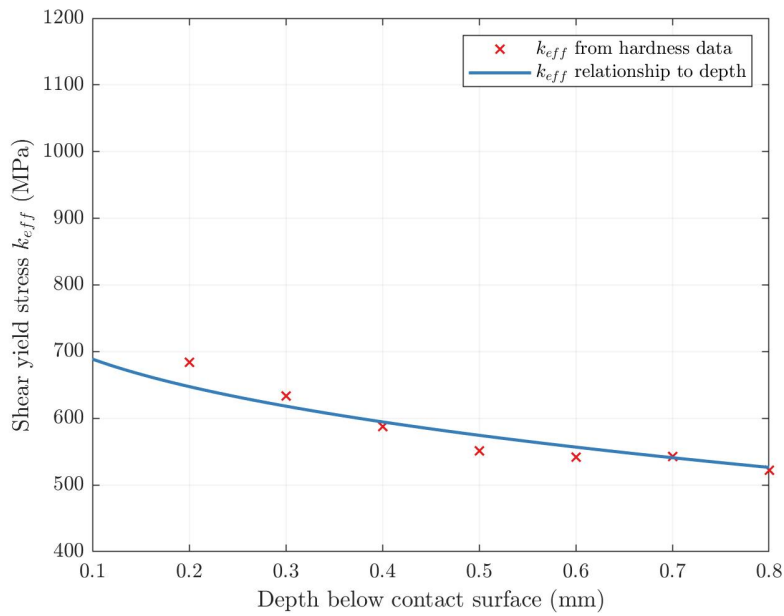
Figure 3.20: Sample 2: R260 HAZ, line of best fit showing the Shear Yield Stress relationship with
depth x, $\qquad k_{eff} = -331.7x^{0.3641} + 832.2$
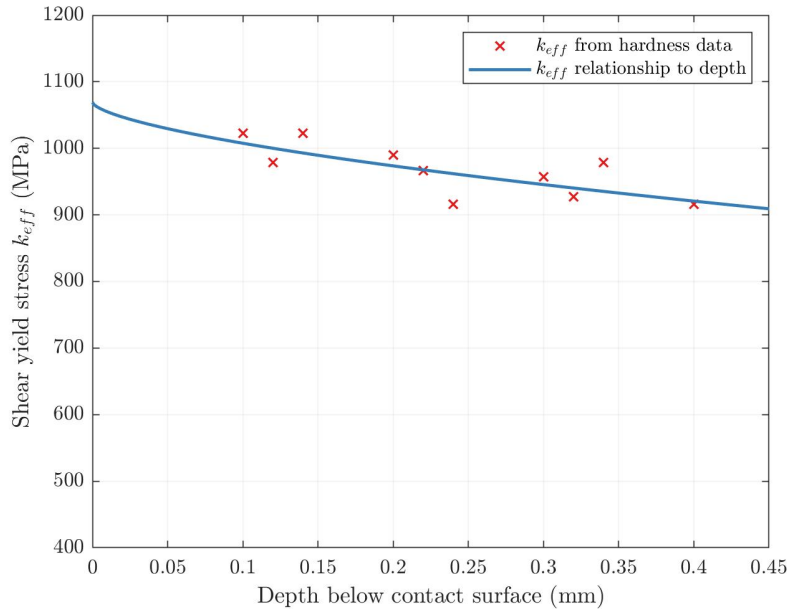
Figure 3.21: Sample 3: MSS laser clad coating, line of best fit showing the Shear Yield Stress relationship with depth x, $k_{eff} = -265.7x^{0.6367} + 1069$

The lines of best fit plotted through these results give the equations for shear yield stress plotted against the depth below the contact surface for each material, shown in Table 3.6 with the goodness of fit parameters. It should be noted that due to the type of fit for the R260 grade rail steel, that shear yield stress calculated from the equation may not be reliable below approximately 0.05 mm.

Material	Shear yield stress fit equation
R260 Substrate	$k_{eff} = 1068x^{-0.1216} - 629.4$
HAZ	$k_{eff} = -331.7x^{0.3641} + 832.2$
MSS Clad coating	$k_{eff} = -265.7x^{0.6367} + 1069$

Table 3.6: Shear stress against depth line of best fit equations and quality of fit to data. Equations required to calculate Effective Shear Yield Stress at the equivalent depths of Plastic Shear Strain measurements that follow in Section 3.4.4.

3.4.4   Strain variation with depth below the running surface

Plastic shear strain γ_p was quantified through the measurement of the plastically deformed microstructure at a range of depths below the contact surface of the samples, using the tangent to the angle θ, as shown in Equation 3.9:

$$\gamma_p = \tan(\theta) \tag{3.9}$$

This is a similar approach to that used in previous investigations [48] and [67] in which shear strain was measured at a single depth. The developed method examined strain at a range of depths from the running band illustrated in Figure 3.22 rather than at a single depth from the running surface as conducted previously.
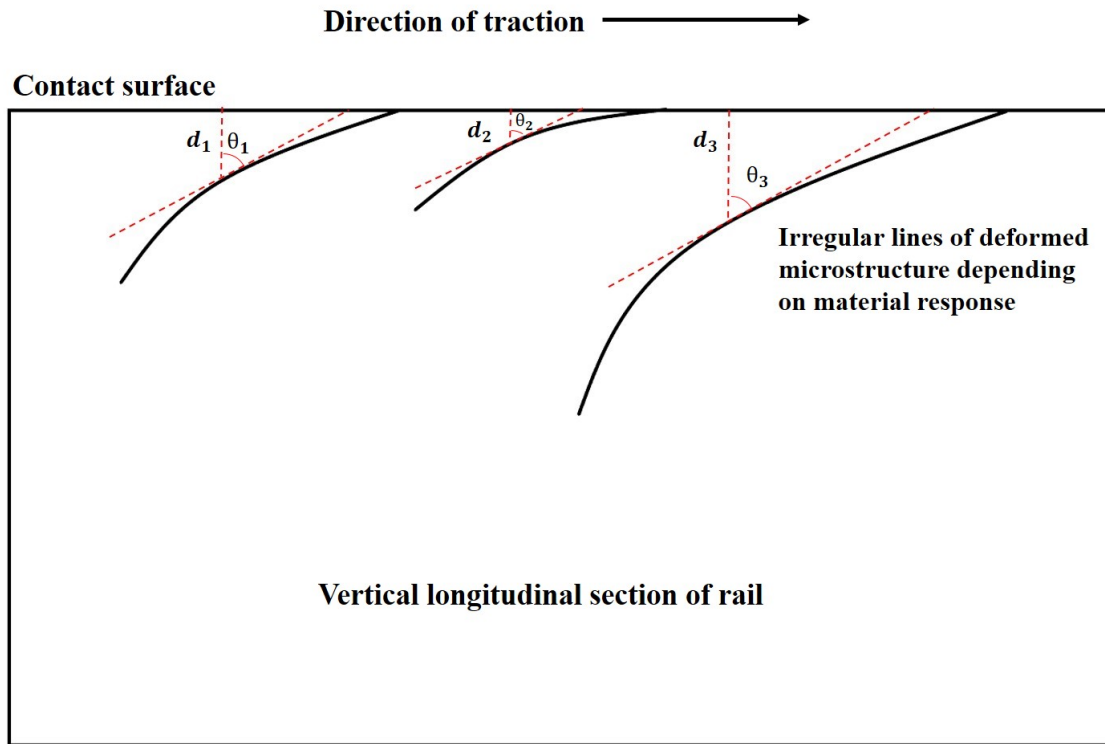
Figure 3.22: Developed method to measure Plastic Shear Strain. Angle of deformation θ measured at variable depths d and recorded as pairs of data to enable the calculation of Shear Yield Stress at the equivalent depths.

This provided information on a range of plastic strains from a single sample whereas previously this was achieved using many samples run for different durations. While there is a significant advantage in the reduced number of samples needed, the evolution of strain with number of contact cycles cannot be determined from a single test. However, as long as test duration is sufficient to take the material to ductility exhaustion evidenced through crack initiation or reaching a constant wear rate, for example, it is possible to determine the end point of the strain accumulation process. Examination at a range of depths is also more appropriate for cases in which materials change with depth, such as crossing from the clad layer to the HAZ and then the substrate. Collecting data at a single fixed depth would be unlikely to adequately capture properties for this case.

Measurements of the deformed microstructure were estimated to have an uncertainty of $\pm 0.5°$ due to the variation of deformation with depth. With the test conditions used, the R260 grade rail steel was found to accumulate the greatest plastic strain of the materials tested, one of the sections from sample 1 is shown in Figure 3.23 with the depth and angles of deformation. The data points from this are presented in Table 3.7, further data points from another cross section from sample 1 are used in addition to provide further assurance when extracting the SYS-PSS curve in Section 3.5. The HAZ and MSS laser clad samples were found to be more resistant to accumulation of plastic shear strain and it was only possible to collect around 10 data points for each of these

materials (Figure 3.24, Table 3.8 and Figure 3.25, Table 3.9 respectively). This is still double the number of data points previously found satisfactory for defining material behaviour in BS11 normal grade rail steel [67]. The thin clad present in the HAZ specimen was particularly useful for understanding how the cladding may 'scale up' to full size rail wheel contacts, illustrating that a coating that is thin relative to the contact stress field size will allow plastic strain accumulation in the substrate below the cladding as shown in Figure 3.24. Importantly, it was found that despite the significant substrate plastic strain accumulation the cladding showed no sign of de-bonding or separation.
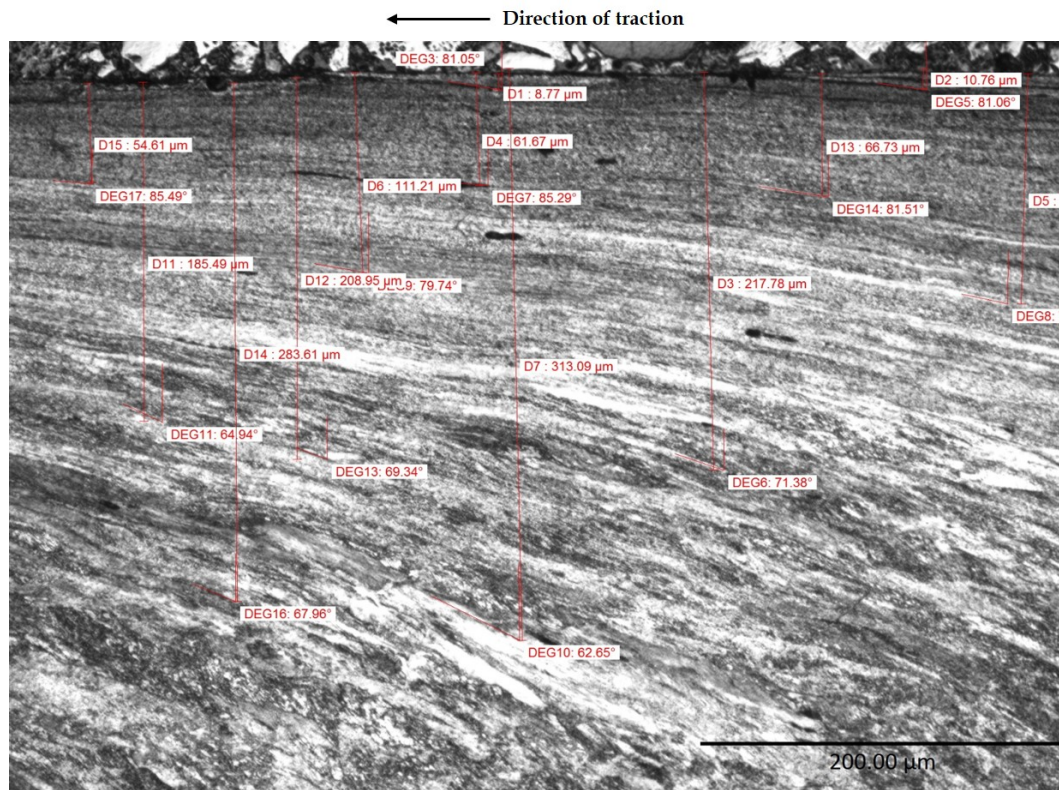
Figure 3.23: Sample 1: Image showing the measured angles of deformation and corresponding depth measurements within the R260 rail material. Measurements taken with Buehler Omnimet 9.5 software under optical microscopy and recorded in Table 3.7

Depth (mm)	Angle of deformation (deg)	Plastic Shear Strain	Shear Yield Stress (MPa)
0.06	85.49	12.68	874
0.06	85.29	12.14	874
0.07	81.51	6.70	846
0.09	81.05	6.35	802
0.11	81.06	6.36	767
0.11	79.74	5.52	767
0.19	64.94	2.14	678
0.21	69.34	2.65	662
0.22	71.38	2.97	655
0.28	67.96	2.47	617
0.31	62.65	1.93	602

Table 3.7: Sample 1: R260 Depth below contact area with corresponding Plastic Shear Strain and Effective Shear Yield Stress using equation from Figure 3.19
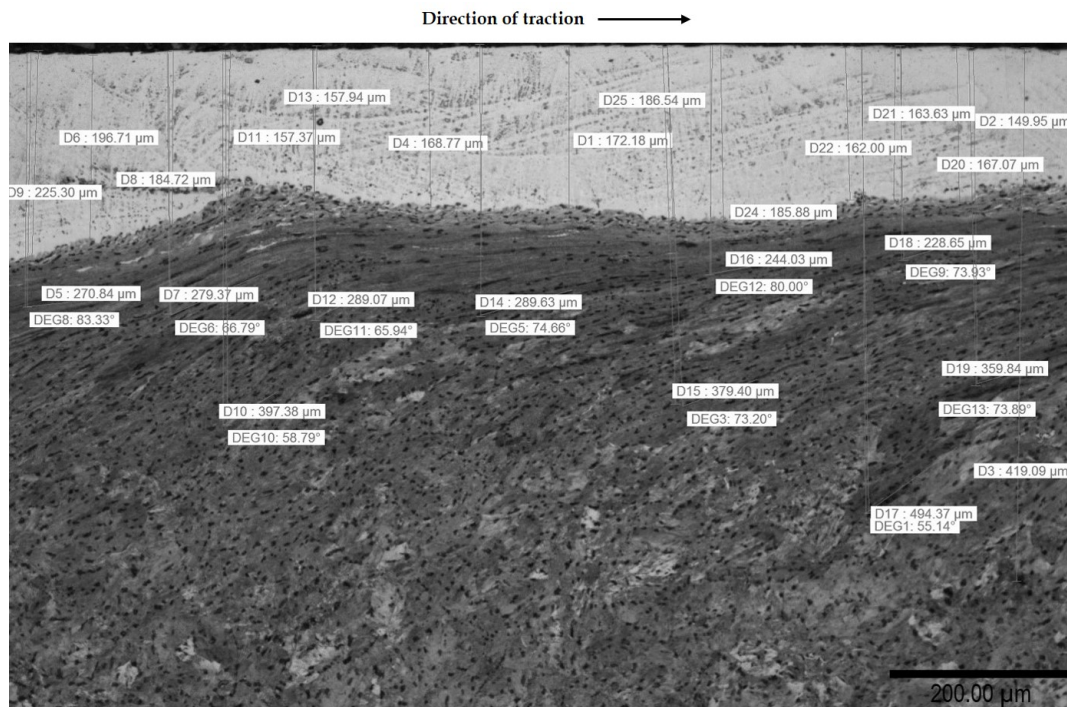
Figure 3.24: Sample 2: Image showing the measured angles of deformation and corresponding depth measurements within the R260 HAZ material. Measurements taken with Buehler Omnimet 9.5 software under optical microscopy and recorded in Table 3.8

Depth (mm)	Angle of deformation (deg)	Plastic Shear Strain	Shear Yield Stress (MPa)
0.05	83.33	8.55	721
0.06	80.00	5.67	713
0.07	73.93	3.47	706
0.09	66.79	2.33	694
0.12	74.66	3.65	679
0.13	65.94	2.24	674
0.19	73.2	3.31	651
0.19	73.89	3.46	651
0.24	58.79	1.65	635
0.33	55.14	1.44	611

Table 3.8: Sample 2: HAZ Depth below contact area with corresponding Plastic Shear Strain and Effective Shear Yield Stress using equation from Figure 3.20
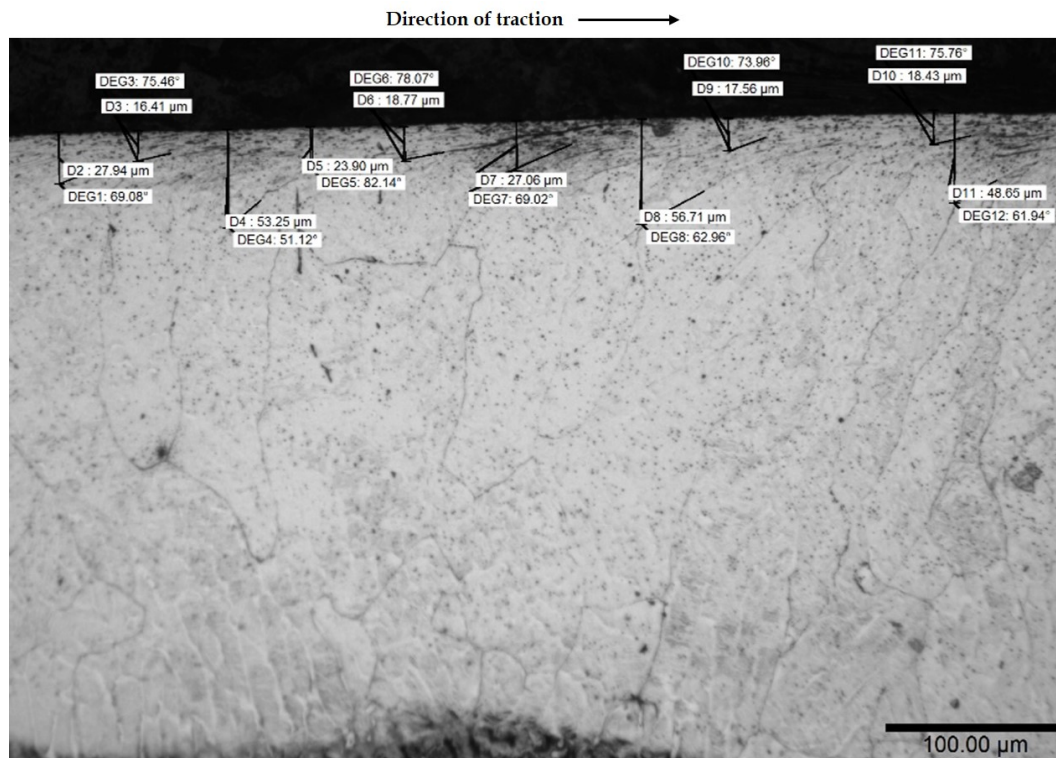
Figure 3.25: Sample 3: Image showing the measured angles of deformation and corresponding depth measurements within the MSS laser clad coating material. Measurements taken with Buehler Omnimet 9.5 software under optical microscopy and recorded in Table 3.9

Depth (mm)	Angle of deformation (deg)	Plastic Shear Strain	Shear Yield Stress (MPa)
0.02	75.46	3.86	1047
0.02	73.96	3.48	1047
0.02	75.76	3.94	1047
0.02	78.07	4.73	1047
0.02	82.14	7.24	1047
0.03	69.02	2.61	1041
0.03	69.08	2.62	1041
0.05	61.94	1.88	1030
0.05	51.12	1.24	1030
0.06	62.96	1.96	1025

Table 3.9: Sample 3: MSS Depth below contact area with corresponding Plastic Shear Strain and Effective Shear Yield Stress using equation from Figure 3.21

Critical strain is the plastic shear strain magnitude at which the material fails through a ductility exhaustion process [75]. In previous work this has been found through development of a steady state wear rate during a series of tests of increasing duration [23]. In the current tests the aim was to extract this information from the limited test samples available, with each test being run to sufficient duration that cracks had begun to initiate at the surface. The angle of plastic deformation at the point of crack initiation, where a crack had subsequently propagated from the surface, was used as the indicator of critical ductility exhaustion failure strain. In the MSS laser clad coating a crack initiation plastic strain of around 86°($\pm$0.5°) was detected indicating a critical strain $\Delta\gamma_c = 14.2$. In the R260 grade rail material a crack initiation plastic strain of around 85°($\pm$0.5°) was detected indicating a critical strain $\Delta\gamma_c = 11.7$. The HAZ was protected by the MSS laser clad coating and therefore did not experience critical strain or crack initiation.

3.5 Extracting the SYS-PSS curve

3.5.1 SYS-PSS at very low strain

The SYS-PSS strain curve and modified Voce equation of the original model was for BS11 rail steel. In creating this curve there was limited material data to base the curve on and as such there was only certainty in the curve from the point were shear strain was greater than 2. To overcome this problem Kapoor et al. [67] trialled two different approaches to provide a relationship of stress-strain at the lower values of strain where $\gamma_p < 2$, referred to as method B and C. Method B uses linear interpolation between the initial shear yield stress k_0 where there would be no plastic strain and the first known data point to build the stress-strain relationship at lower values of strain. Method C assumes that the shear yield stress remains constant at k_0 until the value predicted by the modified Voce curve exceeds it.

Method B and C produced similar results for Kapoor et al. [67], however method C was considered to be slightly better. Method C is selected for use at low levels of plastic shear strain in the

plots in the following section. The modified Voce equation is applicable to much lower values of strain as the measurement of plastic shear strain was done at a range of depths making more data available. A shear stress value equal to the yield stress is assumed to the point where it intercepts the extrapolated Voce equation. The minimum value of strain γ_{min} that the modified Voce equation for method C can be applied for the materials investigated here are shown in Table 3.10. The linear rise at low strain is also calculated by selecting the data point on the Voce equation which creates a continuous line to the intercept as shown by line B. The gradient of these and the minimum value of strain γ_{min} using method B is also presented in Table 3.10.

3.5.2 SYS-PSS curves

Using the equations in Table 3.6, the shear yield stress was calculated at the depths for which the strain data had been recorded enabling the SYS-PSS relationship to be correlated. Considering the estimated uncertainty in plastic strain measurement of $85°(\pm 0.5°)$ the SYS-PSS data plots with error bars are presented in Figures 3.26, 3.27 and 3.28 . A modified Voce equation, Equation 3.10, was fitted to the data points for each material:

$$k_{eff} = m(1 - \exp^{-n(\gamma_p)})^p \tag{3.10}$$

The parameters m, n, p for each material are given from the curve fit in Table 3.10 along with the original BS11 parameters, with the initial yield stress k_0, the critical strain γ_c and the minimum level of strain that the modified Voce equation can be applied from γ_c, as discussed in Section 3.5.1. These parameters are required for modelling ratcheting in Chapter 6.

Parameter	BS11	R260	R260 HAZ	MSS
m	446	1626	728.3	1050
n	0.47	0.003105	0.27749	0.5741
p	0.8	0.195	0.1343	0.02677
k_0 (MPa)	234.4	454.1	508.5	906.0
γ_c	11.5	11.7	11.7	14.2
γ_{min} (Method C)	1.26	0.41	0.26	0.007
γ_{min} (Method B)	2	0.99	0.95	0.41
Gradient (Method B)	35.21	85.27	94.71	243.66

Table 3.10: Material model information including the modified Voce parameters m, n and p, the initial Shear Yield Stress, the critical Shear Strain and the minimum Shear Strain the modified Voce is valid from for the three tested materials R260, R260 HAZ and MSS presented with the original BS11 parameters from the work by Kapoor et al. [67]
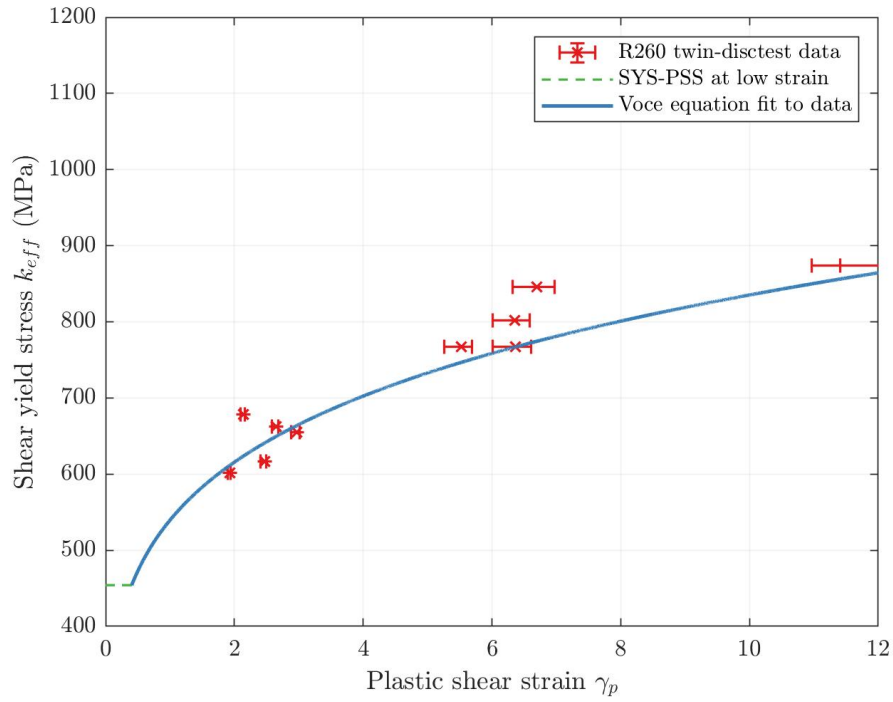
Figure 3.26: Modified Voce equation with parameters for R260 rail material representing the SYS-PSS material response behaviour.
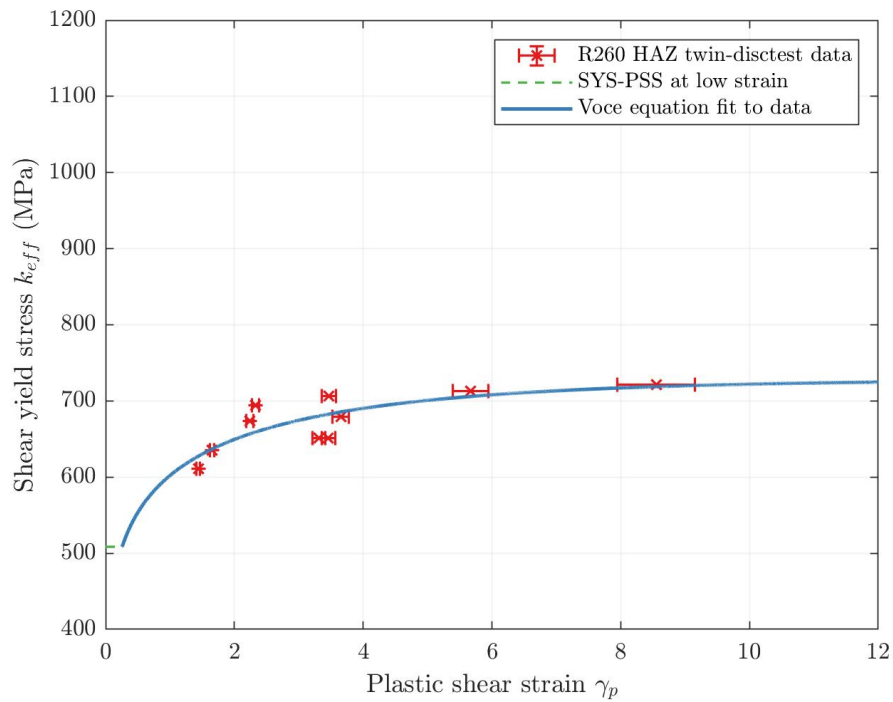
Figure 3.27: Modified Voce equation with parameters for R260 HAZ material representing the SYS-PSS material response behaviour.
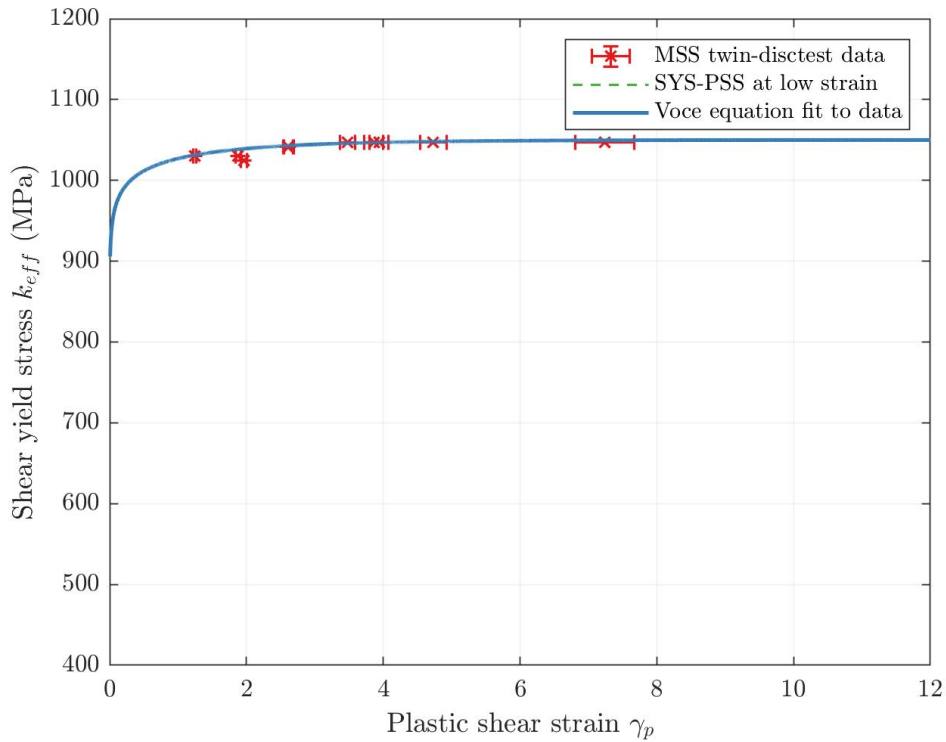
Figure 3.28: Modified Voce equation with parameters for MSS laser clad coating representing the SYS-PSS material response behaviour.

3.6 Validation

The method to obtain the SYS-PSS curve for the material is validated through the analysis of a further R260 grade rail steel sample which was tested under the same twin-disc conditions. Following twin-disc testing the sample was once again sectioned and prepared using the same standard metallographic techniques before microhardness tests and optical microscopy was conducted as described in the analysis methodology. To increase confidence in the method the angle of strain deformation was measured post microscopy using imagej software [152].

Figure 3.29 shows the shear yield stress fit equation for R260 substrate rail from Table 3.2 with the validation data plotted around it. The data from the second R260 disc has a R-square value of 0.94 to the original equation and is therefore accepted for using to calculate the data for the modified Voce equation for this sample. An optical microscopy image taken of the validation sample is shown in Figure 3.30 with the depth and angle measurements created in imagej. These angles were then converted into strain values using Equation 3.9.
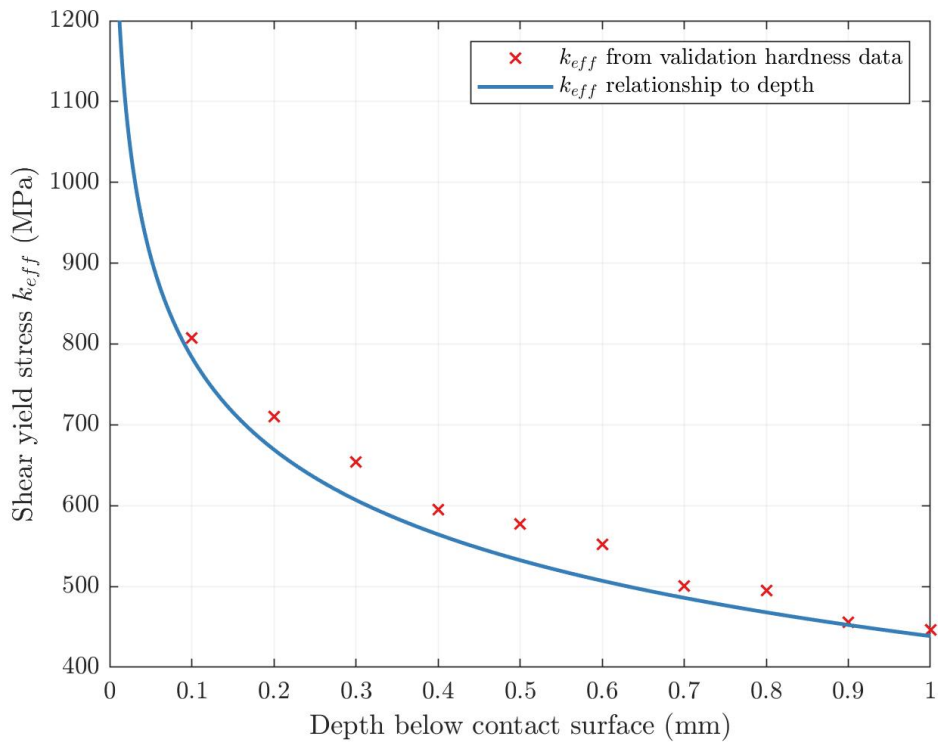
Figure 3.29: Sample 4 experimental data fit to the R260 equation of best fit for Shear Yield Stress relationship with depth shown in Table 3.6.
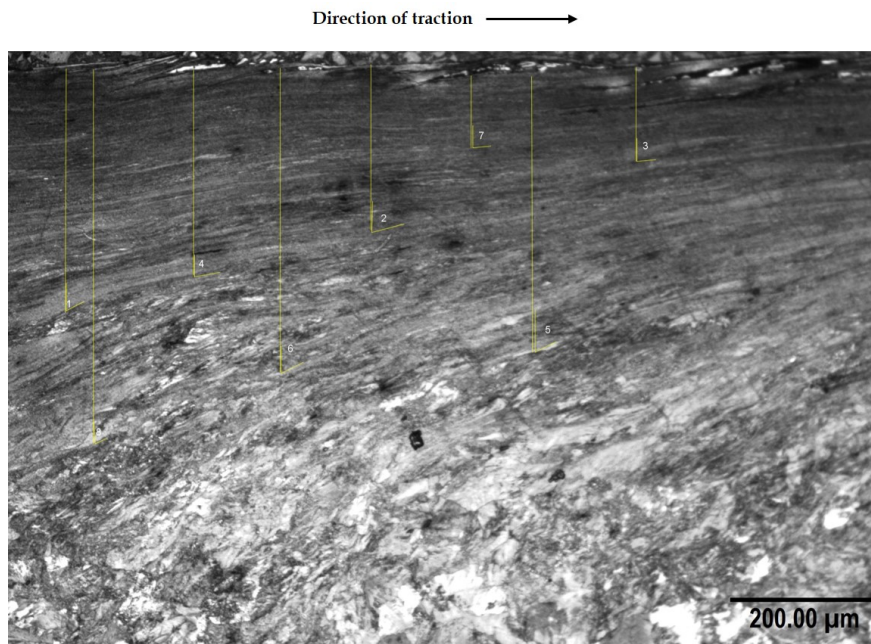
Figure 3.30: Sample 4: Image showing the measured angles of deformation and corresponding depth measurements within the validation R260 rail material. Measurements taken with imagej software on optical microscopy images and recorded in Table 3.11

The strain values taken from the image and the corresponding shear yield stress values, calculated using the shear yield stress fit equation for R260, are plotted in Figure 3.31 with a ±0.5°error bar.

The same modified Voce equation found for the R260 in Section 3.5 is shown in the plot with the validation data. Due to the nature of the material this is accepted as a good fit and validates the method.

Number	Depth (mm)	Angle (deg)	Plastic Shear strain	Shear Yield Stress (MPa)
1	0.16	62.35	1.91	705
2	0.11	73.69	3.42	767
3	0.06	84.81	11.00	874
4	0.14	80.54	6.00	727
5	0.18	63.91	2.04	686
6	0.20	63.44	2.00	669
7	0.05	84.56	10.50	908
8	0.25	69.10	2.62	635

Table 3.11: Sample 4: Validation R260 Depth below contact area with corresponding Plastic Shear Strain and Effective Shear Yield Stress using equation from Figure 3.19
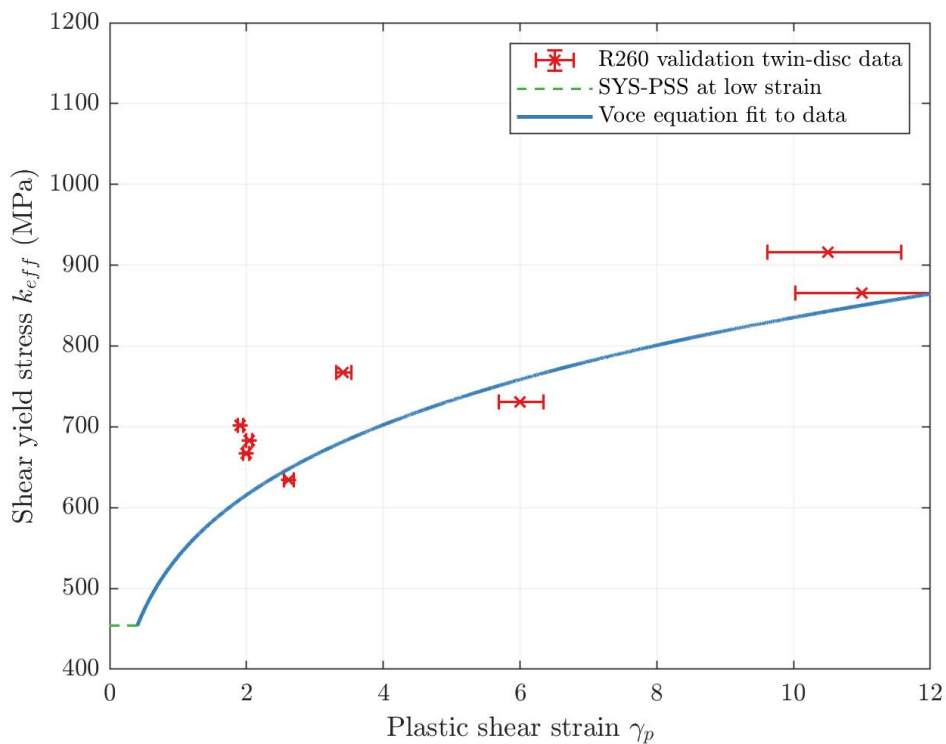
Figure 3.31: Validation: Modified Voce equation with parameters for R260 rail material representing the SYS-PSS material response behaviour.

3.7 Discussion

The experimental and analysis techniques developed in this chapter are shown to enable the extraction of the SYS-PSS relationship of rail materials from a single test condition. The method is comparable to that developed by Kapoor et al. [67] which required multiple tests of increasing cy-

cle lengths. The results of the SYS-PSS relationships for the R260, HAZ and MSS fit to the form of the modified Voce equation which was shown to fit the results for BS11 rail steel tested by Kapoor. The main benefit of the method developed here is the economical characterisation of novel materials which may be costly or limited in manufacture. The developed method is also favourable for coatings as the Kapoor method requires a single measurement of strain at 200 μm below the contact surface, which is not appropriate to coatings which only accumulate shear strain at shallow surface depths. As strain is measured at a range of depths below the contact surface it is possible to have certainty in the modified Voce equation SYS-PSS relation down to much lower values of shear strain than that found for BS11 by Kapoor et al. [67], where an estimation method was chosen for low strain. Considering these benefits the method would be a viable method to characterise novel rail materials in the development stage.

There are limitations to the material response to load characterisation method. The rate at which the strain accumulates can not be determined by this technique and must be found using another method. This is explored further in Chapter 6 where the rate is required for quantifying plasticity within the laser clad coating.

The shear yield data and quantification of plastic flow are independent of any knowledge of the applied stress that generated the flow, in the current case the near surface MSS shear strain is likely to have been driven by surface roughness stress while the greater depth of deformation in the R260 is a bulk stress effect. Despite this difference in cause, the SYS-PSS relationship can still be derived. The analysis could be conducted on the materials directly without running twin-disc experiments, although measurements on unstrained material would be required using part of the material free from deformation, for example, well below the running surface. The main caveat to this would be that the rail must have experienced enough stress to accumulate visible plastic shear strain. This method could be used to analyse track removed from service and an example of applying this method to a different material can be seen in Appendix A for cast manganese.

The R260 substrate rail material, HAZ and MSS laser clad coatings were examined individually for the purpose of providing model input for use in Chapter 6, however, in reality the laser clad rail acts as a system of materials. The laser clad MSS has a very high yield stress, over twice that of the R260 rail steel alone, which makes it highly resistant to ratcheting. The laser clad MSS coating showed evidence of plastic flow only very close to the surface as shown in Figure 3.13, with correspondingly shallow variation in sub-surface hardness after testing. When the laser clad coating is applied to a depth greater than the location of the peak sub-surface stress, the substrate rail is protected and ratcheting in the laser clad rail system is significantly reduced. It can be seen in Figure 3.14 that when the laser clad coating is insufficient in depth then plastic deformation can occur within the substrate rail. This is due to the peak sub-surface stress occurring below the protective laser clad coating. The optimal depth will be explored further within the plasticity modelling in Chapter 6.

3.8 Conclusion

A material response to load characterisation method has been developed in which a rail material sample from a single twin-disc test can provide the data required to derive the respective SYS-PSS curve. The method was designed and demonstrated for conventional rail steel in addition to the highly ratcheting resistant MSS laser clad coating on a R260 grade rail steel substrate. The test and analysis method described was appropriate for all of the materials and the results were comparable to previous, more time consuming test methods.

The MSS laser clad coating has a much higher initial shear yield stress than standard pearlite rail. It was found that plastic flow was confined to a shallow surface layer reaching only 57 μm from the running surface indicating it will be highly ratcheting resistant in service. The HAZ is also shown to be resistant to ratcheting, however the depth of MSS laser clad coating is a crucial factor in laser clad rail system performance. The results indicate that if it is applied too shallow then the substrate rail will accumulate plastic shear strain below the interface.

Following the analysis method flow chart in Figure 3.4, the material response to cyclic loading in modern rail steels can be measured. There is the expectation that rail samples taken from within track can be characterised in this way as the material response is independent of the loading history. In this case the twin disc testing would be eliminated from the analysis method. If the rate of strain accumulation is required, then additional tests of intermediate length will still be required.

The data generated within this chapter will be used in the modelling in Chapter 6 which quantifies plasticity within laser clad coatings. Chapter 6 will also add further experimentation results to determine the rate at which plastic shear strain accumulates. Following the evidence of ratcheting resistance with laser clad coatings seen in this chapter, the following chapter experimentally evaluates the feasibility of applying laser clad coatings as a repair method in-situ.

Chapter 4

Laser clad coatings as a repair method on rail steel

4.1   Introduction

The locations of rail which experience high traffic or dynamic loads may be more prone to wear and RCF. They often require repair as an intervention before damage goes too far, becomes dangerous and requires replacement. Such repairs are often carried out as a weld repair, as discussed in Chapter 2, however it was shown there how these can have their own problems and are susceptible to crack initiation [101, 102, 103]. It is hypothesised that additive manufacturing with laser clad coatings could be utilised as an in-situ method to repair damaged rails, rather than removing them from track. The targeted repair area would experience less impact from the heat process than from a weld repair as the laser is localised and controlled.

This chapter presents the experimental design and results of tests conducted to assess the integrity, surface evolution and rolling contact effect of laser clad repairs. Laboratory scale twin-disc tests are selected once again to investigate the effect of deposited material and repair geometry when the repaired rail is under typical cyclic rail-wheel contact conditions. The results of these repair experiments combined with the material properties described in Chapter 3 will provide input for models in the following chapters.

Following previous research conducted in laser clad coating on rail steel, three candidate cladding materials were selected to be deposited as repair materials into manufactured grooves of varying dimensions on a cylinder of 0.62% carbon steel, representative of R260 grade rail steel commonly found in service across the network. The three candidate materials were laser clad using the one-step powder injection method described in Section 2.4. The candidate materials are i) Martensitic Stainless Steel (MSS) low carbon alloy with 14.64% chromium, ii) R260 grade rail steel with 0.62% carbon steel which is the same as the parent rail steel and iii) Stellite 6 which is cobalt based. The laser clad repairs were manufactured with the same optimal parameters used in Chapter 3 and in work by Lewis et al. [110] the laser process parameters are controlled to avoid the formation of martensite in the HAZ as investigated by Lai et al. [153].

4.2   Experimental methodology

4.2.1   Twin-disc repair samples

To enable the evaluation of in-situ repairs a set of twin-disc tests was designed to simulate rail-wheel contact of a specially manufactured repaired rail disc. The rail discs for the repair tests were manufactured from a cylinder of 0.62% carbon steel. The cylinder had six slots wire eroded from the circumference as shown in Figure 4.1. The repair slots varied in dimension with the aim of assessing a combination of shallow, medium and deep repairs.

Figure 4.1: Photograph of the repair bar during the manufacturing process showing the wire eroded slots for the laser clad repairs.

Each slot was filled with a one-step laser cladding by powder injection with one of the candidate repair materials; R260, MSS or Stellite 6. MSS and Stellite 6 are selected as candidate repair materials following the success seen in coating rail steels with them in research by Lewis et al. [1, 110], powdered R260 rail steel is selected as a material comparable to that used in weld repairs, in which a rail would be repaired with a homogeneous material. The repair sites are labelled 1 to 6 and the corresponding laser clad material, maximum width and maximum depth of the repair sites are shown in Table 4.1. The surface width dimensions of the repair sites can be seen in Figure 4.2.

Repair	Material	Maximum width (mm)	Maximum depth (mm)
1	R260	11.0	3.6
2	MSS	3.1	0.4
3	MSS	6.9	1.5
4	Stellite 6	11.0	4.1
5	MSS	2.9	0.4
6	Stellite 6	5.0	1.2

Table 4.1: Record of repair site number, material, maximum depth and maximum width of each repair site.
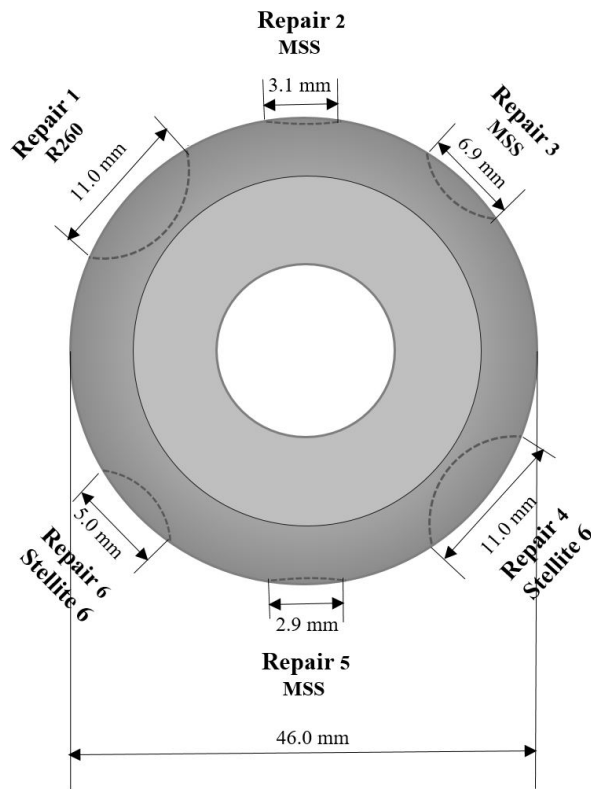
Figure 4.2: Sketch of the repair disc with the repair numbers, materials and width of each repair site.

4.2.2 Twin-disc experimental methodology (SUROS 2)

Twin-disc testing was described in Chapter 3 as a valuable way to replicate rail-wheel contact in the laboratory under high hydrostatic loading. Within the duration of the project a new enhanced twin-disc test machine replaced the original SUROS and was therefore used for the repair tests in this chapter. The new test machine is the TE 72 Two Roller Machine made by Phoenix Tribology, now referred to as SUROS 2, which is designed for the study of traction, wear and rolling contact fatigue under pure rolling or rolling-sliding conditions in dry or lubricated conditions, an image of SUROS 2 is shown in Figure 4.3. The Colchester lathe and ac motor of SUROS are replaced with two ac vector motors in SUROS 2 which are each connected to the test assembly by a timing pulley and were run at a speed of 375 RPM. The test discs are of the same dimensions as those used in SUROS and shown in Figure 3.2, the rail and wheel discs are brought into contact and the load is applied horizontally in SUROS 2 rather than vertically. The connected computer runs the test through the programmed parameters in COMPEND 2000 and slip is created by maintaining a constant speed in the rail disc and the wheel disc running at the speed required to generate the programmed slip level, shown in Equation 3.1.

A system was set up with distilled water, gravity fed through a pipe and clamped over the wheel disc to allow RCF testing in water lubricated conditions to enable investigations into crack initiation and propagation. Test preparation using SUROS 2 were the same as in Chapter 3 and the rail and wheel disc were both cleaned in an ultrasonic isopropanol bath for 2 minutes, the weight and

diameter were then measured and recorded.
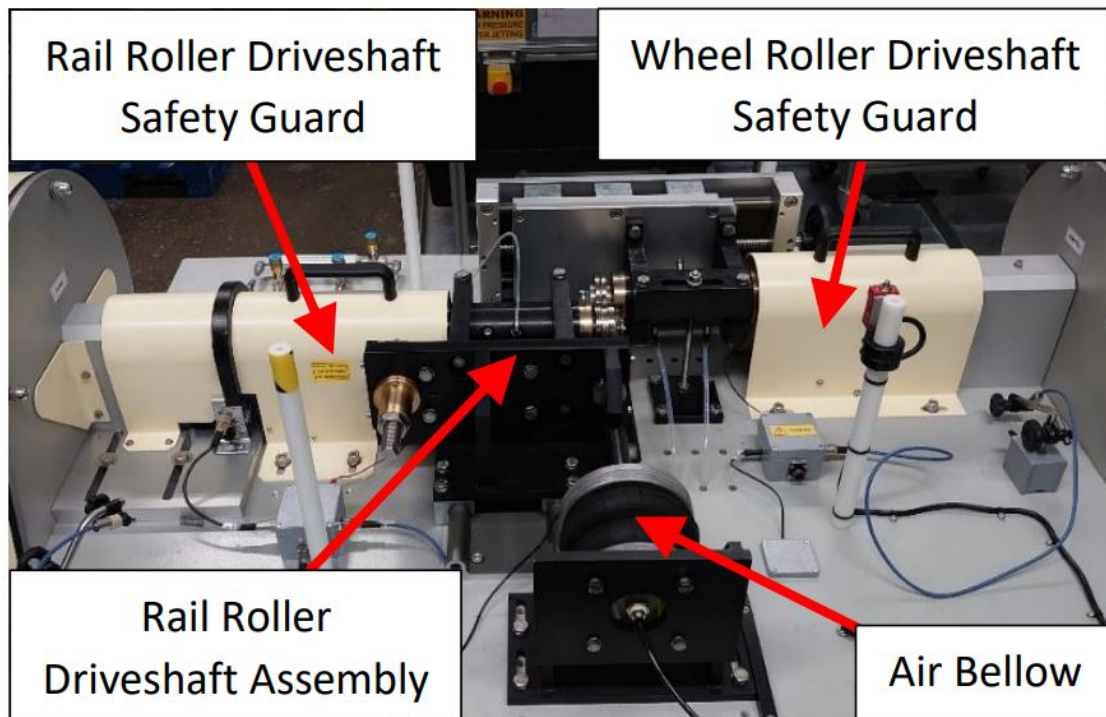
Figure 4.3: Image of new twin-disc test machine; SUROS 2 (TE 72 Two Roller Machine) used to replicate rail-wheel contact in the laboratory.

4.2.3 Repair test plan

The test parameters were chosen to be comparable to previous laser clad twin-disc testing seen in the literature by Lewis et al. [1]. The maximum contact pressure was set at 1500 MPa in all tests and the slip level was set at -1% ± 0.01% to simulate a driving traction. Tests were either run in dry (unlubricated) conditions to assess surface evolution or in a combination of initial dry cycles to generate crack initiation followed by water lubricated conditions to assess RCF crack propagation within the repairs and surrounding material, the tests are summarised in Table 4.2.

Test	Dry cycles	Water lubricated cycles	Water drop rate	p_0 (MPa)	Slip (%)
Ratcheting	30,000	-	-	1500	-1
RCF short	500	5,000	1 per second	1500	-1
RCF long	500	15,000	1 per second	1500	-1

Table 4.2: Summary of twin-disc test plan for laser clad repair discs.

The unlubricated test was run for 30,000 cycles, to ensure that steady state was established and plastic shear strain was accumulated within the sample. With the single repair disc having six different repair sites (of three different materials) deposited around the circumference, the wear of the disc as a whole is inconclusive to how each individual repair wears. The standard method of monitoring diameter and mass at regular intervals (stopping the test every 5,000 cycles) is

conducted for a general comparison to unclad or fully clad twin-disc tests in the literature. An approach is taken to measure the topography of the rail disc at regular intervals throughout the test using the optical (non-contact) Alicona PortableRL Infinite Focus microscope (further referred to as Alicona) to monitor signs of surface modification. The Alicona is able to measure fields of up to 50 x 50 x 26 mm. The Alicona produced high-resolution images and surface profile measurements which can be further analysed post-testing [2].

RCF tests were conducted by running the discs unlubricated for 500 cycles to initiate cracks and plastic deformation [1], followed by wet (water lubricated) cycles, in which 1 drop of distilled water was dropped onto the wheel disc every second [48] in blocks of 5,000 cycles. This ensures that a film of water is maintained at the contact of the discs given the speed of testing. The tests were once again stopped every 5,000 cycles and Alicona images were taken and the disc was weighed and the diameter measured across the base material. The Alicona images were used to identify signs of RCF at the surface. Signs of RCF were identified in two of the repairs after the first 5,000 tests and hence the test was terminated at that point. A further RCF test was conducted and run to 15,000 cycles to generate RCF in the other repair sites. Conventionally eddy current crack detection would be utilised in twin-disc RCF tests, this was tested and the results presented in Section 4.3 indicate that this is not a suitable technique to use for this bespoke set of tests.

After testing all rail disc samples were sectioned to reveal the vertical-longitudinal sub-surface face of the repairs using standard metallographic techniques to achieve a 1 μm diamond polish finish. DuraScan Micro Hardness was used to measure the Vickers hardness of the sub-surface repair materials at a range of depths using a 0.2 kg load. The samples were then etched in 2% Nital (98% Industrial Methylated Spirit (IMS) mixed with 2% nitric acid) for approximately 45 seconds to reveal the repair within the etched R260 grade substrate rail material. The repair integrity, plastic deformation and RCF crack propagation was observed using a combination of optical microscopy and Scanning Electron Microscopy (SEM), the selection of image presented here is based on the clarity of image for the individual repair.
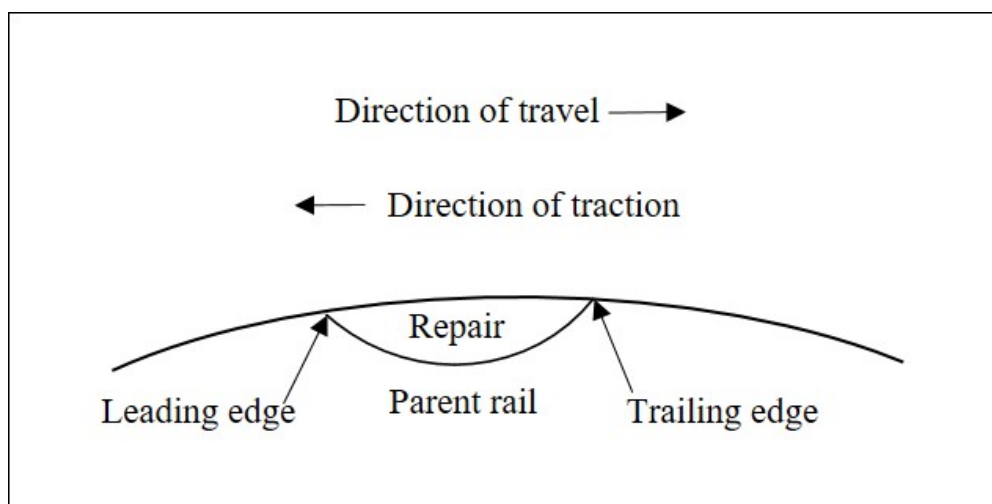
Figure 4.4: Illustration to demonstrate the leading edge and trailing edge of the repair site within the parent rail. The direction of travel and opposing direction of traction across the repair surface is also shown.

The vertical-longitudinal cross section of the repair is referred to throughout the chapter to contain a leading edge (the left side of the repair site in reference to the traction direction) and a trailing edge (the right side of the repair site in reference to the traction direction), as illustrated in Figure 4.4. This is particularly important in analysing the repairs following testing as it is indicative of the direction of traction and can be used to draw comparisons between laser clad repairs and White etching layer (WEL) [106], both of which can consist of a material harder than the surrounding parent rail.

4.3 Evaluation of eddy current testing method for rail repairs

To assess RCF in standard twin-disc tests eddy current crack detection is commonly used as described by Garnham et al. [83]. In this section the suitability of eddy current testing to detect crack growth in laser clad repair samples is evaluated. The Elotest B1 Eddy Current Crack detector was set up with the connected KD21 Rohmann GmbH differential eddy current probe shown in Figure 4.5 positioned at a stand-off of approximately 0.5 mm and a frequency of 1 MHz. The probe remained in a static position over the centre of the repair disc running band, and measures approximately 1.5 mm of track width. The test discs were turned manually at a slow but steady speed to monitor the individual repair sites.

Figure 4.5: Position of KD21 Rohmann GmbH differential eddy current probe positioned over the R1 45 calibration disc.

A standard R1 45 calibration disc of R260 grade rail steel with a spark eroded slot of 3 mm wide and 100 μm at an angle of 45° was initially tested with the probe detecting the crack as expected. The resultant crack trigger of the calibration disc is set between the gates as shown in Figure 4.6a and the tests on the repair discs use this level for comparison. Eddy current testing has been conducted on a range of fully laser clad coated twin-disc samples by Lewis et al. [110] and Hiensch et al. [49] in which no cracks were detected. An untested R260 grade rail steel rail disc with the full surface laser clad with MSS was tested for comparison with this previous research and it can

be seen that no cracks were detected as shown in Figure 4.6b.

(a) Standard R1 45 calibration disc of R260 grade rail steel.

(b) R260 grade rail steel rail disc with full MSS laser clad surface.

Figure 4.6: Eddy current detector signal over a) the standard R1 45 calibration disc of R260 grade rail steel, and b) the R260 grade rail steel rail disc with full MSS laser clad surface.

The difference in this assessment of the method is the discontinuous composition of the repair disc which has the potential to trigger false or multiple readings. Assessing this non-destructive examination method for laser clad coating repairs will aid maintenance inspections in-situ. Testing an untested repair disc with the eddy current it can instantly be seen that the gate is triggered at every interface between parent rail and repair as shown in Figure 4.7.

Figure 4.7: Eddy current detector signal over the untested repair disc, gates triggered at each join between parent rail and repair.

Repeating the eddy current crack detection test on repair discs with known RCF cracks the gate is triggered at the interface of repair site and the parent rail. Figure 4.8a shows the results for a repair disc which had run for 5,000 water lubricated cycles in an RCF test and Figure 4.8b shows the results for a repair disc run for 15,000 water lubricated cycles in a longer test resulting in

visible RCF cracks.

(a) Repair disc after testing for 5,000 cycles   (b) Repair disc after testing for 15,000 cycles

Figure 4.8: Eddy current detector signals over repair discs after RCF testing for a) 5,000 cycles and b) 15,000 cycles. Gates triggered at each join between parent rail and repair and at RCF surface cracks.

Considering Figure 4.7 with an untested repair disc it is concluded that non-destructive eddy current testing is an unsuitable method for the detection of cracks in laser clad repairs. The method is not used in the RCF tests in this chapter and visual surface inspection with Alicona in combination with post-test destructive methods of microscopy observations are selected for analysis.

4.4 Repair material properties prior to testing

The repair material properties and dimensions were observed prior to testing through a combination of Laser-induced Breakdown Spectroscopy (LIBS), optical microscopy and microhardness measurements. A section of the repair cylinder was retained and using standard metallographic methods it was sectioned to reveal each individual repair. Each repair is shown in this section with the repair highlighted through etching in 2% Nital, which etches the substrate rail and the R260 repair but is not corrosive enough to etch the MSS or Stellite 6 repairs. Optical microscopy images were taken to examine the integrity of the interface between repair and parent rail. Hardness results were obtained using the DuraScan microhardness tester with a 0.2 kg load as described in Section 3.3.2.

Chemical analysis was conducted with a hand held Laser Induced Breakdown Spectroscopy (LIBS) device which was used to measure the concentration of elements within the laser clad repairs. A low-energy pulsed laser was fired at the repair site creating a plasma which vaporises a small area of the repair sample surface. The emitted plasma light consisting of the excited electrons and atoms was detected by the spectrometer which measures the wavelength and intensity and identified the chemical elements present using a database of known elements and their corresponding wavelengths and intensities and the concentration of the elements can be quantified [154].

The results of LIBS analysis are beneficial for the repair samples as the laser cladding process parameters will affect the final composition of the metallic powder as it forms the repair. The chemical element analysis of each repair material is presented here with a comparison of each repair site of each material where appropriate. This method provides an ideal method of analysing the repair materials composition as it can be conducted on the test samples studied in this chapter with only minimal surface damage occurring. There are limits to the detection and precision which can be provided by this method, however, for the purpose of investigating the chemical composition of these repair sections it is decided that the method is the most suitable.

4.4.1 R260 repair

The cross section of repair site 1 filled with laser clad R260 powder can be seen in Figure 4.9 after etching with 2% Nital. The repair site is highlighted by the red line and a large heat affected zone can be seen in the surrounding material. The average hardness measured within the R260 repair is 575 $H_{v0.2}$ which is much higher than the substrate R260 material as it has undergone a heat process in application from powder form. The initial year shield stress using Tresca criterion Equation 3.5 is $k_0 = 863$ MPa.
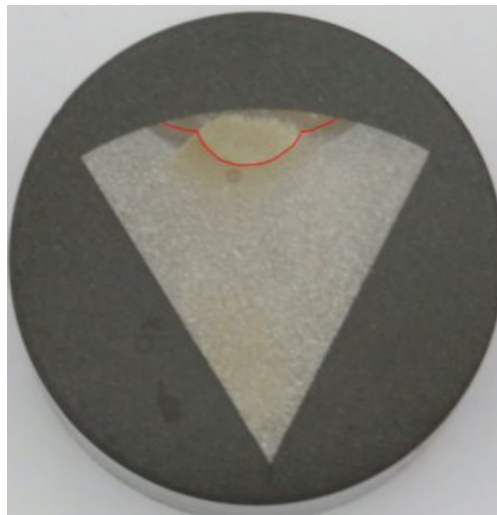
Figure 4.9: Repair 1: R260 repair site highlighted by the red line, prior to testing. Etched parent rail reveals repair site and surrounding heat affected zone.

The LIBS chemical analysis of the R260 repair (Repair site 1) can be seen in Figure 4.10. It can be seen that the main element correctly detected is iron as would be expected in rail steel. R260 is a low-carbon steel alloy commonly with 0.62 - 0.80 wt% carbon, the LIBS results detected a marginally higher carbon content in the R260 repair of 1.00% ±0.10. When the LIBS results are compared with the industry standard data shown in Table 1.1 the low levels of aluminium, chromium, manganese, silicon and vanadium are comparable. The LIBS analysis also detects 3.23% ±0.40 of copper. It does not detect any phosphorus or sulphur which the data sheet suggests should be at low levels of $\leqslant$ 0.025 and 0.008 - 0.025% respectively. According to Li et al. [155] the detection of phosphorus the analysis of phosphorus using LIBS is challenging in air atmosphere due to interference. Similarly, Zhang et al. [156] discuss the difficulties in detecting

sulphur with LIBS alone as oxygen is proposed to interfere with the sulphur atomic emission lines.
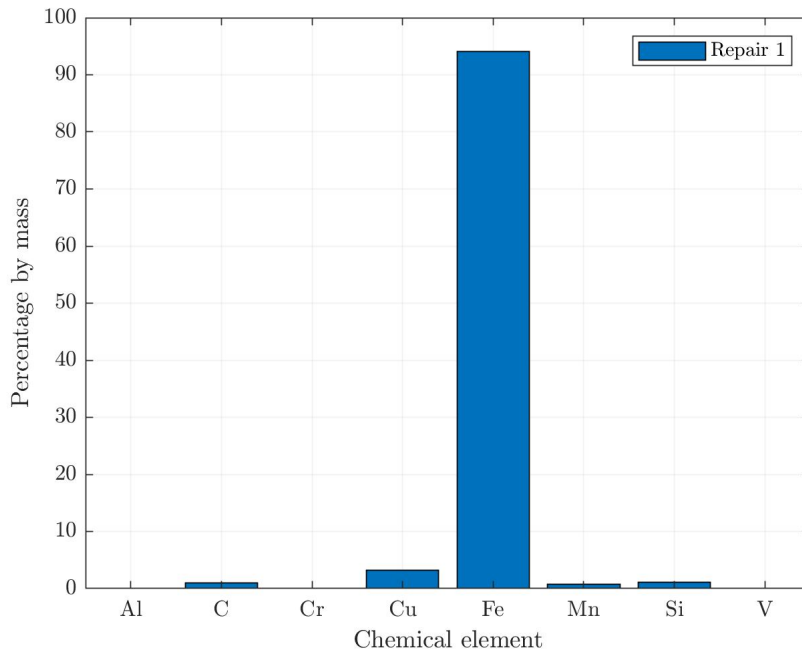
Figure 4.10: Chart showing the chemical element percentage mass of the R260 repair from the data gathered though LIBS analysis.

Optical micrographs of repair site 1 prior to testing are presented here in which a fine grain heat affected zone can be seen between the R260 repair and the unaffected substrate rail. The left and right interface of the repair site to the parent rail is seen to have a strong metallurgical bond in Figure 4.11.
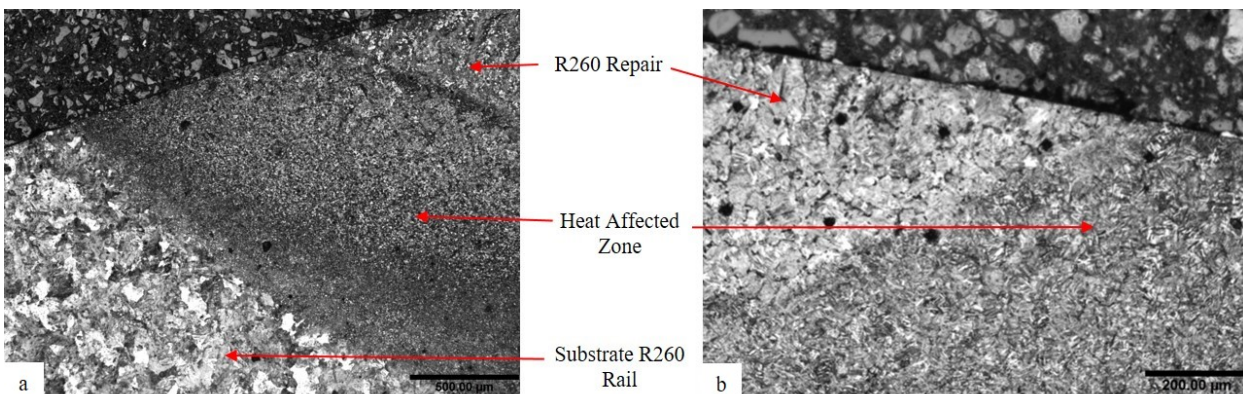
Figure 4.11: Repair 1: optical micrographs of the a) leading edge and b) trailing edge interface of the R260 repair with the R260 parent rail disc, showing the heat affected zone surrounding the repair.

The surface profile of repair 1 was measured with the Alicona before testing and the results are shown in Figure 4.12. Noting that the scale of the profile is given in microns, it can be seen that the surface is relatively smooth and consistent initially.
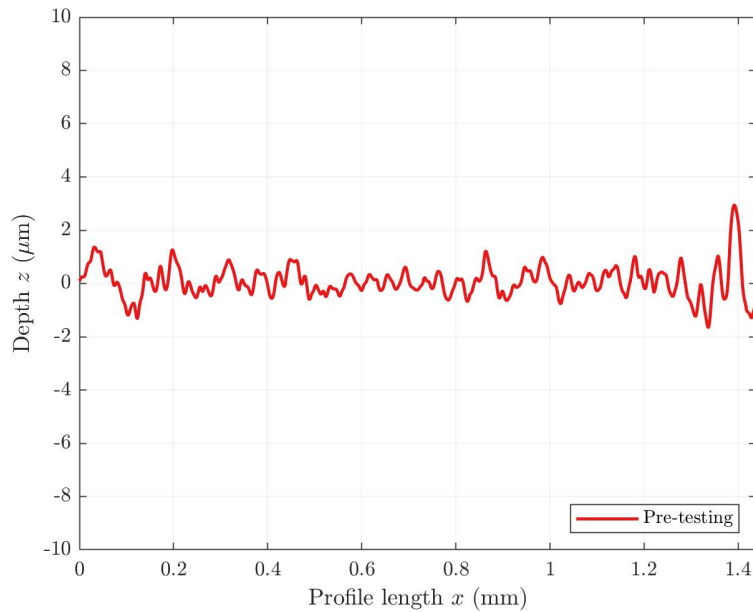
Figure 4.12: Repair 1: R260 repair sites surface profile pre-testing.

4.4.2 MSS repair

The cross section of repair site 2, 3 and 5 can be seen in Figure 4.13, after etching with 2% Nital which etches only the substrate R260 material and reveals the repair site. The hardness of repairs 2, 3 and 5 are 512 $H_{v0.2}$, 511 $H_v0.2$ and 503 $H_{V0.2}$ respectively, which is much lower than the average 606 $H_{v0.2}$ of the fully clad disc in Chapter 3. Using Tresca criterion the average initial shear yield stress of the MSS repairs is $k0 = 763$ MPa.

| (a) Repair 2 | (b) Repair 3 | (c) Repair 5 |
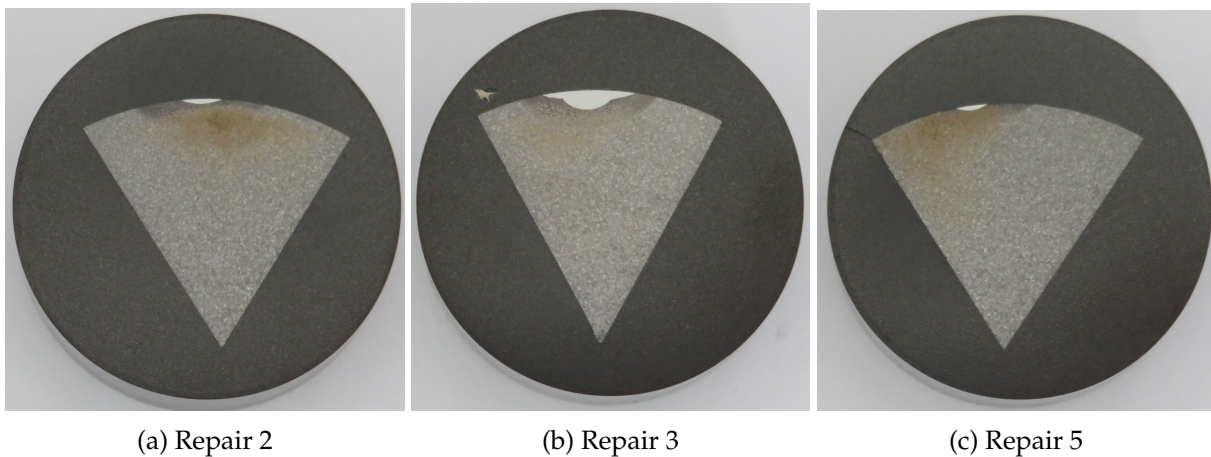
Figure 4.13: Repairs 2,3 and 5: MSS repair sites prior to testing. Etched parent rail reveals repair site and surrounding heat affected zone.

Repair sites 2 and 5 are the smallest manufactured repair slots at a depth of 0.4 mm, repair site 3 is a medium slot with a depth of 1.5 mm, all of which are filled with laser clad MSS.

The LIBS chemical analysis results for repair 2, repair 3 and repair 5 are shown in Figure 4.14. They are identified as the MSS repairs as they are iron based with chromium present. The chemical

composition is slightly different across the three repairs, the small dimensions of repair 2 and repair 5 are considered to make the LIBS results less reliable at these sites. Chromium is predicted in the MSS to be 14.64% from the data in Table 1.1, Repair 3 is comparable with $12.66\% \pm 0.45$ chromium. In repair 2 $6.65\% \pm 1.74$ chromium is detected but the results are inconclusive for repair 5.
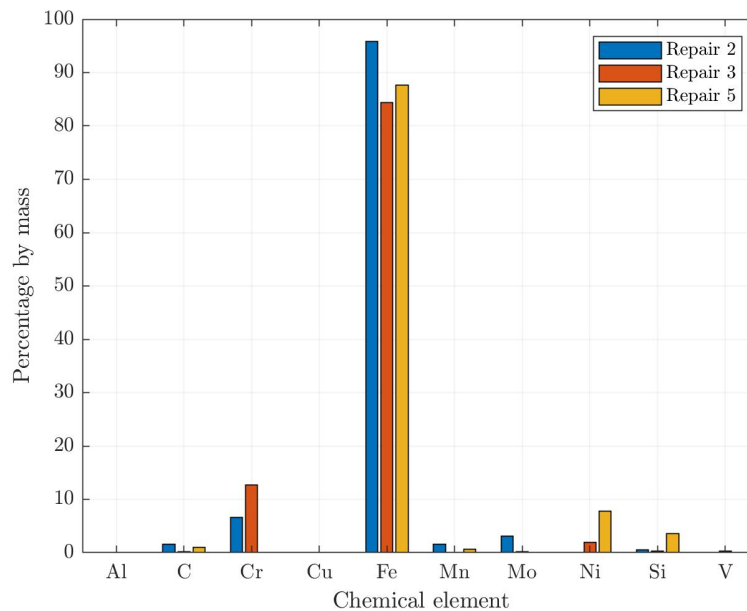
Figure 4.14: Chart showing the chemical element percentage mass of the MSS repairs from the data gathered though LIBS analysis.

Nickel is the next most prominent element in MSS with the data table predicting 3.31%, this is not detected in sample 2 but is quantified at $7.73\% \pm 1.36$ in sample 5 and $1.92\% \pm 0.07$ in sample 3. Of the remaining elements present at low levels, silicon and carbon are detected in all three repairs. Chromium, aluminium and molybdenum are detected in repair 2 and repair 3, manganese is detected in repair 2 and repair 5 and vanadium is only detected in repair 3. Contrary to the data table which for MSS is taken from the research by Lu et al. [2] the LIBS analysis does not detect phosphorus, sulphur, cobalt, tungsten or nitrogen, which is believed to be due to the capability of the analysis in air atmosphere as discussed in Section 4.4.1.

Optical micrographs of repair site 2 prior to testing are presented here in which a small fine grain heat affected zone can be seen between the MSS repair and the unaffected substrate rail. Both interfaces of the repair site to the parent rail are seen to have a strong metallurgical bond with mechanical mixing shown in Figure 4.15. The MSS repairs appear to have been optimally deposited without inclusions. Optical micrographs of repair site 3 prior to testing are presented in Figure 4.16, again with left and right interface of the repair site to the parent rail is seen to have a strong metallurgical bond with mechanical mixing. Optical micrographs of repair site 5 prior to testing are presented in Figure 4.16. It can be seen that the etchant caused some excess dissolution of the sample in the process of revealing the repair. A strong interface between repair and parent rail is still seen.
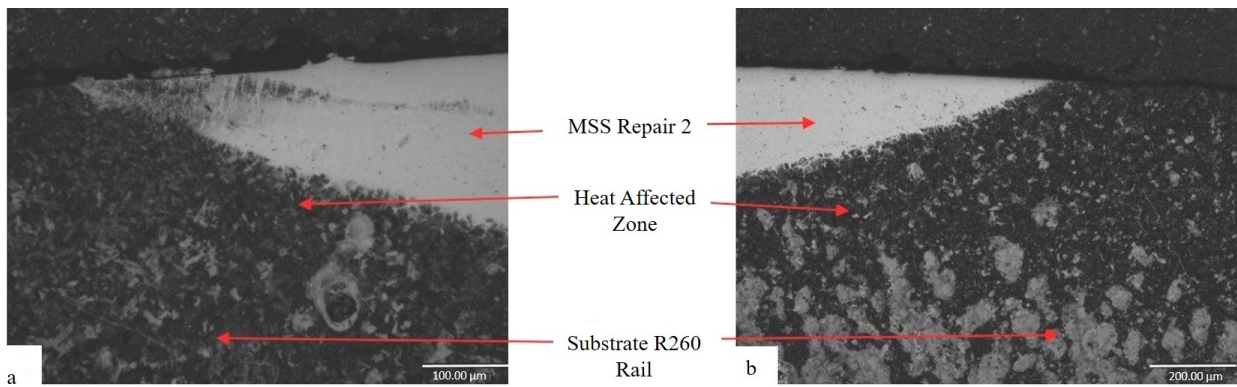
Figure 4.15: Repair 2: Optical micrographs of the a) leading edge and b) trailing edge of the MSS repair with the R260 parent rail disc, showing mechanical mixing at the interface.
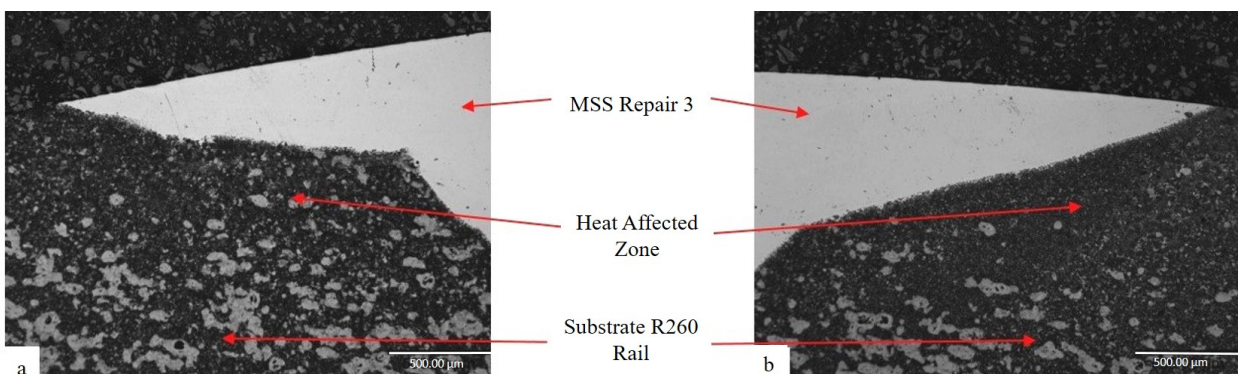
Figure 4.16: Repair 3: Optical micrographs of the a) leading edge and b) trailing edge of the MSS repair with the R260 parent rail disc, showing mechanical mixing at the interface.
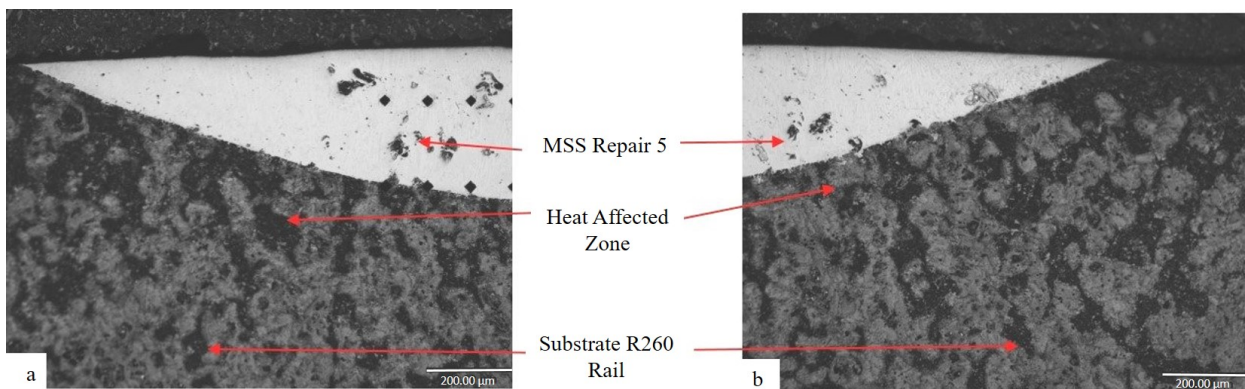
Figure 4.17: Repair 5: Optical micrographs of the a) leading edge and b) trailing edge of the MSS repair with the R260 parent rail disc, showing mechanical mixing at the interface.

The surface profile of repair sites 2, 3 and 5 were measured with the Alicona before testing and the results are shown in Figure 4.18. Noting that the scale of the profile is given in microns, it can be seen that the surface is relatively smooth and consistent initially.
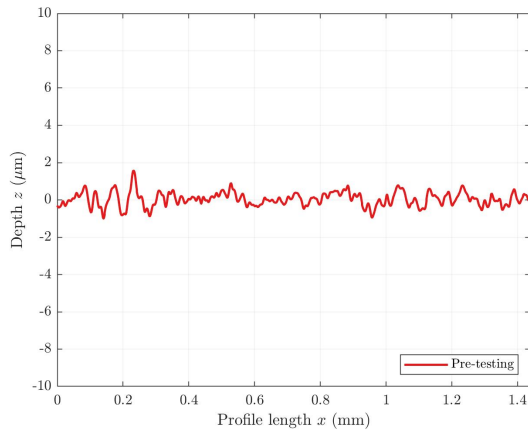
(a) Repair 2 surface profile pre-testing.
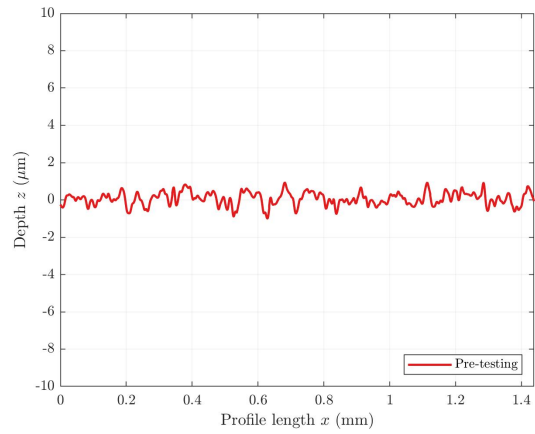
(b) Repair 3 surface profile pre-testing.
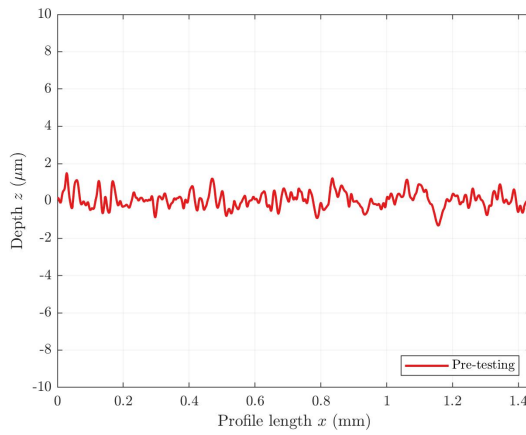
(c) Repair 5 surface profile pre-testing.

Figure 4.18: Repairs 2, 3 and 5: MSS repair sites surface profile pre-testing.

4.4.3 Stellite 6 repair

The cross section of 4.19a repair site 4 and 4.19b repair site 6 can be seen in Figure 4.19, after etching with 2% Nital which etches the substrate R260 material and reveals the repair site.

(a) Repair 4

(b) Repair 6

Figure 4.19: Repairs 4 and 6: Stellite 6 repair sites prior to testing. Etched parent rail reveals repair site and surrounding heat affected zone.

Repair sites 4 is one of the largest with a depth of 4.1 mm, repair site 6 is a medium slot with a depth of 1.2 mm, all of which are filled with laser clad Stellite 6. The hardness of repairs 4 is 505 $H_{v0.2}$ and repair 6 is 545 $H_{v0.2}$. Using Tresca criterion the average initial shear yield stress of the MSS repairs is $k0 = 788$ MPa.

The LIBS chemical analysis results for repair 4 and repair 6 are shown in Figure 4.20. They are identified as the Stellite 6 repairs as they are cobalt based alloys with a carbide phase dispersed in a CoCr alloy matrix [6] which corresponds with the LIBS results. The quantified cobalt in repair 4 and repair 6 are 61.11% $\pm$ 0.83 and 47.14% $\pm$ 0.46 respectively. The quantified chromium in repair 4 and repair 6 are 36.55% $\pm$ 1.77 and 26.57% $\pm$ 0.97 respectively. Comparing the remaining LIBS results with the data shown in Table 1.1, all the expected elements were detected with the exception of nickel.
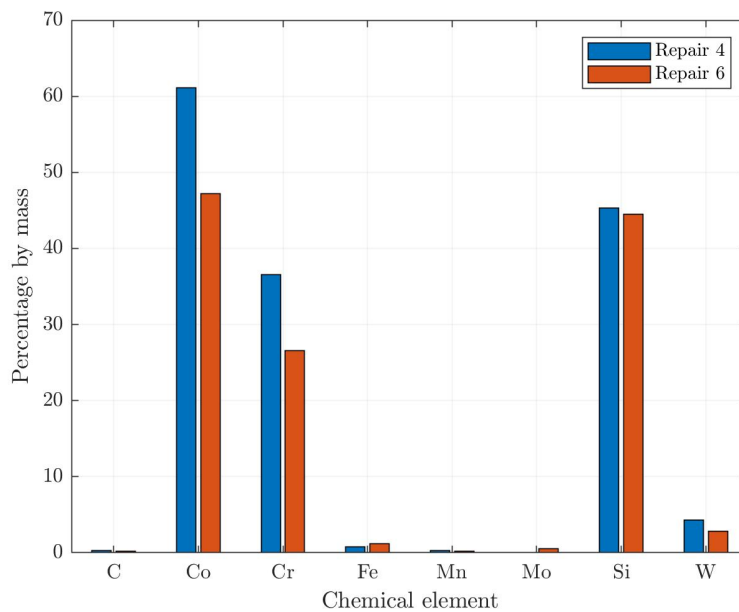
Figure 4.20: Chart showing the chemical element percentage mass of the Stellite 6 repairs from the data gathered though LIBS analysis.

Optical micrographs of repair site 4 prior to testing are presented in Figure 4.21, with left and right interface of the repair site to the parent rail is seen to have a strong metallurgical bond. It can be seen that the etchant caused some excess dissolution of the sample in the process of revealing the repair. Optical micrographs of repair site 4 prior to testing are presented in Figure 4.22. Large inclusions can be seen in the clad repair indicating the process parameters were not optimal for the Stellite 6 powder. The surface profile of repair sites 4 and 6 were measured with the Alicona before testing and the results are shown in Figure 4.23. Noting that the scale of the profile is given in microns, it can be seen that the surface is relatively smooth and consistent initially.
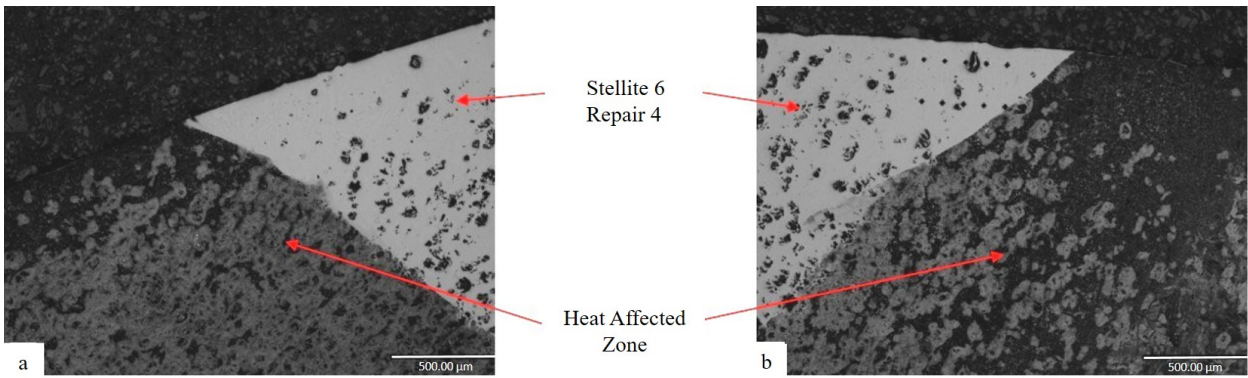
Figure 4.21: Repair 4: Optical micrographs of the a) leading edge and b) trailing edge of the Stellite 6 repair with the R260 parent rail disc, showing mechanical mixing at the interface.
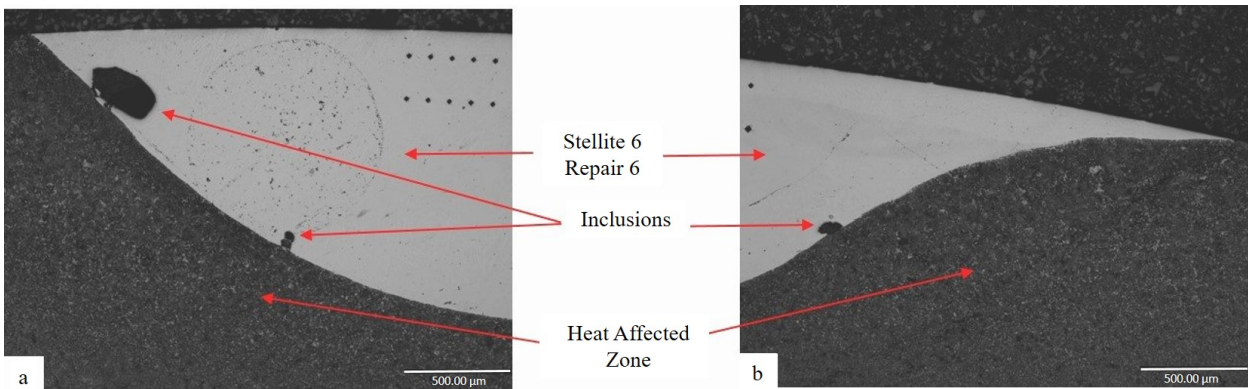
Figure 4.22: Repair 6: Optical micrographs of the a) leading edge and b) trailing edge of the Stellite 6 repair with the R260 parent rail disc, showing inclusions at the interface.
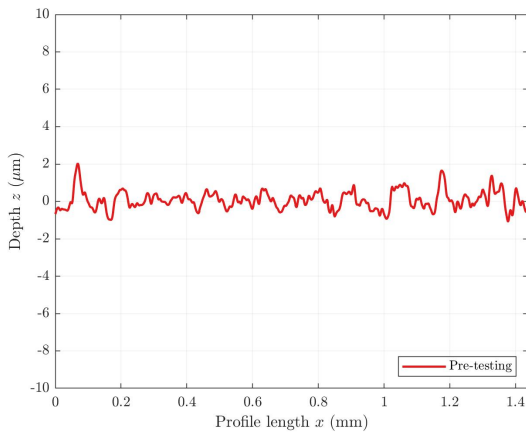
(a) Repair 4 surface profile pre-testing.
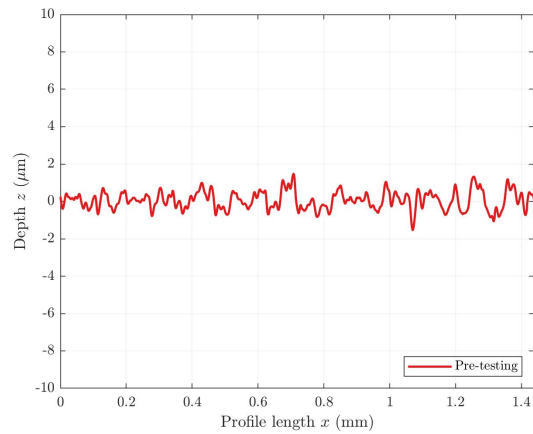
(b) Repair 6 surface profile pre-testing.

Figure 4.23: Repairs 4 and 6: Stellite 6 repair sites surface profile pre-testing.

4.5 Results

4.5.1 Twin-disc test results: Surface evolution

The surface evolution of the repair disc was monitored throughout testing. The wear rate of the repair rail disc stayed below 10 μg/cycle, the test data can be seen in Appendix B, however, it was decided that the wear rate of the disc as a whole is not a good measure of the performance of the repairs. Further investigation through topography measurements and post-test sectioning is required for more accurate analysis.

The surface evolution of the disc was monitored through visual observation every 5,000 cycles. The rail disc surface appears smooth pre-testing and the repairs cannot be seen along the running band. Material flow at the interface of the repairs and parent rail can be seen from 5,000 cycles. The progress of visual surface observations can be seen in Figure 4.24.

Figure 4.24: Visual observation of the progression of surface evolution on the repair disc at regular intervals in the unlubricated test. Material flow can be seen at the interface between the parent rail and repair sites.

The coefficient of traction (CoT), as described in Section 3.4.1, is shown in Figure 4.25 for the repair disc unlubricated test. The test was stopped every 5,000 cycles to monitor the surface topography. The peak CoT remained between 0.33 and 0.36 after each restart of the test, with the exception of between 20,000 and 25,000 cycles which only reached a peak CoT of 0.24. A continued drop in CoT is seen between 10,000 and 20,000 cycles as the test were run in quick succession allowing little change in the surface. The CoT during the last 5,000 cycles remained high compared to the drop in CoT seen in the other intervals. There was an overnight interruption before this final test and it is therefore believed that oxidisation on the surface would have contributed to this.
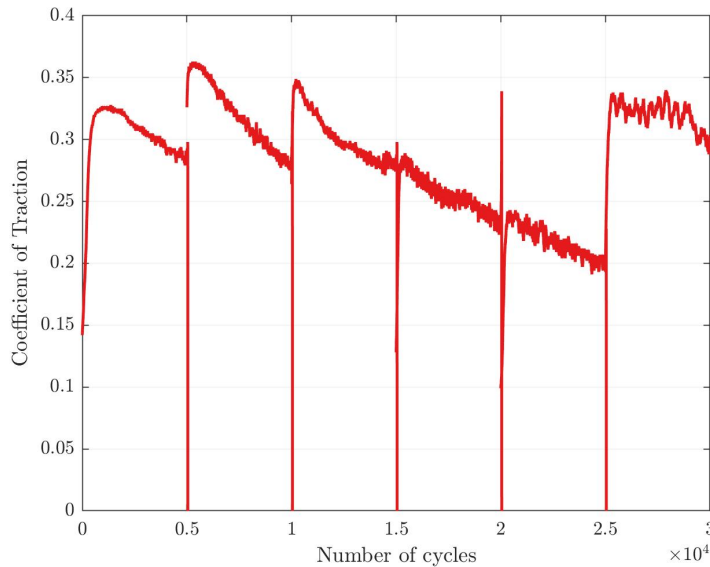
Figure 4.25: Twin-disc coefficient of traction (CoT) for the unlubricated test on repair rail disc, tested at 1500 MPa, -1% slip, 30,000 cycles. The peak CoT is between 0.33 and 0.36 after each restart of the test.

The surface evolution of the individual repairs is studied further through this chapter, categorised into R260 in section 4.5.3, MSS in section 4.5.5 and Stellite in section 4.5.7 for comparison.

4.5.2 Twin-disc test results: Rolling Contact Fatigue

The testing of repair discs in water lubricated conditions is a novel test. The rail disc was run in dry unlubricated contact for 500 cycles to generate plastic deformation within the parent R260 grade rail steel and crack initiation at the surface. Followed by 5,000 cycles with distilled water dripped on to the surface of the wheel disc at a rate of 1 drop per second. The appearance of the repair rail disc was smooth after testing with the repair sites visible on the surface as shown in Figure 4.26.
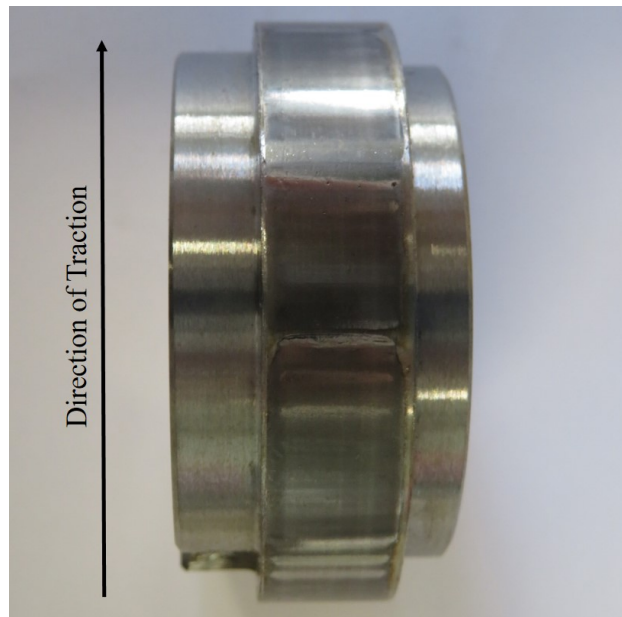
Figure 4.26: Surface appearance of the repair disc after testing for 500 dry cycles and 5,000 wet cycles.

Due to the novelty of this test on repaired discs the initial test was visually inspected for signs of RCF, in the form of a "speckled" surface or visible material loss, after the first 5,000 wet cycles. The clad R260 repair had some visible RCF speckles and hence the test was stopped intentionally to examine this. As expected with a lubricated test there was little material loss compared with a dry test, the wear rate over the total 5,500 cycles was only 0.25 μg/cycle, the test data can be seen in Appendix B. The coefficient of traction for the RCF test is shown in Figure 4.27 with a peak of around 0.39 in the initial dry cycles before dropping to around 0.16 in the wet cycles as would be expected in lubricated contact conditions.
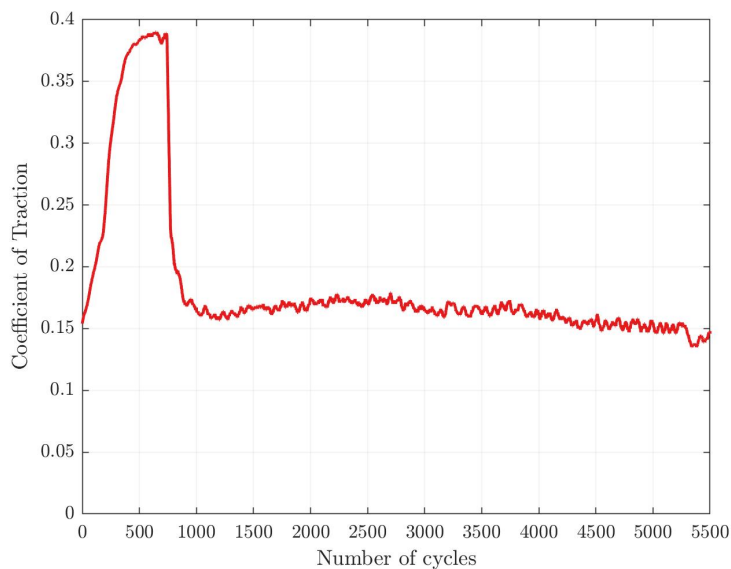
Figure 4.27: Twin-disc coefficient of traction (CoT) for RCF test on repair rail disc, tested at 1500 MPa, -1% slip, 500 dry cycles followed by 5,000 cycles. The peak CoT is 0.39 in the dry cycles and around 0.16 in the wet cycles.

93

The test was repeated and extended to generate further RCF in the other repairs as the only visible surface RCF in the first RCF test was in the R260 repair. The second test ran for 500 dry cycles followed by 15,000 wet cycles with water dripped at a rate of one drop per second again. The disc was visually observed at regular intervals as shown in Figure 4.28, showing visible RCF and surface damage to the parent rail between all repair sites and material flow of the conventional rail steel was observed at the join of the repairs. The R260 repair (repair 1) had visible material loss in the form of dents observed on the surface. The large Stellite 6 repair (repair 4) also had 2 visible dents on the surface, however the medium Stellite 6 repair had no visible RCF. The MSS repairs appeared to have less visible signs of RCF, with only one of the small repairs (repair 5) having minimal speckles on the surface. The test was paused at regular intervals to visually inspect the surface, at the same time the disc was cleaned in isapropanol in a ultrasonic bath before being weighed and measured.
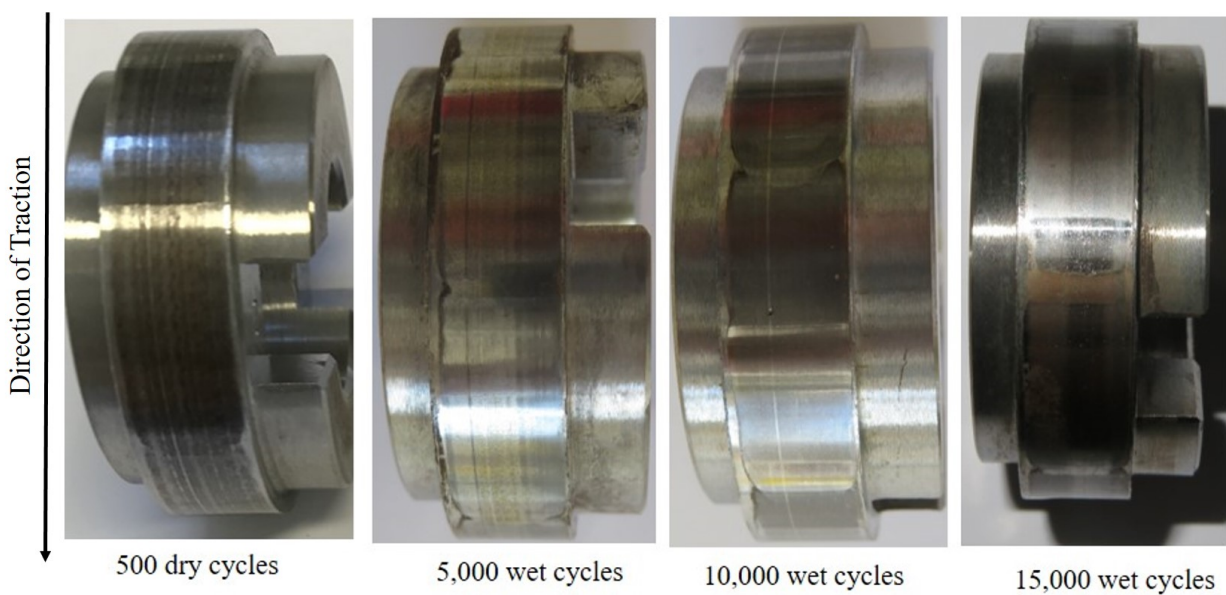
Figure 4.28: Surface appearance of the repair disc after testing for 500 dry cycles and 15,000 wet cycles, observed at regular intervals.

The coefficient of traction plot for the 15,000 cycle RCF test is shown in Figure 4.29with a peak of around 0.38 in the initial dry cycles before dropping to around 0.17 in the wet cycles as would be expected in lubricated contact conditions. There is an anomaly in the CoT in the last 5,000 wet cycles with the peak CoT exceeding 0.4 which would be more likely in dry contact than lubricated. It is expected that debris from RCF passing through the contact was responsible for this. This is further supported by the observation of material loss from one of the MSS repairs shown in Figure 4.55.
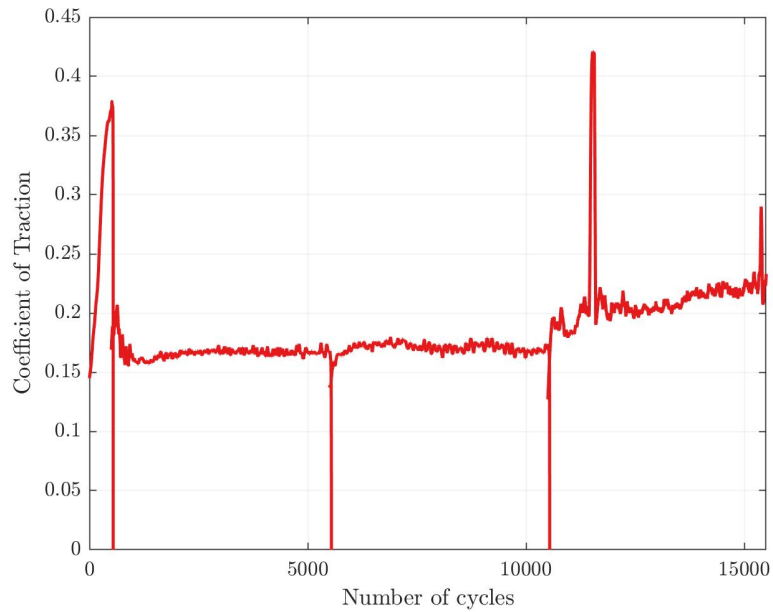
Figure 4.29: Twin-disc coefficient of traction (CoT) for RCF test on repair rail disc, tested at 1500 MPa, -1% slip, 500 dry cycles followed by 15,000 cycles. The peak CoT is 0.38 in the dry cycles and around 0.15 in the wet cycles.

After the SUROS 2 twin-disc tests the discs were sectioned, polished to a 1 μm diamond finish and the repairs were analysed individually, the results of which are presented in the following sections. The average hardness of the repairs after each test was measured on the longitudinal sub-surface cross-section using micro indentation with a 0.2 kg load. The results of which are shown in Figure 4.30.

The pre-test hardness of the R260 clad repair is higher than pre-test R260 grade rail steel and is more in line with a work hardened rail. This is potentially beneficial for a repair which would be applied to serviced rail and would provide continuity of hardness at the surface. The hardness of the R260 clad repair reduced slightly after the unlubricated test to 533 $H_{v0.2}$ and to an average of 401 $H_{v0.2}$ after lubricated RCF testing. This is contrary to the results of the R260 grade rail steel tested in chapter 3 and it appears that R260 applied as a laser clad repair does not work harden and the effective shear yield stress reduces under cyclic loading.

The MSS repairs generally work hardened after cyclic loading as seen in Chapter 3, with the exception of repair 3 after the dry unlubricated test. The extent to which the MSS hardened varied between repairs. The small dimensions of repair 2 and repair 5 presented difficulties to taking measurements which were clear of the surrounding parent rail material.

The Stellite 6 repairs marginally reduced in hardness after the unlubricated test. After the lubricated RCF tests the hardness increased with the larger repair (repair 4) having the higher increase. The Stellite 6 repairs had the highest hardness and hence highest effective shear yield strength of all the candidate repair materials after testing.

95
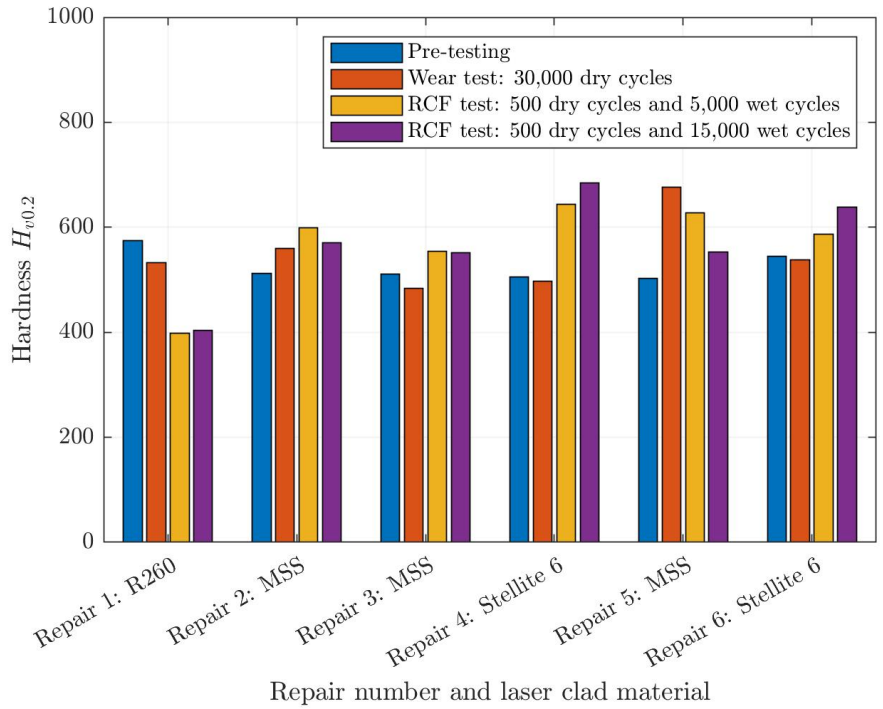
Figure 4.30: Average hardness of the repairs after each test measured on the longitudinal sub-surface cross-section using micro indentation with a 0.2 kg load.

4.5.3 R260 repair: surface evolution

Standard surface roughness measurement Ra (μm) taken along the longitudinal direction of the running band of the repair site is presented in Figure 4.31.
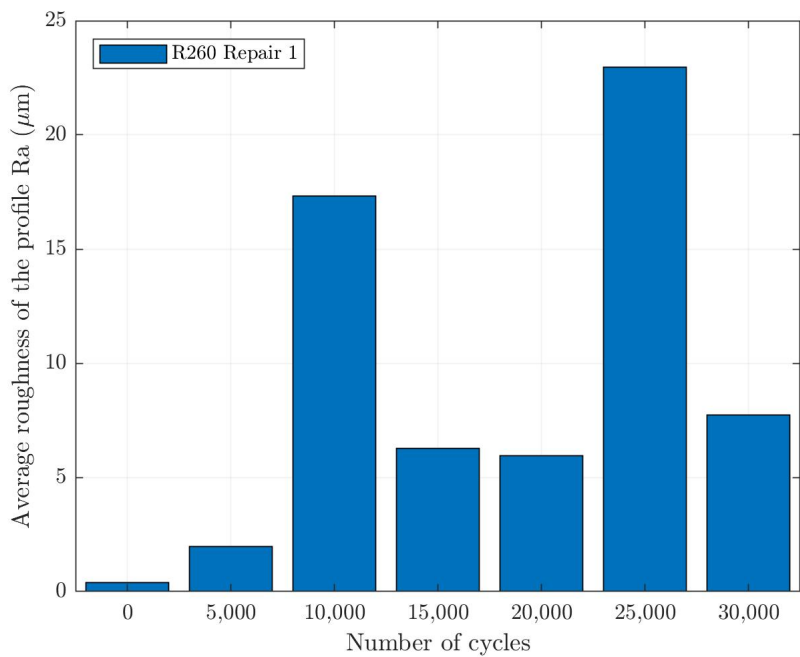
Figure 4.31: R260 repair: repair site 1. Roughness profile measurement Ra, taken at regular intervals throughout the unlubricated test (1500 MPa, -1% slip, 30,000 cycles).

To monitor the surface evolution at the interface of the R260 repair and parent R260 rail at repair site 1, profile roughness measurements were captured with the Alicona after every 5,000 cycles in the unlubricated test run to 30,000 cycles. The variation in Ra values is heavily influenced by the surface flaking, on an otherwise quite uniform flat surface.
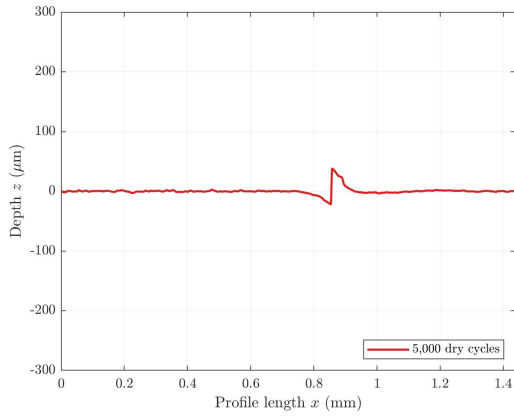
(a) Repair 1 surface profile after 5,000 cycles.
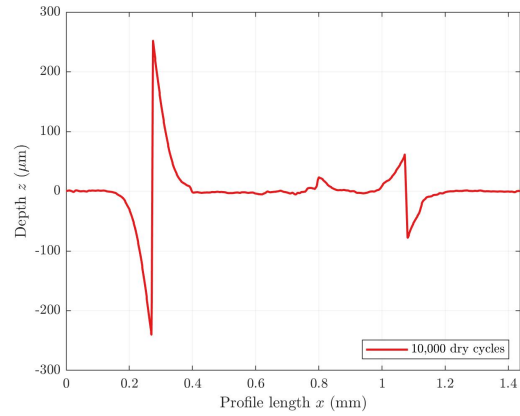
(b) Repair 1 surface profile after 10,000 cycles.
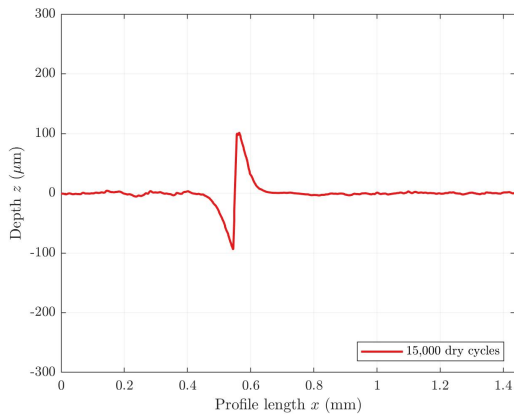
(c) Repair 1 surface after 15,000 cycles.
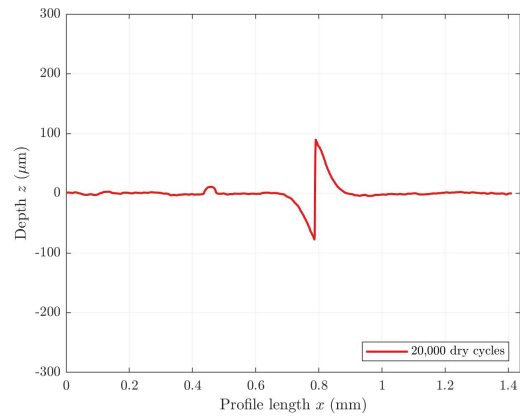
(d) Repair 1 surface profile after 20,000 cycles.
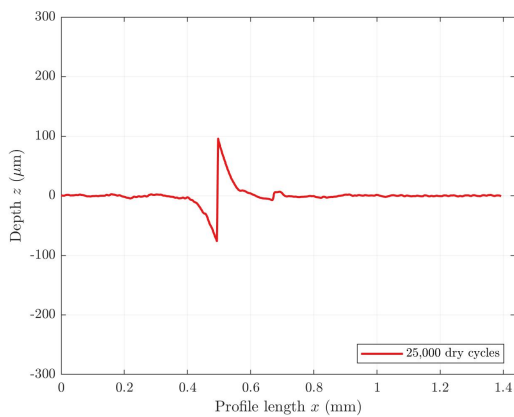
(e) Repair 1 surface profile after 25,000 cycles.
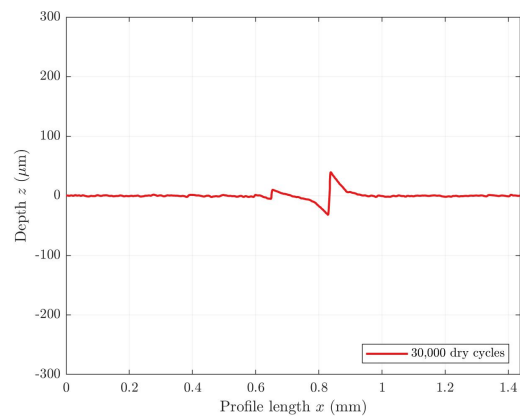
(f) Repair 1 surface profile after 30,000 cycles.

Figure 4.32: R260 Repair: repair site 1: Surface profile pre-testing and at regular intervals throughout the unlubricated test (1500 MPa, -1% slip, 30,000 cycles). Peaks show the flakes formed at the interface of parent rail and repair.

The surface roughness measurements in Figure 4.31 and the surface evolution in Figure 4.32 rep-

resent the surface evolution of the repair site. The peaks in Figure 4.32 show the flakes formed at the interface of parent rail and repair. The formation and delamination of flakes are typical of R260 grade rail steel. Although the data is effected by the presence of flakes across the measurement area, the actual surface profile is seen to remain fairly consistent.

Following the unlubricated test the rail disc was sectioned and repair 1 was removed for analysis. The repair sample was prepared using standard metallographic techniques to achieve a $1\mu m$ diamond polish finish and then etched in 2% Nital. The vertical-longitudinal cross section was then observed with optical microscopy and is shown in Figure 4.33.
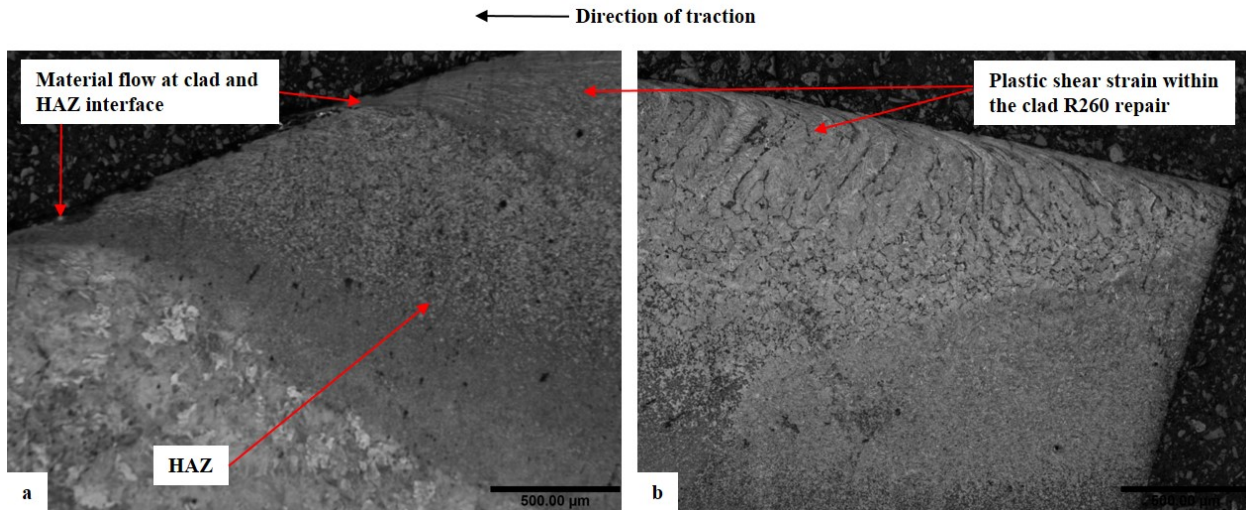
Figure 4.33: Repair 1: Optical micrograph showing material flow in the R260 repair and surrounding heat affected zone in the a) leading edge and b) trailing of repair site 1.

Material flow at the surface can be seen on the interface of the R260 laser clad repair and the heat affected zone, and the interface of the heat affect zone and substrate rail in Figure 4.33a on the leading edge. Plastic shear strain can be seen in the trailing edge of the repair seen in Figure 4.33b. Plastic shear strain down to 140 μm can also be seen at the surface of the middle of the repair site in Figure 4.34, which is a much shallower depth than that seen in the standard R260 rail shown in Figure 3.23 in Chapter 3. The microstructure seen in Figure 4.34 appears to show formation of martensite in the repair down to 730 μm.
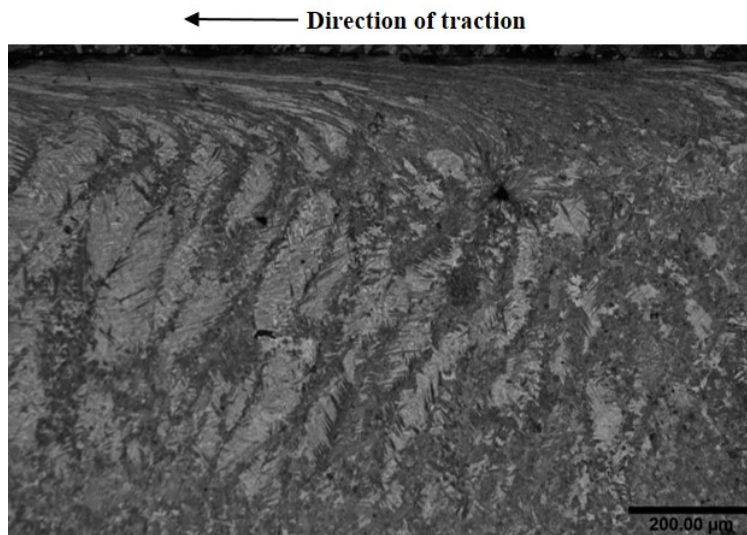
Figure 4.34: Repair 1: Optical micrograph showing plastic shear strain in the centre of the R260 repair to a depth of 140 μm below the contact surface.

4.5.4   R260 repair: RCF results

RCF test 1: 500 dry cycles and 5,000 water lubricated cycles

The surface of the R260 repair was examined with the Alicona after completing the RCF test of 500 dry cycles and 5,000 water lubricated cycles. Figure 4.35a shows surface signs of RCF on the trailing edge of the repair site. The identification of this crack initiation point prompted the decision to stop the test at that point. The rail disc was then sectioned and repair 1 was removed for analysis. The repair sample was once again prepared using standard metallographic techniques to achieve a 1μm diamond polish finish and then etched in 2% Nital.
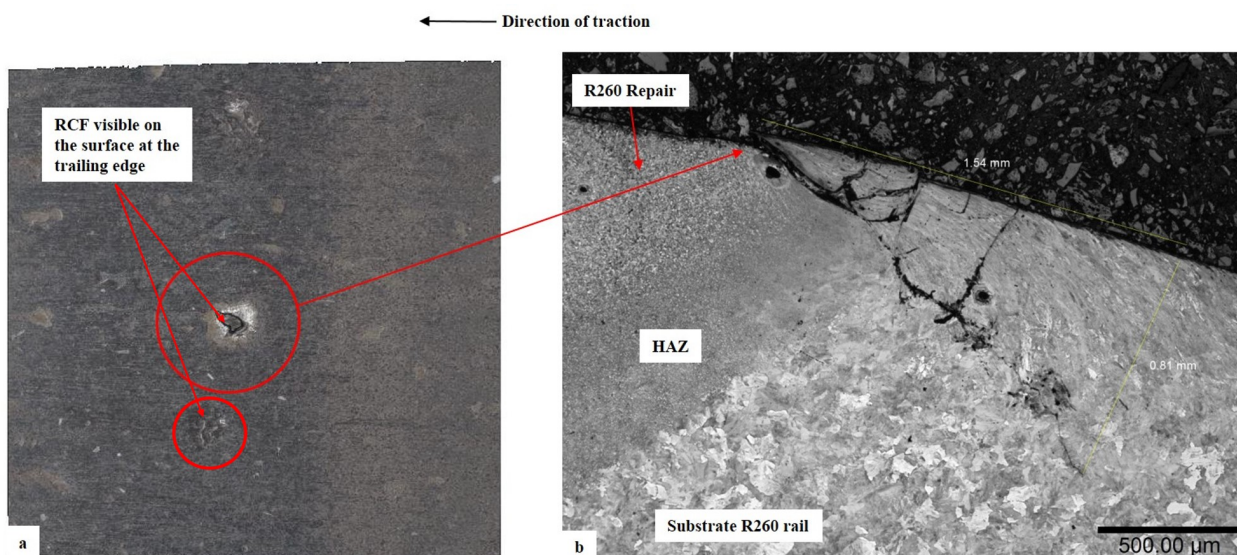
Figure 4.35: Repair 1: Trailing edge of R260 repair after RCF testing of 500 dry cycles followed by 5,000 water lubricated cycles. a) Alicona image showing sign of RCF on the surface and b) Optical micrograph showing network of cracks below the RCF seen on the surface.
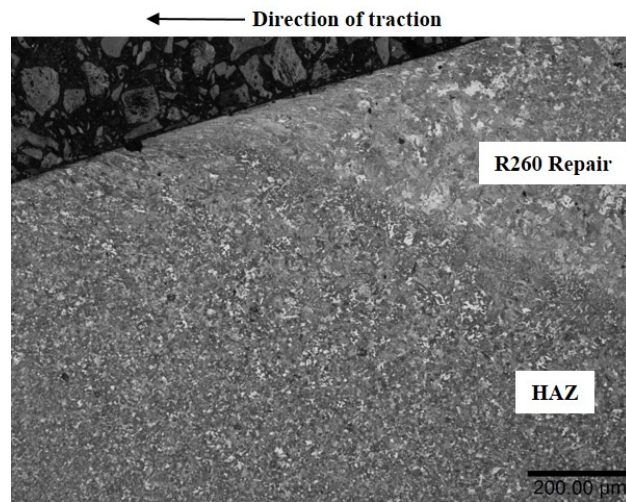
Figure 4.36: Repair 1: Optical micrograph of the R260 repair leading edge after RCF testing of 500 dry cycles followed by 5,000 water lubricated cycles. Material flow at the surface on interface between R260 repair and heat affected zone.

The vertical-longitudinal cross section at the trailing edge was then observed with optical microscopy and the RCF below the surface damage is shown in Figure 4.35b. A significant network of cracks can be seen to a depth of 810 μm below the contact surface. The leading edge of the repair was intact with no signs of RCF, however material flow at shallow levels was identified, comparable to the unlubricated tested R260 repair, as seen in Figure 4.36.

RCF test 2: 500 dry cycles and 15,000 water lubricated cycles

The RCF test was repeated and extended to 500 dry cycles followed by 15,000 water lubricated cycles. During this test the surface was once again monitored with the Alicona and much less RCF was identified. A small amount of surface RCF is identified on the surface shown in Figure 4.37a. After sectioning there were no obvious signs of RCF below the surface and the trailing edge appeared to remain with a strong bond at the interface.
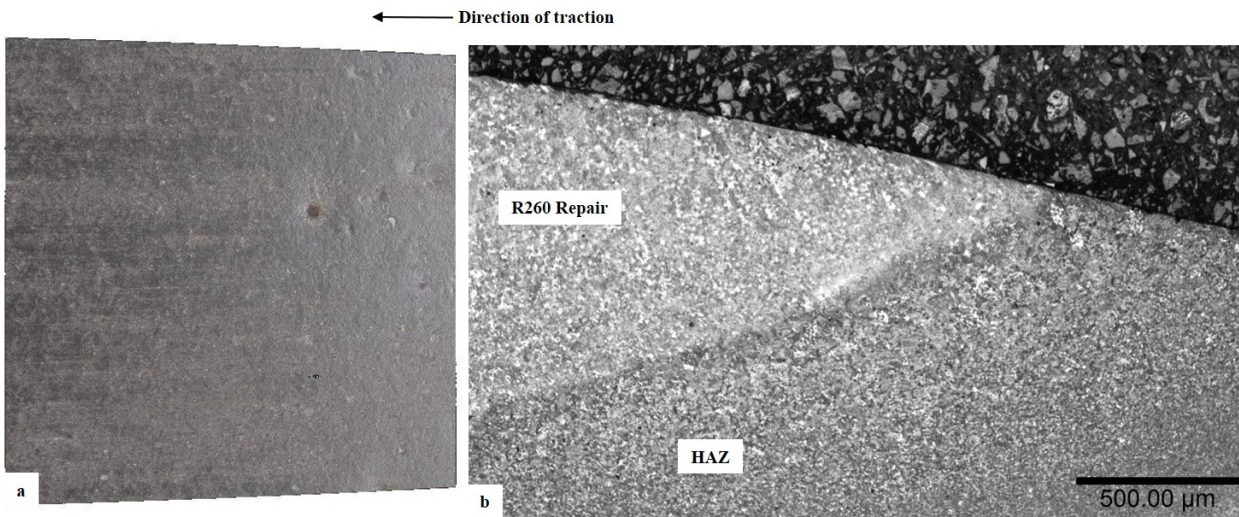
Figure 4.37: Repair 1: R260 repair trailing edge after RCF testing of 500 dry cycles followed by 15,000 water lubricated cycles. a) Alicona image showing little damage on the surface and b) Optical micrograph of the subsurface showing no sign of RCF.
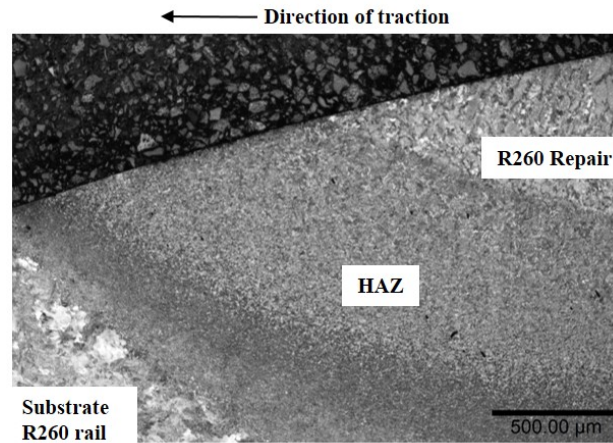
Figure 4.38: Repair 1: Optical micrograph of R260 repair leading edge after RCF testing of 500 dry cycles followed by 15,000 water lubricated cycles. Strong interface between R260 repair, HAZ and parent rail disc with no material flow.

The leading edge of the R260 repair seen in Figure 4.38 had less material flow than the previous tests. The results seen from the 15,000 water lubricated cycles RCF test are in contrast to the network of cracks seen in the shorter RCF test, Figure 4.35. It is possible that a small imperfection or inclusion was present at the surface of the repair site that suffered the excessive RCF crack. This indicates that optimal process parameters would be vital to the safety of an in-situ repair with laser clad R260 steel.

4.5.5 MSS repair: surface evolution

The MSS repairs (repairs 2, 3 and 5) were monitored for surface evolution at the interface between repair and parent rail steel with profile roughness measurements captured with the Alicona every 5,000 cycles in the unlubricated test run to 30,000 cycles. The standard roughness profile

measurement Ra, taken along the longitudinal direction of the running band of the repair sites, are compared across the three MSS repair sites and are presented in Figure 4.39. It is apparent that repair 5 experienced the greatest change in surface modification during the unlubricated test. The method of locating the exact measurement location and the formation of flakes at the surface should be considered when observing the variation in measurements.
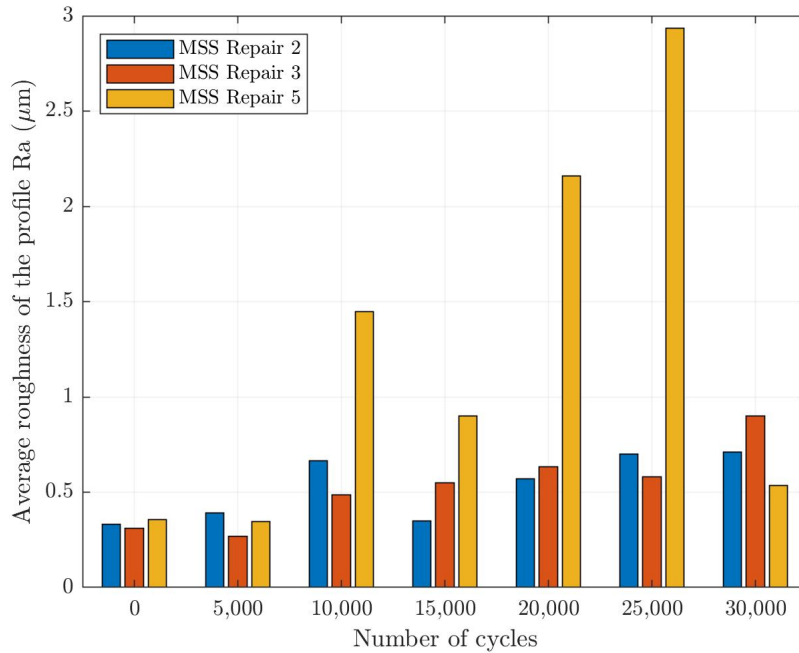
Figure 4.39: MSS repairs: repair sites 2, 3 and 5. Roughness profile measurement Ra, taken at regular intervals throughout the unlubricated test (1500 MPa, -1% slip, 30,000 cycles).

The surface evolution for each MSS repair is shown for each repair in Figures 4.40 to 4.42. The method of locating the exact measurement location and the formation and removal of flakes at the surface should be considered when observing the variation in measurements. It can be seen that repair 5 experienced the most modification at the surface with peaks in roughness (small flakes) forming after 10,000 cycles, 20,000 cycles and 25,000 cycles. There is little change in roughness profile of repair 2 and repair 3 over the 30,000 cycles.
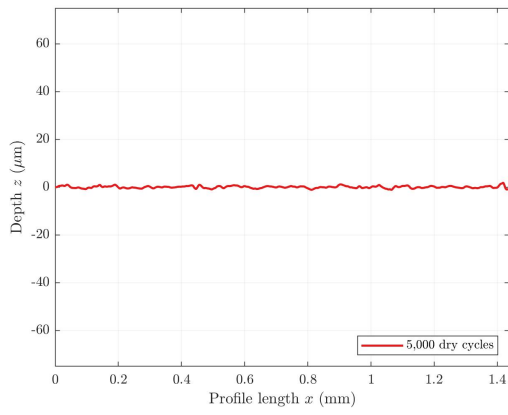
(a) Repair 2 surface profile after 5,000 cycles.
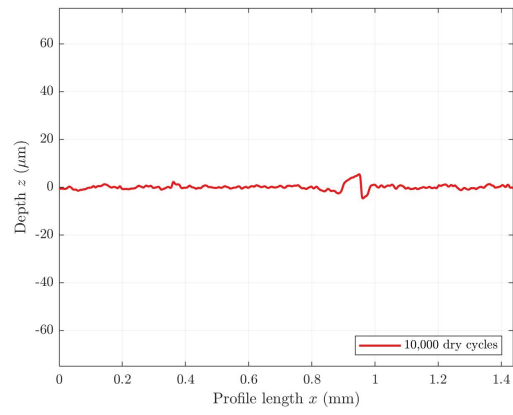
(b) Repair 2 surface profile after 10,000 cycles.
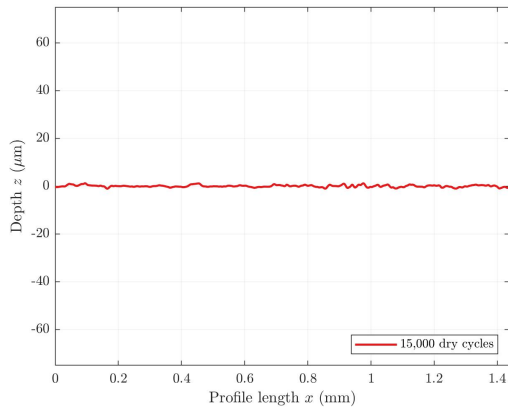
(c) Repair 2 surface after 15,000 cycles.
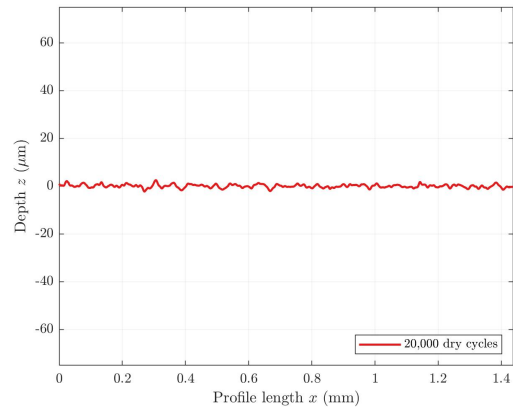
(d) Repair 2 surface profile after 20,000 cycles.
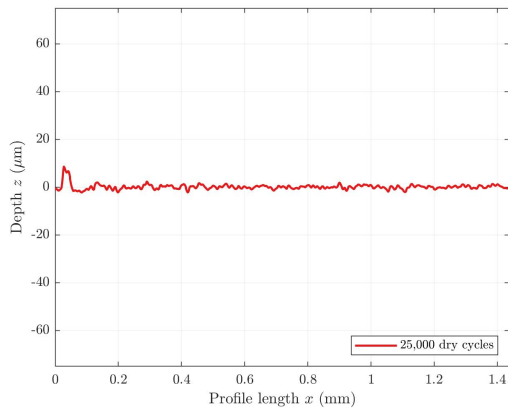
(e) Repair 2 surface profile after 25,000 cycles.
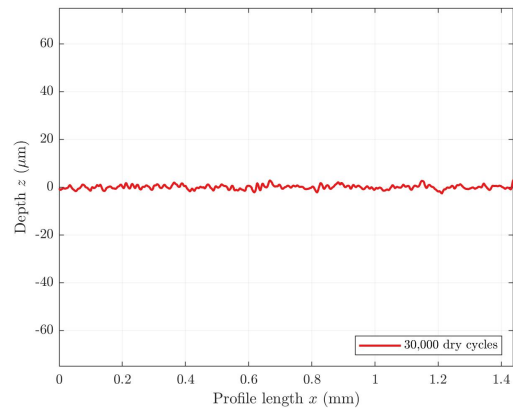
(f) Repair 2 surface profile after 30,000 cycles.

Figure 4.40: MSS Repair: repair site 2. Surface profile pre-testing and at regular intervals throughout the unlubricated test (1500 MPa, -1% slip, 30,000 cycles). Peaks show the flakes formed at the interface of parent rail and repair.
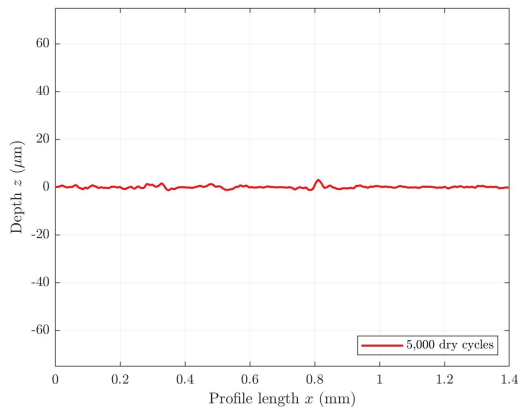
(a) Repair 3 surface profile after 5,000 cycles.
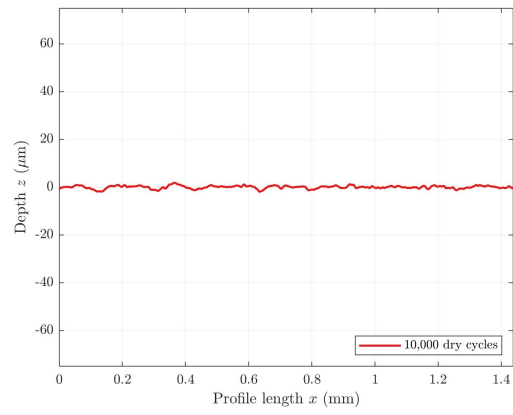
(b) Repair 3 surface profile after 10,000 cycles.
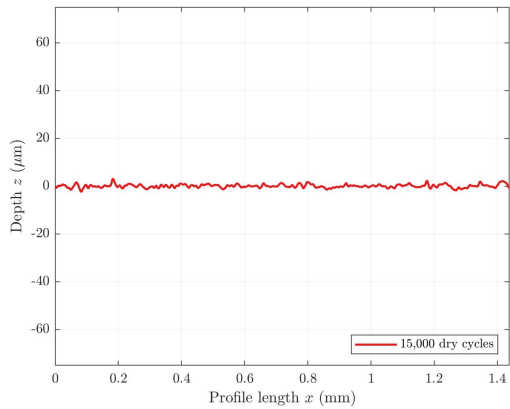
(c) Repair 3 surface after 15,000 cycles.
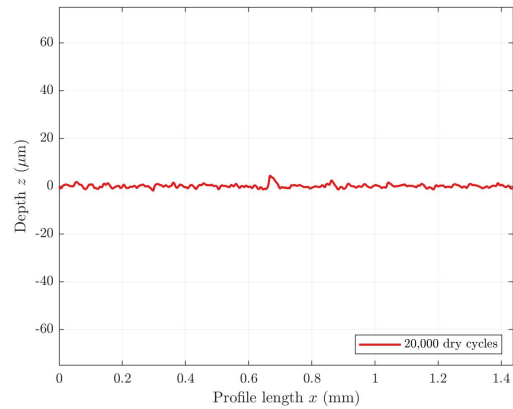
(d) Repair 3 surface profile after 20,000 cycles.
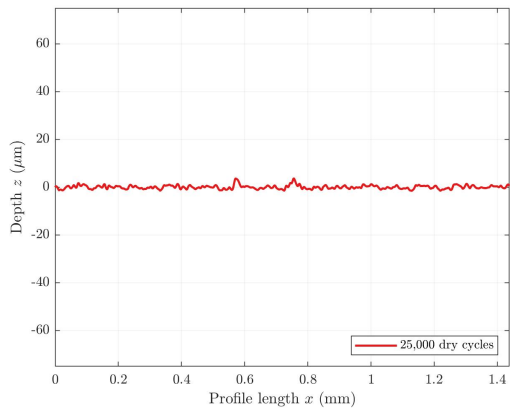
(e) Repair 3 surface profile after 25,000 cycles.
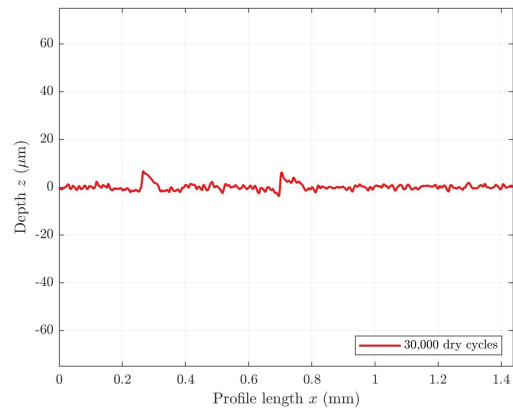
(f) Repair 3 surface profile after 30,000 cycles.

Figure 4.41: MSS Repair: repair site 3. Surface profile pre-testing and at regular intervals throughout the unlubricated test (1500 MPa, -1% slip, 30,000 cycles). Peaks show the flakes formed at the interface of parent rail and repair.
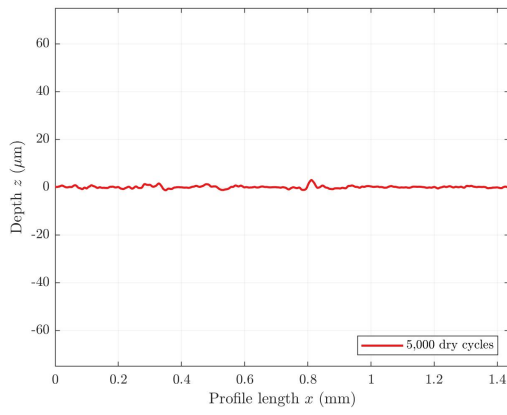
(a) Repair 5 surface profile after 5,000 cycles.
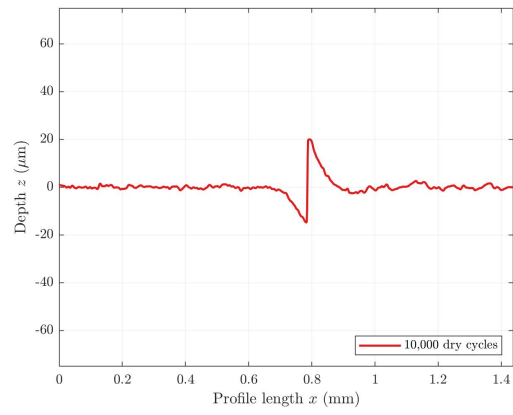
(b) Repair 5 surface profile after 10,000 cycles.
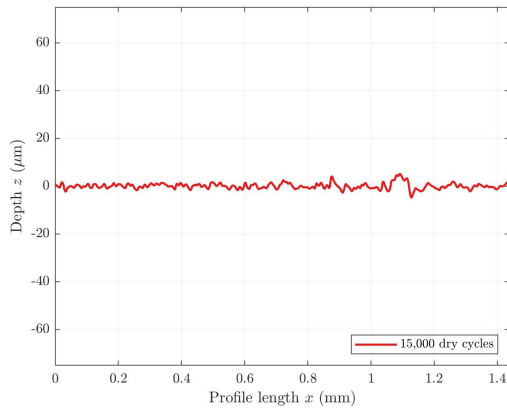
(c) Repair 5 surface after 15,000 cycles.
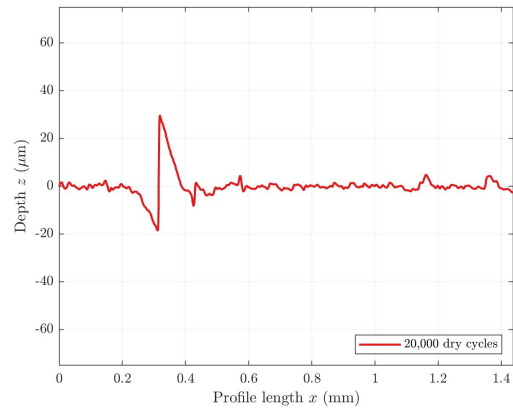
(d) Repair 5 surface profile after 20,000 cycles.
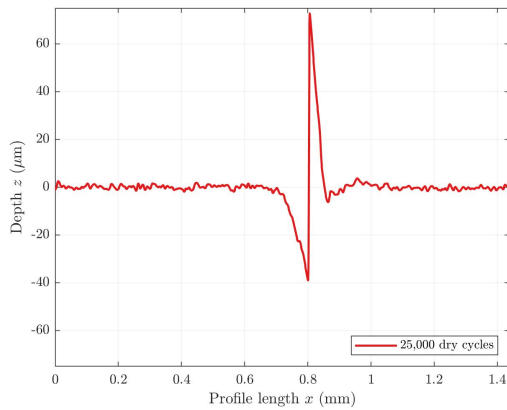
(e) Repair 5 surface profile after 25,000 cycles.
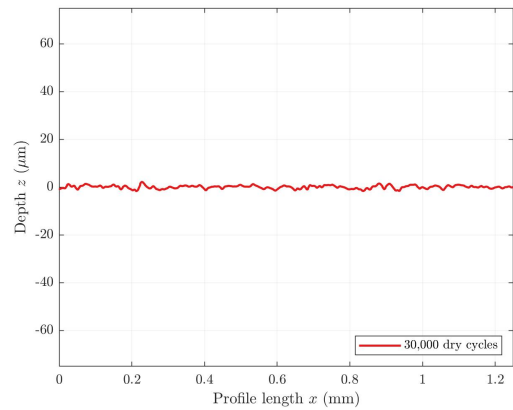
(f) Repair 5 surface profile after 30,000 cycles.

Figure 4.42: MSS Repair: repair site 5. Surface profile pre-testing and at regular intervals throughout the unlubricated test (1500 MPa, -1% slip, 30,000 cycles). Peaks show the flakes formed at the interface of parent rail and repair.

The rail disc was sectioned and repairs 2, 3 and 5 were removed for analysis. Again the repair sample was prepared using standard metallographic techniques to achieve a $1\mu m$ diamond polish finish and then etched in 2% Nital. The vertical-longitudinal cross section was then observed with optical microscopy and is shown in Figures 4.43, 4.44 and 4.45.

Material flow is observed on the leading edge of repair 2, with the clad repair being elongated along the surface compared with the untested repair seen in Figure 4.15a. The trailing edge has an area of deformation compared with the untested repair seen in Figure 4.15b. Repair 2 is a shallow repair and plastic shear strain can be seen in the heat affected zone below the repair.
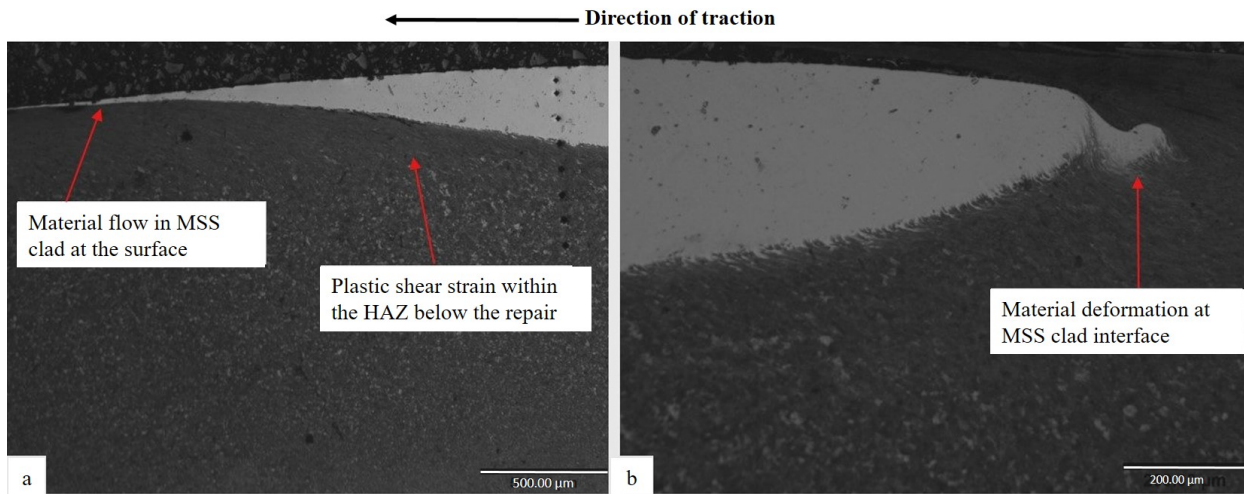
Figure 4.43: Repair 2: MSS repair after 30,000 dry cycles. Optical micrographs showing a) material flow in the leading edge of MSS repair and surrounding heat affected zone, and b) material deformation in the trailing edge.

Repair 3 is a medium depth repair and has a lesser amount of material flow on the leading edge. There is however plastic shear strain and a crack propagating from the surface at the more shallow deposition of clad. Porosity can be seen at the interface below the trailing edge, indicating the process parameters may not have been optimal for the repair. The complexity of repair sample manufacture and limited access to laboratories unfortunately meant that surface damage from sample preparation can be seen in Figure 4.44b.
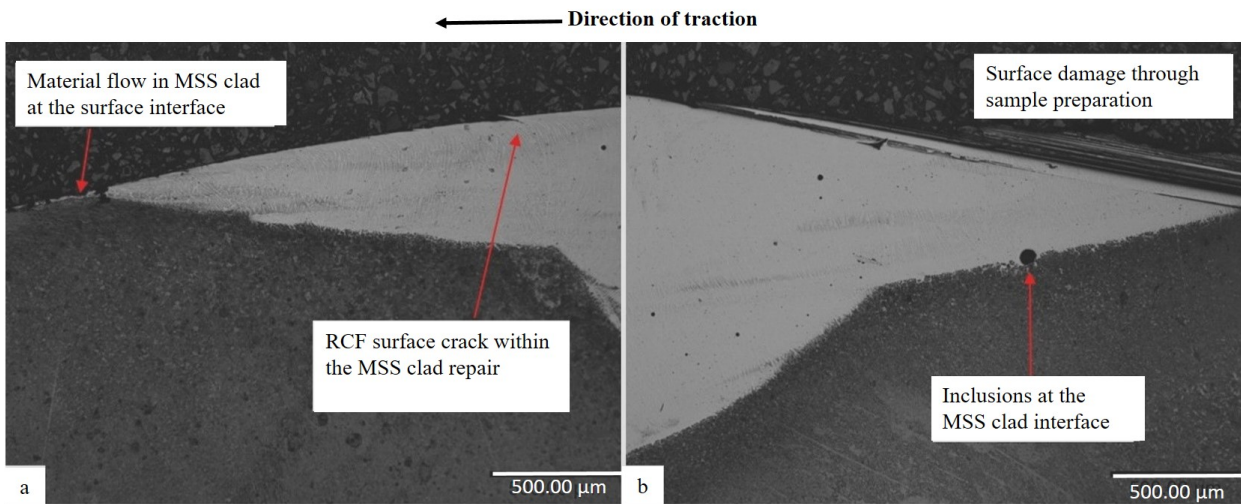
Figure 4.44: Repair 3: MSS repair after 30,000 dry cycles. Optical micrographs showing a) material flow and plastic shear strain at the surface of the leading edge of MSS repair, and b) the trailing edge with inclusion at the repair interface.

Repair 5 is a shallow repair like repair 2 and has performed in the same way in the unlubricated test with elongation of the MSS repair material at the surface on the leading edge. Plastic shear strain is once again seen in the heat affected zone below the repair. The trailing edge is deformed with material swept over in the direction of traction.
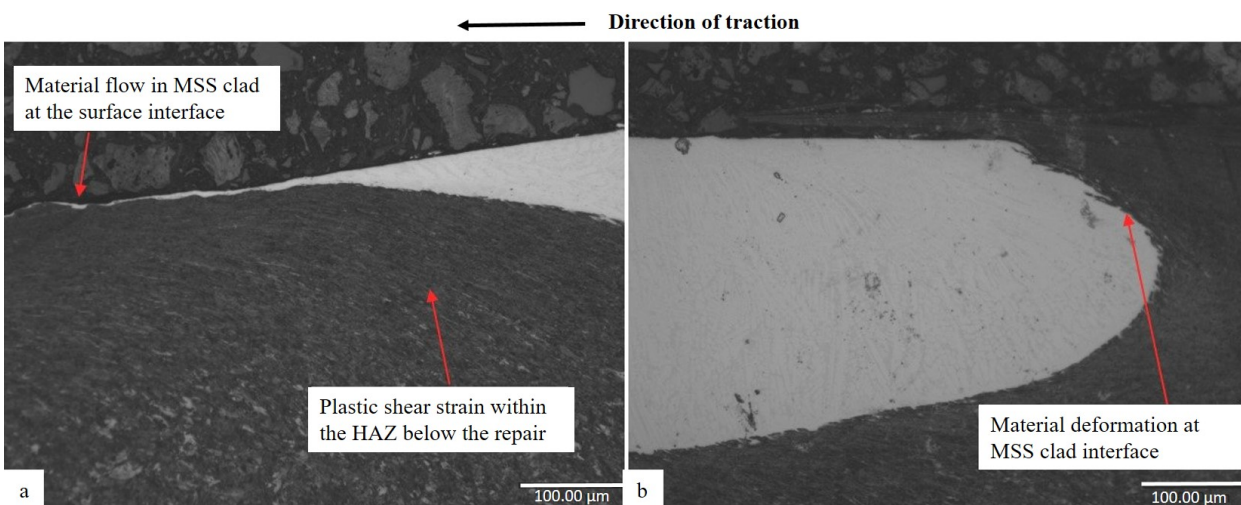
Figure 4.45: Repair 5: MSS repair after 30,000 dry cycles. Optical micrographs showing a) material flow in the leading edge of MSS repair and surrounding heat affected zone, and b) material deformation in the trailing edge.

4.5.6 MSS repair: RCF results

RCF test 1: 500 dry cycles and 5,000 water lubricated cycles

The surface of the MSS repairs was examined with the Alicona after completing the RCF test of 500 dry cycles and 5,000 water lubricated cycles. The MSS repair samples were once again prepared using standard metallographic techniques to achieve a $1\mu m$ diamond polish finish and

then etched in 2% Nital. The vertical-longitudinal cross section at the trailing edge was then observed with optical microscopy or Scanning Electron Microscopy (SEM).
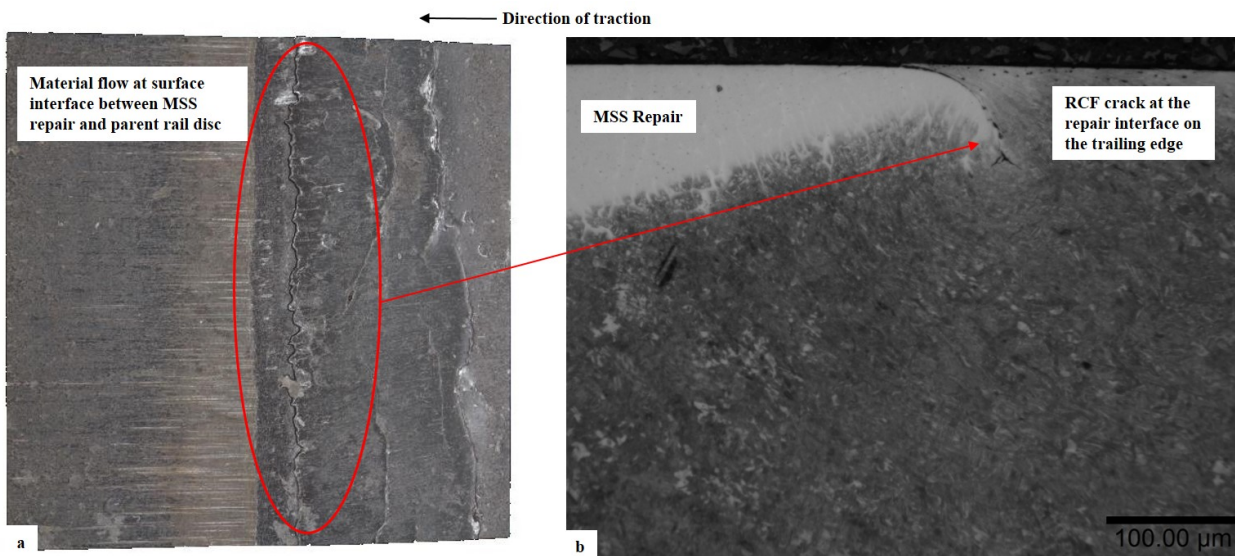
Figure 4.46: Repair 2: MSS repair trailing edge after RCF testing of 500 dry cycles followed by 5,000 water lubricated cycles. a) Alicona image showing material flow on the surface interface and b) optical micrograph showing RCF cracks below surface on the repair interface.

The trailing edge of repair 2 after the 5,000 cycle water lubricated RCF test is shown in Figure 4.46a, where material flow on the surface can be seen, with parent rail flowing over the repair at the interface. Once sectioned an RCF crack can be seen propagating from the surface of the repair interface to a depth of around 7 μm below the surface, shown in Figure 4.46b. The micrograph of the leading edge can be seen in Figure 4.47, with no signs of RCF and only minimal material flow at the surface.
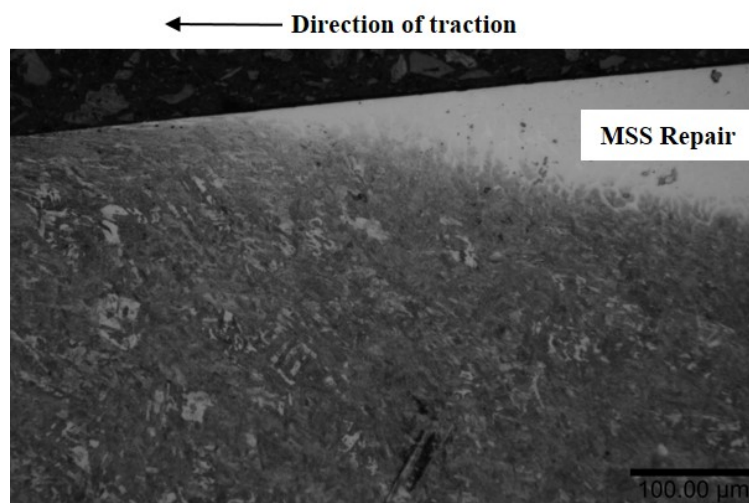
Figure 4.47: Repair 2: Optical micrograph of MSS repair leading edge showing minimal material flow and no signs of RCF.

The trailing edge of repair 3 after the 5,000 cycle water lubricated RCF test can be seen in Figure 4.48, material flow on the surface and a subsurface RCF crack at the interface resemble those seen

in repair 2, yet deeper at around 29 μm below the surface. Similarly the leading edge seen in Figure 4.55 is intact with minimal material flow and no signs of RCF as repair 2 was.
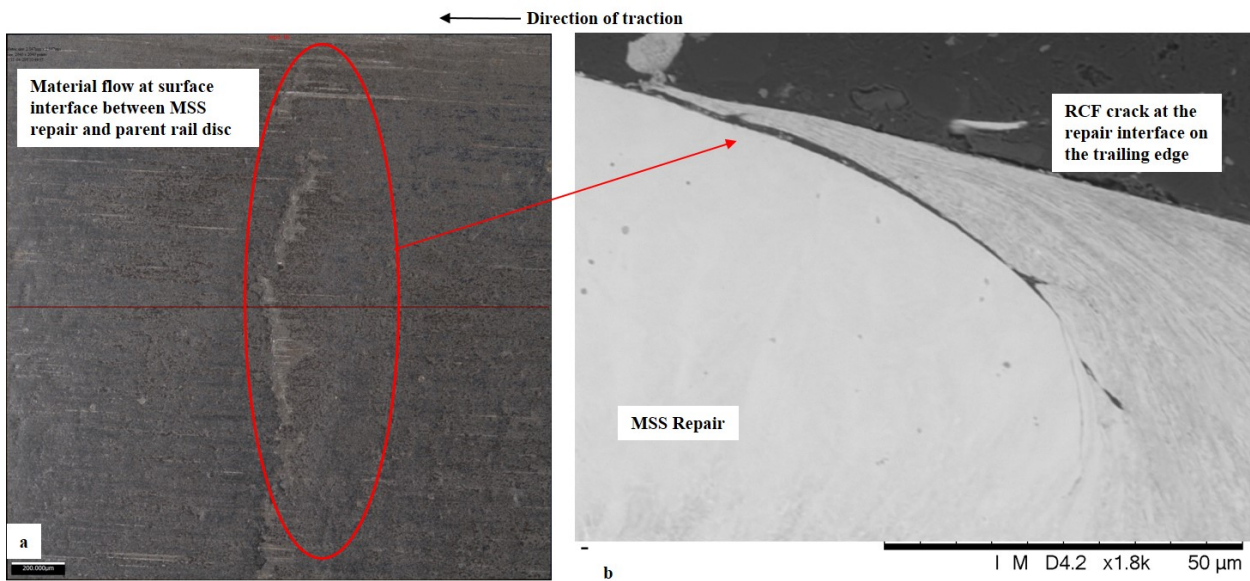
Figure 4.48: Repair 3: MSS repair trailing edge after RCF testing of 500 dry cycles followed by 5,000 water lubricated cycles. a) Alicona image showing material flow on the surface interface and b) SEM image of RCF cracks below surface on the repair interface.
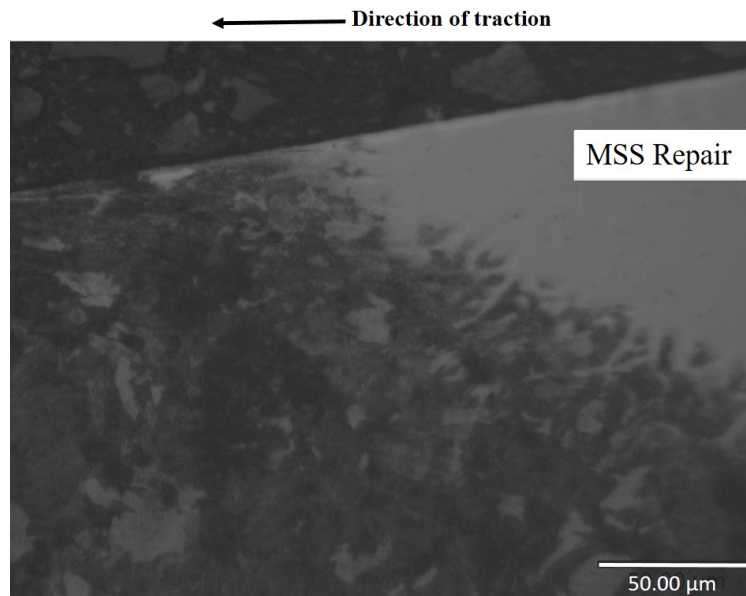
Figure 4.49: Repair 3: Optical micrograph of MSS repair leading edge showing minimal material flow and no signs of RCF.

The surface and subsurface images of repair 5 after the 5,000 cycle water lubricated RCF test are shown in Figure 4.50. Repair 5 appears to have performed differently to repair 2 and repair 3. Material loss is seen on the surface at the interface but there is no sign of subsurface RCF.
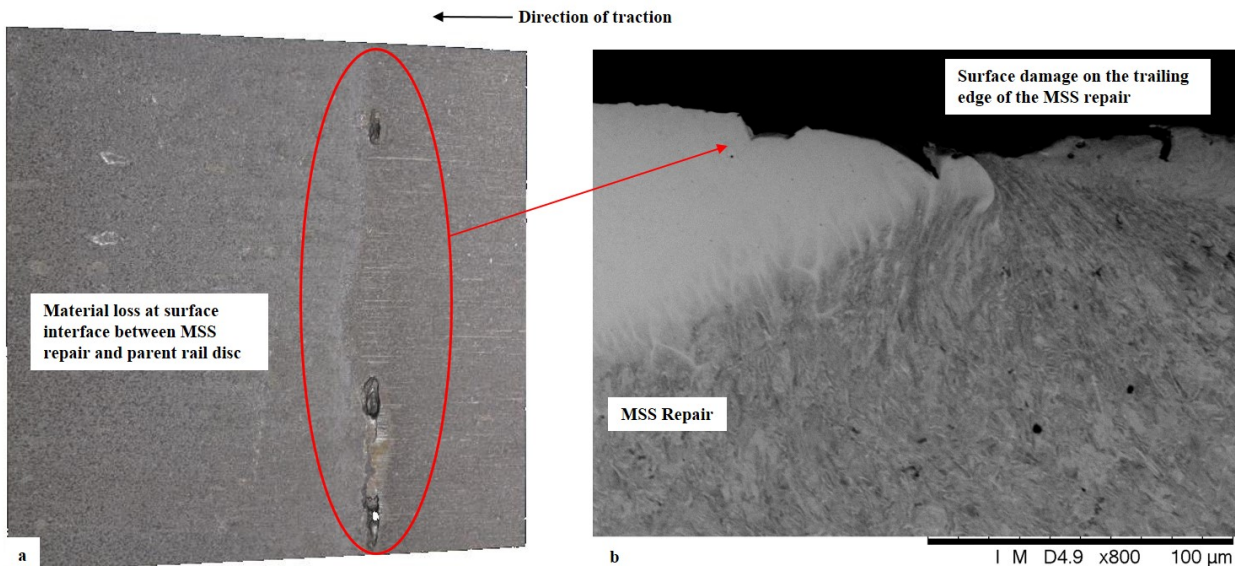
Figure 4.50: Repair 5: MSS repair trailing edge after RCF testing of 500 dry cycles followed by 5,000 water lubricated cycles. a) Alicona image showing damage on the surface interface and b) SEM image of material loss on the surface of the repair.

The leading edge seen in Figure 4.51 also shows a visibly rough damaged surface. This unusual behaviour may be the result of dynamic loading or the presence of a third body within the contact.
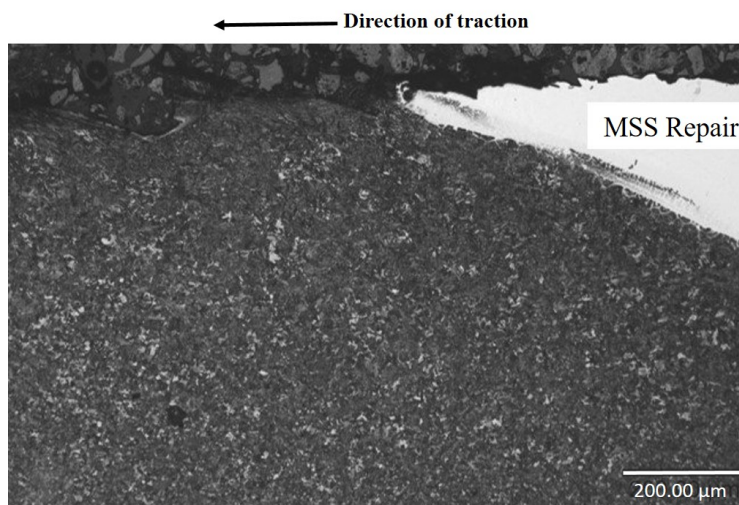
Figure 4.51: Repair 5: Optical micrograph of MSS repair leading edge showing rough damaged surface.

RCF test 2: 500 dry cycles and 15,000 water lubricated cycles

The RCF test was then repeated and extended to 500 dry cycles and 15,000 water lubricated cycles. The trailing edge of repair 2 can be seen in Figure 4.52, the material flow at the interface is once again present as it was in the shorter test. The subsurface RCF crack at the repair interface has propagated into a network of cracks to a depth of approximately 530 μm, following the extra water lubricated cycles.
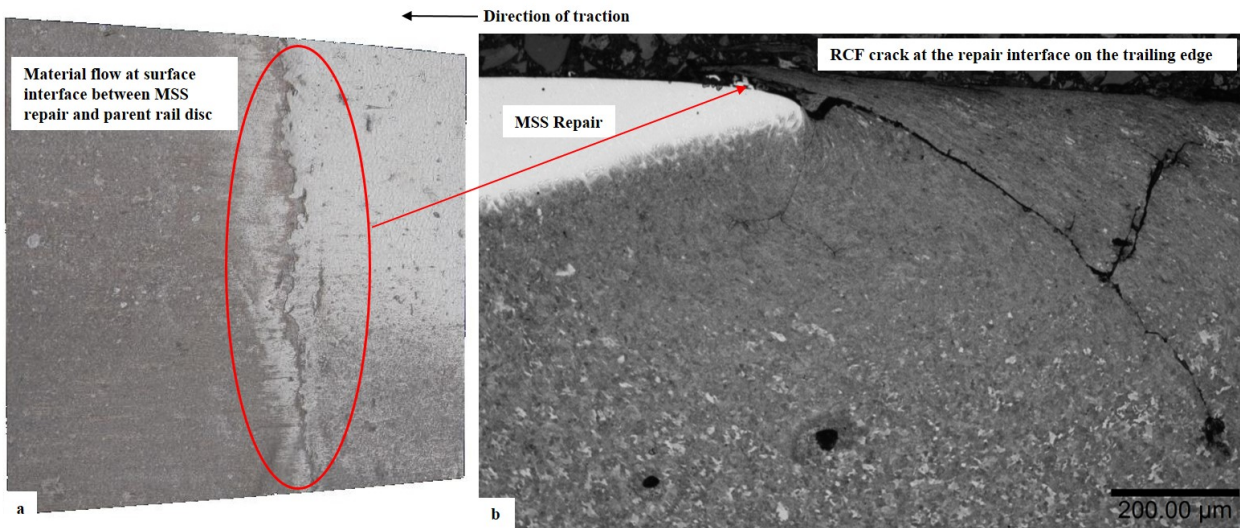
Figure 4.52: Repair 2: MSS repair trailing edge after RCF testing of 500 dry cycles followed by 15,000 water lubricated cycles. a) Alicona image showing material flow on the surface interface and b) Optical micrograph showing network of RCF cracks below surface on the repair interface.

The leading edge of repair 2 shown in Figure 4.53 remains intact with no evidence of RCF or material flow.
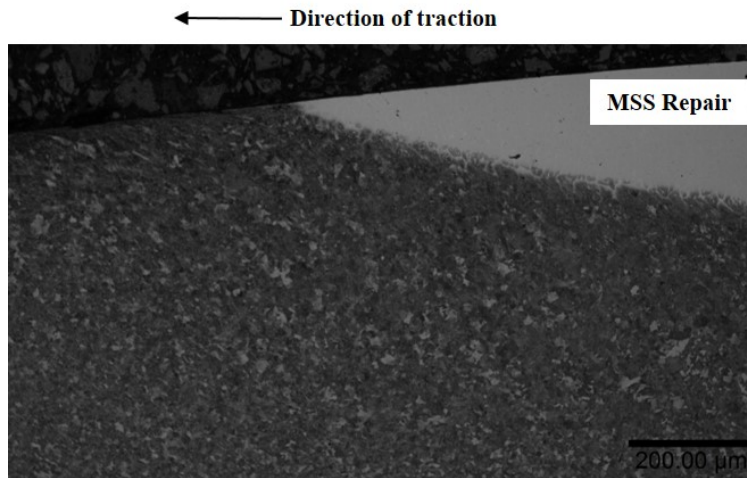
Figure 4.53: Repair 2: Optical micrograph of MSS repair leading edge showing minimal material flow and no signs of RCF.

The trailing edge of repair 3 can be seen in Figure 4.54 with material flow on the surface interface and a small subsurface RCF crack to a depth of 5 μm below the surface.
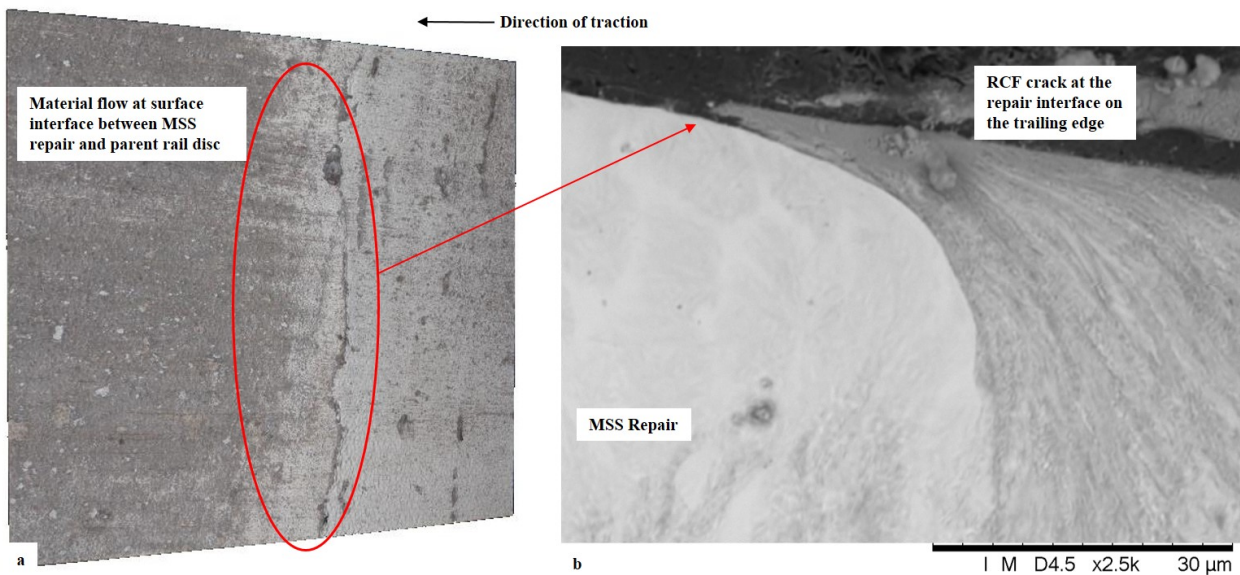
Figure 4.54: Repair 3: MSS repair trailing edge after RCF testing of 500 dry cycles followed by 15,000 water lubricated cycles. a) Alicona image showing material flow on the surface interface and b) SEM image of RCF crack below surface on the repair interface.

A small hollow on the surface of the leading edge can be seen in Figure 4.55a. A fragment of around 62 μm wide and 26 μm deep of the MSS repair can be seen in Figure 4.55b spalling from the surface after sectioning. This could explain the spike in traction seen in Figure ref-fig:REP2CoTplot.
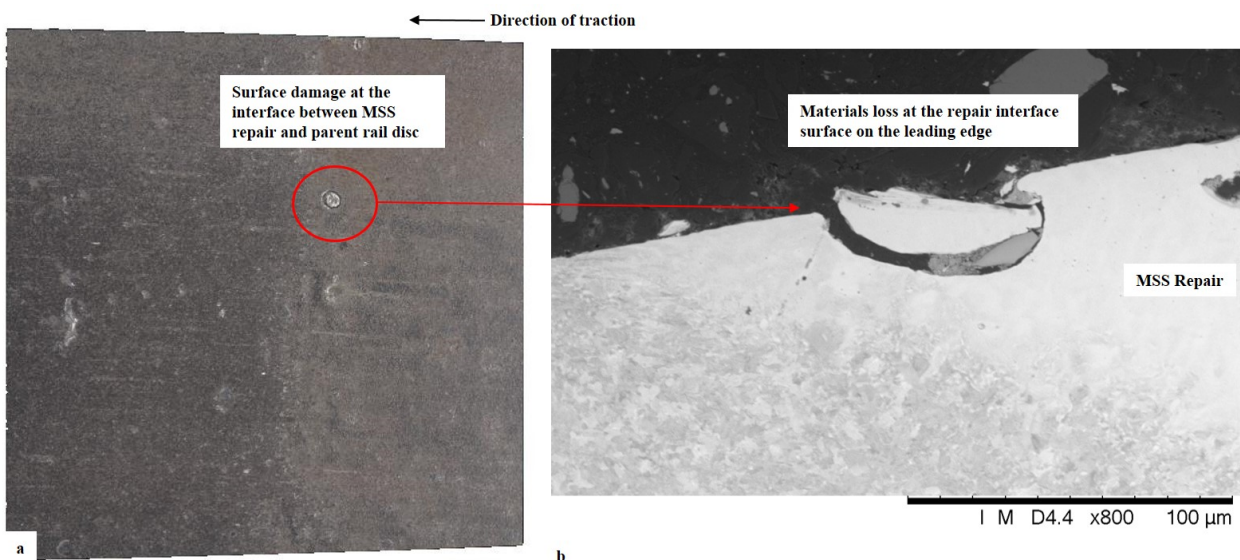
Figure 4.55: Repair 3: MSS repair leading edge after RCF testing of 500 dry cycles followed by 15,000 water lubricated cycles. a) Alicona image showing small hollow on the surface interface and b) SEM image of MSS repair fragment of material spalling from surface.

After the longer RCF test repair 5 behaved in a way more comparable to the other MSS repairs. A small amount of material flow is seen on the surface interface in Figure 4.56a. Once sectioned a small RCF crack at the interface of the repair trailing edge can be seen to a depth of 5 μm. The

leading edge shown in Figure 4.57 is also more aligned with repairs 2 and 3, with no RCF or material flow and no loss of integrity at the interface.
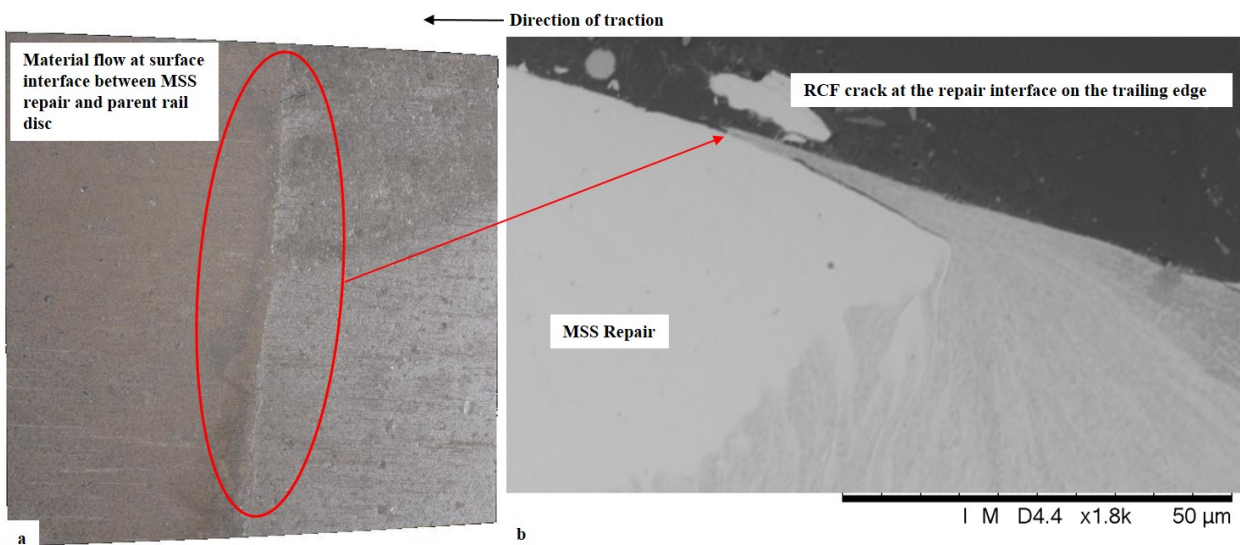
Figure 4.56: Repair 5: MSS repair trailing edge after RCF testing of 500 dry cycles followed by 15,000 water lubricated cycles. a) Alicona image showing small amount of material flow on the surface interface and b) SEM image of RCF crack below surface on the repair interface.
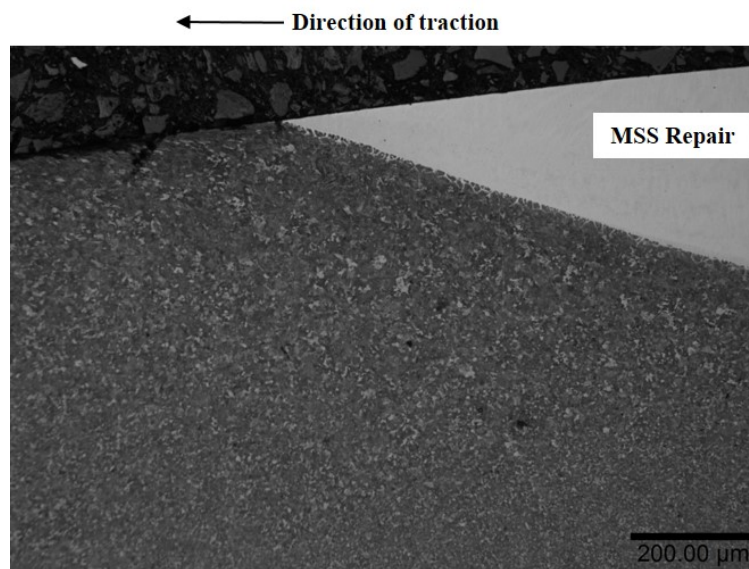
Figure 4.57: Repair 5: Optical micrograph of MSS repair leading edge showing no signs of RCF or material flow.

4.5.7 Stellite 6 repair: surface evolution

The Stellite 6 repairs (repairs 4 and 6) were monitored for surface evolution at the interface between repair and parent rail steel with profile roughness measurements captured with the Alicona every 5,000 cycles in the unlubricated test run to 30,000 cycles. The standard roughness profile measurement Ra, taken along the longitudinal direction of the running band of the repair sites, are compared across the three MSS repair sites and are presented in Figure 4.58. Once again, the nature of locating the exact measurement location and the formation and removal of flakes at the surface should be considered when observing the variation in measurements.
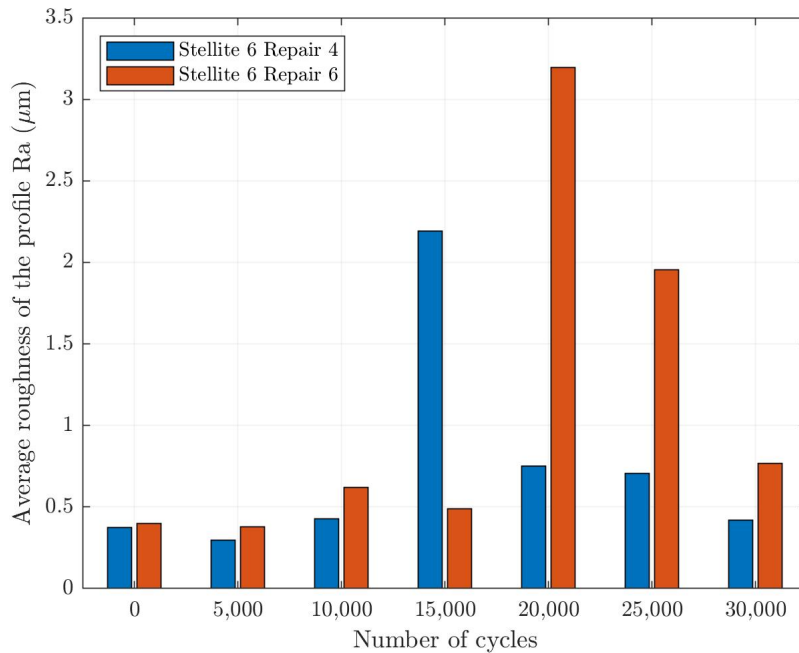
Figure 4.58: Stellite 6 repairs: repair sites 4 and 6. Roughness profile measurement Ra, taken at regular intervals throughout the unlubricated test (1500 MPa, -1% slip, 30,000 cycles).

Considering the surface profile measurements in Figures 4.59 and 4.60 it can be seen that both Stellite 6 repairs perform in a comparable way. The surface appears to become more rough after 10,000 cycles. The data is affected by the presence of surface flakes.
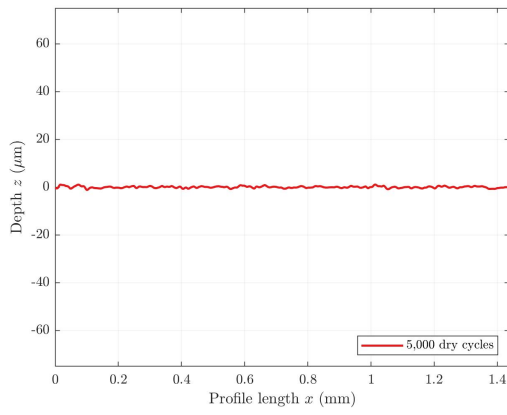
(a) Repair 4 surface profile after 5,000 cycles.
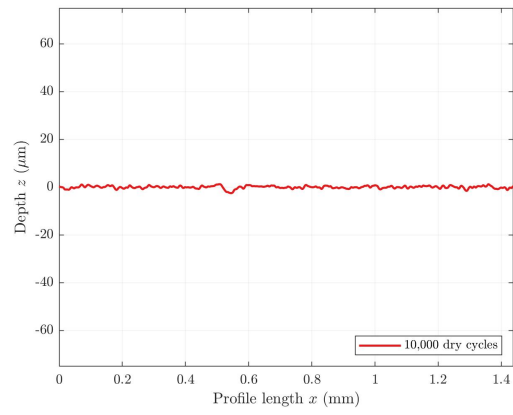
(b) Repair 4 surface profile after 10,000 cycles.
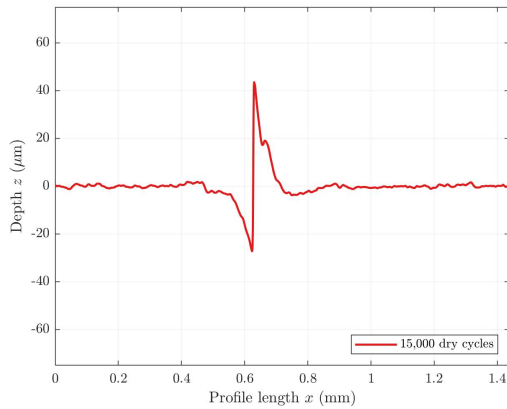
(c) Repair 4 surface after 15,000 cycles.
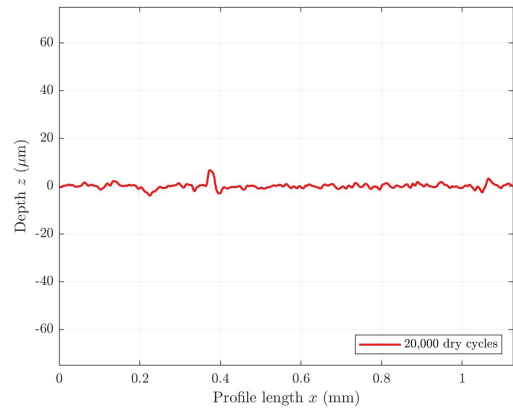
(d) Repair 4 surface profile after 20,000 cycles.
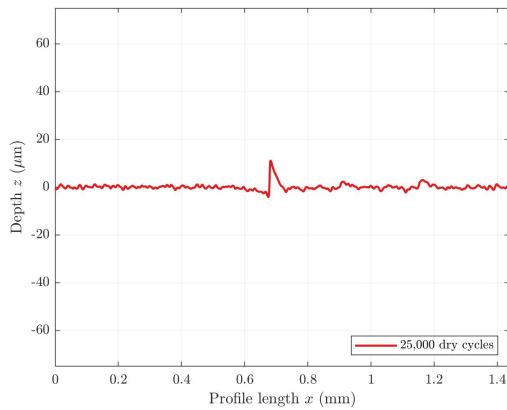
(e) Repair 4 surface profile after 25,000 cycles.
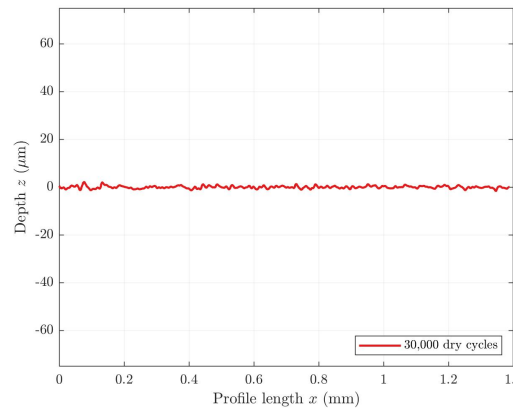
(f) Repair 4 surface profile after 30,000 cycles.

Figure 4.59: Stellite 6 Repair: repair site 4. Surface profile pre-testing and at regular intervals throughout the unlubricated test (1500 MPa, -1% slip, 30,000 cycles). Peaks show the flakes formed at the interface of parent rail and repair.
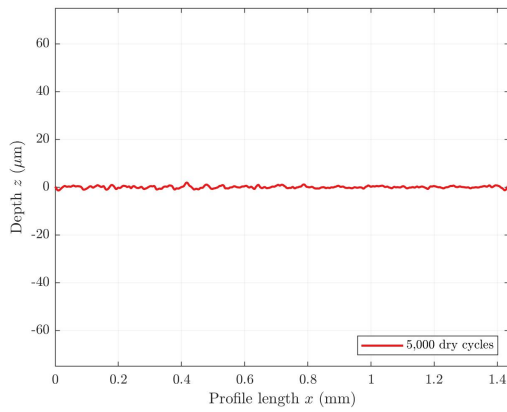
(a) Repair 6 surface profile after 5,000 cycles.
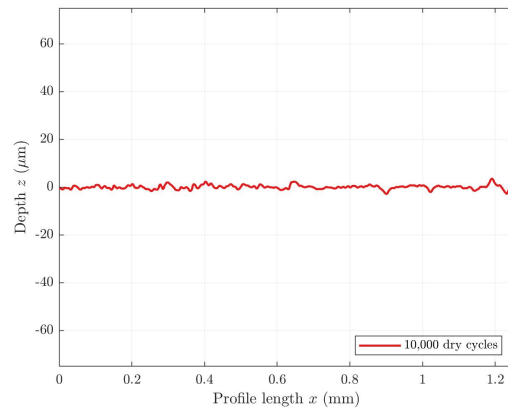
(b) Repair 6 surface profile after 10,000 cycles.
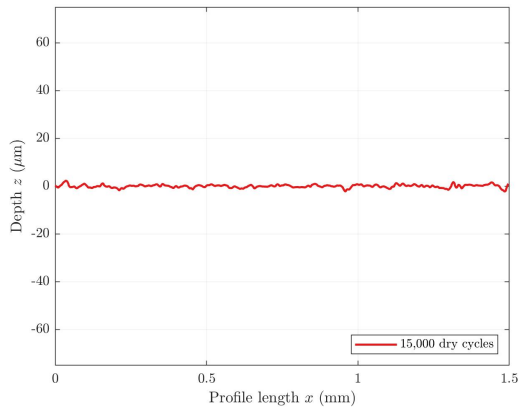
(c) Repair 6 surface after 15,000 cycles.
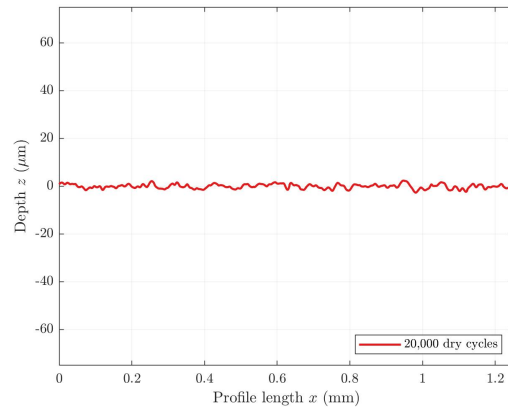
(d) Repair 6 surface profile after 20,000 cycles.
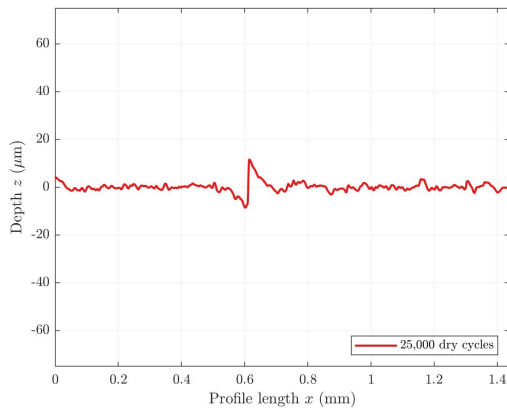
(e) Repair 6 surface profile after 25,000 cycles.
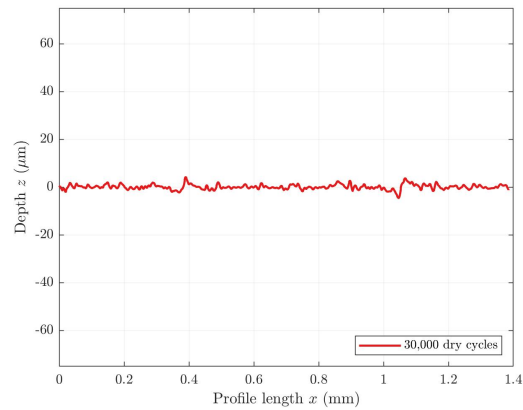
(f) Repair 6 surface profile after 30,000 cycles.

Figure 4.60: Stellite 6 Repair: repair site 6. Surface profile pre-testing and at regular intervals throughout the unlubricated test (1500 MPa, -1% slip, 30,000 cycles). Peaks show the flakes formed at the interface of parent rail and repair.

The rail disc was sectioned and repairs 4 and 6 were removed for analysis. Again the repair samples were prepared using standard metallographic techniques to achieve a $1\mu m$ diamond polish finish and then etched in 2% Nital. The vertical-longitudinal cross section was then observed with optical microscopy and is shown in Figures 4.61 and 4.62. Repair 4 is a deep repair and material flow is observed on the leading edge of repair 4, with the clad repair being elongated along the

surface compared with the untested repair seen in Figure 4.21a. The trailing edge has an area of deformation compared with the untested repair seen in Figure 4.61b.
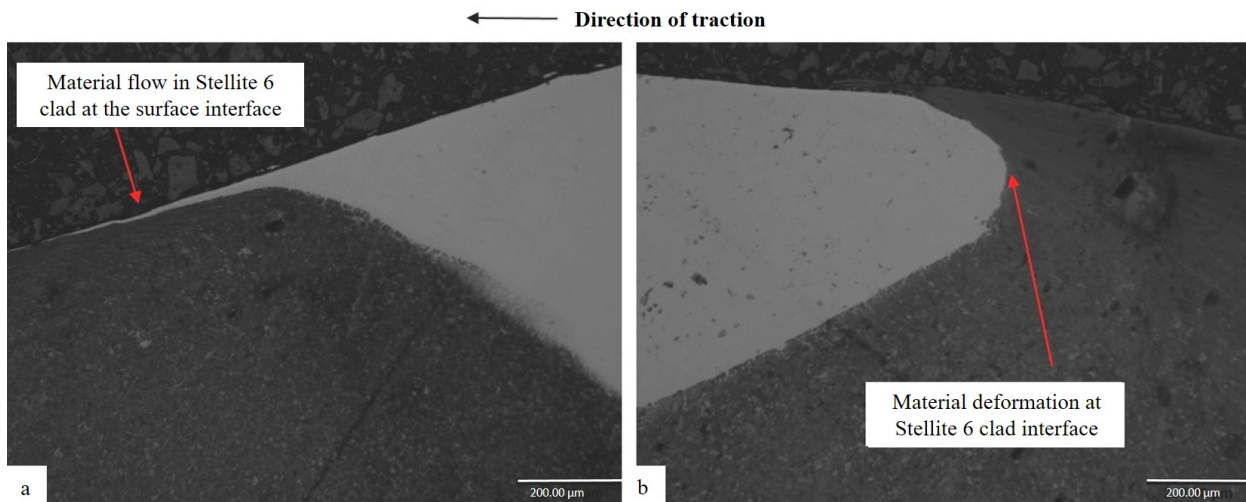
Figure 4.61: Repair 4: Stellite 6 repair after 30,000 dry cycles.Optical migrograph of a) material flow in the leading edge of Stellite repair and b) material deformation in the trailing edge.

Repair 6 experienced surface damage in sectioning but there is some evidence of material flow in the leading edge, Figure 4.62a. A subsurface crack can be seen at the repair interface of the trailing edge to a depth of around 100 μm, with material swept in the direction of traction, Figure 4.62b. The complexity of repair sample manufacture and limited access to laboratories unfortunately meant that surface damage from sample preparation can be seen in Figure 4.62.
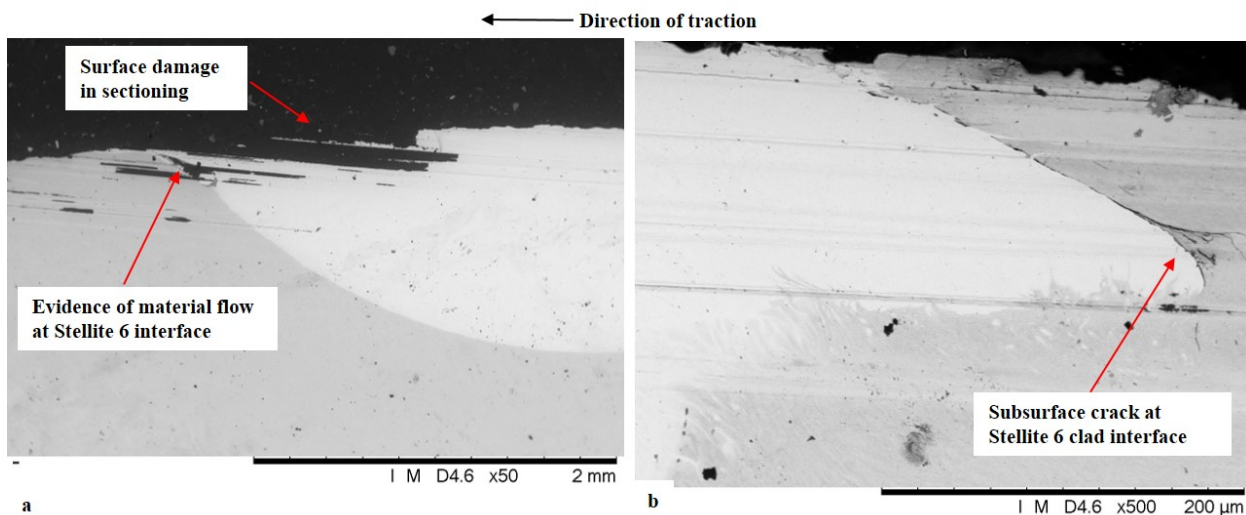
Figure 4.62: Repair 6: Stellite 6 repair after 30,000 dry cycles. Sample surface damage present from sectioning. SEM images showing a) evidence of material flow in the leading edge of Stellite 6 repair and b) material deformation and RCF crack in the trailing edge.

4.5.8   Stellite 6 repair: RCF results

RCF test 1: 500 dry cycles and 5,000 water lubricated cycles

The surface of the Stellite 6 repairs was examined with the Alicona for signs of RCF after 500 dry cycles and 5,000 water lubricated cycles. The vertical-longitudinal cross section at the trailing edge and leading edge was then observed using both optical microscopy and SEM. The surface of repair 4 at the trailing edge can be seen in Figure 4.63a, with some material flow seen at the interface. When examining the cross section of the trailing edge with SEM, Figure 4.63b, subsurface material deformation and surface damage is observed on the trailing edge of the repair. The leading edge of repair 4 has elongation of the repair at the surface seen in Figure 4.64 with material flow in the direction of traction.
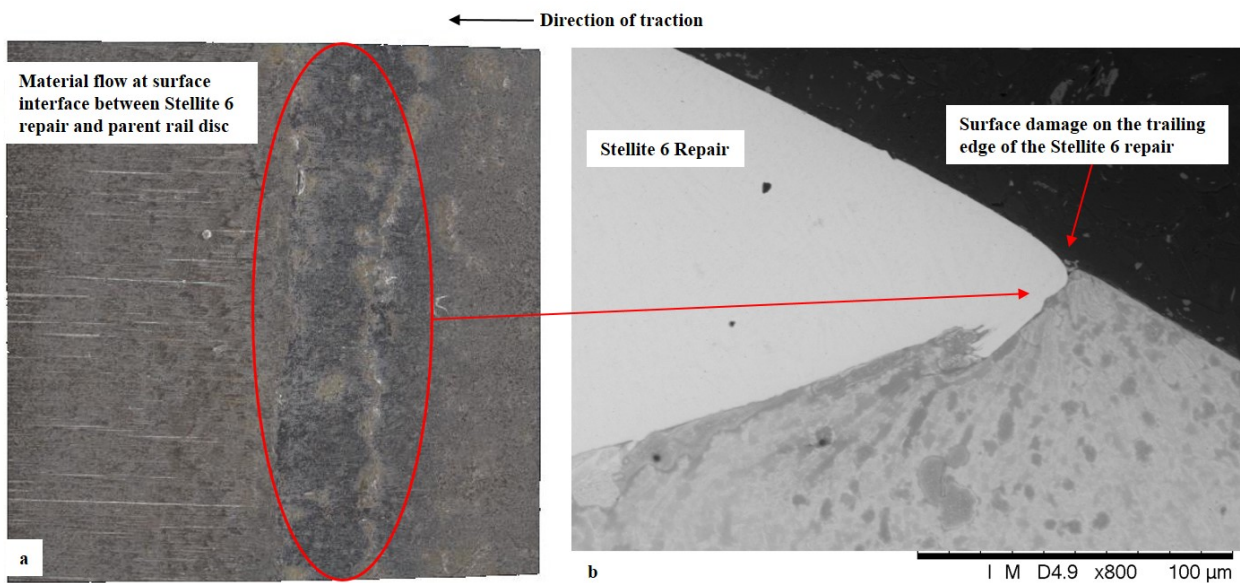
Figure 4.63: Repair 4: Stellite 6 repair trailing edge after RCF testing of 500 dry cycles followed by 5,000 water lubricated cycles. a) Alicona image showing material flow on the surface interface and b) SEM image showing crack initiation at the surface on the repair interface.
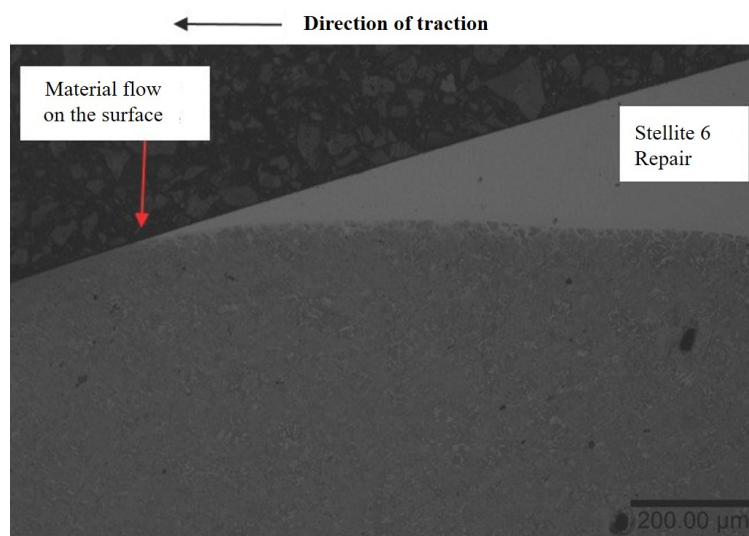
Figure 4.64: Repair 4: Stellite 6 repair leading edge material flow on the surface.

Surface damage at the trailing edge of the repair interface of repair 6 after RCF test 1 can be seen in Figure 4.65a. The SEM image in Figure 4.65b shows subsurface material deformation with material loss shown within the parent R260 rail steel at the interface of the repair.
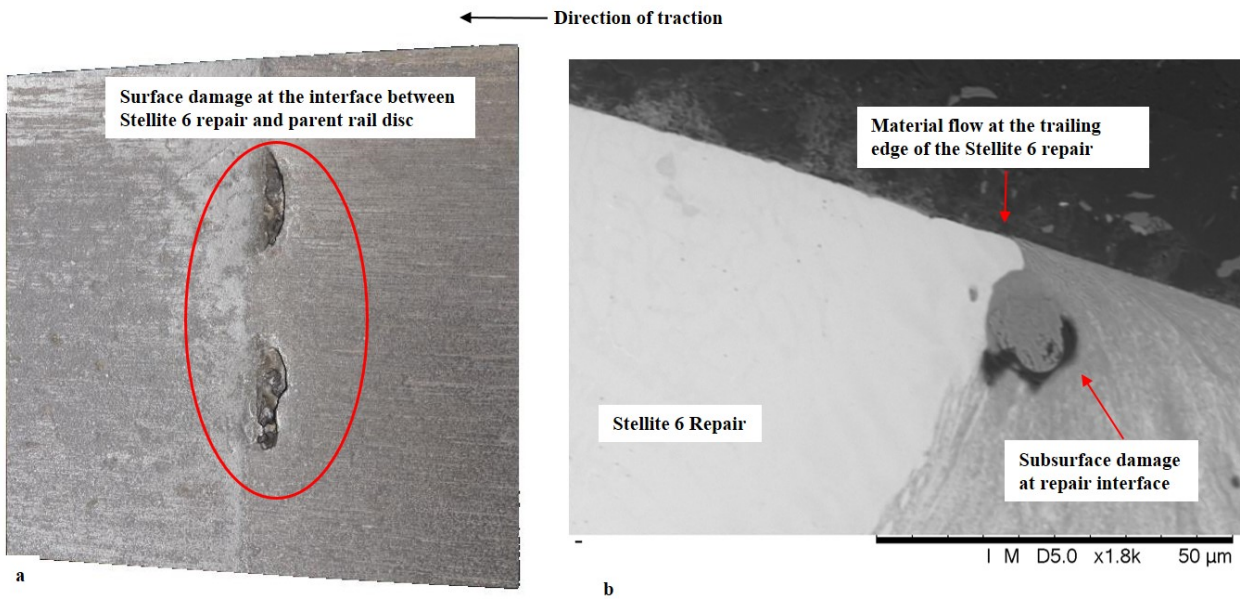
Figure 4.65: Repair 6: Stellite 6 repair trailing edge after RCF testing of 500 dry cycles followed by 5,000 water lubricated cycles. a) Alicona image showing material loss on the surface interface and b) SEM image showing subsurface material deformation within the parent rail on the repair interface.

The leading edge of repair 6 after RCF test 1 is shown in Figure 4.66, the interface is seen to be intact with no material flow or RCF evident.
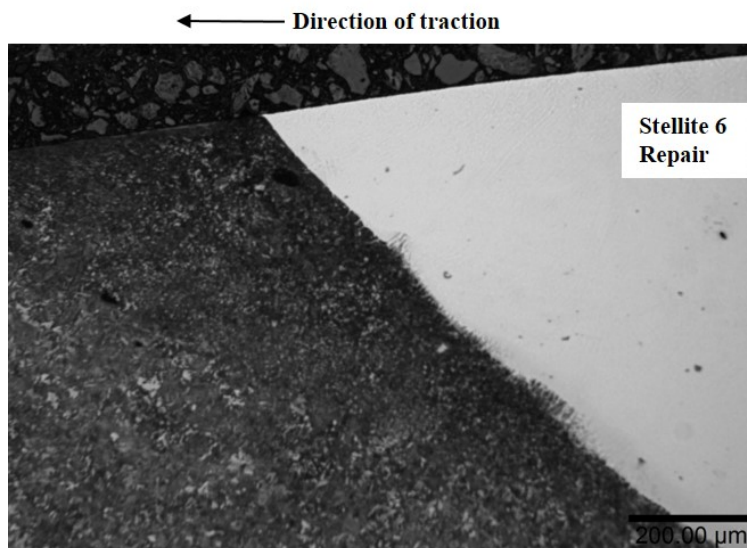
Figure 4.66: Optical micrograph of repair 6 leading edge after RCF testing of 500 dry cycles followed by 5,000 water lubricated cycles showing no sign of RCF or material flow.

RCF test 2: 500 dry cycles and 15,000 water lubricated cycles

Following RCF test 2 which ran for 500 dry cycles and 15,000 water lubricated cycles the surface and subsurface of the Stellite 6 repairs was examined. The surface of the trailing edge of repair 4 can be seen in 4.67a with less material flow than in the shorter RCF test. The subsurface image in Figure 4.67b shows porosity at the surface of the repair, however cracks are not seen to propagate from these. The repair interface is intact on the trailing edge with no signs of material flow or RCF. The surface image of the leading edge of repair 4 is shown in Figure 4.68a with a substantial fragment of material loss from the Stellite 6 repair measuring 513 μm wide and 269 μm deep.
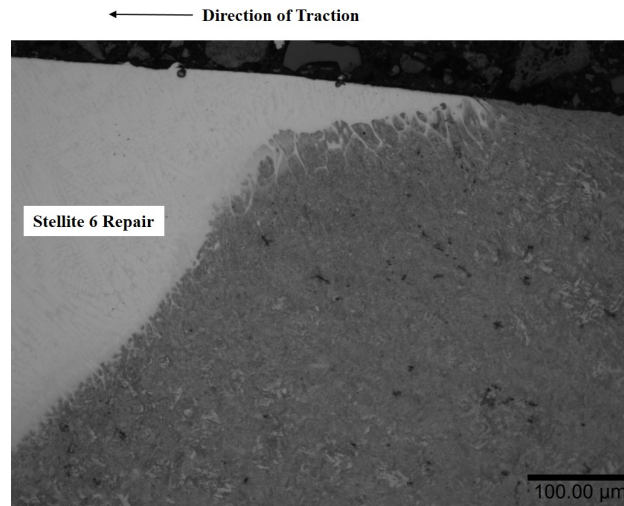
Figure 4.67: Repair 4: Stellite 6 repair trailing edge after RCF testing of 500 dry cycles followed by 15,000 water lubricated cycles. a) Alicona image showing some material flow on the surface interface and b) optical micrograph showing porosity seen on the surface of the repair.
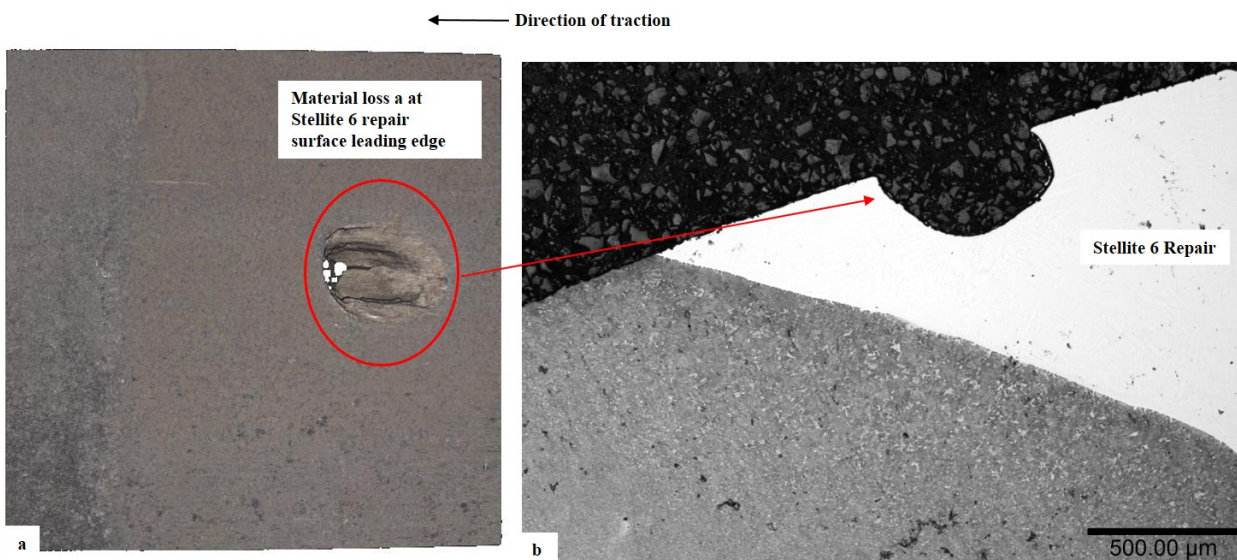
Figure 4.68: Repair 4: Stellite 6 repair leading edge after RCF testing of 500 dry cycles followed by 15,000 water lubricated cycles. a) Alicona image showing substantial material loss on the surface of the repair and b) optical micrograph of the cross section of cavity at the surface of the repair.

The micrograph in Figure 4.68b shows the cross section of the cavity on the surface of the repair. Following evidence of porosity on the trailing edge of repair 4 in Figure 4.67b, it is considered that the cavity could have been caused by an imperfection in the clad caused by process parameters not being optimal in additively manufacturing the repair. Despite this visible loss of material it is observed that the material has tolerated this defect well, with no RCF cracks propagating from this. The Alicona image of the surface of the trailing edge of Repair 6 is shown in Figure 4.69a with an area of surface damage within the Stellite 6 repair and material deformation at the interface measuring 272 μm deep and 63 μm wide. The micrograph in Figure 4.69b shows a large subsurface cavity at the interface where the Stellite 6 repair is no longer bonded to the R260 parent rail. The leading edge of repair 6 is shown in Figure 4.70 with a small amount of material flow at the surface but no signs of RCF at the interface.
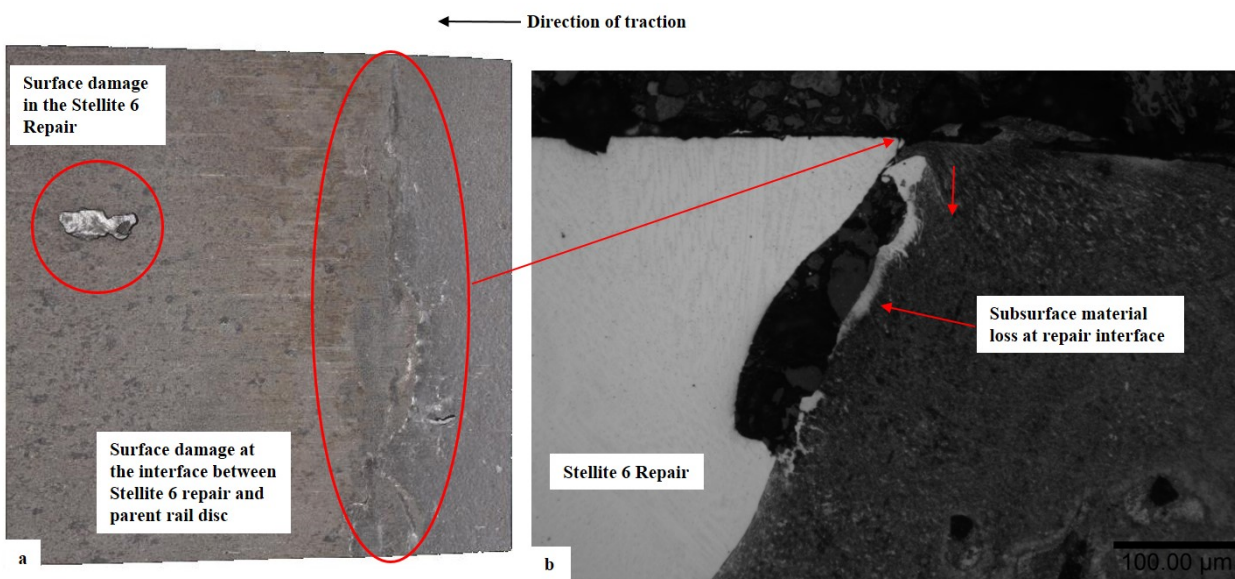
Figure 4.69: Repair 6: Stellite 6 repair trailing edge after RCF testing of 500 dry cycles followed by 15,000 water lubricated cycles. a) Alicona image showing surface damage and material deformation at the interface and b) optical micrograph of the cross section showing subsurface cavity at the interface where the repair is no longer bonded to the parent rail.
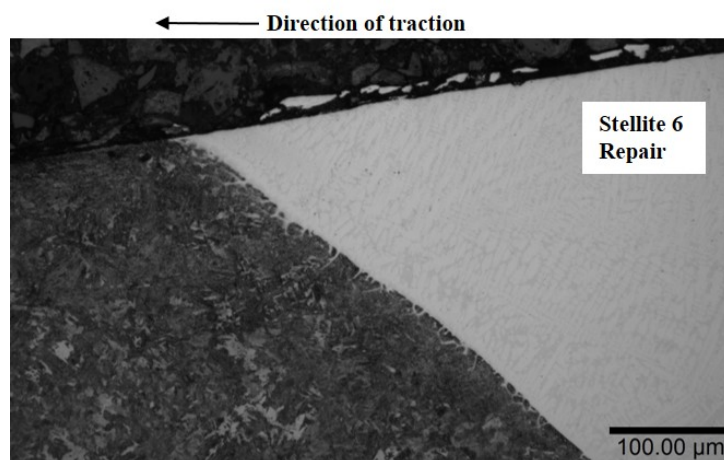
Figure 4.70: Optical micrograph of repair 6 leading edge after RCF testing of 500 dry cycles followed by 15,000 water lubricated cycles showing small amount of material flow at the surface.

4.6 Discussion

The three candidate materials tested here for the purpose of in-situ laser clad repairs had varying success. Laser clad coatings on rail steels have previously been applied to a length or section of rail in a block application, this was the first time that the laser clad coating had been applied in a small channel as a repair. The process parameters used mirrored those which had been successful in the larger applications. As a result of this some characteristics observed in early non-optimal laser clad applications were apparent. The R260 repair had a large heat affected zone and evidence of martensite within the repair, the hardness of the clad R260 was also much higher than standard R260 grade steel. All of which are likely to have been as a result of the pre-heat and duration of cooling which is likely to have been faster in a reduced area. The same extent of heat affected zone was observed by Seo et al. [142] in partial clad specimens.

Inclusions or porosity were identified in some of the MSS and Stellite 6 repairs, which is assumed to be caused by the feed rate or head speed of the laser cladding process or the geometry of the repair channel. When sectioned the medium depth MSS repair site (repair 3) had evidence of inclusions observed in the sample subjected to the unlubricated test and the sample subjected to the longer RCF test, resulting in material spalling from the surface. The two shallow MSS repairs had no signs of porosity or inclusions, suggesting that the laser process parameters were optimal for a cladding closer to the surface.

Both of the Stellite 6 repair sites had inclusions or porosity. After sectioning it was observed that the deep Stellite 6 repair (repair 4) had a large surface cavity and porosity within the repair following the longer RCF test. The medium Stellite 6 repair (repair 6) was seen to have inclusions in the untested repair sample. Following the short RCF test repair 6 was seen to be moving away from the parent rail at the trailing edge and a cavity was seen to be forming at the interface. After the longer RCF test repair 6 had moved away from the parent rail interface and a large subsurface cavity had formed. Inclusions from non-optimal process parameters are assumed to be responsible for this subsurface weakness at the interface. Where inclusions are present the repair materials tolerated these defects well, with no RCF cracks propagating from them.

The interface between repair site and parent rail at the trailing edge was the most vulnerable part of the repairs as seen with areas of white etching layer (WEL) [93]. Hiensch et al. [49] found that stop/start section of laser cladding with a coating of different material properties to the substrate caused joins susceptible to crack initiation. The R260 repair had fewest defects at this interface, with the exception of the short RCF test which saw a substantial network of cracks develop. As the R260 repair did not develop any RCF cracks in the longer RCF test further testing is required to understand the level of crack resistance in this type of repair. RCF cracks were seen at the trailing edge repair interface in MSS repair 2 after the short RCF test and a network of cracks after the longer RCF test, repair 3 after both RCF tests and repair 5 after the long RCF test. RCF cracks were also seen in the Stellite 6 repairs, repair 6 had an RCF crack after the unlubricated test and repair 4 after the shorter RCF test 1. The cracks on the trailing edge of the Stellite 6 and MSS repairs which are significantly harder than the parent rail are representative of the cracks seen around sites of WEL which is also an area which can have hardness of up to three times higher

than the substrate rail [90, 91, 93, 106, 157].

From observing the surface roughness measurements it appeared that the R260 had the most surface modification through the formation of flakes and delamination. This would be expected in comparison with the harder MSS and Stellite 6 laser clad materials as demonstrated from the research on wear rates of laser clad coatings conducted by Lewis et al. [1]. The MSS had the least change in surface roughness of all the materials according to the surface roughness measurements which once again fits with the wear rates found by Lewis et al. [1].

Plastic shear strain was observed in and below some of the repairs. The R260 repair experienced material flow in the repair, heat affected zone and parent rail as would be expected with the homogeneous material. The material selection for non-continuous laser clad coating applications is seen to be important to the integrity of the repair. The clad material must be perfectly compatible in terms of not only ratcheting rate, but also Young's modulus, Poisson's ratio and thermal properties. For a repair this is more important than the extra wear resistant properties, which would actually have a negative effect as the surrounding parent rail wears faster.

The thin MSS repairs (repair 2 and 5) and the thin gradient of the deep Stellite 6 repair (repair 4) where it meets the surface all experienced elongation of the repair material along the surface and ratcheting in the heat affected zone below the repair sites. This characteristic echoes that seen in the test in Chapter 3 in which a thin layer of MSS was laser clad to the R260 substrate rail and shear strain was accumulated in the heat affected zone. This emphasises the importance of coating or repair depth to ensure the peak stresses occur within the coating. The thin gradient to surface in the deep repair causing a lip of thin laser clad coating is therefore not an optimal design. This is an important result to support the future use of non-continuous laser clad coating application.

The test design provided a good method to get an overview of how a range of laser clad coatings would work as in-situ repairs. It was however limited as a true wear rate cannot be deduced with the 6 different repair sites around the disc circumference. The potential dynamic loading as the repair materials behave differently in testing is also limiting and it is suspected that this dynamic loading was responsible for the surface damage of MSS repair 5 after the short RCF test.

4.7   Conclusion

A series of tests have been designed and conducted to evaluate the integrity, surface evolution and RCF resistance for in-situ laser clad repairs with three candidate materials. The tests were run as standard twin-disc tests with the rail discs being manufactured with 6 repairs around the disc surface. Laser clad coatings applied as an in-situ rail repair is a novel application and this is the first time a small repair has been manufactured and tested under cyclic loading. Laser clad coating process parameters have previously been optimised for larger sections of rail rather than small repair sites. The majority of repairs were clad to a good standard, there were a few that had inclusion or porosity although the repairs tolerated these well. To take the method forward the process parameters including the control of pre heating and cooling must be optimised to avoid

the formation of martensite or porosity within the repair and surrounding rail material.

Dry tests were run to evaluate the surface evolution of the repairs with surface roughness measurements and images utilised to analyse the surface evolution as the conventional method to measure wear rate through change in mass was not applicable due to the different repair materials. It can be concluded that the R260 clad repair had a greater level of surface modification than the harder clad materials, however this appeared comparable to standard R260 grade rail steel. The results of this chapter indicate that the geometry of the repairs should be carefully designed to avoid a thin lip towards the surface.

Water lubricated RCF tests were conducted on the repair disc to evaluate crack growth in and around the repair site. It was shown that eddy current crack detector was not suitable for detecting cracks on the repair discs due to the repair interface giving false readings which came from the interface between the repairs and parent rail. RCF cracks were found to most commonly occur on the trailing edge. During the tests the repair material was swept in the direction of traction, driven by the material flow of the parent rail. In many cases where a harder MSS or Stellite 6 repair was present the R260 grade parent rail swept over the repair site on the surface at the interface. It was below this overlap of material that RCF cracks were most regularly found.

For the purpose of a repair the laser clad coating material that appears to be the most favourable is the R260 clad. Being a homogeneous material with the parent rail it has a comparable rate of plastic shear strain accumulation and is therefore less vulnerable to crack initiation points forming at the trailing edge were the parent rail may otherwise flow over the repair. Following the observation of the shallow repairs experiencing ratcheting within the heat affected zone and the subsequent elongation of laser clad repair along the surface, it is concluded that the depth of laser clad coating is important in its success. The following chapter develops a method to better understand and quantify plastic flow within R260 grade rail steel and MSS laser clad coating, which influences the design of the morphology of the repairs and enhancements with laser clad coatings.

Chapter 5

The effect of surface roughness on shallow depth plasticity in laser clad coated rail steels

5.1 Introduction

The resistance to plasticity that laser clad coatings provide is an attractive benefit to applying them to extend the life of railway track components. Plastic shear strain accumulation within the shallow depths of the R260 rail and laser clad coatings was, however, observed in the experimental work in Chapter 3 and Chapter 4. The plastic shakedown limit is the limit of stress above which ratcheting occurs. The laser clad coatings and the R260 rail steel have relatively high yield stress compared with conventional rail material resulting in the plastic shakedown limit being greater than the assumed maximum Hertz contact pressure applied in experiments in this study. It is discussed within the literature review that roughness may explain the depth and magnitude of shallow surface strain accumulation which does develop and is therefore explored in this chapter. It is assumed within Hertz contact theory that the contact is smooth, but in reality no surface is truly tribologically smooth, on a microscopic scale there is a degree of roughness. The asperities on the surfaces of the rail and wheel come into contact which causes the pressure profile to have localised peaks and can cause surface plasticity despite the bulk contact pressure being lower than the shakedown limit. Asperities in a rough surface will create a lower real area of contact and hence higher contact stresses. Methods to both measure and model roughness in contact exist as seen in the literature review in Chapter 2 with differing theories applied.

The complicated nature of rail wheel contact and the potential presence of third body particles from the open tribological system, such as rain, dirt or wear debris, means that characterising the exact surface profile of rail is not feasible or beneficial. A method is developed here in which the simplistic smooth contact model is used with an additional surface contact pressure amplification. This amplification is estimated by calculating the maximum Hertzian contact stress from one high asperity and is used to quantify and understand the magnitude of stresses produced within the shallow surface depths.

A series of surface roughness measurements were taken using the optical (non-contact) Alicona PortableRL Infinite Focus microscope as described in Chapter 4. The surface roughness of R260 grade rail steel, MSS laser clad coating and the R8 wheel was measured before and after twin-disc testing. To estimate the effect of roughness in this investigation a method is developed incorporating a 3-point peak criterion [39, 46] where a peak is considered to be higher than its two closest neighbouring points. The asperities are only considered in the analysis where they appear over the mean line as it is these highest peaks which will be in contact with the opposing surface [38]. From the measurements recorded data samples are extracted to allow analysis of the asperity tip

radius and wavelength. The wavelength λ is approximated by evaluating the number of peaks above the mean line in a sample of length 250 μm and finding the average distance between peaks. The asperity tip radius ρ is calculated as the radius of the circle which passes through the asperity peak and its two closest points as illustrated in Figure 5.1.
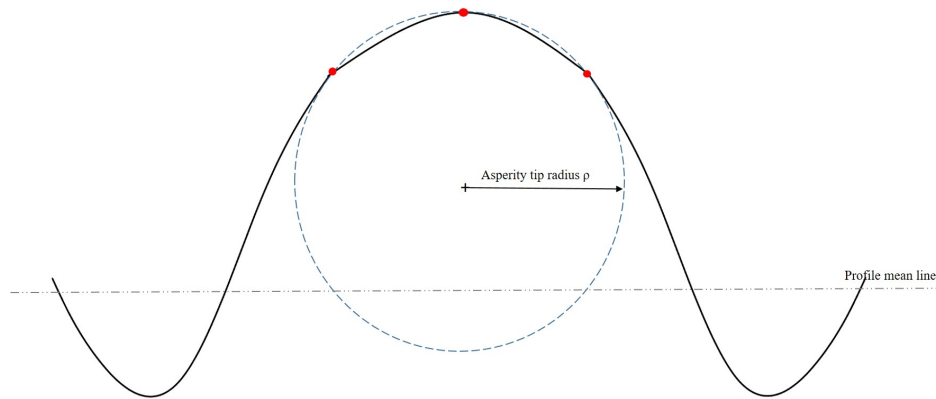
Figure 5.1: Schematic of three point peak asperity tip radius measurement technique.

A method to model the rough contact is then developed inspired by Nowell and Hills [34] which considers each asperity contact to be an individual Hertzian contact which are then superpositioned across the full contact area. This modelling provides the asperity contact half width, maximum contact pressure and the interior stresses beneath the contact, this generated data is developed for application in quantifying plasticity within laser clad rail in Chapter 6.

5.2   Surface roughness Measurements

The R260 grade rail steel and MSS laser clad coating surface roughness measurements are presented in this section taken before and after testing using the Alicona. The profile roughness measurements provided are for Ra, the average roughness of the profile, which is measured around the circumference of the rail disc. The data is further extracted to allow analysis of roughness samples to enable the approximation of the wavelength and asperity tip radius. R260 grade steel rail disc samples and MSS laser clad coated rail disc samples were observed after a series of tests of different lengths to measure the surface roughness evolution. All tests were run in unlubricated twin-disc testing at maximum contact pressure of 1500 MPa with -1% slip. The surface profile measurements of R260 grade rail discs were taken prior to testing, after 2,500 cycles, 5,000 cycles, 7,500 cycles, 10,000 cycles, 20,000 cycles and 30,000 cycles. The surface profile measurements of the MSS laser clad coated rail taken prior to testing, after 2,500 cycles, 5,000 cycles, 7,500 cycles, 10,000 cycles and 30,000 cycles. The values of the surface roughness measurements for the R260 and MSS can be seen in Appendix C.

5.2.1 R260 grade rail steel surface roughness measurements

The evolution of surface profile for the R260 grade rail steel can be seen in the plots in Figure 5.2. Figure 5.3 presents the change in average Ra after each test length which shows a higher Ra value when new as would be expected from manufacturing, the Ra value then fluctuates as wear occurs.
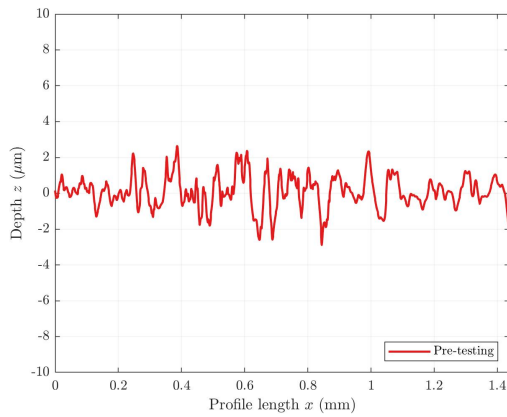
(a) R260 surface profile pre-testing.
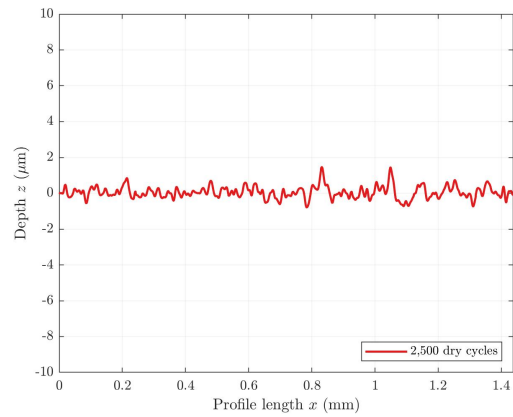
(b) R260 surface profile after 2,500 cycles.
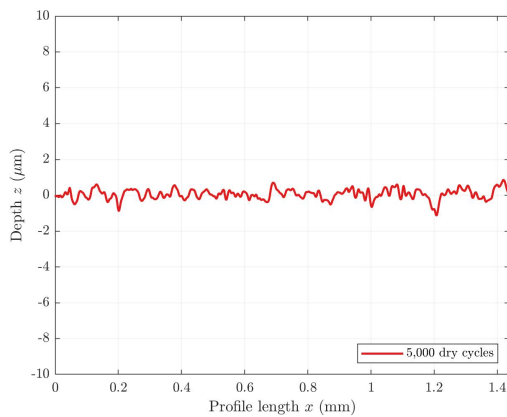
(c) R260 surface after 5,000 cycles.
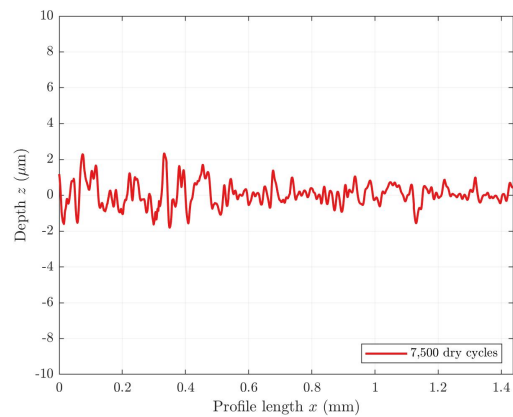
(d) R260 surface profile after 7,500 cycles.
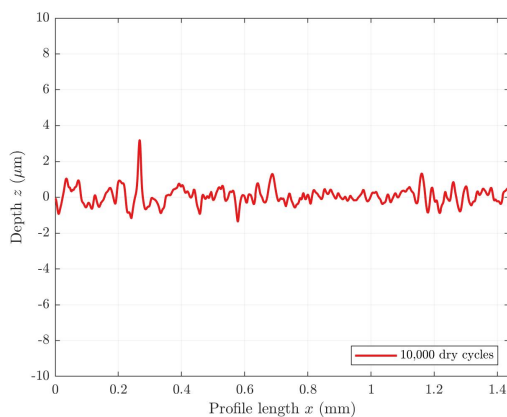
(e) R260 surface profile after 10,000 cycles.
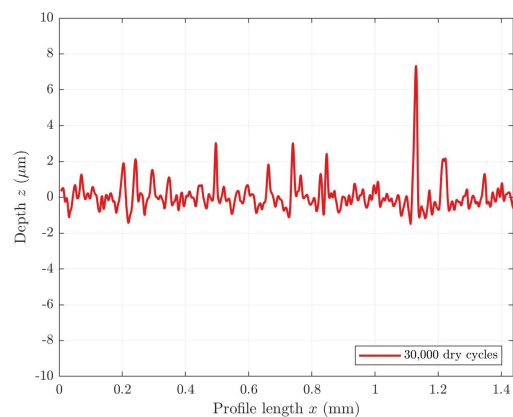
(f) R260 surface profile after 30,000 cycles.

Figure 5.2: R260:Evolution of surface wear measured around the circumference of the disc. Surface height data Ra in R260 grade rail steel taken prior to testing and after dry wear test (1500 MPa, -1% slip) from 2,500 to 30,000 cycles.
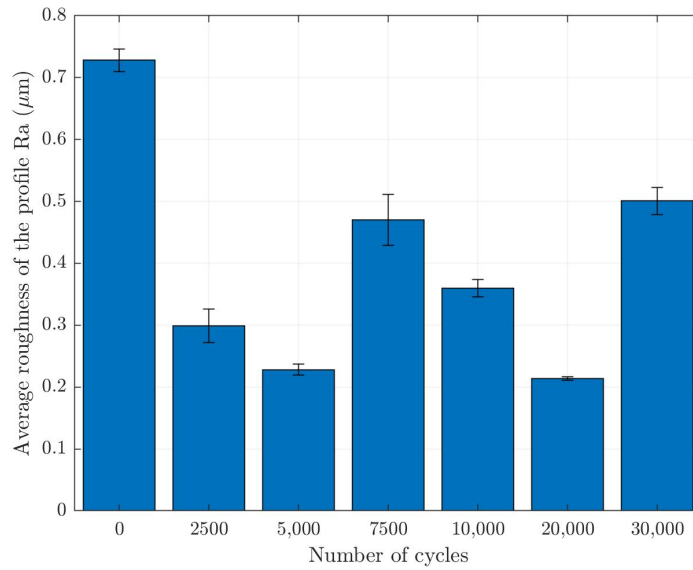
Figure 5.3: R260 surface height data, Ra. Showing the roughness reducing to a lower, but slightly variable, level after the initial manufactured state.

5.2.2 MSS laser clad coating surface roughness measurements

The MSS laser clad coating was monitored for surface changes in the same way as the R260. The evolution of surface profile can be seen in the plots in Figure 5.5 with a high peak after 5,000 cycles which is assumed to be an anomaly in measuring or a dirt particle on the disc. The plot of average Ra is shown in Figure 5.4 indicating a more consistent roughness after the initial manufactured state compared with the R260 grade rail steel.
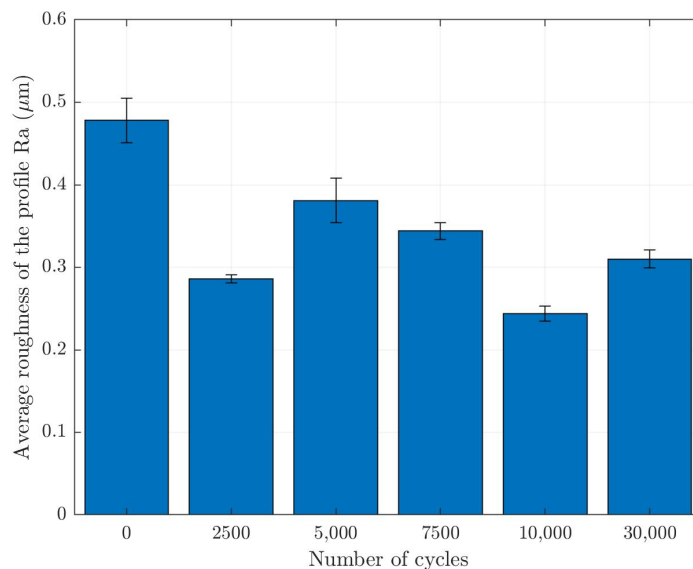
Figure 5.4: MSS laser clad coating surface height data, Ra. Showing the roughness reducing to a lower, but slightly variable, level after the initial manufactured state. Less change from the manufactured state is observed for the MSS laser clad coating compared with the R260 grade steel.
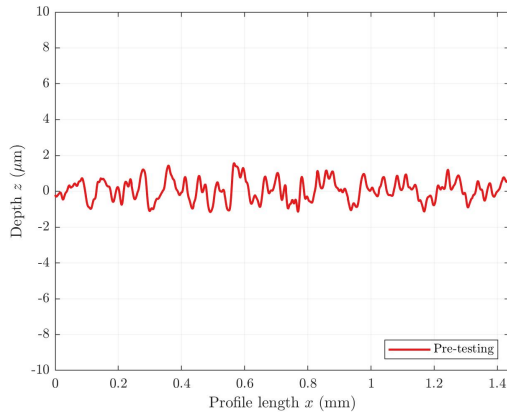
(a) MSS surface profile pre-testing.
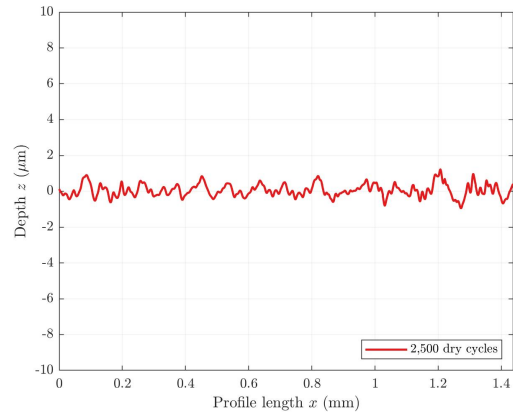
(b) MSS surface profile after 2,500 cycles.
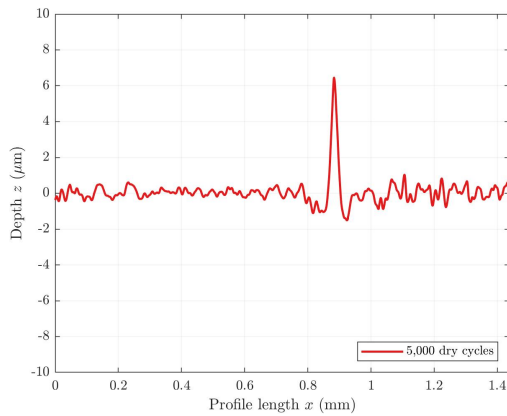
(c) MSS surface after 5,000 cycles.
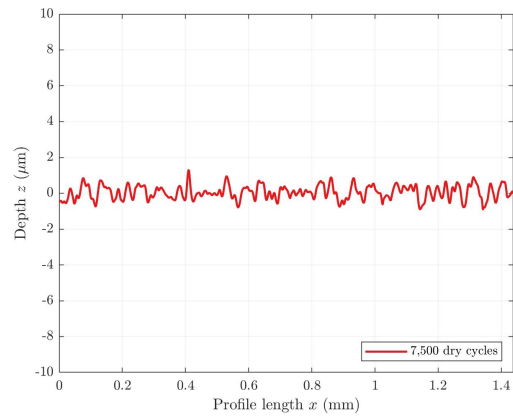
(d) MSS surface profile after 7,500 cycles.
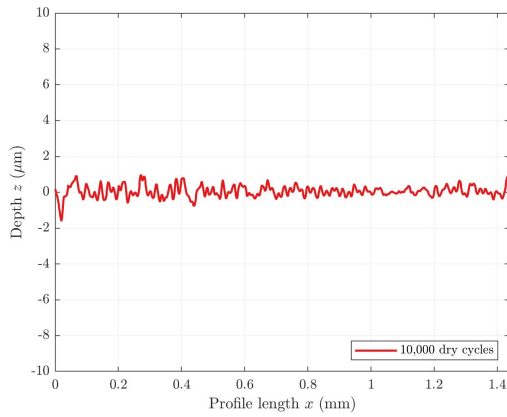
(e) MSS surface profile after 10,000 cycles.
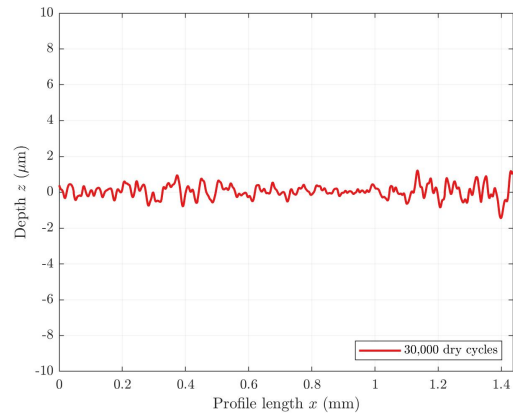
(f) MSS surface profile after 30,000 cycles.

Figure 5.5: MSS: Evolution of surface wear measured around the circumference of the disc. Surface height data Ra in R260 grade rail steel taken prior to testing and after dry wear test (1500 MPa, -1% slip) from 2,500 to 30,000 cycles.

5.3 Estimating asperity tip radius and wavelength

Following the observations and measurements of surface roughness in Section 5.2 a method to approximate the asperity tip radius and wavelength is developed here to enable the subsurface stress field to be modelled according to the surface roughness. The profile roughness data is extracted from the Alicona and a 250 μm sample length is analysed. The images show a 250 μm length sample of the two materials. The series of highlighted asperities show an example of the peaks from which three data points were extracted to calculate the tip radius using Equation 5.1.

$$x^2 + y^2 + Ax + By + C = 0 \tag{5.1}$$

This was solved simultaneously for A, B, C given the three points (x_i, z_i), (x_{i+1}, z_{i+1}), (x_{i-1}, z_{i-1}) as shown in Figure 5.1. The results of A, B, C were then substituted back into Equation 5.1 and transformed into standard form, Equation 5.2, where (h, k) is the coordinate of the centre of the circle with the resulting radius r being the required asperity tip radius ρ.

$$(x - h)^2 + (y - k)^2 = r^2 \tag{5.2}$$

The wavelength as illustrated in Figure 5.6 is approximated over the sample length by dividing the sample length by the number of asperity peaks in the sample. Three approaches were considered for analysing the asperity peaks. The first was to count all peaks above the mean line λ_A, the second was to count peaks with a height greater than 0.1 μm above the mean line λ_B and the final approach is to count asperities with a height greater than 0.25 μm above the mean line λ_C. The effect this has on the wavelength is shown in Table 5.1 for the R260 surface and Table 5.2 for the MSS surface.
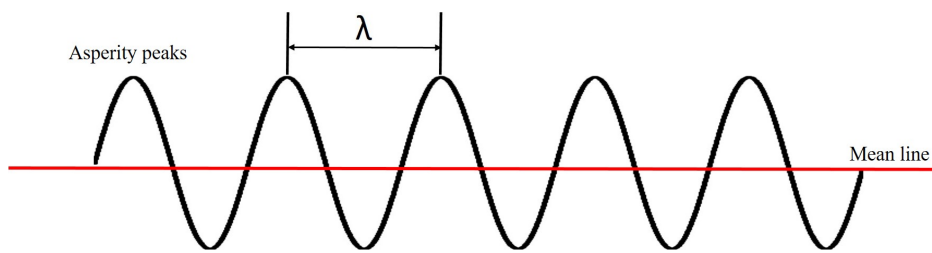
Figure 5.6: Sketch to demonstrate wavelength between asperity peaks above mean line.

Figure 5.7 shows examples of 250 μm length samples of the R260 sample from which the peaks were analysed for asperity tip radius and wavelength. A full series of samples were analysed to evaluate the roughness after testing of successive cycle lengths. Figure 5.8 shows the equivalent data for the MSS laser clad coating. Prior to analysing the results it can be visually observed that the MSS roughness has a longer wavelength with less peaks above the mean line in the sample and they would appear to be generally wider than those seen on the R260 surface indicating a greater asperity tip radius.
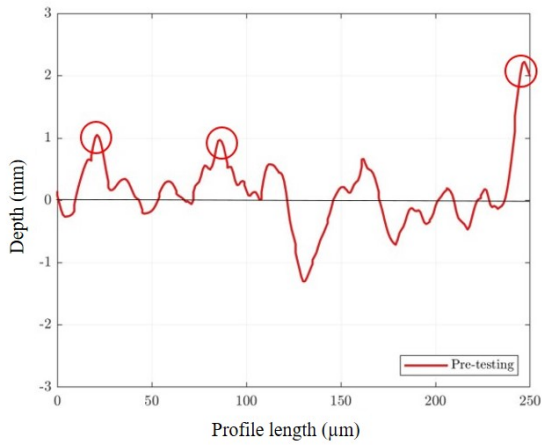
(a) 250 μm sample of R260 prior to testing.
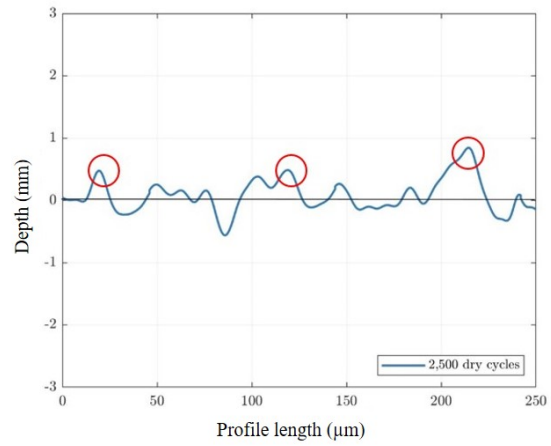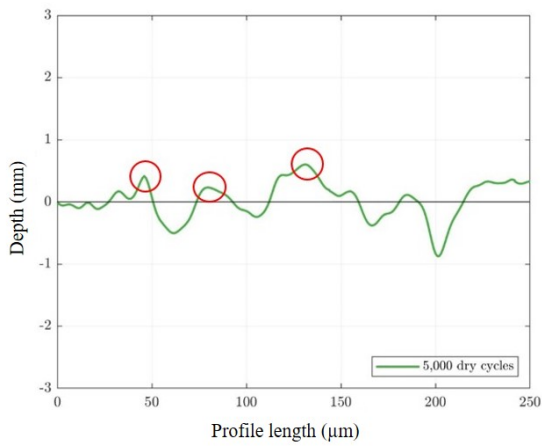
(b) 250 μm sample of R260 after 2,500 cycles.

(c) 250 μm sample of R260 after 5,000 cycles.
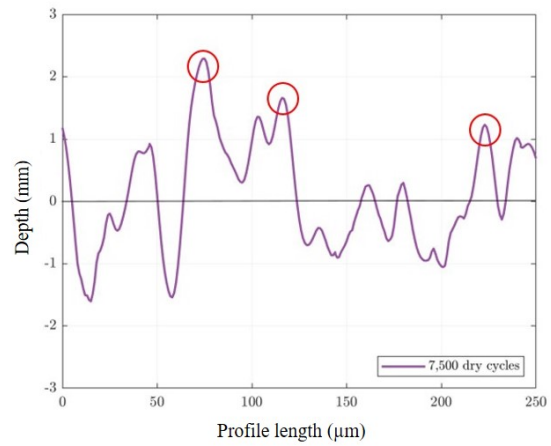
(d) 250 μm sample of R260 after 7,500 cycles.
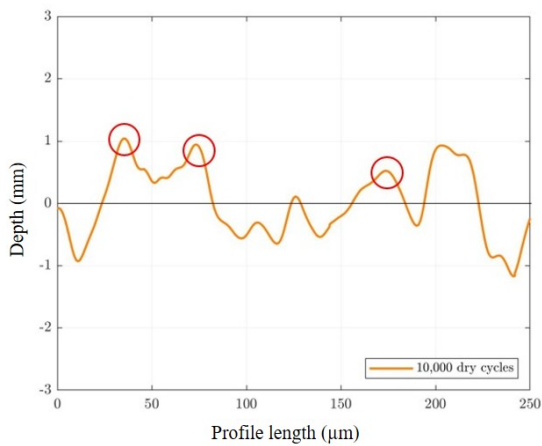
(e) 250 μm sample of R260 after 10,000 cycles.
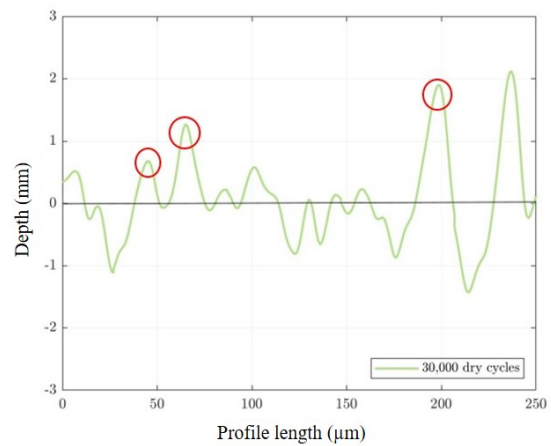
(f) 250 μm sample of R260 after 30,000 cycles.

Figure 5.7: 250 μm sample of the R260 profile roughness measurements prior to testing and after dry wear test (1500 MPa, -1% slip) from 2,500 to 30,000 cycles, used to analyse the wavelength and asperity tip radius measurements.
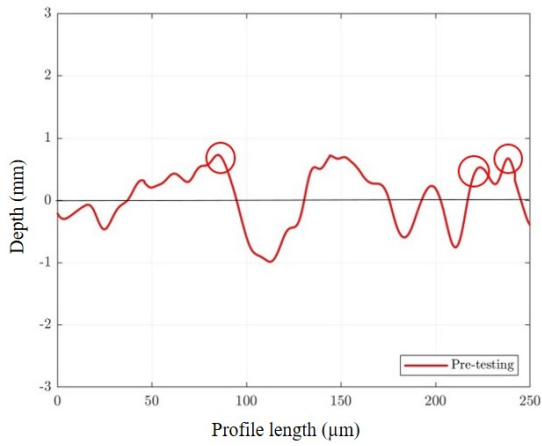
(a) 250 μm sample of R260 prior to testing.
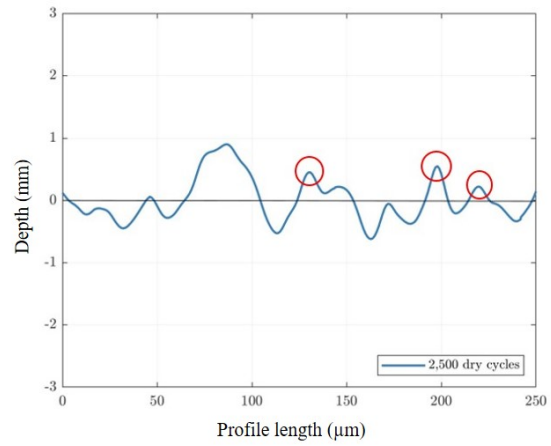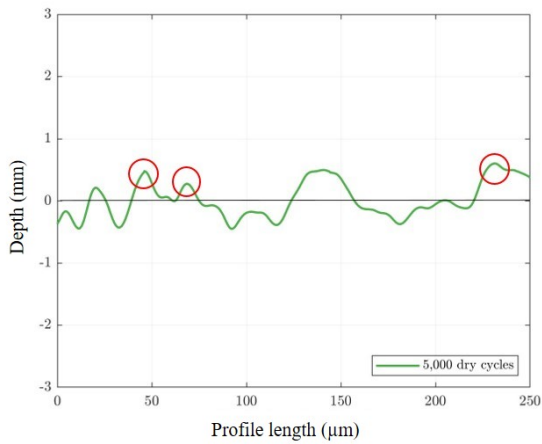
(b) 250 μm sample of R260 after 2,500 cycles.

(c) 250 μm sample of R260 after 5,000 cycles.
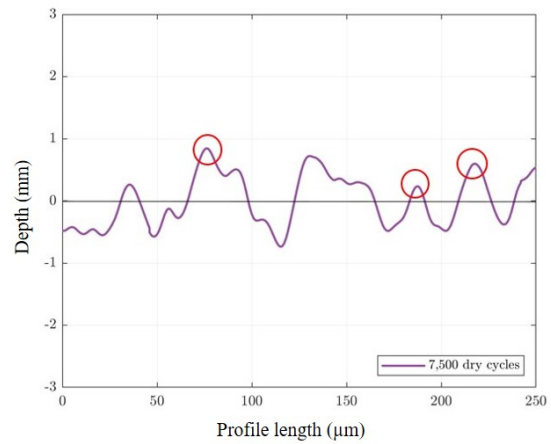
(d) 250 μm sample of R260 after 7,500 cycles.
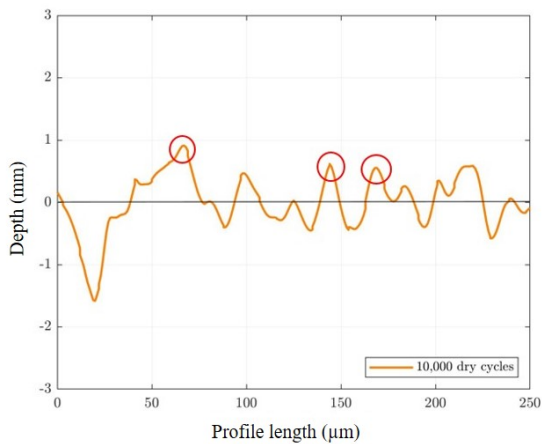
(e) 250 μm sample of R260 after 10,000 cycles.
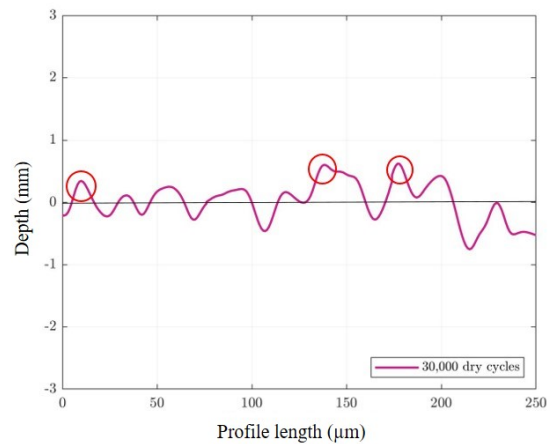
(f) 250 μm sample of R260 after 30,000 cycles.

Figure 5.8: 250 μm sample of the MSS profile roughness measurements prior to testing and after dry wear test (1500 MPa, -1% slip) from 2,500 to 30,000 cycles, used to analyse the wavelength and asperity tip radius measurements.

5.3.1 Asperity tip radius and wavelength results

Using the profile roughness samples in section 5.3 the results are collated and presented here. Table 5.1 shows the average wavelength and asperity tip radius for the R260 rail samples and Table 5.2 shows the same for the MSS laser clad coatings. The results of the three wavelength methods are presented to assess the effect of peak height above the mean line, with λ_A representing all peaks over the mean line, λ_B peaks 0.1 μm over the mean line and λ_C peaks 0.25 μm over the mean line. The difference between these methods varies from sample to sample, with generally less difference seen between λ_B and λ_A. There is less difference in the wavelength methods in the R260 than the MSS as the peaks are generally taller with smaller asperity tip radii across the R260 samples and are more densely spaced resulting in a shorter wavelength. The MSS samples have lower wider peaks with a longer wavelength. The effect of wavelength method sensitivity on asperity contact area and peak pressure is examined further in the following section.

Number of cycles	λ_A (μm)	λ_B (μm)	λ_C (μm)	ρ_{ave} (μm)
0	19.23	19.23	27.78	14.97
2,500	25	27.78	41.67	37.63
5,000	27.78	27.78	50	59.3
7,500	22.72	22.72	22.72	15.67
10,000	25	25	27.78	28.75
20,000	20.83	25	35.71	27.21
30,000	22.72	27.78	41.67	15.38

Table 5.1: R260 wavelength measured using method A, B and C and average tip radius prior to testing and after dry wear test (1500 MPa, -1% slip) from 2,500 to 30,000 cycles.

Number of cycles	λ_A (μm)	λ_B (μm)	λ_C (μm)	ρ_{ave} (μm)
0	22.72	25	27.78	38.18
2,500	41.67	50	83.33	32.35
5,000	41.67	50	62.5	62.28
7,500	31.25	31.25	35.71	32.8
10,000	25	31.25	31.25	24.09
30,000	31.25	31.25	50	33.48

Table 5.2: MSS wavelength measured using method A, B and C and average tip radius prior to testing and after dry wear test (1500 MPa, -1% slip) from 2,500 to 30,000 cycles.

Applying the surface roughness to modelling the peak pressure in the contact and resulting interior stresses the evolution of wavelength and asperity tip radius must be considered. The initial plastic shear strain is expected to occur in the early cycles hence the initial roughness parameters of the material must be applied.

5.4 Hertzian contact modelling for rough surfaces

Surface roughness has been observed with Alicona and the data evaluated to approximate the asperity wavelength and tip radius, this experimental data is now applied within modelling to assess the contact area and pressure. Different approaches to modelling rough contacts are described in Chapter 2.2.2. A method is developed here inspired by the Nowell and Hills method [34, 35] and validated against a boundary element model. It assumes a Hertzian contact at each individual asperity contact. A Hertzian approach is selected as a suitable method due to the contact area being small relative to the overall dimensions.

The Nowell and Hills model uses an iterative method to estimate the asperity contact half width a_n and contact loads P_n across the whole smooth contact area $2b$ consisting of $2N + 1$ asperities. The assumption is made that the mid asperity makes contact centrally at position $x = 0$. The position of the further asperity contacts is calculated as $a_{pos} = 0 \pm n\lambda$ where n is the nth asperity from the centre point of contact. The number of asperity contacts is calculated with the whole contact half width as $N = b/\lambda$. The method assumes one of the bodies in contact is elastic. The initial stage is to calculate an initial estimate of the asperity contact area a_n given the radius of the cylinder R and the asperity tip radius ρ using Equation 5.3:

$$a_n^2 = \frac{4P_n\rho}{\left(\dfrac{1}{\rho} + \dfrac{1}{R}\right)\pi E}(1 - v^2) \tag{5.3}$$

The radius of the cylinder and the radius of the asperity tip radius is a modification of the Nowell and Hills method [34, 35], in which they assumed the cylinder radius was so large relative to the asperity radius that it could be treated as infinite. As the cylinder radius is known and the computational time is not affected this addition helps to improve the model accuracy [158]. A set of equations are then solved sequentially to calculate the total surface displacement due to all $2N + 1$ asperities using Equation 5.4:

$$V(x) = \sum_{n=-N}^{N} (V_n(x) - d) \tag{5.4}$$

The equation for vertical displacement in the paper by Nowell and Hills [34, 35] produces a discontinuity in the surface profile and fails to reach the contacting surface. This is due to an error in a trigonometric identity in a paper by Poritsky et al. [159] as identified in the University of Sheffield report by Fletcher et al. [158]. This correction to the equation eliminates the discontinuity and allows the surfaces to meet. The vertical displacement within its contact patch of an asperity ($|x - \lambda n| \leqslant a_n$) is therefore defined using Equation 5.5:

$$V_n(x) = -\frac{2P_n}{\pi E}(1 - v^2)\left[\frac{(x - \lambda n^2)}{a_n^2} - \ln|Z| - \frac{1}{2Z^2} - \frac{1}{2}\right] \tag{5.5}$$

where X is defined by Equation 5.6.

$$X = \left| \frac{x - \lambda n}{a_n} \right| + \sqrt{\frac{(x - \lambda n)^2}{a_n^2} - 1} \tag{5.6}$$

The displacement of asperity outside of its contact patch ($|x - \lambda n| > a_n$) is defined using Equation 5.7:

$$V_n(x) = -\frac{2P_n}{\pi E}(1 - v^2)\left[\ln|X| + \frac{1}{2X^2} - \ln|Z| - \frac{1}{2Z^2} \right] \tag{5.7}$$

where Z is defined by Equation 5.8.

$$Z = \frac{|\lambda n|}{a_n} + \sqrt{\left(\frac{\lambda n}{a_n}\right)^2 - 1} \tag{5.8}$$

The displacement of the asperities $V(\lambda i)$ must then fit on the full contact surface displacement by substituting in Equation 5.9, for $i = -N, -N+1, \ldots -1$ and $i = 1, 2, \ldots N$. There is no displacement equation for the central asperity as all displacements are found relative to the origin, hence the central asperity pressure can be found through introducing also Equation 5.10:

$$V(\lambda i) = \frac{x^2}{2R} \tag{5.9}$$

$$P = \sum_{n=-N}^{N} P_n \tag{5.10}$$

The new values of P_n are substituted back into Equation 5.3 and the process is repeated until the values of P_n and a_n converge.

5.5 Contact area and maximum contact pressure

The model which was redeveloped in Maple software was used here to estimate the asperity contact width and pressure for the combinations of asperity tip radius ρ and wavelength λ_A in section 5.3.1. The initial simulations using the model are presented in this section using parameters representative of twin-disc testing to allow comparison with experimental results. The simulations within the rough surface Hertzian contact model are representative of twin-disc testing at 1500 MPa, with load $P = 7140$ N, Poisson's ratio $v = 0.3$, rail disc radius $R = 23.5$ mm, Young's modulus $E = 210$ GPa, the coefficient of traction is assumed as $\mu = 0.4$.

Figure 5.9 presents the model results for the contact half widths a_n and maximum contact pressures P_n at each asperity contact for the R260 rail using the asperity tip radius ρ and wavelength λ pairs given in Table 5.1. Given the evolution of surface roughness during testing and the resulting range of ρ and λ the number of asperity contacts across the whole contact half width b varies very little, with between 11 and 15 asperities in contact. The highest amount being in contact when the

material is new. The resulting asperity contact widths, pressures and normalised pressure for the central asperity contact of the R260 can be seen in Table 5.3 where an average value after testing is presented due to the random variation shown by Ra. The maximum contact pressure at the asperity contacts is between 3.40 and 6.01 times higher than the bulk Hertzian contact.

State	N	a_n (μm)	P_n MPa	P_n/P_0
Manufactured	15	2.19	8430	5.62
Average after testing	12.5	3.42	7012	4.73

Table 5.3: R260 surface roughness results showing the number of asperity contacts in the bulk contact half width, the central asperity half width a_n and asperity maximum Hertzian contact pressure P_n and the normalised asperity load P_n/P_0.

Figure 5.10 shows the model results for a_n and P_n at each asperity contact for the MSS using the radius ρ and wavelength λ pairs given in Table 5.2. There is a narrow range of asperities between 7 and 13, with the largest amount prior to testing.

The resulting asperity contact widths, pressures and normalised pressure for the central asperity contact of the MSS can be seen in Table 5.4. The maximum contact pressure at the asperity contacts is between 3.83 and 5.59 times higher than the bulk Hertzian contact.

State	N	a_n (μm)	P_n MPa	P_n/P_0
Manufactured	13	3.79	5750	3.83
Average after testing	9.2	4.52	7286	4.86

Table 5.4: R260 surface roughness results showing the number of asperity contacts in the bulk contact half width, the central asperity half width a_n and asperity maximum Hertzian contact pressure P_n and the normalised asperity load P_n/P_0.

(a) Maximum Hertzian contact pressure for R260 surface roughness prior to testing.
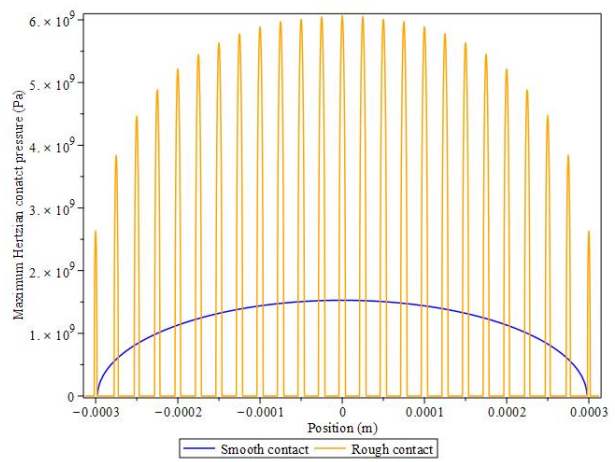
(b) Maximum Hertzian contact pressure for R260 surface roughness after 2,500 cycles.
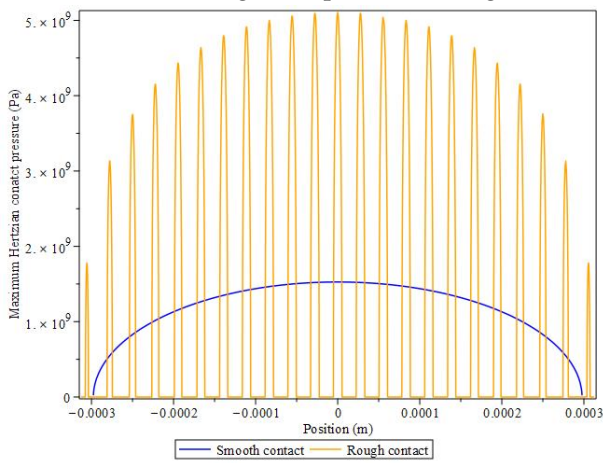
(c) Maximum Hertzian contact pressure for R260 surface roughness after 5,000 cycles.
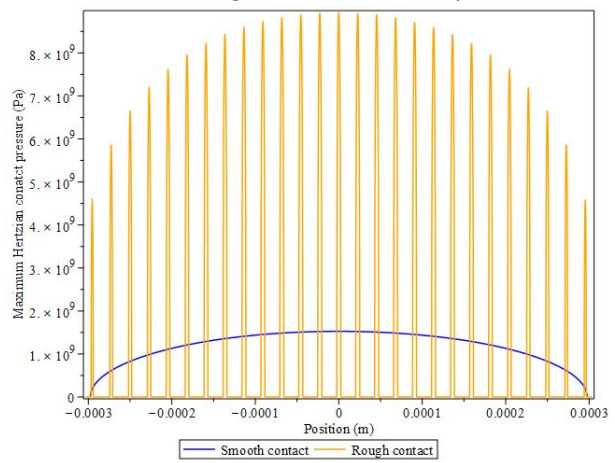
(d) Maximum Hertzian contact pressure for R260 surface roughness after 7,500 cycles.
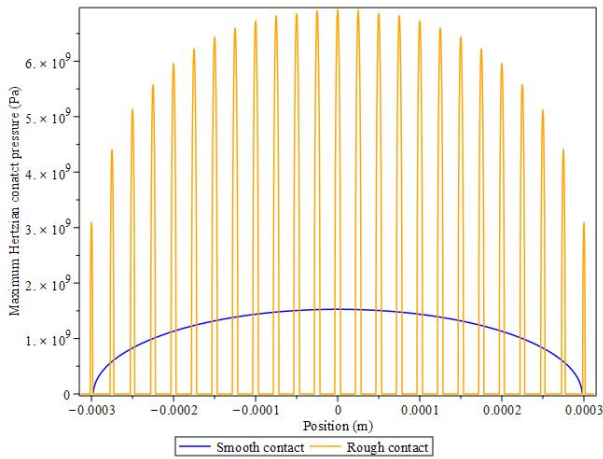
(e) Maximum Hertzian contact pressure for R260 surface roughness after 10,000 cycles.

(f) Maximum Hertzian contact pressure for R260 surface roughness after 30,000 cycles.

Figure 5.9: Maximum Hertzian contact pressures calculated from the wavelength and asperity tip radius measurement for the range of surface roughness's for R260 grade rail steel prior to testing and after dry wear test (1500 MPa, -1% slip) from 2,500 to 30,000 cycles, compared with the maximum Hertzian contact pressure for the smooth bulk contact.

(a) Maximum Hertzian contact pressure for MSS surface roughness prior to testing.
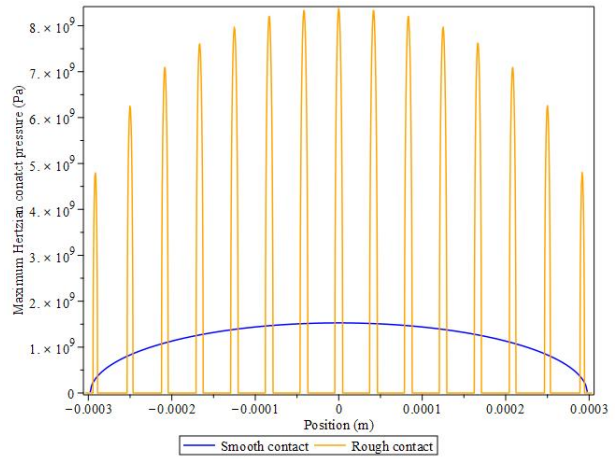
(b) Maximum Hertzian contact pressure for MSS surface roughness after 2,500 cycles.
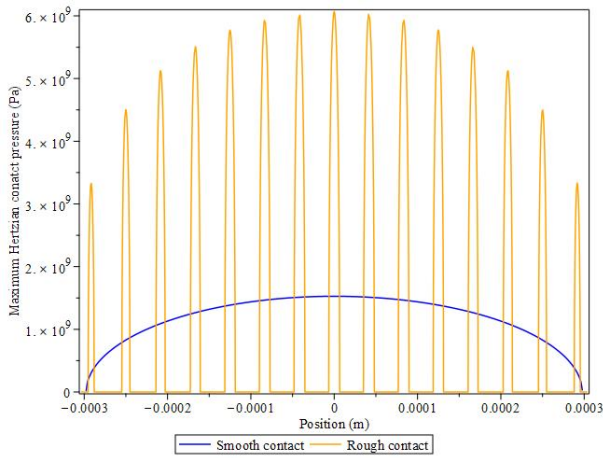
(c) Maximum Hertzian contact pressure for MSS surface roughness after 5,000 cycles.
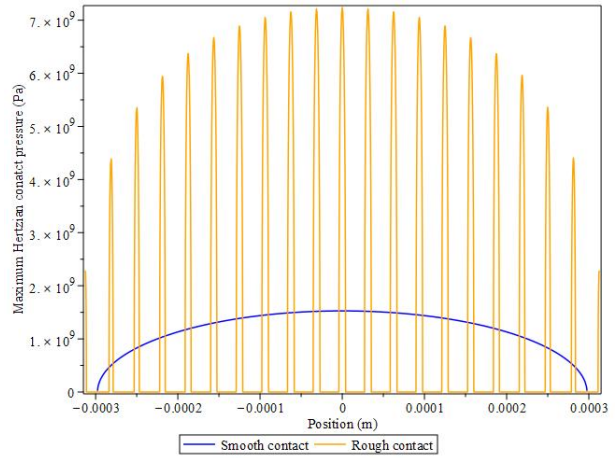
(d) Maximum Hertzian contact pressure for MSS surface roughness after 7,500 cycles.
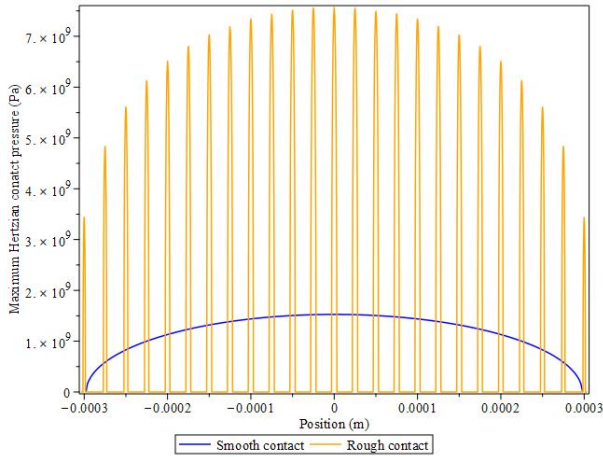
(e) Maximum Hertzian contact pressure for MSS surface roughness after 10,000 cycles.

(f) Maximum Hertzian contact pressure for MSS surface roughness after 30,000 cycles.

Figure 5.10: Maximum Hertzian contact pressures calculated from the wavelength and asperity tip radius measurement for the range of surface roughness's for MSS laser clad coating prior to testing and after dry wear test (1500 MPa, -1% slip) from 2,500 to 30,000 cycles, compared with the maximum Hertzian contact pressure for the smooth bulk contact.

5.6 Rough contact subsurface stress

The absolute maximum subsurface shear stress generated by each of the rough surface contacts was calculated within the Maple model and verified with a boundary element model (BEM) by Fletcher et al. [158]. The range of rough Hertzian contacts is compared with the smooth Hertzian contact to assess the effect this has on the position and magnitude of the sub surface stresses. For a fair comparison all test parameters continue to be set as they were in Section 5.5 with a maximum bulk/smooth contact pressure of $p_0 = 1500$ MPa and CoT $\mu = 0.4$.

To calculate the stresses generated from the rough surface the individual asperity Hertzian contacts are used to calculate the maximum sub surface stress. The depth is normalised by the whole contact half width b and the maximum shear stress is normalised by the maximum Hertzian contact pressure of the bulk contact p_0. The occurrence of the maximum shear stress is much closer to the surface with the rough Hertzian contacts than with the smooth contact.

The peak shear stress in the R260 grade rail steel is between $0.06b$ and $0.08b$ depending on the level of roughness, compared with $0.37b$ for the smooth contact. The magnitude of maximum shear stress is also reduced with the rough contacts compared with the smooth. This corresponds to the results of Nowell and Hills [34] in which they represent the level of stress with a normalised von Mises plot and show that with more asperity contacts the stresses reduce and approach the surface.

The peak shear stress in the MSS laser clad coating is between $0.07b$ and $0.11b$ depending on the level of roughness, compared with $0.37b$ for the smooth contact. The magnitude of maximum shear stress is in the same range as the R260 grade rail steel but marginally lower below the contact surface.

5.7 Discussion

The surface topography of the R260 grade rail steel and MSS laser clad coating are shown to vary in line with wear during testing. The MSS laser clad coating that experiences less wear saw less change in roughness profile measurement Ra than the R260 grade rail steel. A peak occurred in the maximum peak to valley height Rt after 5,000 cycles in the MSS after which it settled to a steady value. The R260 experienced this peak after 30,000 cycles indicating that the surface continues to evolve for longer than the laser clad coating.

The maximum Ra value for both materials is observed in the untested material. This value is lower in the MSS laser clad coating than the R260. It can be assumed that the early maximum shear stresses and resulting strain accumulation will have been influenced most by this initial roughness. The measurements of the R260 grade rail were relatively low in comparison with Lu et al. [2] measurements in which large wear flakes were observed after testing under the same conditions. This is likely to be due to the position on the rail disc in which the Alicona measurements were taken. In these tests the purpose was to assess the general surface roughness. The location was carefully chosen to ensure that the measurements were not affected by large wear flakes on the surface.

The method to measure the surface roughness with the Alicona is an effective way to gather the information for analysis. The main benefit of the Alicona is that it is portable so it has the potential to be used on rail in the field to further extend roughness modelling to other rails. It can be used on a variety of flat or curved components to take rapid measurements meaning it could be used in the field without causing long track closures. A limitation to modelling rough surfaces is that due to the fractal nature of surfaces the accuracy of the results is determined by the resolution of the measurement instrumentation. For the complicated simulation of rail-wheel contact which is an open tribological system with changing levels of friction and potential dynamic loading a good approximation of surface roughness is a beneficial addition to the development of rail-wheel contact modelling. The level of accuracy possible with the focus-variation technology of the Alicona is favourable over older probe based profilometers.

Asperity contact modelling required the wavelength and asperity tip radius to be evaluated for the rough surfaces. The wavelength was assessed considering all peaks above the mean line, peaks over 0.1 μm and peaks over 0.25 μm. The difference in wavelength measurements varied between the methods for each observed surface topography. The largest discrepancy was in the MSS coating after 2,500 cycles. The untested material which is considered as the most important surface roughness had little difference between the three methods. It is therefore decided that including all peaks over the mean line is the favourable method to use for analysis. This is to ensure that all possible asperity contacts are considered.

The asperity tip radius varied during testing as the surface experienced wear. The largest asperity tip radius was observed after 5,000 cycles in both the R260 grade rail steel and the MSS laser clad coating. After this peak the asperity tip radius dropped and after 30,000 cycles had returned to a similar value to the initial untested material. Measurements of surface roughness wavelength and asperity tip radius are sparse within the literature and it is believed to be the first time this analysis has been done for laser clad coatings.

Each asperity was assumed to be an individual Hertzian contact. The asperity tip wavelength and radius were used within an iterative Hertzian asperity contact model based on a method developed by Nowell and Hills [34] to calculate the maximum contact pressure and contact half width for each asperity across the bulk contact. The results of this show the maximum contact pressure at the mid contact asperity to be up to 6 times higher than the assumed bulk contact for R260 and up to 5.6 times higher for the MSS laser clad coating. The Hertzian contact method was selected due to the compatibility with the bulk contact.

The depth of the maximum shear stress was significantly closer to the surface for the rough contact compared with the smooth bulk contact. This supports the experimental findings of shear strain accumulation in the shallow depths seen in Chapters 3 and 4. Considering the untested material, the MSS laser clad coating and R260 grade rail steel had similar maximum shear stress values and depths with the R260 peak being at $0.06b$ and a normalised stress value of 0.34 compared with the MSS peak being at $0.07b$ and a normalised stress value of 0.33 when simulated with a CoT $\mu = 0.4$.

The method to measure the wavelength and asperity may be seen to be subjective as an average

of radii could change based on the chosen peaks and the wavelength can change based on the level of peaks counted. Despite this it can be seen that there is little difference in subsurface shear stress for each of the different surface roughness profiles after each interval of test cycles for either the MSS or R260. This indicates that the methods selected are adequate to achieve an initial analysis of the effect to material response caused by rough surface contact compared with smooth Hertzian contacts. This method could therefore be used to assess the surface topography and asperity contact of other rail materials.

5.8   Conclusion

A study has been conducted to establish the surface topography of R260 grade rail steel and MSS laser clad coatings, the maximum asperity contact pressure and contact half width generated by this and the influence this has on sub surface shear stress. Alicona PortableRL Infinite Focus microscope was used to produce high-resolution images and 3D surface profile measurements which were analysed to estimate the wavelength of asperity peaks and asperity tip radius. These were then used to calculate the maximum Hertzian contact pressure and half width for the asperities across the bulk contact before the sub surface shear stress were calculated for the rough surface contact.

The MSS laser clad coating was shown to be smoother than the R260 grade rail steel, with the untested roughness being $Ra = 0.478\mu$m for the MSS and $Ra = 0.728\mu$m for the R260 grade rail steel. The MSS laser clad coating surface had a longer wavelength between asperity peaks and wider asperity tips resulting in fewer asperities in contact than the R260. The surface roughness of the untested R260 and MSS was predicted to have more asperities in contact than after wear had occurred during testing. The subsurface shear stress experienced in the early cycles highly influences the material response. Considering the minimal difference in depth and magnitude of subsurface stress after the different cycle lengths, it is decided that for analysis the initial surface roughness parameters prior to testing can be assumed.

It was shown that the maximum contact pressure was around 6 times higher than the bulk contact for R260 grade rail steel and around 5.6 times higher in the MSS laser clad coating. The sub surface shear stress was seen to be much closer to the contact surface with the rough contact compared to the bulk contact. This is in agreement with the experimental findings of shear strain accumulation in the shallow depths seen in Chapters 3 and 4. The surface roughness measurements, contact pressure, contact half widths and sub surface shear stresses measured and calculated in this chapter will contribute to the modelling of plasticity within laser clad coatings in Chapter 6.

Chapter 6

Quantifying plasticity in laser clad coatings on rail steels

6.1 Introduction

Following the experimental chapters in which plastic shear strain accumulation was observed in varying magnitudes and depths in the rail steels and to a lesser extent the laser clad coatings, the focus of this chapter is the development of a method to quantify such plasticity. The quantification of ratcheting within rail is a key part of predicting the safety and life cycle within railway track components and informs preventative maintenance planning. Since damage accumulation mechanism appear to be the same but on a lower scale quantifying the micro levels of plastic damage accumulation in clad layers is therefore similarly important. The aim of the work in this chapter is to understand plastic flow resistance of harder materials and the depth of coating required to benefit rail and extend lifespan. The layer model provides a suitable method to quantify plastic shear strain accumulation as the layers can accommodate different material properties found throughout the laser clad rail.

Initial modelling of plasticity within laser clad coatings was conducted using the layer model by Fletcher as part of the European Union's Horizon 2020 Shift2Rail/In2Track project [141]. Estimates of material properties were estimated by a scaled increase of the material response parameters found for BS11 rail by Kapoor et al. [67]. This novel work sees plastic shear strain within low carbon martensitic stainless steel (MSS) alloy with 14.64% chromium modelled for the first time using material properties found through experiments in Chapter 3. It is also the first time that plastic deformation below the interface of a laser clad coated rail has been quantified. The modelling presented here is necessary to inform the design of laser clad coating applications to ensure that the coating depth is sufficient to prevent ratcheting in the substrate rail, which in turn can cause surface elongation of a repair as seen in Chapter 4.

Plastic shear strain accumulation, also referred to as ratcheting, is described in Chapter 2.3.1. High compressive and shear loading on the relatively small contact area of wheel on rail along with a combination of rolling and sliding results in stresses exceeding the rail material's yield point and consequently in plastic strain occurring. Repeated cyclic loading in this manner can result in incremental plastic shear strain accumulation in a process known as ratcheting, leading to large scale plastic deformation within conventional rail steels. The yield point of laser clad coatings is considerably higher than that of conventional rail steels, hence ratcheting is reduced.

Applying an additively manufactured laser clad coating with wear and fatigue resistant properties is a promising method to extend the lifespan of railway track components, however, strain accumulation remains a factor determining the life of the surface. Plastic deformation within the

top 20 μm of laser clad coated martensitic stainless steel (MSS) with 14.64% chromium is shown in the literature [2] and is seen predominantly within these depths in the experiments in Chapter 3, extending to a maximum depth of 56 μm. This shallow depth of material flow is a marked improvement in comparison with the unclad R260 grade rail steel and is in turn expected to reduce crack initiation sites at the surface of the rail. Despite the visually observed reduction in material flow this is not yet well defined for laser clad coatings on rail steels.

The layer model developed by Kapoor et al. [67] was reimplemented by one of the original authors David Fletcher in 2018 [141] in the open source database PostgreSQL [160] with a script written in the open source general purpose scripting language PHP [161], used to run the simulations . Using a database system improves the efficiency of the model as the large amount of generated data can be easily stored. This reimplementation of the model retained the material properties of the BS11 rail steel on which the original layer model was developed. New and novel rail materials such as the R260 rail steel and laser clad coatings have much higher shear yield strengths than BS11 and further developments to the layer model are presented throughout this chapter to make the model relevant to modern day rail materials. Modelling methods which predict ratcheting within the bulk rail are not able to predict the shallow surface ratcheting in the coatings therefore a new method is developed here to account for surface plasticity.

6.2 Plasticity modelling methodology

The literature review in Chapter 2 showed that modelling plasticity with a numerical method, the "layer model", is an effective way to simulate tens of thousands of ratcheting cycles and calculate the corresponding strain accumulation in a short amount of time. The layer model is a validated method to model plastic strain accumulation within standard grade rail steel and is a numerical method. The model is based on the assumption of a semi-elliptical Hertzian contact, with a maximum Hertzian pressure P_0, on a rail half space which is discretised into horizontal parallel layers of even depth δz as illustrated in Figure 6.4 to a depth of ten times the contact half width, no plastic deformation would be present in the lowest layers at this depth. This is entered into an iterative process over N cycles calculating the maximum shear stress at each depth z. This method allows tens of thousands of wheel passes to be simulated in just a few minutes.

The model is dependent on the SYS-PSS data found under high hydrostatic loading in Chapter 3. Figure 6.1 shows the input variables which can be changed for a range of wheel-rail simulations, the material parameters which must be set specifically for the materials to be simulated, and the output of information which can be achieved from this.
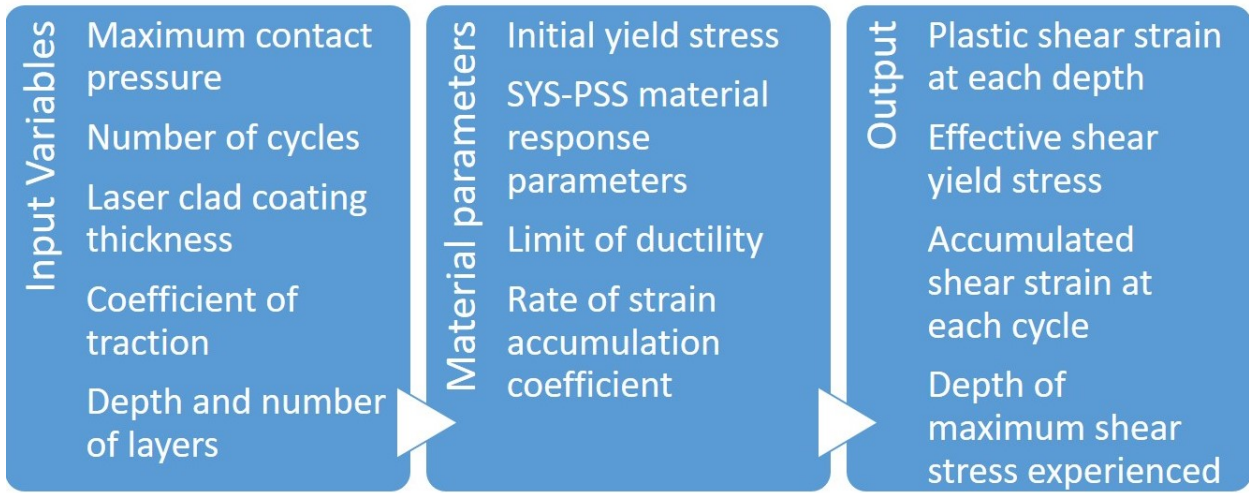
Figure 6.1: Simplified layer model process with input variables, material parameters and model output

The Hertzian line contact assumed to represent the wheel-rail contact produces a well-defined stress distribution below the surface of the material. Within the model, the maximum shear stress τ_{zxmax} is found by searching in each layer, in both the x direction and z direction and selecting the largest value of τ_{zx}, Equation 6.1 [162], in the area surrounding the contact, where θ is the angle of the applied tangential force which is assumed to be in the direction of the x-axis and is hence set as $\theta = 0$. It can be assumed that all points within the rail will experience the same range of stresses as the wheel travels across the rail, and selecting the maximum shear stress is sufficient due to being the controlling factor of the ratcheting process.

$$\tau_{zx} = P_0(\mu z \sin(\theta)(1 - (sV^{\frac{1}{2}})^{-1}) \tag{6.1}$$

where

$$s^2 = \frac{1}{2}(x^2 + z^2 - 1 + ((x^2 + z^2 - 1)^2 + 4z^2)^{\frac{1}{2}})$$
$$V = (1 + s^2)^{-1} \tag{6.2}$$

Due to the work hardening nature of rail steel, the effective shear yield stress k_{eff} at each cycle must be calculated to allow for this material response to cyclic loading. This effective shear yield stress is found using the modified Voce equation, Equation 6.3 [51]. The parameters for this equation are found for the MSS laser clad coating, R260 grade rail steel and R260 HAZ in Chapter 3.

$$k_{eff} = m \left(1 - e^{-n\gamma_p}\right)^p \tag{6.3}$$

The increment of plastic shear strain $\Delta\gamma_p$ for each cycle is calculated from the maximum shear stress τ_{zxmax} and effective yield stress k_{eff} using Equation 6.4 and is calculated for each itera-

tion until the material critical strain limit γ_c is reached where it is assumed that the material has reached ductility exhaustion. The constant 0.00237 is specific to the BS11 rail steel the layer model was based on and this is recalculated for the MSS-R260 rail alloy in Section 6.6.

$$\Delta\gamma_p = 0.00237 \left(\frac{\tau_{zxmax}}{k_{eff,N-1}} - 1 \right) \tag{6.4}$$

The strain accumulation Equation 6.4 with the layered representation of the rail was used by Kapoor et al. [67] in a Matlab routine. They found that ten to twenty thousand cycles could be computed in just a few minutes using this method. This rapid computing time along with the ability to use real material response properties is the reason it is chosen for this project as many other methods such as finite element analysis would be slower and much more computing intensive to compute such long runs relevant to the expected full lifespans of rail.

The final part of the model is referred to as variable-friction loading by Kapoor et al. [67]. The friction levels (referred to within this thesis as coefficient of traction) as a wheel passes over a rail will in reality vary across the contact and with environmental conditions, with a wet rail having a significantly lower coefficient of friction than a dry rail. A simplified approach for modelling was developed within the original model. Coefficient of traction data from twin-disc testing from Tyfour et al. [23] was used to run the methods. The model is developed here and simulations are presented to demonstrate the depth and magnitude of peak plastic shear strain accumulation in the laser clad rail.

6.3 Coefficient of traction method analysis

The method used by Kapoor et al. [67] to incorporate the coefficient of traction is extended and analysed here. The coefficient of traction is important to the modelling as it influences the depth of the peak shear stress within the rail. This occurs below the surface with low tractive forces (below 0.25) and rises towards the surface as tractive forces increase. During the initial development of the layer model it was decided by Kapoor et al. [67] that creating a varying coefficient of traction for each cycle would be unrealistic as it would not be possible to collect the same data in a real railway environment. Instead they tested two methods, the first was an upper bound - lower bound approach, using the most extreme traction values observed in testing to explore the difference in results. The second, which was found to be the most successful, was a 'block' friction method where the coefficient of traction record from the twin disc tests was split into an initial high traction coefficient μ_1 for the first few thousand cycles and reduced to a lower traction coefficient μ_2 for the subsequent cycles.

Following Kapoor et al. [67] rationale that creating a function to represent varying coefficient of traction for each cycle would be unrealistic a sensitivity test is conducted here to determine whether increasing the number of blocks representing the coefficient of traction throughout the cycles improves the accuracy of the layer model. Using the block coefficient of traction approach the maximum shear stress τ_{zxmax} is calculated for the first block of N_1 cycles with μ_1 and used to calculate the incremental shear strain accumulation for the block length. This is then repeated for

the second block of N_2 cycles using μ_2. The coefficient of traction curve can be divided into further blocks to improve the results and a sensitivity analysis is conducted here to create an accurate yet time efficient method.

Each different loading block n has its start and end cycle and corresponding coefficient of traction μ_n entered within the PHP file. When the PHP file is run a series of loops are called for each separate loading block calculating the corresponding maximum shear yield stress τ_{zxmax} through a function set up in the postgreSQL database, here τ_{zxmax} is calculated for each μ_n using Equation 6.1 and a table is created for each block to store the data.

The coefficient of traction data from the SUROS twin-disc tests conducted in Chapter 3 is shown in Figure 3.11. The test data for the R260 grade substrate Sample 1 is used here in developing model and analysing the block coefficient of traction method. The MSS laser clad coating is not used at this point due to the high yield stress and shallow surface deformation which would make validation of the model results from the change in CoT blocks difficult to spot at this point of development. All simulations during the development of the CoT blocks are run at 1500 MPa and a twin-disc size contact radius of 0.31 mm, with material model parameters for R260 grade rail steel given in Table 3.10 which are applied throughout the cross section of rail in contact (ie. unclad rail). Three different block systems are trialled here to assess the most efficient block method within the layer model. The CoT plot for sample 1 is taken and divided into 2 blocks, 6 blocks and 15 blocks as illustrated in Figure 6.2.

For each of the three scenarios the mean value of CoT is calculated over a given number of cycles, ensuring that the peak CoT value is encapsulated. Each block is numbered n, the start and end cycle for each block and the mean CoT of each block are calculated and demonstrated for the R260 2 block method is presented in Tables 6.1. The start and end cycle for each block and the mean CoT for the 6 and 15 block method can be seen in Appendix D. These values were then applied within the layer model to run the sensitivity analysis for number of loading blocks with changing CoT.

Loading block	Start cycle	End cycle	CoT
1	0	7499	0.43
2	7500	30000	0.38

Table 6.1: Start and end cycles with average Coefficient of Traction when divided into 2 blocks for R260 grade rail steel.
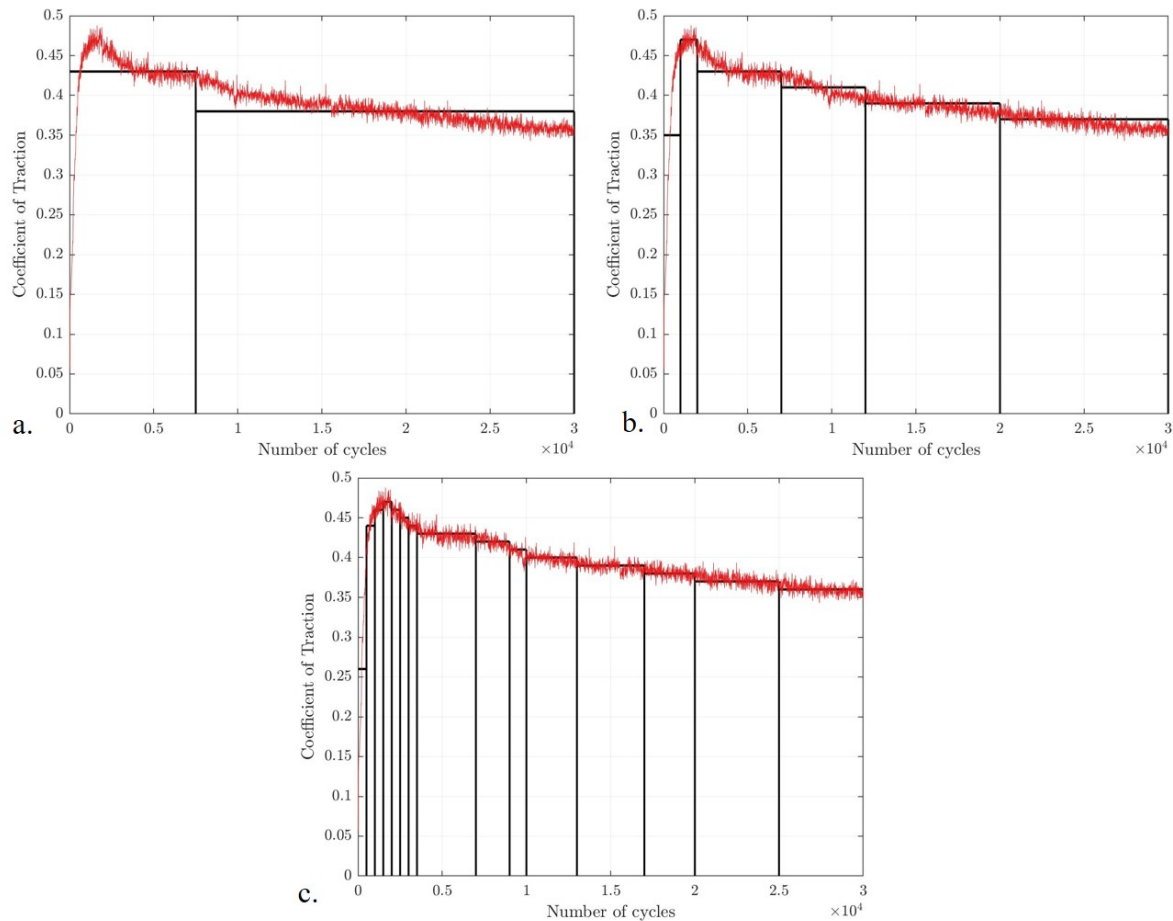
Figure 6.2: Coefficient of Traction curve from R260 sample 1 divided into a range of CoT blocks for modelling. a) 2 blocks, b) 6 blocks and c) 15 blocks.

Simulations were run in the layer model to test the effect of the number of CoT blocks using the R260 grade steel material parameters with a contact pressure of 1500 MPa and contact half width 0.31 mm for 30,000 cycles. The overall effect of CoT and the peak shear stress on plastic shear strain accumulation after 30,000 cycles are shown in Figure 6.3. It can be seen that there is very little difference in the final accumulation of plastic shear strain with the different number of CoT blocks given the small scale of the graph. At the maximum subsurface strain at a depth of around 0.12 mm the 2 block and 15 block methods produce very similar results whilst the 6 block method is a little higher. The 6 block method has its peak CoT in the early cycles whilst the 15 block method rises at a more steady rate to the peak CoT. The 2 block method doesn't reach the really high peak CoT, rather it runs a fairly high CoT for a longer amount of cycles.

The simulation computing time was significantly increased with the additional loading blocks. Given the very small difference between the results of the 2 block and the 15 block method it was decided that the original 2 block method should continue to be used here. When simulations are run in the layer model and R260 is the surface material in the contact, the CoT blocks continue to be set as $\mu_1 = 0.43$ for the first 7,499 cycles and $\mu_2 = 0.38$ subsequently, as shown in Figure 6.3 which is taken from the experimental work in Chapter 3.
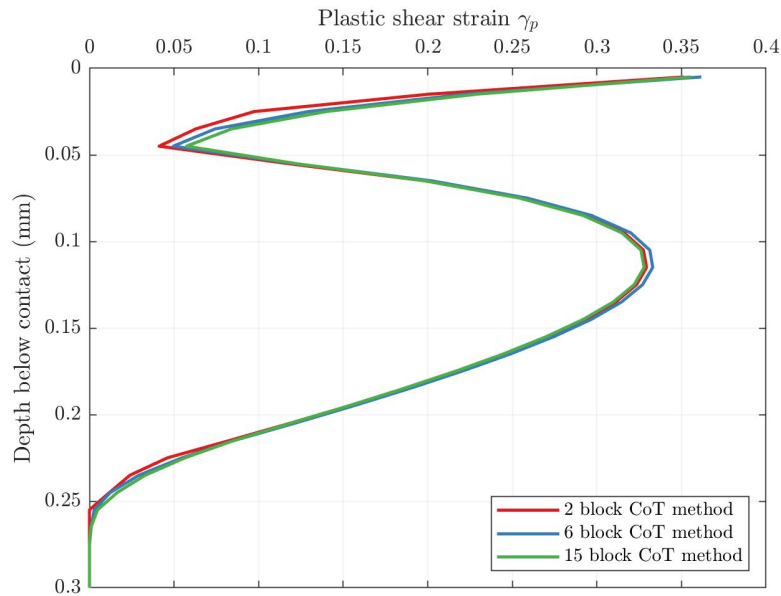
Figure 6.3: CoT block method analysis result. Showing the difference in plastic shear strain accumulation using 2,6 and 15 blocks.

The CoT for the MSS laser clad coating was found to be lower in the experimental work in Chapter 3. The CoT curve from that work was divided into 2 blocks and the start and end cycle with corresponding CoT value for the 2 block are shown in Table 6.2.

Loading block	Start cycle	End cycle	CoT
1	0	9999	0.38
2	10000	30000	0.32

Table 6.2: Start and end cycles with average Coefficient of Traction when divided into 2 blocks for MSS laser clad coating.

Figure 6.3 demonstrates the typical pattern of plastic shear strain accumulation in rail steels, with a high strain accumulation at the surface, a reduction in the area below this and then more highly strained material below, this is in line with the Hertzian contact stress distribution. This can be difficult to observe in micrographs of highly deformed rail material as the high plastic shear strain in the lower depths will have swept along the area with the reduction in strain accumulation. A link can be made to these different levels of strain accumulation and a common feature of wear tests, shown by Tyfour et al. [23], in which the wear rate rises and falls before reaching steady state. As initial wear occurs at the surface the material exposed below is less strained and as this is worn away the next exposed level is more strained.

6.4   Developing the model for laser clad coatings

The development of the layer model for bi-material systems is a suitable approach to quantify plasticity in laser clad coatings, as the model can be adopted to accommodate different material

properties at required depths within the model. In order to utilise the empirical ratcheting "layer" model described in Section 6.2 for the laser clad rail system it is developed to accommodate the different materials within the new MSS-R260 clad component. Within the model the material is divided into layers of depth δz and material properties for each layer are set according to the position in clad or substrate rail as illustrated in Figure 6.4. In this illustration three material zones are shown to enable the material properties of the Heat Affected Zone to be incorporated. This allows a more realistic model incorporating the change in material properties acquired from the heat input during the laser cladding process.
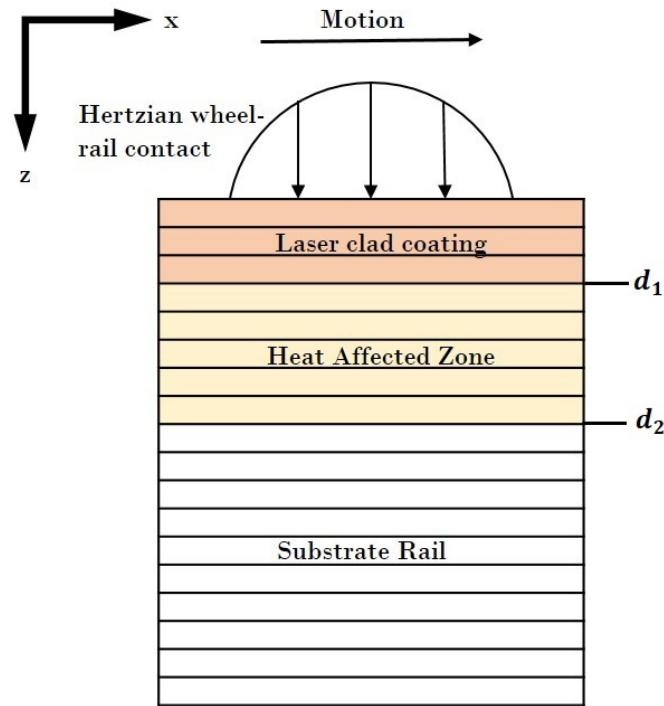
Figure 6.4: Representation of layer model with laser clad coating, HAZ and substrate rail subject to a Hertzian wheel-rail contact.

The layer model has been enhanced here to enable the three material property zones to be input. The laser clad coating of depth d_1 can be incorporated into the model by setting the MSS material properties where $z \leqslant d_1$. The HAZ of depth d_2 can be incorporated into the model by setting the HAZ material properties where $d_1 < z < d_2$. The substrate rail is then incorporated into the model by setting the HAZ material properties where $z \geqslant d_2$. This can be easily adapted to accommodate different depths of coating and heat affected zone and different materials where the SYS-PSS relation is known.

In the PHP script the material properties were added for the three different material zones; the MSS clad coating, HAZ and R260 substrate rail. The database was then run with a function to set up cells applying the correct properties for the material by selecting the material properties for the R260 substrate rail where $z > d_2$, the HAZ where $z > d_1$ and $z < d_2$ and the clad properties where $z < d_1$. This was a new development to enable a three material rail to be modelled with the ability to easily change the depth of the material zones. A series of iterations was then run to calculate the effective shear stress and plastic shear strain accumulation until the limit of ductility is reached

using the equations in Section 6.2. The material properties for the MSS laser clad coating, the R260 HAZ and R260 substrate rail found through experimentation under high hydrostatic loading in Chapter 3 were entered into the layer model. This is a significant improvement on previous work as the In2Track work [141] attempted to model plasticity using estimates for the material properties based on scaling up the BS11 material properties.

The shallow depth of plastic deformation seen in the twin-disc test results in Chapter 3, suggests that it may be driven by surface roughness as discussed in Chapter 5. As the new materials strain harden plasticity accumulation at a bulk level is limited. The original layer model, being based on softer rail steels, is very good at predicting bulk plastic deformation in materials which have low yields in comparison to the loads being applied. With the development of both harder steels and coatings, with much higher yield strengths than conventional rail steels, the incorporation of an additional function for surface roughness is required to correctly represent the contact pressures and subsurface stresses which cause plastic deformation in the top few microns. Without this development the layer model results cannot provide an insight into the level of plastic shear strain experienced by modern rail materials and coatings.

In the layer model simulations the plastic shear strain in the bulk rail is calculated using the standard Hertzian contact. Additionally the plastic shear strain in the shallow surface depths is calculated by using the surface contact pressure amplification calculated from the high asperity contact estimated in Chapter 6. It was shown that the untested material roughness was the most influential surface topography and are therefore assumed here. The asperity at the centre of the bulk contact produces the micro contact with the largest Hertzian contact pressure. For a 1500 MPa bulk contact over 0.31 mm half contact width, the micro contact for R260 grade rail steel is considered to be 8434 MPa with a contact half width of 2.19 μm. The micro contact for MSS laser clad coating is considered to be 5751 MPa with a contact half width of 3.79 μm.

6.5   Material model

The layer model was initially developed for rail materials with much lower yield strength values than that of modern rail steels and indeed laser clad coatings. The successful modelling of rail-wheel contact with the layer model is reliant on a well defined Shear Yield Stress - Plastic Shear Strain (SYS-PSS) curve with data generated under rolling-sliding high hydrostatic loading as demonstrated by Kapoor et al. [67] for BS11 rail in the original model development. In Chapter 3 twin-disc testing was conducted and analysis led to the SYS-PSS relationship being represented by a modified Voce equation in the form of Equation 6.3 for R260 grade rail steel, R260 HAZ and MSS laser clad coating. The material model parameters required within the layer model are m, n and p of the modified Voce equation, the shear yield stress k_0 and the limit of ductility or critical strain γ_c. The minimum strain value γ_{min} at which the Voce equation is valid using method C or method B and the gradient of the linear rise using method B as discussed in Section 3.5.1 are also required in the development. The material model parameters are presented in Table 3.10.

Within Chapter 3 a method was developed, in which shear stress and shear strain data points are collected at varied depths below the contact surface, provides confidence in the stress-strain

relationship to fairly low levels of strain. For the low levels of strain below the Voce equation threshold two methods were initially considered, method C in which the k_{eff} value is considered to be equivalent to k_0 is used and method B in which the linear rise from the k_{eff} value to the point on the modified Voce curve where the experimental data first fits closely, as described in Chapter 3.5.1. Kapoor et al. [47] find little difference between the two methods when applied to the layer model and state that they found method C to give slightly better results in simulations.

Both layer model methods (B and C) for low strain values were both tested with the reimplemented model run with the material properties for the original BS11 rail steel material properties. A notable discontinuation at γ_{min} was observed when using method C. This was considerably reduced by implementing method B. It was therefore decided that method B with a linear rise at low strain was the optimal method to be adopted in the development of the model.

6.5.1 Effect of load dependency on hardness measurements

The plastic shear strain within the material model for R260 grade rail steel is of a much lower magnitude than that seen in the shallower depths in the experimental results in the previous chapters after 30,000 cycles with a maximum contact pressure of 1500 MPa. When the material properties of MSS laser clad coating are applied to the reimplemented model no plastic shear strain is seen to accumulate at all, which once again is not representative of what is seen in the shallow surface depths. The inclusion of sub surface stresses from rough surface contact will address the shallow level ratcheting but not the magnitude.

The unexpected low level of ratcheting predicted, indicated that the shear yield stresses generated using the parameters from Table 3.10 are artificially high. The initial shear yield stress for the R260 grade rail steel was shown in Table 3.2 to be $k_0 = 454.1$ MPa. Converting this to a tensile yield stress using Tresca criterion Equation 3.4, $\sigma_y = 908.2$ MPa. Tensile yield stress of R260 grade rail steel can be found within the literature, Nikas et al. [163] conducted bi-axial torsion-compression tests and found the tensile yield stress to be $\sigma_y = 534.2$ MPa. Yazici et al. [164] conduct tensile tests and state the tensile yield strength as $\sigma_y = 564$ MPa, both of which are significantly different to the values found in Chapter 3.

Converting hardness values to shear yield stress is a known method, however there can be variation in hardness results depending on the applied load. Lower indenter loads can cause artificially high levels of hardness. A series of tests by Wilby [165] show the hardness to reach a steady value between $Hv_{5.0}$ and $Hv_{10.0}$ and the hardness measured at $Hv_{0.2}$ was 5.4 % higher than the steady hardness value. Considering this correction for load dependency the average hardness of the untested R260 rail material is calculated at $H_0 = 286$ HV ($H_0 = 2805.7$ MPa).

Further improvements to the correlation between tensile yield strength (MPa) and Vickers hardness are made by Wilby [165] through analysis of published data and experimental work. Through the collected data a line of best fit is placed through the collated data points and an improved relationship is shown in Equation 6.5.

$$\sigma_y = 2.676 Hv - 166.596 \qquad (6.5)$$

Although the underlying tests remain the same throughout, the correction to load dependency and the further addition of the relationship of tensile yield strength and hardness, the stresses experienced are more comparable to the softer BS11. The recalculated shear yield stress to depth x equations are presented in Table 6.3.

Material	Shear yield stress fit equation
R260 Substrate	$k_{eff} = -5359x^{-0.01952} + 5638$
HAZ	$k_{eff} = -231.6x^{0.3641} + 581.1$
MSS Clad coating	$k_{eff} = -200.5x^{0.6367} + 807.1$

Table 6.3: Shear stress against depth line of best fit equations and quality of fit to data recalculated using load dependency correction.

Using this and the corrected hardness value the tensile yield stress of the R260 grade rail steel is $\sigma_y = 598.74$ MPa, which is more in line with the literature. The shear yield strength using Tresca criterion Equation 3.4 is then $k_0 = 299.37$. Repeating this for the HAZ and MSS laser clad coating the modified Voce fits are re-calculated for each material and presented in Figure 6.5. The new parameters are then shown in Table 6.4 including the gradients for method B.
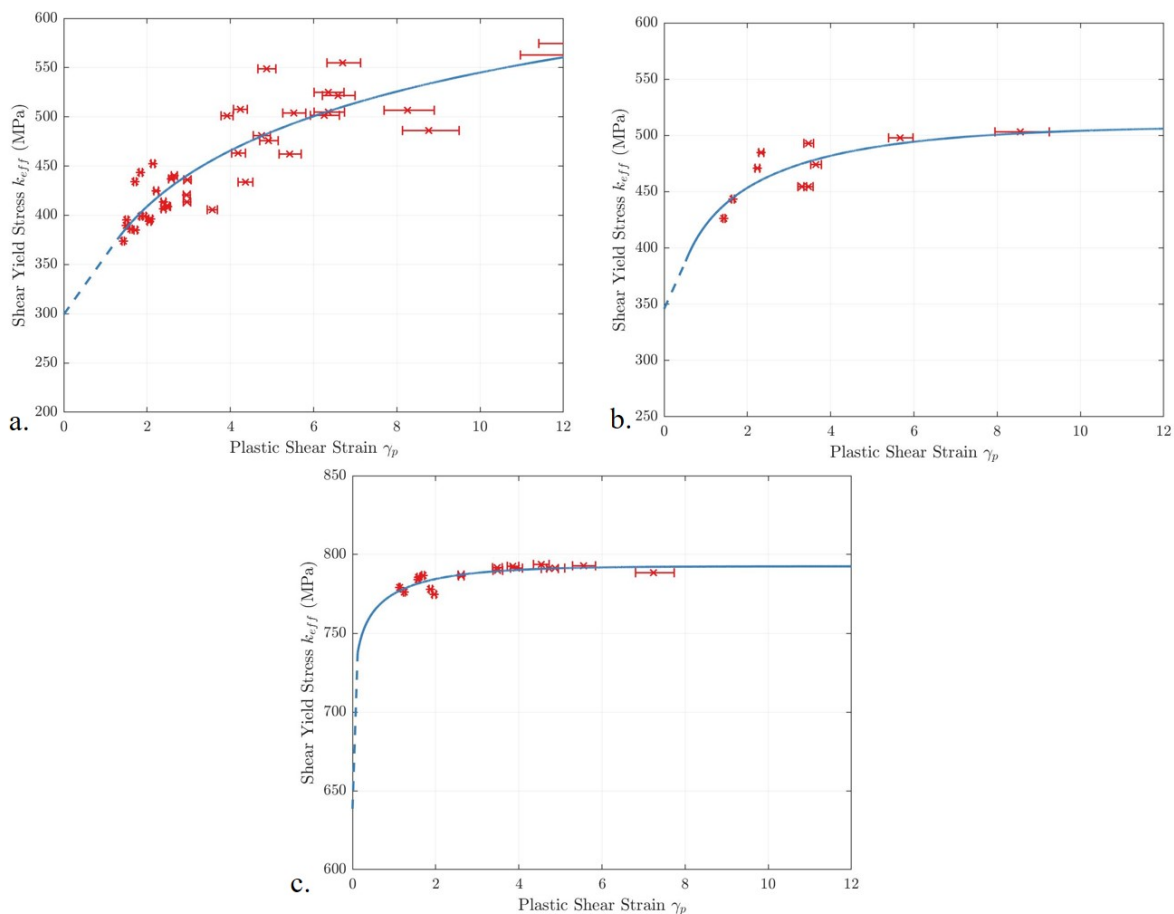
Figure 6.5: Modified Voce equation following load dependency correction, representing the SYS-PSS material response behaviour. a) R260 grade rail steel, b) R260 HAZ and c) MSS laser clad coating.

Parameter	BS11	R260	R260 HAZ	MSS
m	446	664.4	508.5	792.5
n	0.47	0.0466	0.2775	0.5755
p	0.8	0.2006	0.1343	0.02681
k_0 (MPa)	234.4	299.37	345.79	638.57
γ_c	11.5	11.7	11.7	14.2
γ_{min} (Method B)	2	0.407	0.517	0.123
Gradient (Method B)	35.21	59.18	81.78	804.24

Table 6.4: Material model information modified with load dependency correction, including the parameters m, n and p, the initial Shear Yield Stress, the critical Shear Strain and the minimum Shear Strain the modified Voce is valid from for the three tested materials R260, R260 HAZ and MSS presented with the original BS11 parameters from the work by Kapoor et al. [67]

The decision was made to use the modified Voce equations derived in this way in the plasticity modelling in the remaining section of this chapter.

6.6 Rate of strain accumulation

Within the reimplemented layer model the rate of incremental strain accumulation is carried over from the original model which is specific to the BS11 rail steel, shown in Equation 6.4 as a value of 0.00237. This rate is represented by c in Equation 6.6 and is independent of stress, described as "the conversion factor of net ratcheting load, taking into consideration the number of cycles run at that load, to ratcheting strain" in twin-disc experimental work by Tyfour et al. [48]. Briefly, the model works by fitting a linear relationship between $P_r N_{eff}$, which is the product of net ratcheting load P_r (Equation 6.7) and number of effective cycles N_{eff} (cycles where $\mu > 0.25$), and plastic shear strain γ_p measured at 0.05 mm below the surface.

$$\Delta \gamma_p = c P_r N_{eff} \tag{6.6}$$

Tyfour measured surface strain at 0.05 mm below the contact to minimise the effect of delamination at the surface. The plot of γ_p against $P_r N_{eff}$ was then used to evaluate the value of c empirically. The net ratcheting load P_r is calculated, Equation 6.7, as the difference between the effective ratcheting load P_{eff}, Equation 6.8, and the plastic shakedown P_s limit corresponding to the coefficient of friction.

$$P_r = max(0, P_{eff} - P_s) \tag{6.7}$$

$$P_{eff} = \frac{p_0}{k_{eff}} \tag{6.8}$$

Tyfour et al. [48] refer to the shakedown map in Hills et al. [166], from which they read the value

153

of plastic shakedown P_s limit corresponding to the coefficient of friction. The very similar value of elastic modulus in the laser clad coating and R260 grade rail steel as shown in Figure 3.9, and the equal Poisson's ratio allow the assumption of this method. The newer materials with the higher values of effective shear yield stress k_{eff} has the potential to create a negative net ratcheting load P_r numerically, as the plastic shakedown P_s value can be higher than the effective ratcheting load P_{eff} which physically is not correct. Therefore, the addition of the maximum value in Equation 6.7 is to select either $P_{eff} - P_s$ where strain has accumulated or 0 where it has not, to avoid an unrealistic negative accumulation of strain. The Tyfour et al. [48] method is adapted here for the new and novel rail materials by using the maximum contact pressure p_0 from the roughness contact pressures found in Section 5.5.

The rate of shear strain accumulation is calculated here for the R260 grade rail steel and the MSS laser clad coating through a series of twin disc tests. To find the rate of plastic shear strain accumulation required to enable the modelling of the MSS laser clad coating and the R260 grade substrate rail a further series of twin disc tests was required to capture the accumulation rate prior to reaching a steady state. A lower range of cycles is therefore considered here, assessing the effective shear yield stress k_{eff} and the plastic shear strain γ_P at 0.05 mm below the surface for bulk shear strain accumulation, which Tyfour considered to be the closest reliable measurement to the surface without the influence of de-lamination closer to the surface. The tests were conducted using SUROS 2 as described in Section 4.2.2 and were run with a 1500 MPa and -1% slip in unlubricated conditions for a range of cycle lengths. The results of the tests and the corresponding rate of accumulation c are presented in the following subsections. The rate of accumulation at shallow depths is considered by using the stresses generated using the surface contact pressure amplification estimated from the high asperity contact, the bulk level ratcheting is calculated using the bulk stress.

6.6.1 Bulk strain accumulation rate in R260 grade rail steel

The rate of strain accumulation in R260 grade rail steel is calculated from a range of twin disc tests in which R260 grade rail steel rail discs were run for 2,500, 5,000, 7,500 and 10,000 cycles. To enable the calculation of rate of strain accumulation c in Equation 6.6 the test data from the twin-disc experiments is required for analysing the effective number of cycles N_{eff} where $\mu > 0.25$ and the effective coefficient of traction μ_{eff} calculated as the mean coefficient of traction over N_{eff}. The plots in Figure 6.6 show the CoT data from the four twin-disc tests for R260 grade rail steel.
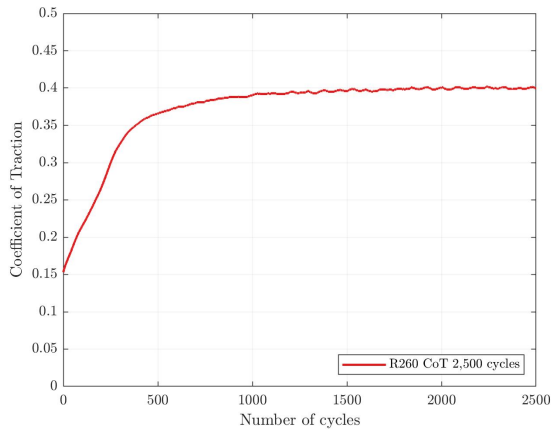
(a) Coefficient of Traction over 2500 cycles
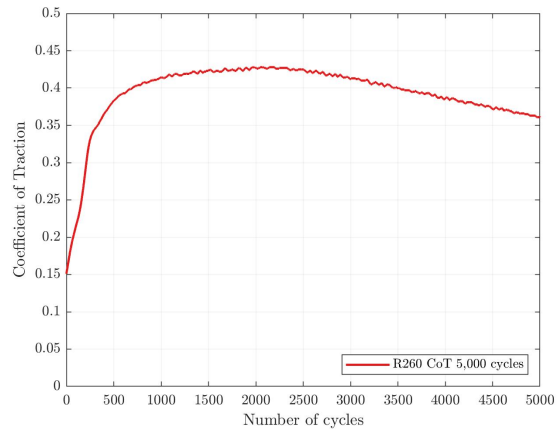
(b) Coefficient of Traction over 5000 cycles
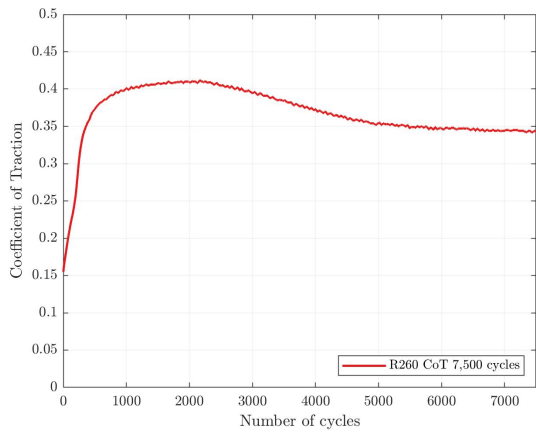
(c) Coefficient of Traction over 7500 cycles
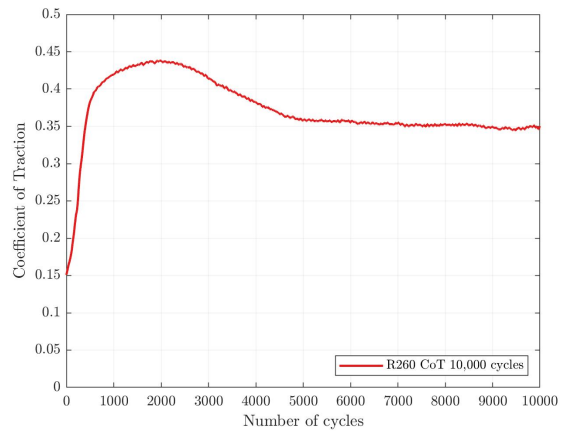
(d) Coefficient of Traction over 10000 cycles

Figure 6.6: Twin-disc test results showing Coefficient of Traction for the rate of accumulation tests for R260 grade rail steel.

The plastic shakedown limit P_s corresponding to μ_{eff} is read from the Hills et al. [166] shakedown map for two elastically similar cylinders rolling with partial slip. These required parameters are calculated and presented in Table 6.5.

After testing all samples were sectioned, mounted, ground and polished using standard metallographic techniques. The hardness was measured at 0.05 mm below the surface using a Durascan microhardness tester with a 0.2 kg load as described in Section 3.3.2 and the effective shear yield stress k_{eff} was calculated from this using Equation 3.8. The results of this are presented in Table 6.5. The samples were then etched in 2% Nital to reveal the microstructure and the optical micrographs for each sample are shown in Figure 6.7. The angle of deformation was measured at 0.05 mm below the surface using imagej [152] software and converted into a measurement of strain using Equation 3.9, the results are presented in Table 6.5.
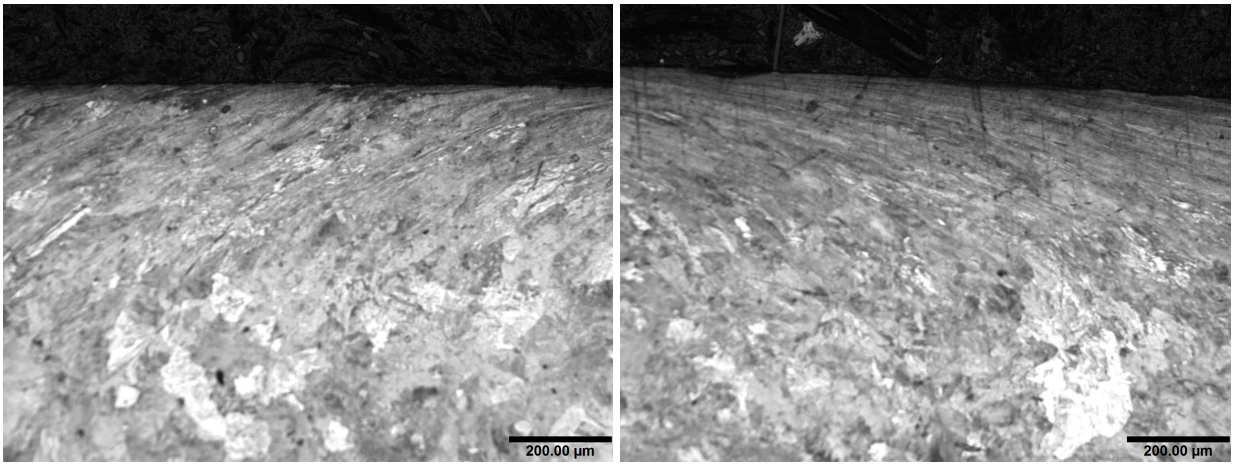
(a) Strain accumulation in R260 grade rail steel after 2,500 cycles.

(b) Strain accumulation in R260 grade rail steel after 5,000 cycles.
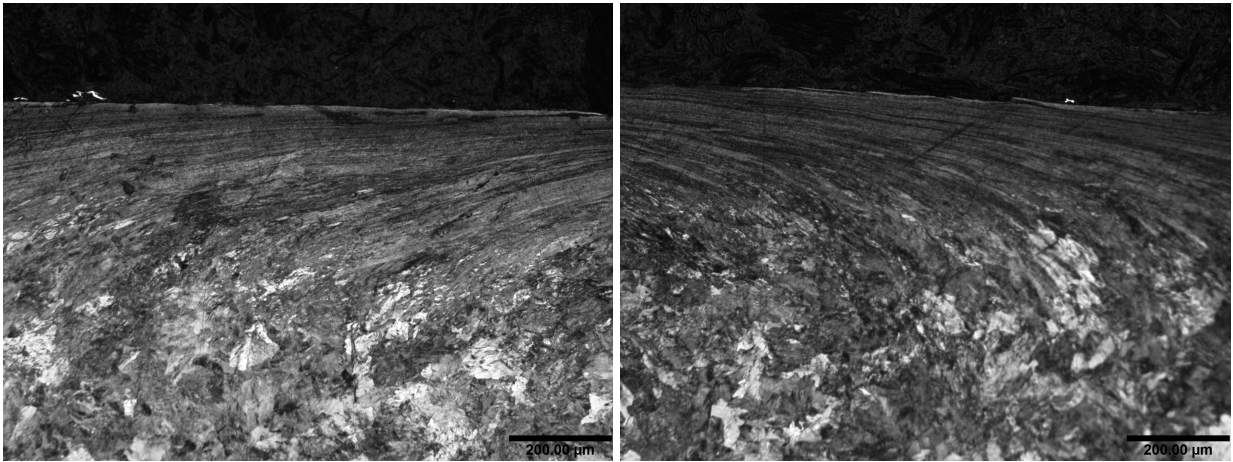
(c) Strain accumulation in R260 grade rail steel after 7,500 cycles.

(d) Strain accumulation in R260 grade rail steel after 10,000 cycles.

Figure 6.7: Low cycle ratcheting in R260 grade rail steel to enable the calculation of rate of shear strain accumulation.

The final parameter required for the calculation of rate of strain accumulation is the maximum contact pressure p_0. For the bulk contact the maximum contact pressure is 1500 MPa. Using the experimental data effective ratcheting load p_{eff} was calculated using Equation 6.8 and the net ratcheting load P_r using Equation 6.7, these are shown in Table 6.5 for the bulk contact, with $P_r N_{eff}$ which is required for plotting against plastic shear strain γ_p to establish the linear relationship and calculate the rate of strain accumulation c.

Cycles	N_{eff}	μ_{eff}	P_s	k_{eff} (MPa)	Strain γ_p	p_{eff}	P_r	$P_r N_{eff}$
2500	2346	0.38	2.7	402.11	1.62	3.73	1.03	2417
5000	4890	0.40	2.5	472.81	3.80	3.17	0.67	3289
7500	7367	0.37	2.8	501.16	6.75	2.99	0.19	1400
10000	9808	0.38	2.7	561.55	6.00	2.67	0	0

Table 6.5: R260 bulk contact measurements and calculations required for the rate of strain accumulation.

The value of $P_r N_{eff}$ had decreased by 7500 cycles for the bulk contact and by 10,000 cycles for the micro contact, indicating that a steady state of accumulation had been reached by this point. Using the data prior to steady state a line of best fit was placed through the data points with a linear relationship as Tyfour et al. [48] did. The result for R260 grade rail steel bulk rate of strain accumulation is shown in Figure 6.9. The resulting gradient gives the rate of accumulation in the bulk rail as $c = 0.0009853$.
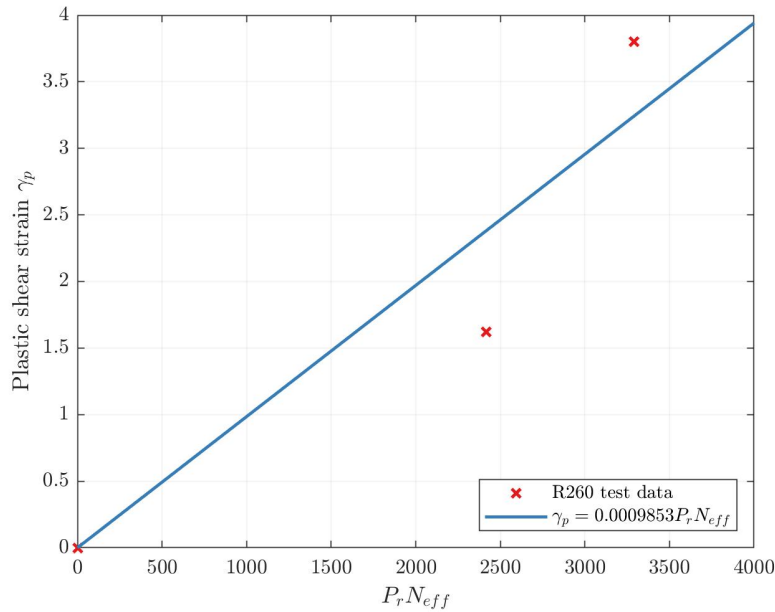
Figure 6.8: Linear method used to find rate of shear strain accumulation within R260 bulk rail steel.

The rate of strain accumulation in the R260 HAZ is assumed to be equal to the R260 bulk accumulation for modelling as it was not possible to collect data for this zone from low cycle tests due to the complex manufacture of developing a laser clad layer to a consistent thin depth to assess the HAZ over multiple tests.

6.6.2 Surface strain accumulation rate in R260 grade rail steel

The same test samples are used to calculate the rate of surface strain accumulation in the R260 grade rail steel, however, the maximum Hertzian contact pressure at the central asperity point is 8434 MPa for the micro contact . Table 6.6 provides the parameters required for the calculation of rate of strain for shallow surface depths.

Cycles	N_{eff}	μ_{eff}	P_s	k_{eff} (MPa)	Strain γ_p	p_0 (MPa)	p_{eff}	P_r	$P_r N_{eff}$
2500	2346	0.38	2.7	595.14	1.62	6070	15.10	12.40	29080
5000	4890	0.40	2.5	699.78	3.80	5101	10.79	8.29	40532
7500	7367	0.37	2.8	741.75	6.75	8940	17.84	15.04	110790
10000	9808	0.38	2.7	831.13	6.00	6930	12.34	9.64	94558

Table 6.6: R260 micro contact measurements and calculations required for the rate of strain accumulation.

A line of best fit was placed through the data points with a linear relationship in the same way as the bulk contact in the previous section. The result for R260 grade rail steel surface rate of strain accumulation is shown in Figure 6.9. The resulting gradient gives the rate of accumulation in the shallow surface levels of the rail as $c = 0.00006428$.
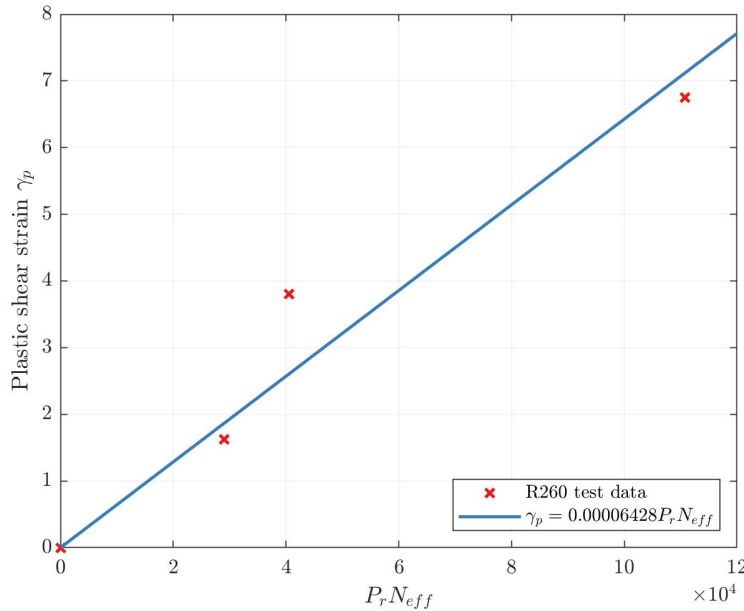
Figure 6.9: Linear method used to find rate of shear strain accumulation within shallow surface depths of R260 grade rail steel.

6.6.3 Surface strain accumulation rate in MSS laser clad coating

The rate of strain accumulation in MSS laser clad coating is calculated from twin disc tests in which R260 grade rail discs with a 1 mm MSS laser clad coating were run for 5,000, 7,500 and 10,000 cycles. The experimental data is analysed here to calculate the rate of strain in the coating, due to the ratcheting resistance of the material the rate is only calculated in the shallow surface depths. The coefficient of traction for the four MSS twin-disc tests are shown in Figure 6.10. The effective number of cycles N_{eff}, where $\mu > 0.25$, and the effective coefficient of traction μ_{eff} calculated as the mean coefficient of traction over N_{eff} are defined. The plastic shakedown limit P_s corresponding to μ_{eff} is read from the Hills et al. [166] shakedown map for two elastically similar cylinders rolling with partial slip. These required parameters are presented in Table 6.7.
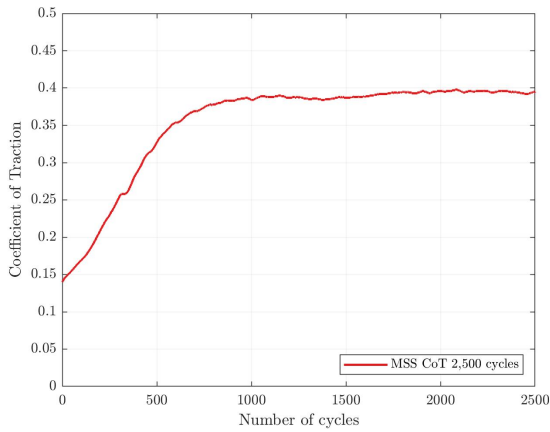
(a) Coefficient of Traction over 2,500 cycles
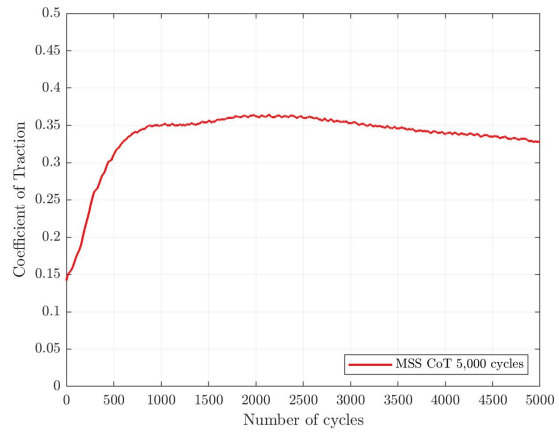
(b) Coefficient of Traction over 5,000 cycles
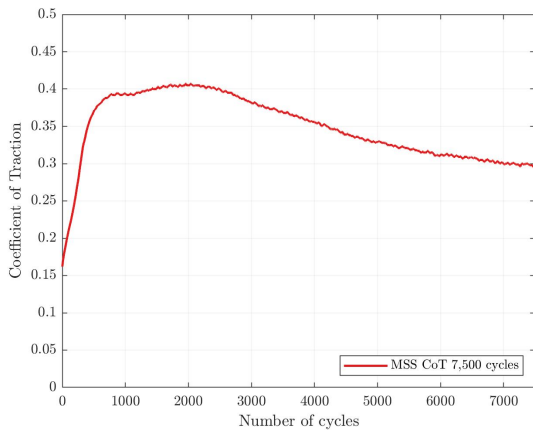
(c) Coefficient of Traction over 7,500 cycles
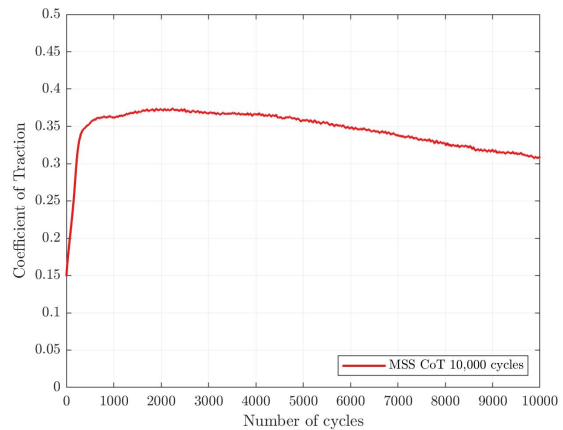
(d) Coefficient of Traction 10,000 cycles

Figure 6.10: Twin-disc test results showing Coefficient of Traction for the rate of accumulation tests for MSS laser clad coating.

After testing all samples were sectioned, mounted, ground and polished using standard metallographic techniques. The subsurface hardness was once again measured using a Durascan microhardness. The samples were then etched to reveal the microstructure as described in Section 3.2.2. It has been seen throughout the previous chapters that the MSS laser clad coatings only accumulate shear strain in the shallow surface depths. The method of measuring strain 0.05 mm below the surface is not suitable for the laser clad coating and the angle of deformation is measured at 0.01 mm instead. The images of the subsurface cross section in Figure 6.11 are SEM rather than optical to enable the shallow deformation to be observed and measured. Although signs of sample contamination can be observed after 10,000 cycles, the angle of deformation can still be measured.
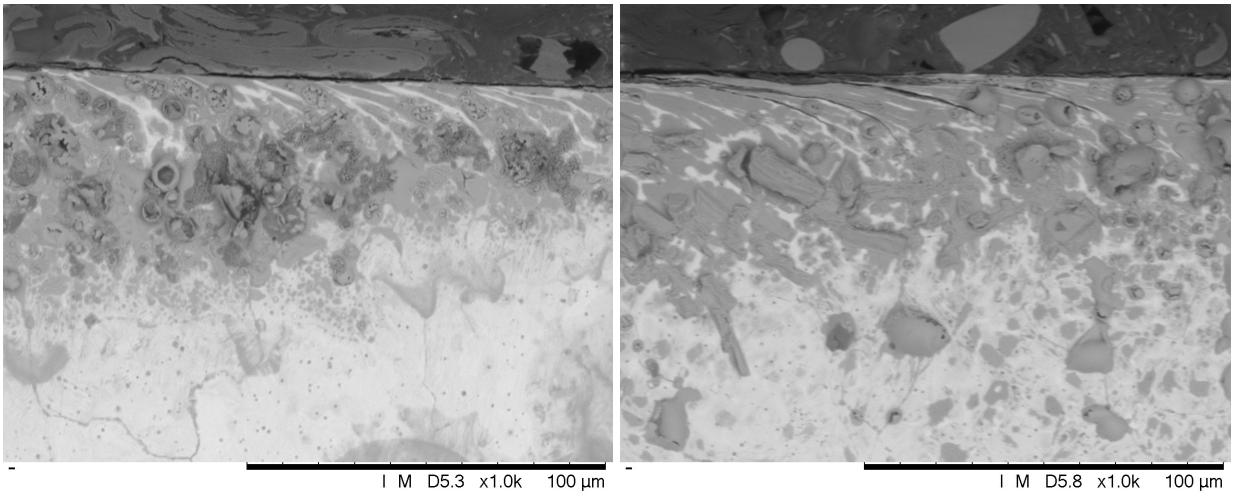
(a) Strain accumulation in MSS laser clad coating after 5,000 cycles.

(b) Strain accumulation in MSS laser clad coating after 7,500 cycles.

(c) Strain accumulation in MSS laser clad coating after 10,000 cycles. (Sample contaminated however the angle of deformation could still be gathered.)

Figure 6.11: Low cycle ratcheting in MSS laser clad coating to enable the calculation of rate of shear strain accumulation.

The analysis results for the MSS laser clad coating and the calculated effective ratcheting load p_{eff}, net ratcheting load P_r, the maximum contact pressure from the central asperity contact p_0 and $(P_r)N_{eff}$ are all presented in Table 6.7

Cycles	N_{eff}	μ_{eff}	P_s	k_{eff} (MPa)	Strain γ_p	p_0 (MPa)	p_{eff}	P_r	$(P_r)N_{eff}$
5000	4782	0.34	3.1	625.31	1.4	6070	8.71	5.61	26849
7500	7351	0.35	3	625.31	2.5	7240	10.39	7.39	54357
10000	9897	0.35	3	625.31	2.27	7570	10.87	7.86	77872

Table 6.7: MSS micro contact measurements and calculations required for the rate of strain accumulation.

Using this data a line of best fit is placed through the data point with a linear relationship to calculate the rate of accumulation c. The results for MSS are shown in Figure 6.12. The resulting gradient gives the constant $c = 0.00003596$ which indicates that the rate of strain accumulation is even lower than the R260 grade rail steel.
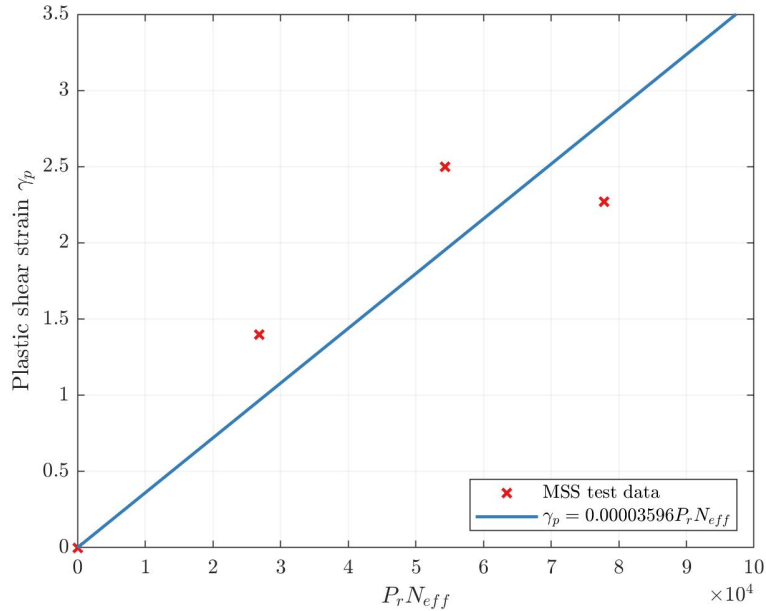
Figure 6.12: Linear method used to find rate of accumulation with "shear strain as a function of net ratcheting load and number of cycles"

6.7 Model simulations

The work in this chapter has developed the empirical ratcheting model with the correct layers, material properties and contact parameters representative of modern rail steels and laser clad coated rail steels. Simulations are run in this section to investigate the depth of plastic shear strain in small scale rail-wheel contacts for validation and are then extended to full scale rail-wheel contacts. Simulations are run on unclad R260 grade rail steel for validation. The contact parameters from the surface roughness model are simulated in the empirical ratcheting model to investigate the shallow plastic shear strain experienced by the rail materials. The rough contact model is run separately to the bulk model due to the extensive computing time generated by the very small layer size δz where the plastic shear strain occurs at the very surface of the material.

6.7.1 Quantifying bulk plasticity in R260 grade rail steel

The initial simulation shows the level of plastic shear strain at bulk levels in R260 grade rail steel. This is based on an unclad R260 grade rail steel with a maximum contact pressure of 1500 MPa and a 0.31 mm contact half width for 30,000 cycles. It can be seen in Figure 6.13 that this type of contact causes the peak shear strain to be around 115 μm below the contact surface at a magnitude of around 6.65. The strain has reduced to zero by 575 μm below the contact surface (normalised depth of 1.85b, where b is the contact half width) indicating the material is unchanged below this

level. The model is validated by independent comparison of a twin-disc test run in the same conditions as those modelled here, by Christoforou et al. [81]. In which it is reported that plastic shear strain is present to a depth of 570.62 μm.
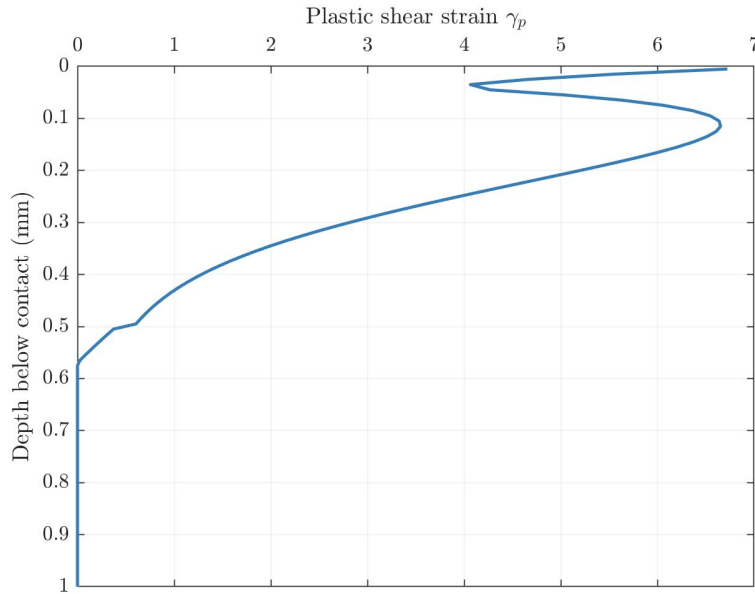
Figure 6.13: Plastic shear strain accumulation in the bulk of R260 grade rail steel, using only the smooth bulk contact stresses. Peak shear strain around 575 μm below the contact surface at a magnitude of 6.65.

6.7.2 Quantifying surface plasticity in R260 grade rail steel

The next simulation is conducted to investigate the surface level of plastic shear strain accumulation in R260 grade rail steel. This is based on an unclad R260 grade rail steel with a maximum micro contact pressure of 8434 MPa and a 2.19 μm micro contact half width for 30,000 cycles. This simulation is a key area of novelty as it is successful in predicting the surface level of plastic shear strain not seen in the literature to date. It can be seen in Figure 6.14 that this type of contact causes the peak shear strain to be around 0.75 μm below the contact surface at a magnitude of around 10.33. The surface strain has reduced to zero by 25 μm below the contact surface (normalised depth of 11.4b_a, where b_a is the micro contact half width).
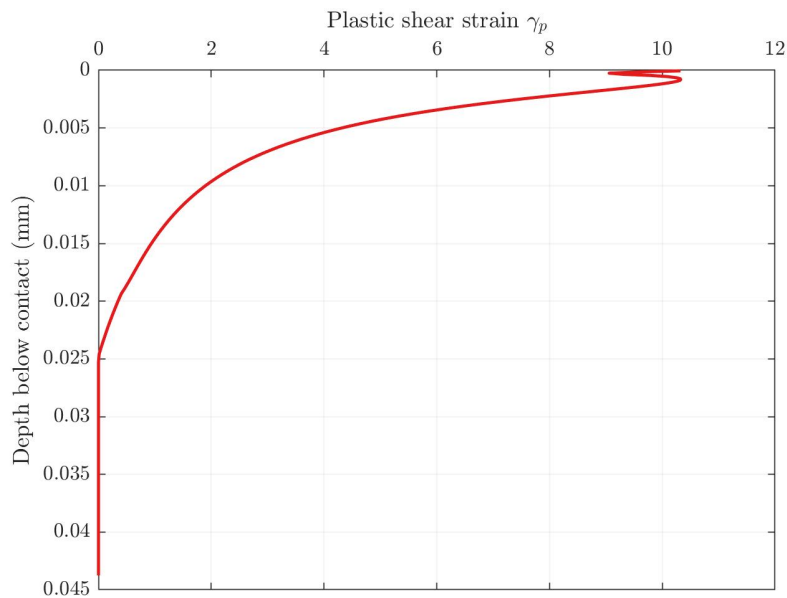
Figure 6.14: Plastic shear strain accumulation in the shallow surface depths of R260 grade rail steel. Peak shear strain around 25 μm below the contact surface at a magnitude of 10.33.

Plotting the shear strain accumulation from the surface amplification, from the asperity contact, and shear strain accumulation from the bulk smooth contact together in Figure 6.15 it becomes clear to see the high surface shear strain accumulation which could would previously have been neglected. The surface amplification from the asperity contact provides a better explanation of the surface shear strain accumulation in the materials with high yield strength.
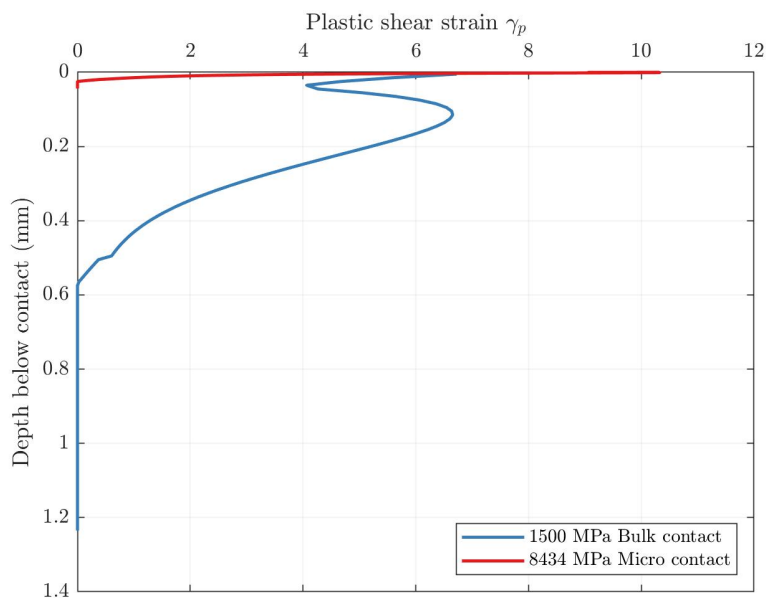
Figure 6.15: Combined plastic shear strain accumulation in the surface layers and bulk of R260 grade rail steel. Indicating the importance of including surface roughness when quantifying plasticity in new and novel rail materials.

In reality the surface stress does not diminish at 25 μm below the contact surface, rather the super-positioning of neighbouring asperities would extend to the bulk contact. The method chosen here is to focus on the estimated surface amplification which provides the maximum effect on ratcheting and the more established smooth contact method for the bulk ratcheting.

6.7.3 Quantifying surface plasticity in MSS laser clad steel

The MSS laser clad coating only experiences surface plasticity, the bulk contact does not predict any strain within the material due to the high yield strength of the material. The surface rough-ness micro contact is therefore considered to be the most critical for simulations for quantifying plasticity within the MSS laser clad coating. This is based on a 1 mm MSS laser clad coating with a maximum micro contact pressure of 8434 MPa and a 2.19 μm micro contact half width. It can be seen in Figure 6.16 that this type of contact causes the peak shear strain to be around 1.5 μm below the contact surface at a magnitude of around 1.96. The strain has reduced to zero by 13 μm (normalised depth 5.94b_a) below the contact surface. This is slightly lower than that seen in the experimental data.
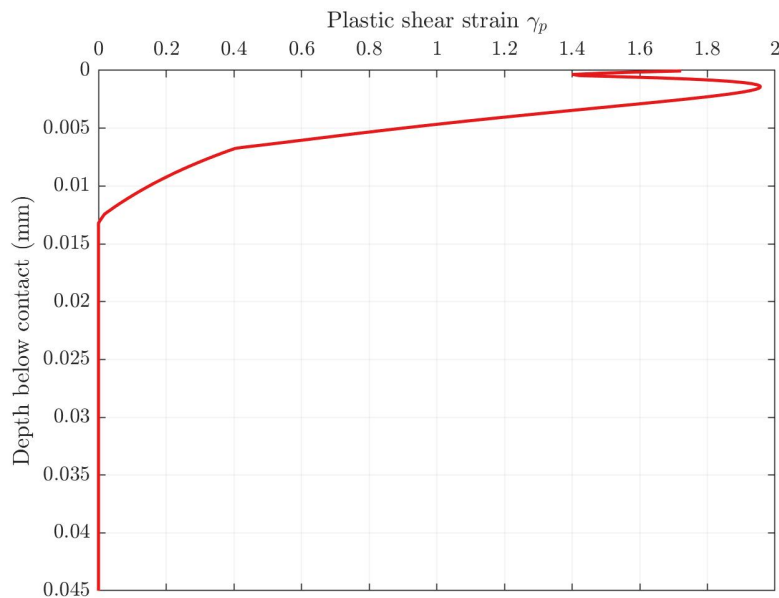
Figure 6.16: Plastic shear strain accumulation in the shallow surface depths of MSS laser clad coating. Peak shear strain around 1.5 μm below the contact at a magnitude of 1.96.

6.7.4 The influence of HAZ in sub surface plasticity in laser clad rail steel

The effect of the HAZ is considered here below a 0.15 mm laser clad coating, based on an MSS laser clad R260 grade rail steel with a maximum contact pressure of 1500 MPa and a 0.31 mm contact half width for 30,000 cycles. Assuming a HAZ at 0.75 mm below the laser clad coating as measured in Chapter 3, the depth of ratcheting in the HAZ is 450 μm (normalised depth 1.45b) compared with 550 μm (normalised depth 1.77b) if no HAZ is present in the R260 grade rail steel. The maximum magnitude of plastic shear strain accumulation is shown to be 4.36, this remains the same if the depth of HAZ is reduced to 0.1 mm as shown in Figure 6.17.
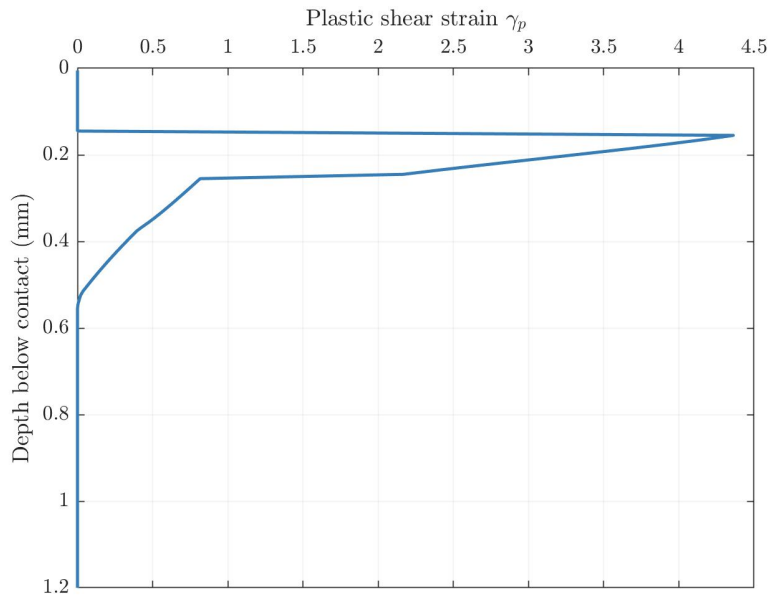
Figure 6.17: Plastic shear strain accumulation in substrate rail below 0.15 mm MSS laser clad coating. HAZ depth reduced to 0.1mm.

The results of these simulations are interesting, due to the higher shear yield stress of the HAZ it would be expected that there would be greater plastic ratcheting using the R260 substrate rail parameters. Considering the modified Voce equations for R260 and HAZ, it can be seen in Figure 6.5a and 6.5b that the SYS-PSS relationship has a different rise between the two materials. In the R260 stress is shown to continue to rise with strain, however, the HAZ reaches more of a plateau. It is believed that the large amount of data available for the R260 is partly responsible for this difference in relationship. The results generated using the parameters for the HAZ are more aligned with the magnitude of ratcheting seen in Figure 3.14.

The strain predicted using the R260 and HAZ parameters differ in magnitude, although the difference in depth is marginal. In the design of an additively manufactured laser clad coating with the aim of eradicating plastic shear strain in both the coating and substrate rail it is the depth which is of the most importance. The depth of ratcheting suggests that a laser clad coating greater than $450\mu m$ (normalised depth 1.45b) is required assuming a HAZ is present to protect the substrate rail without any bulk ratcheting in contacts up to 1500 MPa. In this case only the surface shear strain accumulation shown in Figure 6.16 would be present.

6.7.5 Quantifying full scale plasticity in MSS laser clad coated rail steel

Following the quantification of bulk and surface plasticity in small scale rail-wheel contacts simulations are now presented for full-scale rail-wheel contact. Assuming the surface topography remains the same on the laser clad rail when applied to a full scale rail, a maximum bulk contact pressure of 1500 MPa on a 7 mm contact half width, 665 asperities would be in contact. Using the methods described in Chapter 5 the maximum contact pressure at the mid asperity would be 8996 MPa over a 2.44 μm contact half width. This mid asperity contact pressure is used here

to provide a surface amplification within the simulation here to show the surface roughness in full-scale rail-wheel contact.

The results in Figure 6.18 show the peak plastic shear strain accumulation around 1 μm below the below the contact surface with a magnitude of 3.75 after 30,000 cycles. The surface strain has reduced to zero by 13.6 μm below the contact surface. Compared with the small scale surface shear strain accumulation the peak shear strain is slightly closer to the surface but at a greater magnitude, however in both simulations the strain is to a similar depth.

Considering then, the bulk plasticity within a full-scale laser clad rail, a maximum contact pressure of 1500 MPa over 7 mm contact half width is simulated for 30,000 cycles. A 1 mm laser clad coating with a further 1 mm HAZ is used to illustrate the protection a laser clad coating can provide. Figure 6.19 shows that this type of contact causes the peak shear strain to be around 1.98 mm below the contact surface at a magnitude of around 4.33. The surface strain has reduced to zero by 12.38 mm below the contact surface (normalised depth 1.77b). This is the point where the HAZ returns to standard R260 substrate material. At the interface between laser clad coating and HAZ the magnitude of ratcheting is 1.95.
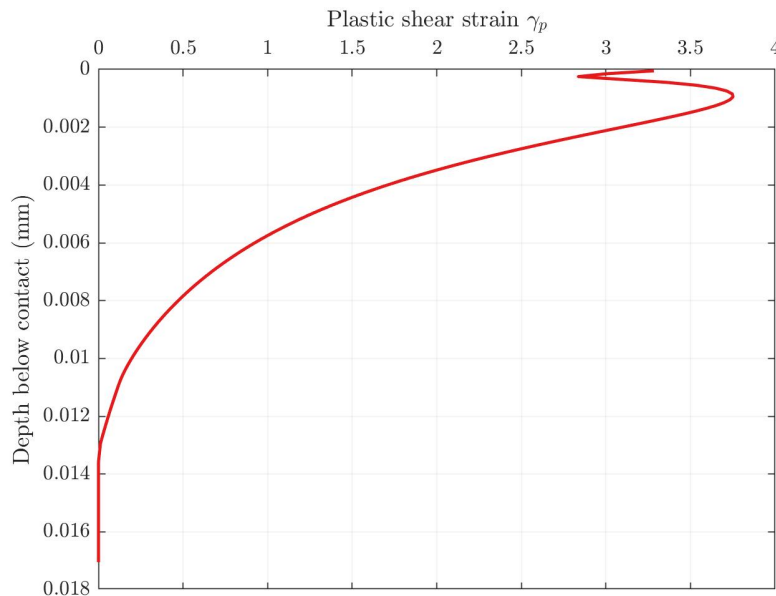
Figure 6.18: Full scale plastic shear strain accumulation in 1 mm MSS laser clad coating on a R260 substrate rail with 1 mm HAZ. Peak shear strain around 1 μm below the contact surface at a magnitude of 3.75.
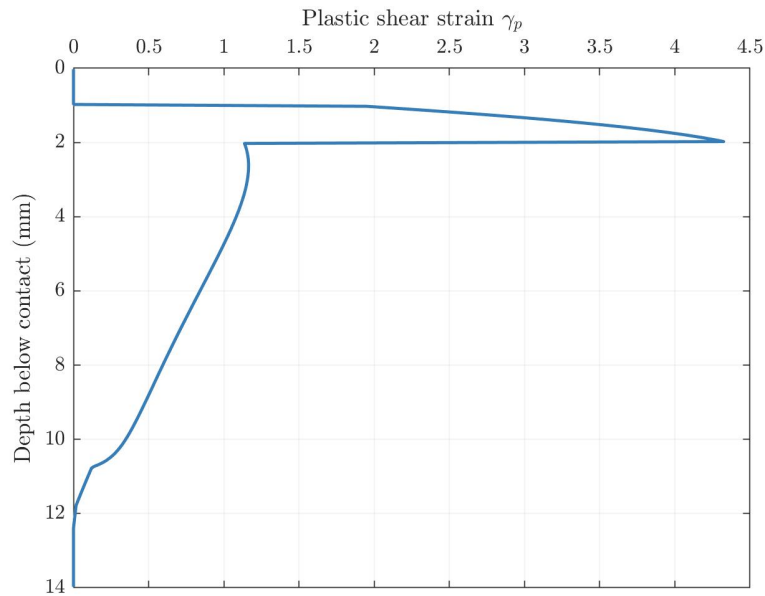
Figure 6.19: Full scale plastic shear strain accumulation in 1 mm MSS laser clad coating on a R260 substrate rail with 1 mm HAZ. Peak shear strain around 1.87 mm below the contact surface at a magnitude of 4.33.

It was shown in the small-scale simulations that the HAZ reduced the overall depth of the plastic shear strain accumulation. This is found to be true in the full-scale with the depth of shear strain accumulation reducing to 10.18 mm (normalised depth 1.45b) below the contact surface where the substrate rail is assumed to consist wholly of HAZ material properties.

Taking the full-scale simulations into consideration, a laser clad coating greater than 10.18 mm is required to protect the substrate rail without any bulk ratcheting in contacts up to 1500 MPa. As laser clad coatings are deposited in beads of around 1 mm thick, this level of deposition could be time consuming and costly. Laser clad coatings have been shown in small scale tests to be successfully applied to 2 mm. Figure 6.20 shows that this type of contact causes the peak shear strain to be around 2.63 mm below the contact surface at a magnitude of around 4.69 after 30,000 cycles. The surface strain has still reduced to zero by 12.38 mm below the contact surface. This deeper MSS laser clad coating creates a higher level of plasticity at the interface than the thinner laser clad coating although this interface is further away from the surface. In application, consideration must be made to the position in track where the cladding is present to avoid the material moving and cracks initiating as seen in Chapter 4.
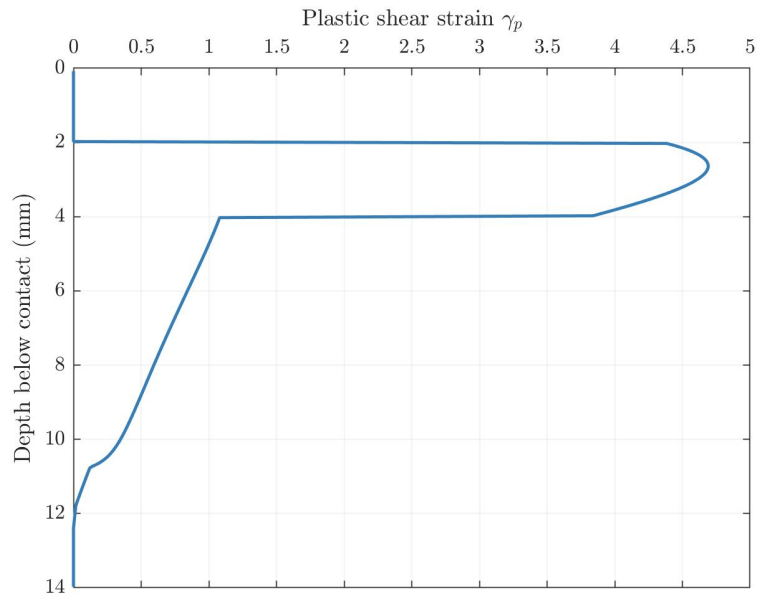
Figure 6.20: Full scale plastic shear strain accumulation in 2 mm MSS laser clad coating on a R260 substrate rail with 2 mm HAZ. Peak shear strain around 2.63 mm below the contact surface at a magnitude of 4.69.

6.8 Discussion

The results found through simulations within this chapter show that bulk plasticity within a rail can be reduced by applying a laser clad coating. The thickness required to completely eradicate plastic shear strain accumulation is relatively deep, at just over 10 mm, compared with the typical 1 mm clad deposition. When a thinner deposit of MSS laser clad coating is applied, a level of plastic shear strain accumulation is seen at the interface. This material flow below the interface is reflective of that seen in twin-disc tests in Chapter 3 and Chapter 4, which was seen to create a crack initiation point in the latter.

Knowledge added from this chapter is that of the resulting plastic shear strain accumulation at the contact surface produced by asperity micro contacts. Without this addition to the model it is not possible to explain why ratcheting occurs in materials with shear yield stress higher than the applied bulk stress. This can be applied to many new rail materials including the MSS laser clad coating. The importance of the surface roughness is evident and must be utilised for new rail materials where the materials high yield strength would cause potentially high magnitudes of surface shear strain accumulation to otherwise be neglected.

The importance of load dependency in hardness testing was identified through the development of the layer model. Once the load corrected modified Voce equation parameters were applied within the ratcheting model the resulting predicted plastic shear strain was found to be representative of tests conducted by Christoforou et al. [81]. This validation of the layer model with these parameters further indicates the value of the load dependency work conducted by Wilby [165].

Lu et al. [2] found that cladding a leaner/harder grade of rail steel improved the wear rate and hardness compared with lower grade rail steels. The simulations within this chapter show the HAZ to affect the level of plastic shear strain within the substrate rail. Further research to control the HAZ would be beneficial to reduce the risk of material flow at the interface. The properties of the HAZ would be dependent on the substrate material and lower grade rails could be further tested.

Following on from the empirical ratcheting model by Kapoor et al. [47] and reimplemented by Fletcher et al. [141], the model has been developed within this chapter for new and novel rail materials. The method was effective and was able to generate tens of thousands of wheel passes quickly. Other than the micro contact work discussed above the other main additions which were made included the addition of the extra zones and material properties for the R260 grade rail steel, HAZ and MSS laser clad coating. The rate of strain accumulation was also found experimentally to improve the accuracy of results. The block method to simulate CoT was investigated for improvement but the effect of this was minimal and it increased computing time significantly.

The results of this chapter indicate that the layer model can be applied to any new rail material once the material properties have been found as described throughout this thesis. The method chosen here is to focus on the estimated surface amplification which provides the maximum effect on ratcheting and the more established smooth contact method for the bulk ratcheting. This prevents excessive calculations, providing the peak at both the surface and within the bulk over tens of thousands of contact cycles without taking an excessive amount of computing time. The model could be further extended to incorporate multiple asperity contacts, although this has the potential to slow the model excessively. The layer model and material data reduce the requirement for extensive experimentation on laser clad coatings and can be used to indicate required targeted tests.

It is possible to approximately scale the model from small-scale to full-scale contacts. The ratio of depth to contact width could be considered that $d = \alpha b$ where d is the coating depth , b is the contact half width and α is a scaling factor. From this it can be seen that a 1 mm deep clad coating on a twin disc specimen ($b = 0.31$ mm) is equivalent to a 22.58 mm deep clad coating on a full scale contact ($b = 7$ mm). Creating a coating depth of 0.15 mm on a SUROS disc provides a comparable test for a more realistic 3.39 mm deep clad coating on a full scale rail contact.

6.9   Conclusion

Ratcheting in laser clad coated rail steels is quantified here for the first time using the comprehensive investigation into the material response from Chapter 3 and the development of a numerical model to predict the plastic shear strain accumulation. Within this chapter the empirical ratcheting model known as the layer model has been developed for new and novel rail materials.

The model was adapted to include multiple zones and hold accurate material properties found experimentally. The rate of strain accumulation was found through further twin-disc tests and the rate was found to be slower in the MSS laser clad coating. Initial simulations indicated that

the material properties found in Chapter 3 did not generate the magnitude of plastic shear strain accumulation seen in experiments, this led to further research indicating the load dependency in hardness tests, which is not standardised across rail research.

The depth of laser clad coating required to eradicate plastic shear strain accumulation in R260 grade rail exposed to bulk contact loads of up to 1500 MPa is around 10 mm (approximately 1.45 times the contact half width). A depth less than this results in plastic shear strain accumulation in the substrate rail below the interface. It was shown that the material flow below the interface poses a risk in Chapter 3 and Chapter 4 and can cause material flow and crack initiation.

The key finding in this chapter is predicting the very near surface plastic shear strain accumulation arising from the micro contacts from the surface roughness. This helps to explain the phenomenon of rail materials with high yield stress experiencing ratcheting when traditional models would not predict it to occur. The surface plastic flow appears to be inevitable, even in a hard laser clad coating. This highlights that although a material like MSS appears to be highly ratcheting resistant, maintenance including monitoring is still vital in the safety of the rail.

Chapter 7

Discussion

A detailed discussion has been presented at the end of each chapter. Here, a high level discussion links together the work presented throughout the thesis. This discussion is split into a focus on scientific additions to knowledge and industry application.

7.1 Scientific additions to knowledge

The work conducted within this thesis consisted of both experimental work and modelling. The techniques used in both were selected to allow the new and novel rail materials to be thoroughly analysed following tens of thousands of cycles conducted in a time efficient manner. The material response to load, characterised in Chapter 3 and the effect of contacting rough surfaces in Chapter 5 were used in the quantifying of plastic shear strain in Chapter 6. The testing of laser clad repairs in Chapter 4 gave a further opportunity to investigate the plastic ratcheting, heat affected zone and integrity of laser clad coatings applied in a non continuous application.

A novel method to measure the Shear Yield Stress - Plastic Shear Strain in rail materials was presented initially. This work allowed a detailed characterisation of material properties and material response to load for the R260 grade rail and MSS laser clad coating. Initial attempts to quantify plastic ratcheting highlighted that the method to characterise SYS-PSS was affected by the load dependency on hardness tests. Incorporating the correction for load dependency enhanced the results of the layer model in line with experimental results. The heat affected zone was considered separately and analysis of this zone was conducted by evaluating the shear yield stress and plastic shear strain of the material below the laser clad coating. When applying the material properties of the HAZ to the plastic ratcheting model the magnitude of plasticity was representative of that seen below the thin application of laser clad coating in the experimental results. The rate of strain accumulation could not be determined using the method developed to characterise material response to load which was a limitation of the method. A separate set of tests was required to calculate this for application to the ratcheting model.

The laser clad MSS has a very high yield stress and showed evidence of plastic flow only very close to the surface. The original layer model was unable to predict surface ratcheting in the laser clad coating using the bulk maximum Hertzian contact pressure assumed. It was therefore presumed that surface roughness was responsible for the shallow surface strain accumulation. The complex rail-wheel contact which is an open tribological system with changing levels of friction and potential dynamic loading would prove almost impossible to model an accurate surface profile. A method was therefore developed to estimate the amplification in contact pressure generated by the rough surface contact. The results of this show the maximum contact pressure at the mid contact asperity to be up to 6 times higher than the assumed bulk contact for R260 and

up to 5.6 times higher for the MSS laser clad coating. The addition of this to the layer model allowed a prediction of ratcheting which accounted for the shallow surface shear strain seen in the experimental results.

7.2 Industry application

Additive manufacturing with laser clad coatings can be used to extend the life of railway tracks through either repair or enhancement. In-situ repairs would provide a new method of rail repair, the laser process is a targeted and localised technique providing the potential to reduce the risks associated with high heat input. Laser clad coatings on rail steels have previously been applied to a length or section of rail in a block application, this was the first time that the laser clad coating had been applied in a small channel as a repair. When the laser clad coating is applied to a depth greater than the location of the peak sub-surface stress, the substrate rail is protected and ratcheting in the laser clad rail system is significantly reduced. A laser clad coating of approximately 1.45 times the contact half width is advised to protect the substrate rail. It was shown in the repairs that shallow clad depths are prone to plastic ratcheting below the repair site. The gradient of the repair interface should therefore be designed to avoid this.

The selection of laser clad material was shown to be critical in the application of an in-situ repair. The clad material must be perfectly compatible in terms of not only ratcheting rate, but also Young's modulus, Poisson's ratio and thermal properties. For a repair this is more important than the extra wear resistant properties, which would actually have a negative effect as the surrounding parent rail wears faster. The R260 was shown to be the best repair material, when applied as a repair the hardness was higher than that of newly manufactured R260, this could be a useful property for repair when the parent rail has undergone strain hardening, enhancing the homogeneity across the rail.

The successful application of such coatings is shown throughout this work to be partly dependent on the laser parameters, such as laser power and feed rate, being optimised. Laser clad parameters require further optimisation for non-continuous repair sites, as pre-heat and duration of heating is likely to be faster when applied to a smaller area than the more established continuous application. This optimisation will prevent some characteristics observed in early non-optimal laser clad applications, control the heat affected zone and prevent the formation of martensite.

Methods developed within this work for the analysis of laser clad coating on rail steels are applicable to other aspects of track analysis and maintenance. The Alicona is portable and therefore has the potential to be used on rail in the field, enabling the surface roughness of rail to be analysed. The Alicona can provide quick and accurate measurements without causing long track closures and its focus-variation technology is favourable over older probe based profilometers. Surface roughness measurements from different locations in track can feed back into further ratcheting modelling and it can also be used to monitor surface changes over time.

The eddy current trial conducted in Chapter 4 assessed a method of non-destructive examination in laser clad coatings. It was found that the whilst eddy current can be used on continuous laser

clad components, it is not suitable for laser clad repairs. This was due to false triggers at the interface of each repair site. It must therefore be noted that eddy current testing is not suitable where in-situ laser clad repairs have been applied.

The method developed to extract the Shear Yield Stress - Plastic Shear Strain relationship of a rail material can be applied to any rail removed from service. The method is a viable method to characterise novel rail materials in the development stage and also to test serviced rail as the shear yield data and quantification of plastic flow are independent of any knowledge of the applied stress that generated the flow. The analysis could be conducted on the materials directly without running twin-disc experiments, although measurements on unstrained material would be required using part of the material free from deformation, for example, well below the running surface. The main caveat to this would be that the rail must have experienced enough stress to accumulate visible plastic shear strain. This method could be used to analyse track removed from service.

Chapter 8

Conclusions and further work

8.1 Conclusions

The aim set out at the beginning of this thesis was to quantify plastic damage and identify its causes and consequences in novel rail materials consisting of low carbon Martensitic Stainless Steel MSS alloy with 14.64% chromium applied through laser cladding to 0.62% carbon steel alloy substrates. This has been achieved by developing a method to characterise material response to cyclic loading in novel materials, experimentally testing laser clad repairs, studying the surface topography of conventional rail steel and laser clad coatings and using a numerical method to quantify plasticity within laser clad coated rails.

Additively manufactured laser clad coatings were considered as a method to enhance longer lengths of railway track components and as an in-situ repair method. In respect to laser clad coating as an enhancement technique it is found that plasticity is reduced to the shallow depths within the laser clad coating (around 50 μm below the contact area) which is an improvement compared to the unclad R260 grade rail steel (around 400 μm below the contact area). The depth of laser clad coating is shown to be critical to the effectiveness of the enhancement, with plastic deformation observed below the laser clad coating in the heat affected zone (HAZ) when it is applied to a very shallow depth.

Applying powdered R260 grade rail steel to the R260 substrate rail was found to provide the most successful laser clad repair. Applying a much harder laser clad material saw the different strain rates of the two materials cause uneven deformation and as a result crack initiation points were observed at the interface on the trailing edge. This characteristic of repairing with a harder material was shown to be comparable to areas of White Etching Layer (WEL) and as such is not seen to be a favourable method of repair. The shallow repairs experienced plastic deformation in the HAZ below and surrounding the repair as seen in the enhancement method tests. The harder laser clad repair materials were pushed along with the plastic deformation within the surrounding rail. This caused the repair to become elongated and much thinner at the leading edge. Although a harder material is not recommended as a repair, this material flow must be considered and further testing would be required if it was to be applied at an Insulated Block Joint (IBJ).

The laser clad coating method is at a stage of development where optimised parameters such as pre-heat, laser power and flow rate can be readily achieved by specialist laser cladding operators for full components, this controls the level and microstructure of the heat affected zone. It was seen in the repair tests, however, that the HAZ is less well controlled around the small repairs, which was attributed to the smaller area for heat dissipation and hence a faster cooling rate. The material response to cyclic loading was measured for the HAZ, considering it as a separate material. The HAZ was found to be much harder than the R260 substrate rail as such the yield stress

in this zone was found to be higher, in conjunction with the laser clad coating the HAZ can be beneficial in further protecting the substrate rail.

Characterising the material response to load required a novel method to be developed due to the small sample sizes and the high resistance to ratcheting. The developed method proved to be successful and it was discovered that the loading history was not relevant to the extraction of the SYS-PSS curve, which was derived from a sample which had been run under conditions, where the maximum contact pressure and coefficient of traction were high enough to generate strain accumulation. The method is therefore expected to be transferable to rail samples removed from track. Using twin-disc testing to generate the strain under high hydrostatic loading provided a realistic method to represent rail-wheel contact and was suggested within the literature to be more reliable than tensile tests. A further benefit to the method is that it is much quicker and more cost effective than other methods which involve extensive testing.

Despite the improvements to wear and RCF resistance seen previously with the application of a laser clad coating, plasticity is still seen within the shallow depths below the rail-wheel contact. Standard modelling with a smooth Hertzian contact does not predict the ratcheting observed in the laser clad coatings due to the high yield stress of the material. To explain this the surface roughness was assumed to create a series of individual asperity Hertzian contacts superpositioned across the full contact area. To allow accurate modelling surface topography was measured using an Alicona PortableRL Infinite Focus microscope. The MSS laser clad coating and R260 grade rail steel had different levels of roughness with the MSS having less asperities in contact across the full contact width. The MSS asperities in contact had wider asperity tip radii than the R260.

It was shown through numerical simulation that the peak subsurface stresses were predicted to be much closer to the surface, supporting the results seen in experimentation. The maximum Hertzian contact pressure produced by the assumed asperity contacts was shown to be up to 6 times higher than the smooth contact depending on the surface roughness, explaining the level of ratcheting observed in the shallow surface depths of the laser clad coating. Through analysis of the unlubricated twin-disc tests at 1500 MPa, the rail-wheel contact with MSS laser clad coating had a lower peak coefficient of traction (μ=0.38) than the R260 grade rail steel (μ=0.43). Although lower than the standard grade rail steel the level of CoT was still in the range which pushes the peak stresses towards the surface.

Through the simulation of ratcheting using the adapted layer model with the novel addition of a surface amplification from the central asperity contact, the effect of surface roughness was seen as surface plasticity was modelled for the first time. This explained the phenomenon of ratcheting when the applied shear stress is lower than the rail material's yield stress. The potentially negative influence of the HAZ was shown within the layer model results, with a higher magnitude of plastic shear stain accumulation seen in the HAZ compared with the substrate material. To completely eliminate ratcheting within the rail for loads of up to 1500 MPa, it was shown that a laser clad coating deposition of around 10 mm (normalised depth 1.45b) would be required.

This thesis has provided contributions to the current literature in respect to laser clad coating as

a method to enhance and repair rail, the effect of surface roughness in contact mechanics and characterisation methods for novel materials. The results from testing laser clad coatings as an in-situ repair method shows that material selection is vital to ensure the repair is compatible with the substrate rail. This research therefore helps to steer the development of laser clad repairs to further study suitable materials. Testing full laser clad coatings has confirmed that with optimised laser parameters a successful enhancement can be achieved. Knowledge is added here that the depth of laser clad coating must be sufficient enough to encompass the peak shear stress in the contact to avoid plastic deformation below the coating.

The research presented here which studied the effect of surface roughness on maximum Hertzian contact subsurface stress helps to explain why ratcheting can still occur in new and novel rail materials. This work was limited to the MSS laser clad coating and R260 grade rail steel within this thesis, but opens the area to further research by highlighting the requirement to incorporate this in modern rail material development. Through the consideration of the conclusions presented in this section it can be seen that this thesis has been successful in meeting its aim of quantifying plastic damage and identifying its causes and consequences in additively manufactured railway track components with premium laser clad coatings.

8.2   Future work

Following the research presented in this thesis there are several areas discovered which could be studied in the future to further add to knowledge, which can be divided into additive manufacturing and surface roughness in contact mechanics. The research into the effect of surface roughness and its influence on the plastic deformation has been successful in explaining the ratcheting in new and novel rail materials. This has been limited to the MSS laser clad coating and R260 grade rail steel which are the focus materials within this thesis. This could be extended to other modern rail materials such as alternative laser clad coatings like Stellite, high performance (HP) rail materials or cast manganese crossing components. This work could involve characterising the material response to cyclic loading using the method developed in Chapter 3, followed by surface topography measurements and the application of the layer model developed for asperity contacts. Initial tests with cast manganese are presented in Appendix A, however, further testing and analysis is required due to the complexity of twinning induced plasticity rather than ratcheting in manganese alloys [167].

The research to develop laser clad coatings as a repair method can be further developed. The laser process parameters require optimisation to control the heat input and post process cooling to ensure that the HAZ is controlled and prevents the formation of martensite. The optimised parameters will also ensure that an inclusion free deposition is achieved consistently with a strong bond at the interface. This work would be best achieved with the expertise of laser cladding manufacturers who will be able to scale the process parameters from the successful full scale coatings applied previously. The research in this thesis indicated that R260 grade rail steel had the most effective repair when repaired with laser clad powdered R260. Work must now be done to optimise the laser clad process for R260 material in small repair sites. This homogeneity of materials

ensured that the rate of ratcheting was continuous avoiding crack initiation at the interface.

Once the laser cladding process parameters are optimised for an R260 repair further small scale repair tests are required to assess wear and RCF. An approach could be taken to replicate the twin-disc tests done in this thesis in both dry and water lubricated conditions. To assess the surface evolution, integrity, RCF and wear rate of the R260 repair it would be advisable to have repair discs manufactured with just one repair site per disc. A base case R260 disc could be used to compare the wear of the repair discs. This method would avoid any influence from dynamic loading from the harder materials across the rail disc surface.

The following stage in developing the method as an in-situ repair would be to design an engineering process which can make the laser cladding machinery portable. De Becker et al. [168] propose an addition of a robotic arm to a maintenance train to create a fully automated application with a weld repair. A similar method would be appropriate for applying laser clad coatings as in-situ repairs. A United States patent can also be found for an on-site steel rail laser processing engineering vehicle from October 2020 from Zeng et al. [169]. An area of consideration within this research is health and safety. The laser cladding process uses a class 4 laser [170] which is both a fire hazard and personal injury hazard. A way to safely contain and cover the laser whilst working in-situ must be incorporated into the design.

Additional research questions remain unanswered within the area of laser cladding as an enhancement for the life extension of railway track components. Firstly, due to the residual stresses created in the laser clad coating process, as demonstrated by Narayana et al. [128], can a continuously welded rail be enhanced with laser clad coating whilst maintaining a stress free state? Secondly, for a rail enhancement with a MSS laser clad coating how can maintenance be conducted? Can grinding be conducted on the hard coating and what effect does this have on the surface topography?

When applied in-situ the effects of environmental factors could cause porosity in the clad coating through imperfect process parameters, can this be tolerated? This work is currently in progress through the manufacture of twin-discs deliberately clad with less than optimised parameters. Rail discs have been X-Ray scanned with 'custom 450 kVp/225 kVp hutch' CT system at the University of Southampton [171] prior to testing and after standard twin-disc tests. This preliminary work was undertaken during the research but was outside the scope of this project to fully explore this approach. Once completed it has the potential to demonstrate how cracks propagate within poorly deposited clad coatings.

Further research could be conducted following the new modelling of the effect that surface roughness has on contact mechanics and ratcheting. The work conducted here is a first step in understanding why ratcheting occurs within rail materials where the shear yield stress is higher than the applied shear stress. The modelling within this thesis focused on the stress experienced as a result of the single mid asperity maximum contact pressure, however, this could be extended to create a full contact of super-positioned micro contacts.

References

[1] S. R. Lewis, S. Fretwell-Smith, P. S. Goodwin, L. Smith, R. Lewis, M. Aslam, D. I. Fletcher, K. Murray, and R. Lambert, "Improving rail wear and RCF performance using laser cladding," *Wear*, vol. 366-367, pp. 268–278, 2016.

[2] P. Lu, S. R. Lewis, S. Fretwell-Smith, D. L. Engelberg, D. I. Fletcher, and R. Lewis, "Laser cladding of rail; the effects of depositing material on lower rail grades," *Wear*, vol. 438-439, no. September, 2019.

[3] British Steel, "Steel products for rail applications UK-manufactured profiles and grades," British Steel, Tech. Rep., 2020. [Online]. Available: https://britishsteel.co.uk/media/323531/british-steel-uk-rail-profiles-and-grades.pdf

[4] "HP335 Rail for combatting rolling contact fatigue and wear - Technical data sheet," 2017. [Online]. Available: https://britishsteel.co.uk/media/40422/hp335-data-sheet.pdf

[5] S. L. Guo, D. Y. Sun, F. C. Zhang, X. Y. Feng, and L. H. Qian, "Damage of a Hadfield steel crossing due to wheel rolling impact passages," *Wear*, vol. 305, no. 1-2, pp. 267–273, 2013.

[6] Deloro Stellite, "Stellite TM 6 Alloy," Tech. Rep., 2008.

[7] S. Lewis, R. Lewis, P. Goodwin, S. Fretwell-Smith, D. Fletcher, K. Murray, and J. Jaiswal, "Full-scale testing of laser clad railway track; Case study – Testing for wear, bend fatigue and insulated block joint lipping integrity," *Wear*, vol. 376-377, pp. 1930–1937, apr 2017.

[8] Department for Transport, "Rail Factsheet," Department for Transport, Tech. Rep., 2019. [Online]. Available: https://assets.publishing.service.gov.uk/government/uploads/system/uploads/attachment{_}data/file/851082/rail-factsheet-2019.pdf

[9] Department for Transport., "Rail Factsheet Desember 2020," 2020. [Online]. Available: https://assets.publishing.service.gov.uk/government/uploads/system/uploads/attachment{_}data/file/942425/rail-factsheet-2020.pdf

[10] High Speed 2 Ltd, "Capacity - more freight by rail." [Online]. Available: https://www.hs2.org.uk/why/capacity/capacity-more-freight-by-rail/

[11] Office of Rail and Road, "Passenger Rail Usage 2020-21 Quarter 2," Office of Rail and Road, Tech. Rep., 2020.

[12] Office of Rail and Road., "Passenger Rail Usage 2021-22 Quarter 1," 2021. [Online]. Available: https://dataportal.orr.gov.uk/media/2010/passenger-rail-usage-2021-22-q1.pdf

[13] Office of Rail and Road.., "Rail Industry Finance (UK) - 2019-20," Office of Rail and Road, Tech. Rep., 2020.

[14] F. Schmid, *Best practice in wheel-rail interface management for mixed-traffic railways*. Hampshire: University of Birmingham Press, 2010.

[15] C. Esveld, *Modern railway track*. Delft: MRT Productions, 2001.

[16] British Steel, "Flat bottomed vignole rail." [Online]. Available: https://britishsteel.co.uk/what-we-do/rail/flat-bottomed-vignole-rail/

[17] U. Olofsson and Y. Lyu, "Open System Tribology in the Wheel-Rail Contact-A Literature Review," *Applied Mechanics Reviews*, vol. 69, no. 6, nov 2017.

[18] M. Masoumi, E. A. A. Echeverri, A. P. Tschiptschin, and H. Goldenstein, "Improvement of wear resistance in a pearlitic rail steel via quenching and partitioning processing," *Scientific Reports*, vol. 9, no. 1, pp. 1–12, dec 2019.

[19] J. Perez-Unzueta and J. H. Beynon, "Microstructure and wear resistance of pearlitic rail steels," *Wear*, p. 173182, 1993.

[20] British Steel, "High Performance (HP)." [Online]. Available: https://britishsteel.co.uk/what-we-do/rail/flat-bottomed-vignole-rail/high-performance-hp/

[21] "British Steel SF heat-treated range." [Online]. Available: https://britishsteel.co.uk/media/40420/sf-range-data-sheet.pdf

[22] R. Lewis and U. Olofsson, *Wheel-rail interface handbook*. Oxford: Woodhead Publishing, 2009.

[23] W. R. Tyfour, J. H. Beynon, and A. Kapoor, "The steady state wear behaviour of pearlitic rail steel under dry rolling-sliding contact conditions," *Wear*, vol. 180, no. 1-2, pp. 79–89, 1995.

[24] ESDU, "Contact Phenomena. II: Stress Fields and Failure Criteria in Concentrated Elastic Contacts Under Combined Normal and Tangential Loading." *Engineering Sciences Data Unit, Data Items*, 1984.

[25] U. Olofsson, Y. Zhu, S. Abbasi, R. Lewis, and S. Lewis, "Tribology of the wheel-rail contact-aspects of wear, particle emission and adhesion." *Vehicle System Dynamics*, vol. 51, no. 7, pp. 1091–1120, 2013.

[26] Railway Group Standard, "Compatability requirements for braking systems of rail vehicles," pp. 1–67, 2016. [Online]. Available: https://www.rssb.co.uk/standards-catalogue/CatalogueItem/GMRT2045-Iss-4

[27] S. Fukagai, H. P. Brunskill, A. K. Hunter, R. S. Dwyer-Joyce, and R. Lewis, "Transitions in rolling-sliding wheel/rail contact condition during running-in," *Tribology International*, vol. 149, sep 2020.

[28] H. Hertz, "Ueber die Berührung fester elastischer Körper." *Journal für die reine und angewandte Mathematik*, vol. 92, pp. 156–171, 1882.

[29] W. Yan and F. D. Fischer, "Applicability of the Hertz contact theory to rail-wheel contact problems," *Archive of Applied Mechanics*, vol. 70, pp. 255–268, 2000.

[30] M. B. Marshall, R. Lewis, R. S. Dwyer-Joyce, and S. Björklund, "Experimental Characterization of Wheel-Rail Contact Patch Evolution," *Journal of Tribology*, 2006.

[31] K. Johnson, *Contact Mechanics*, 9th ed. Cambridge: Cambridge University Press, 2003.

[32] A. Kapoor, F. J. Franklin, S. K. Wong, and M. Ishida, "Surface roughness and plastic flow in rail wheel contact," *Wear*, vol. 253, pp. 257–264, 2002.

[33] T. Nogi and T. Kato, "Influence of a hard surface layer on the limit of elastic contact: Analysis using a real surface model." *Japanese Journal of Tribology*, vol. 42, pp. 270–271, 1997.

[34] D. Nowell and D. A. Hills, "Hertzian Contact of Ground Surfaces," *Journal of Tribology*, vol. 111, no. 1, pp. 175–179, jan 1989.

[35] D. Nowell, D. Hills, and J. O'Connor, "An Analysis of Fretting Fatigue," *Proc. ImechE Int. Conf. on tribology - Friction, lubrication and wear fifty years on*, pp. 965–973, 1987.

[36] A. Mihailidis, V. Bakolas, and N. Drivakos, "Subsurface stress field of a dry line contact," *Wear*, vol. 249, no. 7, pp. 546–556, jul 2001.

[37] A. Martini, B. Escoffier, Q. Wang, S. B. Liu, L. M. Keer, D. Zhu, and M. Bujold, "Prediction of subsurface stress in elastic perfectly plastic rough components," *Tribology Letters*, vol. 23, pp. 243–251, 2006.

[38] J. Greenwood and J. Williamson, "Contact of nominally flat surfaces." *Proceedings of the Royal Society of London. Series A. Mathematical and Physical Sciences*, vol. 295(1442), pp. 300–319, 1966.

[39] J. Greenwood, "A Unified Theory of Surface Roughness," *Proceedings of the Royal Society of London. Series A, Mathematical and Physical Sciences*, vol. 393, pp. 133–157, 1984.

[40] W. R. Chang, I. Etsion, and D. B. Bogy, "An Elastic-Plastic Model for the Contact of Rough Surfaces," *Journal of Tribology*, vol. 109, no. 2, pp. 257–263, apr 1987.

[41] R. L. Jackson and I. Green, "A statistical model of elasto-plastic asperity contact between rough surfaces," *Tribology International*, vol. 39, no. 9, pp. 906–914, sep 2006.

[42] R. Jackson and I. Green, "A Finite Element Study of Elasto-Plastic Hemispherical Contact Against a Rigid Flat," *Journal of Tribology*, vol. 127, pp. 343–354, 2005.

[43] A. Majumdar and B. Bhushan, "Role of fractal geometry in roughness characterization and contact mechanics of surfaces," *Journal of Tribology*, vol. 112, no. 2, pp. 205–216, apr 1990.

[44] Y.-F. Gao and A. F. Bower, "Elastic-Plastic Contact of a Rough Surface with Weierstrass Profile," *Source: Proceedings: Mathematical, Physical and Engineering Sciences*, vol. 462, no. 2065, pp. 319–348, 2006.

[45] A. Jourani, "Effect of 3D fractal dimension on contact area and asperity interactions in elastoplastic contact," *AIP Advances*, vol. 6, no. 5, p. 055309, may 2016.

[46] A. Pogačnik and M. Kalin, "How to determine the number of asperity peaks, their radii

and their heights for engineering surfaces: A critical appraisal," *Wear*, vol. 300, no. 1-2, pp. 143–154, mar 2013.

[47] A. Kapoor and K. L. Johnson, "Plastic ratchetting as a mechanism of metallic wear," *Proceedings of the Royal Society A: Mathematical, Physical and Engineering Sciences*, vol. 445, no. 1924, pp. 367–381, 1994.

[48] W. R. Tyfour, J. H. Beynon, and A. Kapoor, "Deterioration of rolling contact fatigue life of pearlitic rail steel due to dry-wet rolling-sliding line contact," *Wear*, vol. 197, no. 1-2, pp. 255–265, 1996.

[49] E. Hiensch, F. Franklin, and J. Nielsen, "Prevention of RCF damage in curved track through development of the Infra-star two-material rail," *Fatigue and Fracture of engineering materials and structures*, vol. 26, 2003.

[50] A. Kapoor, "A re-evaluation of the life to rupture of ductile metals by cyclis plastic strain." *Fatigue & Fracture of Engineering Materials and Structures*, vol. 17, no. 2, pp. 201–219, feb 1994.

[51] A. Kapoor and F. Franklin, "Tribological layers and the wear of ductile materials," *Wear*, vol. 245, no. 1-2, pp. 204–215, oct 2000.

[52] A. F. Bower, "Influence of Strain Hardening on the Cumulative Plastic Deformation Caused By Repeated Rolling and Sliding Contact." *Cambridge University, Engineering Department, (Technical Report) CUED/C-Mech*, vol. 37, no. 4, 1987.

[53] A. C. Athukorala, D. V. De Pellegrin, and K. I. Kourousis, "A unified material model to predict ratcheting response in head-hardened rail steel due to non-uniform hardness distributions," *Tribology International*, vol. 111, pp. 26–38, 2017.

[54] J. L. Chaboche, "Time-independent constitutive theories for cyclic plasticity," *International Journal of Plasticity*, vol. 2, no. 2, pp. 149–188, jan 1986.

[55] Y. Zhu and L. H. Poh, "A finite deformation elasto-plastic cyclic constitutive model for ratchetting of metallic materials," *International Journal of Mechanical Sciences*, vol. 117, pp. 265–274, oct 2016.

[56] C. L. Pun, Q. Kan, P. J. Mutton, G. Kang, and W. Yan, "An efficient computational approach to evaluate the ratcheting performance of rail steels under cyclic rolling contact in service," *International Journal of Mechanical Sciences*, vol. 101-102, pp. 214–226, 2015.

[57] C. L. Pun, D. Welsby, and P. Mutton, "Shakedown analysis of three premium rail steels subjected to multiaxial cyclic loading conditions," *Proceedings of the 11th International Conference on Contact Mechanics and Wear of Rail/wheel Systems, CM 2018*, pp. 803–811, 2018.

[58] A. F. Bower and K. L. Johnson, "Plastic flow and shakedown of the rail surface in repeated wheel-rail contact," *Wear*, vol. 144, no. 1-2, pp. 1–18, apr 1991.

[59] D. A. Hills and D. W. Ashelby, "The influence of residual stresses on contact-load-bearing capacity," *Wear*, vol. 75, no. 2, pp. 221–239, jan 1982.

[60] M. Ekh, A. Johansson, H. Thorberntsson, and B. Lennart Josefson, "Magnus Ekh Models for Cyclic Ratchetting Plasticity-Integration and Calibration," 2000. [Online]. Available: http://asmedigitalcollection.asme.org/materialstechnology/article-pdf/122/1/49/5746663/49{_}1.pdf

[61] C. O. Frederick and P. J. Armstrong, "A mathematical representation of the multiaxial Bauschinger effect," *Materials at High Temperatures*, vol. 24, no. 1, pp. 1–26, 2007. [Online]. Available: https://www.researchgate.net/publication/233517426{_}A{_}Mathematical{_}Representation{_}of{_}the{_}Multiaxial{_}Bauscinger{_}Effect

[62] Y. Jiang and H. Sehitoglu, "Rolling contact stress analysis with the application of a new plasticity model," *Wear*, vol. 191, no. 1-2, pp. 35–44, jan 1996.

[63] A. Johansson, B. Pålsson, M. Ekh, J. C. Nielsen, M. K. Ander, J. Brouzoulis, and E. Kassa, "Simulation of wheel–rail contact and damage in switches & crossings," *Wear*, vol. 271, no. 1-2, pp. 472–481, may 2011.

[64] R. Skrypnyk, "Prediction of plastic deformation and wear in railway crossings – Comparing the performance of two rail steel grades," *Wear*, vol. 428-429, pp. 302–314, jun 2019.

[65] R. Skrypnyk, J. C. O. Nielsen, M. Ekh, ·. Björn, and A. Pålsson, "Metamodelling of wheel-rail normal contact in railway crossings with elasto-plastic material behaviour," *Engineering with Computers*, vol. 35, pp. 139–155, 2019. [Online]. Available: https://doi.org/10.1007/s00366-018-0589-3

[66] A. Kapoor, "Wear by plastic ratchetting," *Wear*, pp. 119–130, 1997.

[67] A. Kapoor, J. H. Beynon, D. I. Fletcher, and M. Loo-Morrey, "Computer simulation of strain accumulation and hardening for pearlitic rail steel undergoing repeated contact," *The Journal of Strain Analysis for Engineering Design*, 2004.

[68] K. A. Meyer, M. Ekh, and J. Ahlström, "Modeling of kinematic hardening at large biaxial deformations in pearlitic rail steel," *International Journal of Solids and Structures*, vol. 130-131, pp. 122–132, jan 2018.

[69] K. A. Meyer, D. Nikas, and J. Ahlström, "Microstructure and mechanical properties of the running band in a pearlitic rail steel: Comparison between biaxially deformed steel and field samples," *Wear*, vol. 396-397, pp. 12–21, feb 2018.

[70] K. A. Meyer, J. Ahlström, and M. Ekh, "Characterization of yield surface evolution due to large plastic shear strains in pearlitic rail steel," *Proceedings of the 11th International Conference on Contact Mechanics and Wear of Rail/wheel Systems, CM 2018*, pp. 745–752, 2018.

[71] F. Franklin, I. Widiyarta, and A. Kapoor, "Computer simulation of wear and rolling contact fatigue," *Wear*, vol. 251, no. 1-12, pp. 949–955, oct 2001.

[72] D. I. Fletcher, F. J. Franklin, and A. Kapoor, "Image analysis to reveal crack development using a computer simulation of wear and rolling contact fatigue." *Fatigue and Fracture of Engineering Materials and Structures*, vol. 26, pp. 957–967, 2003.

[73] F. Franklin and A. Kapoor, "Modelling wear and crack initiation in rails," in *ImechE Part F: J. Rail and Rapid Transit*, 2006.

[74] F. Franklin, J. Garnham, D. Fletcher, C. Davis, and A. Kapoor, "Modelling rail steel microstructure and its effect on crack initiation," *Wear*, vol. 265, no. 9-10, pp. 1332–1341, oct 2008.

[75] J. E. Garnham, F. J. Franklin, D. I. Fletcher, A. Kapoor, and C. L. Davis, "Predicting the life of steel rails," *Proceedings of the Institution of Mechanical Engineers, Part F: Journal of Rail and Rapid Transit*, vol. 221, no. 1, pp. 45–58, jan 2007.

[76] S. Wong, A. Kapoor, and J. Williams, "Shakedown limits on coated and engineered surfaces," *Wear*, vol. 203-204, pp. 162–170, mar 1997.

[77] I. N. Dyson, J. A. Williams, and A. Kapoor, "The effect of surface hardening on the elastic shakedown of elliptical contacts," *Proceedings of the Institution of Mechanical Engineers, Part J: Journal of Engineering Tribology*, vol. 213, no. 4, pp. 287–298, apr 1999.

[78] J. Archard, "Contact and Rubbing of Flat Surfaces," *Journal of Applied Physics*, vol. 24, no. 8, pp. 981–988, 1953.

[79] J. Williams, *Engineering Tribology*.   New York: Oxford University Press, 1994.

[80] R. Lewis, R. S. Dwyer-Joyce, U. Olofsson, J. Pombo, J. Ambrósio, M. Pereira, C. Ariaudo, and N. Kuka, "Mapping railway wheel material wear mechanisms and transitions:," *Proceedings of the Institution of Mechanical Engineers, Part F: Journal of Rail and Rapid Transit*, vol. 224, no. 3, pp. 125–137, mar 2010.

[81] P. Christoforou, D. I. Fletcher, and R. Lewis, "Benchmarking of premium rail material wear," *Wear*, vol. 436-437, p. 202990, oct 2019.

[82] N. P. Suh, "An overview of the delamination theory of wear," *Wear*, vol. 25, pp. 111–124, 1973.

[83] J. Garnham and J. H. Beynon, "The early detection of rolling-sliding contact fatigue cracks," *Wear*, vol. 144, 1991.

[84] E. Magel, P. Mutton, A. Ekberg, and A. Kapoor, "Rolling contact fatigue, wear and broken rail derailments." *Wear*, vol. 366-367, pp. 249–257, 2016.

[85] T. Anderson, *Fracture mechanics: fundamentals and applications*, 2nd ed.   Florida: CRC Press LLC, 1995.

[86] S. H. Mai, A. Gravouil, M. L. Nguyen-Tajan, and B. Trollé, "Numerical simulation of rolling contact fatigue crack growth in rails with the rail bending and the frictional contact," *Engineering Fracture Mechanics*, no. 174, pp. 196–206, 2017.

[87] D. I. Fletcher, P. Hyde, and A. Kapoor, "Growth of multiple rolling contact fatigue cracks driven by rail bending modelled using a boundary element technique," *Proceedings of the*

Institution of Mechanical Engineers, Part F: Journal of Rail and Rapid Transit, vol. 218, no. 3, pp. 243–253, may 2004.

[88] D. I. Fletcher, L. Smith, and A. Kapoor, "Rail rolling contact fatigue dependence on friction, predicted using fracture mechanics with a three-dimensional boundary element model," *Engineering Fracture Mechanics*, vol. 76, no. 17, pp. 2612–2625, nov 2009.

[89] D. I. Fletcher, "Numerical simulation of near surface rail cracks subject to thermal contact stress," *Wear*, 2014.

[90] R. I. Carroll and J. H. Beynon, "Rolling contact fatigue of white etching layer: Part 1. Crack morphology," *Wear*, vol. 262, no. 9-10, pp. 1253–1266, apr 2007.

[91] O. Vargolici, P. Merino, A. Saulot, J. Cavoret, S. Simon, F. Ville, and Y. Berthier, "Influence of the initial surface state of bodies in contact on the formation of white etching layers under dry sliding conditions," *Wear*, vol. 366-367, pp. 209–216, nov 2016.

[92] P. Clayton and M. B. P. Allery, "Metallurgical Aspects of Surface Damage Problems in Rails," *Canadian Metallurgical Quarterly*, vol. 21, no. 1, pp. 31–46, 1982.

[93] Q. Lian, G. Deng, A. Al-Juboori, H. Li, Z. Liu, X. Wang, and H. Zhu, "Crack propagation behavior in white etching layer on rail steel surface," *Engineering Failure Analysis*, vol. 104, pp. 816–829, oct 2019.

[94] C. L. Pun, Q. Kan, P. J. Mutton, G. Kang, and W. Yan, "A single parameter to evaluate stress state in rail head for rolling contact fatigue analysis," *Fatigue & Fracture of Engineering Materials & Structures*, vol. 37, no. 8, pp. 909–919, aug 2014.

[95] A. Dey, J. Kurz, and L. Tenczynski, "Detection and evaluation of rail defects with non-destructive testing methods," *19th World Conference on Non Destructive Testing*, pp. 1–9, 2016.

[96] Network Rail, "Ultrasonic Rail Inspection." [Online]. Available: https://cdn.networkrail. co.uk/wp-content/uploads/2019/06/Ultrasonic-Rail-Inspection-v1.pdf

[97] J. Kalousek, P. Sroba, and C. Hegelund, "Analysis of rail grinding tests and implications for corrective and preventative grinding," *Heavy Haul Railway Conference.*, 1989.

[98] P. Hyde and D. Fletcher, "Planning Rail Grinding Using Crack Growth Predictions*," *Journal of Mechanical Systems for Transportation and Logistics*, vol. 3, no. 1, 2010.

[99] E. Magel, M. Roney, J. Kalousek, and P. Sroba, "The blending of theory and practice in modern rail grinding." *Fatigue and Fracture of Engineering Materials and Structures*, vol. 26, no. 10, pp. 921–929, oct 2003.

[100] Network Rail, "Head wash repair (HWR) technique for the removal of rail head defects in flat bottomed rails," *Network Rail Certificate of Acceptance - Railtech International*, 2013.

[101] H. K. Jun, J. W. Seo, I. S. Jeon, S. H. Lee, and Y. S. Chang, "Fracture and fatigue crack growth analyses on a weld-repaired railway rail," *Engineering Failure Analysis*, vol. 59, pp. 478–492, jan 2016.

[102] H.-K. Jun, D.-W. Kim, I.-S. Jeon, S.-H. Lee, and Y.-S. Chang, "Investigation of residual stresses in a repair-welded rail head considering solid-state phase transformation," *Fatigue and Fracture of Engineering Materials and Structures*, vol. 40, pp. 1059–1071, 2017.

[103] B. L. Josefson and J. W. Ringsberg, "Assessment of uncertainties in life prediction of fatigue crack initiation and propagation in welded rails," *International Journal of Fatigue*, vol. 31, no. 8-9, pp. 1413–1421, aug 2009.

[104] E. Mortazavian, Z. Wang, and H. Teng, "Repair of light rail track through restoration of the worn part of the railhead using submerged arc welding process," *International Journal of Advanced Manufacturing Technology*, vol. 107, no. 7-8, pp. 3315–3332, 2020.

[105] R. Kumar and H. K Arya, "Experimental Determination of Cooling Rate and its Effect on Microhardness in Submerged Arc Welding of Mild Steel Plate (Grade c-25 as per IS 1570)," *Journal of Material Science & Engineering*, vol. 03, no. 02, 2013.

[106] L. Xin, V. Markine, and I. Shevtsov, "Analysis of the effect of repair welding/grinding on the performance of railway crossings using field measurements and finite element modeling," *Proceedings of the Institution of Mechanical Engineers, Part F: Journal of Rail and Rapid Transit*, vol. 232, no. 3, pp. 798–815, mar 2018.

[107] J. Gao, W. Zhai, and Y. Guo, "Wheel-rail dynamic interaction due to rail weld irregularity in high-speed railways," *Proceedings of the Institution of Mechanical Engineers, Part F: Journal of Rail and Rapid Transit*, vol. 232, pp. 249–261, 2018.

[108] L. Sexton, S. Lavin, G. Byrne, and A. Kennedy, "Laser cladding of aerospace materials," *Journal of Materials Processing Technology*, vol. 122, no. 1, pp. 63–68, mar 2002.

[109] N. Almeida, L. Candido, G. Faria, M. Fernandes de Lima, and V. Trindade, "Laser Cladding and Thermal Spray Coatings on Steel Pipe Serving the Oil and Gas Industry," *Journal of Material Science & Engineering*, vol. 5, no. 5, 2016.

[110] S. Lewis, R. Lewis, and D. Fletcher, "Assessment of laser cladding as an option for repairing/enhancing rails," *Wear*, vol. 330-331, pp. 581–591, may 2015.

[111] A. Clare, O. Oyelola, J. Folkes, and P. Farayibi, "Laser cladding for railway repair and preventative maintenance," *Journal of Laser Applications*, vol. 24, no. 3, p. 032004, aug 2012.

[112] A. T. Clare, O. Oyelola, T. E. Abioye, and P. K. Farayibi, "Laser cladding of rail steel with Co–Cr," *Surface Engineering*, vol. 29, no. 10, pp. 731–736, nov 2013.

[113] S. Niederhauser and B. Karlsson, "Fatigue behaviour of Co-Cr laser cladded steel plates for railway applications," in *Wear*, 2005.

[114] M. Hiensch, P. O. Larsson, O. Nilsson, D. Levy, A. Kapoor, F. Franklin, J. Nielsen, J. W. Ringsberg, and B. L. Josefson, "Two-material rail development: Field test results regarding rolling contact fatigue and squeal noise behaviour," *Wear*, vol. 258, no. 7-8, pp. 964–972, mar 2005.

[115] S. Niederhauser and B. Karlsson, "Mechanical properties of laser cladded steel," *Material Science and Technology*, vol. 19, 2003.

[116] J. L. Olofsson, "Patent: Method for improving the properties of railway wheels," 1998.

[117] W. J. Wang, J. Hu, J. Guo, Q. Y. Liu, and M. H. Zhu, "Effect of laser cladding on wear and damage behaviors of heavy-haul wheel/rail materials," *Wear*, 2014.

[118] W.-J. Wang, Z.-K. Fu, J. Guo, Y.-Q. Zhang, Q.-Y. Liu, and M.-H. Zhu, "Investigation on Wear Resistance and Fatigue Damage of Laser Cladding Coating on Wheel and Rail Materials under the Oil Lubrication Condition," *Tribology Transactions*, vol. 59, no. 5, pp. 810–817, sep 2016.

[119] F. C. Robles Hernández, A. O. Okonkwo, V. Kadekar, T. Metz, and N. Badi, "Laser cladding: The alternative for field thermite welds life extension," *Materials and Design*, 2016.

[120] Z. Fu, H. Ding, W. Wang, Q. Liu, J. Guo, and M. Zhu, "Investigation on microstructure and wear characteristic of laser cladding Fe-based alloy on wheel/rail materials," *Wear*, vol. 330-331, pp. 592–599, may 2015.

[121] W. J. Wang, Z. K. Fu, X. Cao, J. Guo, Q. Y. Liu, and M. H. Zhu, "The role of lanthanum oxide on wear and contact fatigue damage resistance of laser cladding Fe-based alloy coating under oil lubrication condition," *Tribology International*, 2016.

[122] Q. Lai, R. Abrahams, W. Yan, C. Qiu, P. Mutton, A. Paradowska, and M. Soodi, "Investigation of a novel functionally graded material for the repair of premium hypereutectoid rails using laser cladding technology," *Composites Part B: Engineering*, vol. 130, pp. 174–191, dec 2017.

[123] T. W. Institute, "The Cladding of Rail Sections," The Welding Institute, Tech. Rep. October, 2019.

[124] A. A. Siddiqui and A. K. Dubey, "Recent trends in laser cladding and surface alloying," p. 106619, feb 2021.

[125] J. W. Ringsberg, A. Skyttebol, and B. L. Josefson, "Investigation of the rolling contact fatigue resistance of laser cladded twin-disc specimens: FE simulation of laser cladding, grinding and a twin-disc test," *International Journal of Fatigue*, vol. 27, no. 6, pp. 702–714, jun 2005.

[126] H. ming Guo, Q. Wang, W. jian Wang, J. Guo, Q. yue Liu, and M. hao Zhu, "Investigation on wear and damage performance of laser cladding Co-based alloy on single wheel or rail material," *Wear*, 2015.

[127] A. Wu, J. Ren, Z. Peng, H. Murakawa, and Y. Ueda, "Numerical simulation for the residual stresses of Stellite hard-facing on carbon steel," *Journal of Materials Processing Technology*, vol. 101, 1998.

[128] A. Narayanan, M. Mostafavi, T. Pirling, S. Kabra, R. Lewis, M. J. Pavier, and M. J. Peel, "Residual stress in laser cladded rail," *Tribology International*, vol. 140, no. March, p. 105844, 2019.

[129] T. Roy, A. Paradowska, R. Abrahams, Q. Lai, M. Law, P. Mutton, M. Soodi, and W. Yan, "Effect of Cladding Direction on Residual Stress Distribution in Laser Cladded Rails," *World Academy of Science, Engineering and Technology International Journal of Civil and Environmental Engineering*, vol. 11, 2017.

[130] L. Meng, W. Zhao, K. Hou, D. Kou, Z. Yuan, X. Zhang, J. Xu, Q. Hu, D. Wang, and X. Zeng, "A comparison of microstructure and mechanical properties of laser cladding and laser-induction hybrid cladding coatings on full-scale rail," *Materials Science and Engineering A*, vol. 748, pp. 1–15, mar 2019.

[131] L. Meng, X. Zeng, K. Hou, Q. Hu, and D. Wang, "Effect of laser cladding and laser-induction hybrid cladding coatings on the bending properties and fracture behavior of rails," *Surface and Coatings Technology*, vol. 374, pp. 1038–1050, sep 2019.

[132] T. Roy, Q. Lai, R. Abrahams, P. Mutton, A. Paradowska, M. Soodi, and W. Yan, "Effect of deposition material and heat treatment on wear and rolling contact fatigue of laser cladded rails," *Wear*, vol. 412-413, pp. 69–81, oct 2018.

[133] Q. Lai, R. Abrahams, P. Mutton, C. Qiu, A. Paradowska, M. Soodi, T. Roy, and W. Yan, "Laser Cladding for Railway Repair: Influence of Depositing Materials and Heat Treatment on Microstructural Characteristics," in *ICRT 2017: Railway Development, Operations, and Maintenance - Proceedings of the 1st International Conference on Rail Transportation*, 2018, pp. 452–463.

[134] F. J. Franklin, G. J. Weeda, A. Kapoor, and E. J. M. Hiensch, "Rolling contact fatigue and wear behaviour of the infrastar two-material rail," in *Wear*, 2005.

[135] Y. Zhu, W. Wang, R. Lewis, W. Yan, S. R. Lewis, and H. Ding, "A Review on Wear Between Railway Wheels and Rails Under Environmental Conditions," *Journal of Tribology*, vol. 111, 2019.

[136] T. Roy, R. Abrahams, A. Paradowska, Q. Lai, P. Mutton, M. Soodi, P. Fasihi, and W. Yan, "Evaluation of the mechanical properties of laser cladded hypereutectoid steel rails," *Wear*, pp. 432–433, 2019.

[137] Q. Lai, R. Abrahams, W. Yan, C. Qiu, P. Mutton, A. Paradowska, X. Fang, M. Soodi, and X. Wu, "Effects of preheating and carbon dilution on material characteristics of laser-cladded hypereutectoid rail steels," *Materials Science and Engineering A*, vol. 712, pp. 548–563, jan 2018.

[138] R. Lewis and S. Lewis, "Twin-Disc Assessment of Friction, Wear and Fatigue Performance of Laser Clad Rail as an Alternative to Direct Replacement of Worn Rail," University of Sheffield, Tech. Rep., 2015.

[139] R. Lewis, P. Christoforou, W. J. Wang, A. Beagles, M. Burstow, and S. R. Lewis, "Investigation of the influence of rail hardness on the wear of rail and wheel materials under dry conditions (ICRI wear mapping project)," *Wear*, vol. 430-431, pp. 383–392, jul 2019.

[140] J. W. Ringsberg, F. J. Franklin, B. L. Josefson, A. Kapoor, and J. C. Nielsen, "Fatigue evaluation of surface coated railway rails using shakedown theory, finite element calculations, and lab and field trials," *International Journal of Fatigue*, vol. 27, no. 6, pp. 680–694, jun 2005.

[141] Network Rail, "IN2TRACK D2.2 Enhanced S and C Whole system Analysis, Design and Virtual validation," Tech. Rep. February 2019, 2019. [Online]. Available: https://projects.shift2rail.org/s2r{_}ip3{_}n.aspx?p=IN2TRACK

[142] J. W. Seo, J. C. Kim, S. J. Kwon, and H. K. Jun, "Effects of Laser Cladding for Repairing and Improving Wear of Rails," *International Journal of Precision Engineering and Manufacturing*, vol. 20, no. 7, pp. 1207–1217, 2019.

[143] A. S. Nellian, K. E. Tan, H. J. Hoh, J. H. L. Pang, I. Christian, and S. Y. Chua, "Microstructure and Wear Performance Assessment of Laser Cladded Rail Steel for Service Life Extension at Sharp-Radius Curves," in *2018 International Conference on Intelligent Rail Transportation, ICIRT 2018*. Institute of Electrical and Electronics Engineers Inc., feb 2019.

[144] M. Watson, P. Christoforou, P. Herrera, D. Preece, J. Carrell, M. Harmon, P. Krier, S. Lewis, R. Maiti, W. Skipper, E. Taylor, J. Walsh, M. Zalzalah, L. Alhadeff, R. Kempka, J. Lanigan, Z. S. Lee, B. White, K. Ishizaka, R. Lewis, T. Slatter, R. Dwyer-Joyce, and M. Marshall, "An analysis of the quality of experimental design and reliability of results in tribology research," *Wear*, vol. 426-427, pp. 1712–1718, apr 2019.

[145] D. Fletcher and J. Beynon, "Development of a machine for closely controlled rolling contact fatigue and wear testing," *Journal of testing and evaluation*, 2000.

[146] P. Benham, R. Crawford, and C. Armstrong, *Mechanics of engineering materials*, 2nd ed. Harlow: Longman, 1996.

[147] M. Ashby, H. Shercliff, and D. Cebon, *Materials: Engineering, science, processing and design*. Butterworth-Heinemann, 2009.

[148] M. F. Ashby, *Engineering materials 1 : an introduction to properties, applications and design*. Elsevier Butterworth-Heinemann, 2005.

[149] W. Oliver and G. Pharr, "An improved technique for determining hardness and elastic modulus using load and displacement sensing indentation experiments," *Journal of Materials Research*, vol. 7, no. 06, pp. 1564–1583, jun 1992.

[150] Bruker, "Hysitron TI Premier Nanoindenter." [Online]. Available: https://www.bruker.com/en/products-and-solutions/test-and-measurement/nanomechanical-test-systems/hysitron-ti-premier-nanoindenter.html

[151] J. Lukes, "Sample analysis report - Clad coating on rail," Bruker, Prague, CZ, Tech. Rep., 2019.

[152] ImageJ Software, "Image Processing and Analysis in Java." [Online]. Available: https://imagej.nih.gov/ij/docs/intro.html

[153] Q. Lai, R. Abrahams, W. Yan, C. Qiu, P. Mutton, A. Paradowska, M. Soodi, and X. Wu, "Influences of depositing materials, processing parameters and heating conditions on material characteristics of laser-cladded hypereutectoid rails," *Journal of Materials Processing Technology*, vol. 263, pp. 1–20, jan 2019.

[154] D. A. Cremers, "Handbook of laser-induced breakdown spectroscopy [electronic resource]," *John Wiley and Sons*, 2013.

[155] C. M. Li, Z. M. Zou, X. Y. Yang, Z. Q. Hao, L. B. Guo, X. Y. Li, Y. F. Lu, and X. Y. Zeng, "Quantitative analysis of phosphorus in steel using laser-induced breakdown spectroscopy in air atmosphere," *Journal of Analytical Atomic Spectrometry*, vol. 29, no. 8, pp. 1432–1437, 2014.

[156] W. Zhang, R. Zhou, K. Liu, J. Yan, Q. Li, Z. Tang, X. Li, Q. Zeng, and X. Zeng, "Sulfur determination in laser-induced breakdown spectroscopy combined with resonance Raman scattering," *Talanta*, vol. 216, p. 120968, aug 2020.

[157] A. Al-Juboori, D. Wexler, H. Li, H. Zhu, C. Lu, A. McCusker, J. McLeod, S. Pannil, and Z. Wang, "Squat formation and the occurrence of two distinct classes of white etching layer on the surface of rail steel," *International Journal of Fatigue*, vol. 104, pp. 52–60, nov 2017.

[158] D. I. Fletcher and A. Wilby, "Implementation of Nowell & Hills ground surface contact paper," Tech. Rep., 2021. [Online]. Available: https://docs.google.com/document/d/1LSgqfBjmmQOWZuWrPyOeI5Hjna9jSwy7/edit

[159] H. Poritsky, "Stresses and Deflections of Cylindrical Bodies in Contact With Application to Contact of Gears and of Locomotive Wheels," *Journal of Applied Mechanics*, vol. 17, no. 2, pp. 191–201, jun 1950.

[160] "PostgreSQL: The world's most advanced open source database." [Online]. Available: https://www.postgresql.org/

[161] "PHP: Hypertext Preprocessor." [Online]. Available: https://www.php.net/

[162] ESDU, "Contact Phonemena III: Calculation of individual stress cmponents in concentrated elastic contacts under combined normal and tangential loading." *Engineering Sciences Data Unit, Data Items*, may 1985.

[163] D. Nikas, X. Zhang, and J. Ahlström, "Evaluation of local strength via microstructural quantification in a pearlitic rail steel deformed by simultaneous compression and torsion," *Materials Science and Engineering: A*, vol. 737, pp. 341–347, nov 2018.

[164] O. Yazici, S. Yilmaz, and S. Yildirim, "Microstructural and Mechanical Properties Examination of High-Power Diode Laser-Treated R260 Grade Rail Steels Under Different Processing Temperatures," *Metallurgical and Materials Transactions A 2018 50:2*, vol. 50, no. 2, pp. 1061–1075, dec 2018.

[165] A. Wilby, "Load dependency," University of Sheffield, Tech. Rep., 2021.

[166] D. A. Hills, D. Nowell, and A. Sackfield, *Mechanics of elastic contacts*. Butterworth-Heinemann, 1993.

[167] X. Guo, S. Zaefferer, F. Archie, and W. Bleck, "Dislocation and twinning behaviors in high manganese steels in respect to hydrogen and aluminum alloying," *Procedia Structural Integrity*, vol. 13, pp. 1453–1459, jan 2018.

[168] J. Dobrzanski, Y. M. Goh, D. De Becker, J. Dobrzanski, Y. M. Goh, and L. Justham, "Towards the development of a deposition technology for an automated rail repair system." *UKRAS20 Conference: "Robots into the real world" Proceedings*, vol. 3, pp. 100–102, 2020.

[169] Zeng, "United States Patent: Onsite steel rail laser processing engineering vehicle," jan 2020.

[170] Gov UK, "Laser radiation: safety advice." [Online]. Available: https://www.gov.uk/government/publications/laser-radiation-safety-advice/laser-radiation-safety-advice{#}laser-classes

[171] University of Southampton, "Multidisciplinary, Multiscale, Microtomographic Volume Imaging." [Online]. Available: https://www.southampton.ac.uk/muvis/about/equipment/hutch.page

[172] C. Mahlami and X. Pan, "An overview on high manganese steel casting," *Advanced Sustainable Foundry*, 2014.

[173] R. Harzallah, A. Mouftiez, E. Felder, S. Hariri, and J.-P. Maujean, "Rolling contact fatigue of Hadfield steel X120Mn12," *Wear*, vol. 269, pp. 647–654, 2010.

Appendices

A SYS-PSS curve for alternative substrate rail materials

Cast Manganese crossing components

Cast manganese, also known as Hadfield steel, is often used in crossings, where high impact occurs. Cast manganese has 11-13% manganese and 1-1.3% carbon, maintaining a Mn/C ratio of 10:1. This composition provides work hardening properties under impact, starting at around 200 Hv and reaching up to 600 Hv under impact as reported by Mahlami et al. [172], ideal for typical loading at a crossing nose. Harzallah et al. [173] report surface hardness of 1000 Hv after 150,000 cycles in rolling contact tests. Along with impact resistance Hadfield steel has high values of elongation, this combination ensures that the cast components are not brittle. A sample of a cast manganese steel was removed from a cast manganese crossing nose and the microstructure can be seen in the optical micrograph in Figure 1.
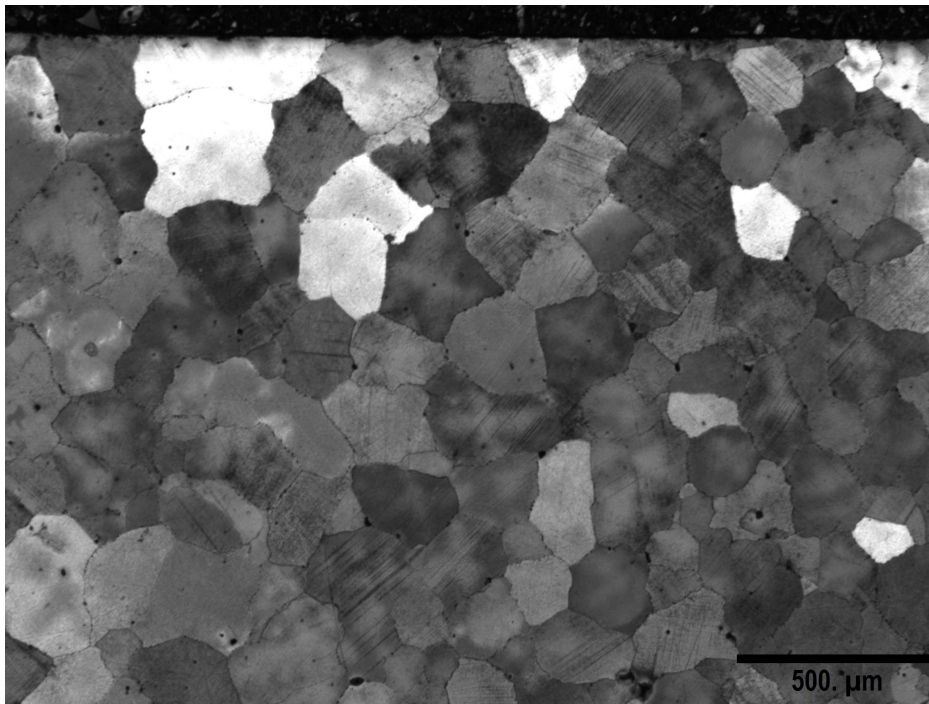
Figure 1: Optical micrograph showing the microstructure of cast manganese rail steel removed from a crossing nose.

Cast-manganese also known as Hadfield steel is often used for components like crossing noses. This is due to its ability to rapidly strain harden, providing more durability where rails experience much higher lateral forces and impact as trains change direction. Despite the material being chosen for its desirable characteristics and durability, its lifespan still remains finite and is a costly component to repair or replace. A laser clad coating could be considered as a method to expand the life of such components. When exposed to high temperature cast manganese is prone to the formation of martensite, hence the controlled and localised laser cladding process could be beneficial as an alternative to weld repair. The SYS-PSS of this material is therefore required for

modelling.

A twin-disc manganese sample was manufactured from a crossing nose removed from service. This was subjected to twin-disc testing at 1500 MPa, -1% slip for 30,000 cycles. The wear rate of the tested rail disc was 9.28 μg and the wear rate of the wheel disc was 29.57 μg. The initial average hardness of the material is 257.5 $H_{v0.2}$ (2526.5 MPa) with initial shear yield stress $k_0 = 842.2$ MPa. The increase in hardness after testing can be seen in Figure 2.
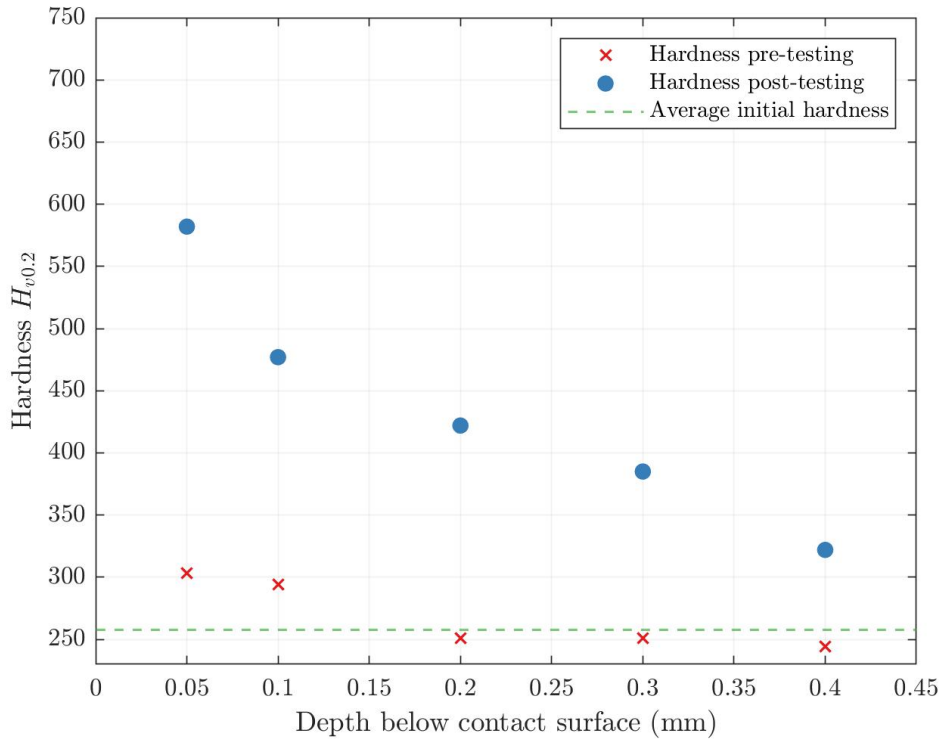
Figure 2: Manganese. Increase in hardness after testing at 1500 MPa, -1% slip and 30,000 cycles compared with material hardness pre-testing

The hardness measurements and corresponding effective shear yield stress values for the cast manganese, after testing for 30,000 cycles in the test conditions described above, are shown in Table 1. The relationship between depth and effective shear yield stress is found from the line of best fit to this data, shown in Figure 3.

Depth (mm)	0.05	0.1	0.2	0.3	0.4	0.5	0.6	0.7	0.8	0.9	1
Hv	582	477	422	385	322	318	294	299	282	280	219
k_{eff}	951.6	779.9	690.0	629.5	526.5	519.9	480.7	488.9	461.1	457.8	358.1

Table 1: Cast manganese: depth below contact surface (mm), hardness pre-testing, hardness post-testing and effective Shear Yield Stress
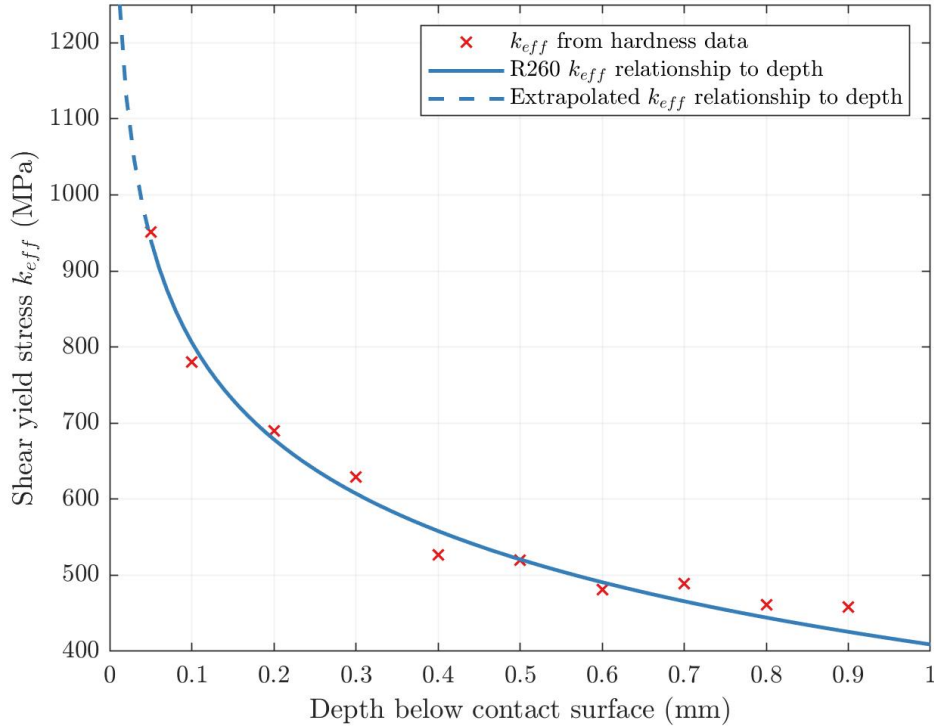
Figure 3: Cast manganese steel, line of best fit showing the Shear Yield Stress relationship with depth x, $\qquad k_{eff} = 1926x^{-0.08143} - 1517$

The equation for the relationship between effective shear yield stress and depth is shown in Equation 1.

$$k_{eff} = 1926x^{-0.08143} - 1517 \qquad\qquad (1)$$

An optical microscopy image of the twin-disc cast manganese sample was used to measure the angles of deformation, and is shown in Figure 4 with the data points recorded in Table 2 along with the corresponding plastic shear strain and effective shear yield stress using Equation 1.
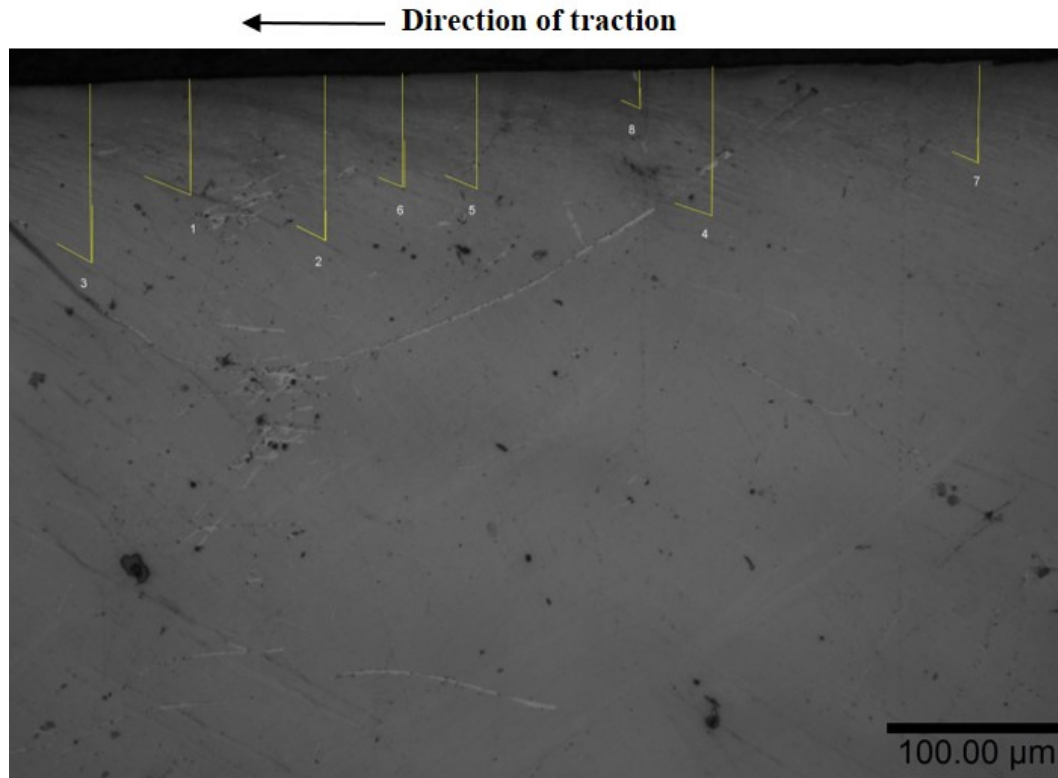
Figure 4: Image showing the measured angles of deformation and corresponding depth measurements within the cast manganese steel . Measurements taken with imagej software on optical microscopy and recorded in Table 2 strain angle measurements with imagej

Angle number	Depth (mm)	Angle of deformation (deg)	Plastic Shear Strain	Shear Yield Stress (MPa)
1	0.065	68.20	2.50	889
2	0.092	63.44	2.00	822
3	0.099	61.45	1.84	808
4	0.084	71.57	3.00	839
5	0.063	64.25	2.07	895
6	0.064	68.20	2.50	892
7	0.054	64.68	2.11	926
8	0.021	66.04	2.25	1121

Table 2: Cast Manganese depth below contact area with corresponding Plastic Shear Strain and Effective Shear Yield Stress using equation from Figure 3.19

Using the data points presented in Table 2 the SYS-PSS curve is found as the line of best fit as shown in Figure 5. Equation 2 provides the modified Voce equation for cast manganese.

$$k_{eff} = 924.3(1 - \exp^{-8.256(\gamma_p)})^{588800} \tag{2}$$
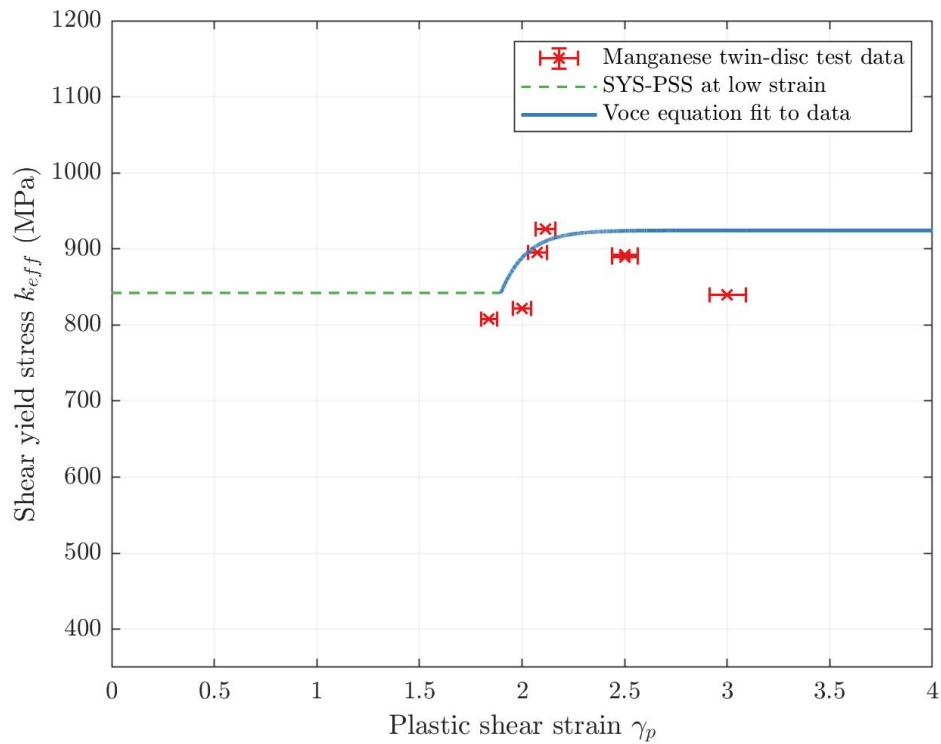
Figure 5: Modified Voce equation with parameters for cast manganese steel representing the SYS-PSS material response behaviour fit to the experimental data.

Similarly to the BS11 rail steel studied by Kapoor et al. [67] the SYS-PSS relationship at low strain is uncertain as seen in Figure 5. The modified Voce equation if valid where $\gamma_{min} \geqslant 1.9$. The critical strain value is not found due to no evidence of the deformation leading to crack initiation points at the surface under the test conditions used here.

B   Repair test extended results

Repair test twin-disc results

More detailed results from the repair tests in Chapter 4 are presented here. The results from the dry wear test of the repair disc which was run to 30,000 cycles are presented in Table 3, including the mass and diameter of the rail and wheel disc measured every 5000 cycles when the test was stopped. The results of the RCF test which ran for 500 dry and 5,000 wet cycles are presented in Table 4, including the mass and diameter of the rail disc and wheel disc before the test and after the combined 500 dry and 5000 wet cycles. Table 5 shows the results of the RCF test which ran for 500 dry and 15,000 wet cycles. The average hardness measurements of the repairs before and after each of the tests are presented in Table 6.

Cycles	Rail mass (g)	Wheel mass(g)	Rail diameter (mm)	Wheel diameter (mm)
Before testing	161.9120	169.3497	45.67	47.03
5000	161.8994	169.3431	45.67	46.92
10000	161.8650	169.2865	45.75	46.89
15000	161.8149	169.1539	45.73	46.89
20000	161.780	169.0511	45.68	46.84
25000	161.7534	168.9466	45.67	46.53
30000	161.7194	168.7047	45.65	46.44

Table 3: Repair disc 1 wear tests - Sample mass and diameter measurements before and after twin-disc testing.

Cycles	Rail mass (g)	Wheel mass(g)	Rail diameter (mm)	Wheel diameter (mm)
Before testing	161.8040	169.4820	45.75	46.99
5000 wet	161.8026	169.4740	45.75	46.92

Table 4: Repair disc 3 RCF tests - Sample mass and diameter measurements before and after twin-disc testing.

Cycles	Rail mass (g)	Wheel mass(g)	Rail diameter (mm)	Wheel diameter (mm)
Before testing	161.9940	169.2978	45.78	47.02
500 dry	161.9913	169.2635	45.78	47.00
5000 wet	161.9887	169.2542	45.77	47.08
10000 wet	161.9853	169.2488	45.75	46.91
15000 wet	161.9815	169.2427	45.68	46.91

Table 5: Repair disc 2 wear tests - Sample mass and diameter measurements before and after twin-disc testing.

Repair	Material	Pre-test	Wear test	5,000 cycle RCF test	15,000 cycle RCF test
1	R260	575	533	398	404
2	MSS	512	560	599	571
3	MSS	511	484	554	551
4	Stellite 6	505	497	644	684
5	MSS	503	677	627	553
6	Stellite 6	545	538	587	638

Table 6: Average hardness of the repairs before and after each test

Repair roughness profile results

The following tables present the evolution of surface roughness parameters for each of the repair sites. The parameters shown are Ra the average roughness of the profile, Rq the root mean square roughness of profile, Rt the maximum peak to valley height of the roughness profile and Rz the mean peak to valley height of roughness profile at intervals of 5,000 cycles during the wear test run at 1500 MPa, -1% slip to 30,000 cycles.

Cycles	Ra (μm)	Rq (μm)	Rt (μm)	Rz (μm)
Pre testing	0.407	0.571	4.653	2.583
5000	1.960	5.280	60.568	15.414
10000	17.339	43.927	489.297	158.1996
15000	6.273	18.334	198.240	52.254
20000	5.937	15.729	164.871	42.939
25000	22.978	42.702	375.690	120.529
30000	7.722	16.906	17.384	52.467

Table 7: Evolution of surface profile measurements of the R260 repair during the dry wear test up to 30,000 cycles.

Number of cycles	Ra	Rq	Rt	Rz
0	0.333	0.439	3.346	2.053
5000	0.391	0.499	3.362	2.366
10000	0.665	1.074	10.130	4.740
15000	0.349	0.450	2.469	2.18
20000	0.569	0.725	4.863	3.575
25000	0.701	1.146	10.91	4.712
30000	0.710	0.917	6.085	4.516

Table 8: Evolution of surface profile measurements of MSS repair 2 during the dry wear test up to 30,000 cycles.

Number of cycles	Ra	Rq	Rt	Rz
0	0.310	0.387	2.204	1.769
5000	0.268	0.337	2.065	1.513
10000	0.485	0.626	3.787	2.677
15000	0.548	0.728	5.391	3.698
20000	0.633	0.973	9.495	4.317
25000	0.581	0.767	5.298	3.794
30000	0.901	1.342	10.391	6.038

Table 9: Evolution of surface profile measurements of MSS repair 3 during the dry wear test up to 30,000 cycles.

Number of cycles	Ra	Rq	Rt	Rz
0	0.355	0.46	2.999	2.305
5000	0.344	0.508	4.286	2.305
10000	1.449	3.413	34.871	9.439
15000	0.899	1.221	9.872	5.638
20000	2.159	4.800	48.630	15.945
25000	2.934	9.178	111.899	25.900
30000	0.534	0.662	3.891	2.803

Table 10: Evolution of surface profile measurements of MSS repair 5 during the dry wear test up to 30,000 cycles.

Number of cycles	Ra	Rq	Rt	Rz
0	0.376	0.488	3.231	2.243
5000	0.298	0.376	2.320	1.794
10000	0.428	0.575	4.247	2.678
15000	2.191	5.927	71.53	20.835
20000	0.753	1.152	10.625	5.501
25000	0.705	1.292	15.248	5.663
30000	0.421	0.543	3.738	2.607

Table 11: Evolution of surface profile measurements of Stellite 6 repair 4 during the dry wear test up to 30,000 cycles.

Number of cycles	Ra	Rq	Rt	Rz
0	0.401	0.530	3.259	2.296
5000	0.377	0.480	3.374	2.189
10000	0.619	0.846	6.434	4.152
15000	0.489	0.642	4.458	3.121
20000	3.197	7.680	82.807	20.524
25000	1.955	4.561	73.936	23.643
30000	0.769	1.053	8.815	5.253

Table 12: Evolution of surface profile measurements of Stellite 6 repair 6 during the dry wear test up to 30,000 cycles.

C Surface roughness extended results

Wavelength and Asperity tip radius data

More detailed results from the surface roughness investigation of R260 grade rail steel and MSS laser clad coating in Chapter 5 are presented here. Tables 13 and 14 show a more detailed results table for the number of asperity peaks measured over the 250 μm sample for R260 and MSS respectively, from which the wavelength was calculated.

Wavelength/ Number of cycles	0	2500	5000	7500	10000	20000	300000
Asperities (A) $\geqslant 0\mu$m	13	10	9	11	10	12	11
Asperities (B) $\geqslant 0.10\mu$m	13	9	9	11	10	10	9
Asperities (C) $\geqslant 0.25\mu$m	9	6	5	11	9	7	6
λ_A (μm)	19.23	25.00	27.78	22.72	25.00	20.83	22.72
λ_B (μm)	19.23	27.78	27.78	22.72	25.00	25.00	27.78
λ_C (μm)	27.78	41.67	50.00	22.72	27.78	35.71	41.67

Table 13: Number of asperity peaks measured over the 250 μm sample and the associated wavelength for R260 grade rail steel.

Number of cycles	0	2500	5000	7500	10000	300000
Asperities (A) $\geqslant 0\mu$m	11	6	6	8	10	8
Asperities (B) $\geqslant 0.10\mu$m	10	5	5	8	8	8
Asperities (C) $\geqslant 0.25\mu$m	9	3	4	7	8	5
λ_A (μm)	22.72	41.67	41.67	31.25	25.00	31.25
λ_B (μm)	25.00	50.00	50.00	31.25	31.25	31.25
λ_C (μm)	27.78	83.33	62.50	35.71	31.25	50.00

Table 14: Number of asperity peaks measured over the 250 μm sample and the associated wavelength for MSS laser clad coating.

Rough surface measurement record

The following tables present the evolution of surface roughness parameters for the R260 and MSS. The parameters shown are Ra the average roughness of the profile, Rq the root mean square roughness of profile, Rt the maximum peak to valley height of the roughness profile and Rz the mean peak to valley height of roughness profile after unlubricated twin-disc tests run at 1500 MPa, -1% slip to 30,000 cycles.

Number of cycles	Ra	Rq	Rt	Rz
0	0.728	0.956	6.110	4.200
2500	0.299	0.419	3.157	2.003
5000	0.228	0.293	1.989	1.361
7500	0.470	0.650	4.725	3.043
10000	0.360	0.490	4.562	2.554
20000	0.214	0.274	1.766	1.297
30000	0.501	0.835	9.049	4.665

Table 15: Evolution of surface profile measurements of R260 grade rail steel during the dry wear test up to 30,000 cycles.

Number of cycles	Ra	Rq	Rt	Rz
0	0.478	0.90	2.972	2.436
2500	0.286	0.367	2.223	1.679
5000	0.381	0.752	8.331	2.958
7500	0.344	0.424	2.557	1.909
10000	0.244	0.326	2.633	1.507
30000	0.308	0.394	2.596	1.831

Table 16: Evolution of surface profile measurements of MSS laser clad coating during the dry wear test up to 30,000 cycles.

D Coefficient of traction loading blocks

Loading block	Start cycle	End cycle	CoT
1	0	999	0.35
2	1000	1999	0.47
3	2000	6999	0.43
4	7000	11999	0.41
5	12000	19999	0.39
6	20000	30000	0.37

Table 17: Start and end cycles for Coefficient of Traction in 6 blocks.

Loading block	Start cycle	End cycle	CoT
1	0	499	0.26
2	500	999	0.44
3	1000	1499	0.46
4	1500	1999	0.47
5	2000	2499	0.46
6	2500	2999	0.45
7	3000	3499	0.44
8	3500	6999	0.43
9	7000	8999	0.42
10	9000	9999	0.41
11	10000	12999	0.40
12	13000	16999	0.39
13	17000	19999	0.38
14	20000	24999	0.37
15	25000	30000	0.36

Table 18: Start and end cycles for Coefficient of Traction in 15 blocks.